Investigating the Critical Quality Attributes of mRNA-Loaded Lipid Nanoparticles and Their Biomolecular Corona Using Novel Analytical Pipelines

Thesis presented by

Rand Abdulrahman

Supervised by Professor Zahra Rattray & Professor Yvonne Perrie

In fulfilment of the requirement of the degree of

Doctor of Philosophy

2026

Strathclyde Institute of Pharmacy and Biomedical Sciences

University of Strathclyde

Glasgow, UK

Industry supervisors: Dr Kevin Treacher & Dr Robin Capomaccio

Global Product Development, Pharmaceutical Technology & Development, Operations

AstraZeneca

Macclesfield, UK

Declaration of Authenticity

This thesis is the result of the author's original research. It has been composed by the author and has not been previously submitted for examination which has led to the award of a degree. The copyright of this thesis belongs to the author under the terms of the United Kingdom Copyright Acts as qualified by University of Strathclyde Regulation 3.50. Due acknowledgement must always be made of the use of any material contained in or derived from this thesis.

This thesis was written by the author using original research conducted by author in between 1st October 2022 until 1st February 2026. This thesis has not been previously submitted for examination or led to an award.

Signed: *Rand Abdulrahman*

Date: 10th Feb 2026

Acknowledgements

Firstly, I would like to thank my family for their continuous support and encouragement to continue my academic studies. They all have been my main source of encouragement each day throughout the PhD, even though they are miles away.

I extend my gratitude all my supervisors, Professor Zahra Rattray, Professor Yvonne Perrie, Dr Kevin Treacher and Dr Robin Capomaccio. They all provided me with continuous encouragement, thoughtful guidance and constructive feedback. Apart from enriching this project with scientific contributions, they also contributed significantly to my personal growth. I am very thankful to AstraZeneca Pharmaceuticals (Global Product Development, Pharmaceutical Technology & Development, Operations, Macclesfield UK) for funding and believing in the value and potential of this project.

Additionally, my sincere thanks are to Dr Muattaz Hussain for his expert support in lipid nanoparticle synthesis. The insightful discussions we had enriched and refined my approach to formulation science. I would also like to thank Dr Robin Capomaccio at AstraZeneca Pharmaceuticals and Ms Panida Punnabhum, the research technician of Multiscale Metrology Suite at University of Strathclyde for their constant guidance with the flow-field flow fractionation instrument. Their expert advice and training on the instrument helped me with the execution of the experimental work.

I am sincerely grateful to all members of the lab of Professor Zahra Rattray and Professor Nicholas Rattray for their valuable contributions. Our insightful discussions and collaborative knowledge-sharing significantly enriched my experience. I am sincerely thankful to my friends Lamina, Laura, Ana, and Haniah for their continued support and encouragement throughout my PhD, despite the distance between us. I am also thankful to the wonderful friends I made in Scotland. Although the list is long, Abdullah Al-Sultan, Lisa, Rana, Lina, Burcu, Rawan, Zainab, Rahaf, Lana, Ashish, Varun and Manal quickly became cherished friends and extended a warm welcome to me in Scotland from my very first day. In conclusion, I am thankful to myself for the self-belief and maintaining resilience throughout this PhD journey.

Abstract

Lipid nanoparticles (LNPs) have emerged as a promising platform for messenger RNA (mRNA) encapsulation, as demonstrated by their pivotal role during the coronavirus disease 2019 (COVID-19) pandemic. Despite the availability of several mRNA vaccines on the market and ongoing clinical trials, thorough characterization of formulation Critical Quality Attributes (CQAs), particularly in terms of stability and interactions with biological systems forming the biomolecular corona remains a complex challenge.

This thesis established an advanced and efficient separation and characterization platform to evaluate three LNP prototypes distinguished by their cationic/ionizable lipid components, DOTAP, MC3, and SM-102. Initially, the stability of the DOTAP-LNP prototype was assessed alongside the development of a characterization method employing Asymmetric Flow Field-Flow Fractionation combined with multiple in-line optical detectors (AF4-MD) in Chapter 2. Subsequent *in vitro* cytotoxicity assessments of this prototype together with existing literature indicated cytotoxic effects associated with DOTAP-LNPs. Based on these findings, the study proceeded with alternative prototypes, MC3 and SM-102-LNPs. Biomolecular corona studies of two LNP prototypes with Bovine Serum Albumin (BSA) revealed that while both LNPs exhibited altered attributes following biomolecular corona formation, the changes were more pronounced for MC3-LNPs compared to SM-102-LNPs in Chapters 3-4. To further investigate whether SM-102-LNPs could inhibit significant affinity to other biomolecules, their interaction with High-Density Lipoprotein (HDL) was examined in Chapter 5. This analysis revealed that biomolecular corona formation of SM-102-LNPs is biomolecule-specific. Downstream analysis of the separated fractions led to the development of a gentle isolation pipeline for effectively separating LNPs from associated biomolecules.

Overall, this thesis has established a foundational framework for the separation and characterization of CQAs for mRNA-LNPs. The findings demonstrate the potential of employing orthogonal, high-resolution separation techniques in the early prototyping of mRNA-LNP formulations and their nano-bio interactions. Furthermore, this work highlights the necessity of establishing standardised, robust, and versatile analytical platforms, such as the one developed herein, to enable the rapid characterisation of mRNA-LNP formulations. Such approaches can support regulatory decision-making by providing optimised protocols based on orthogonal analytical techniques, thereby accelerating the development and translation of these delivery systems.

Research Outputs

Publications

Rand Abdulrahman, Panida Punnabhum, Robin Capomaccio, Kevin Treacher, Yvonne Perrie, Zahra Rattray. *Multi-detector frit-inlet asymmetric flow field-flow fractionation method development for nanoparticle mixtures: Deeper analysis beyond ISO quality standards.* Analytical Methods, 2026. Analytical Methods. 2026. https://doi.org/10.1039/D5AY01758K
Rand Abdulrahman: Writing – review & editing, Writing – original draft, Methodology, Investigation, Formal analysis, Data curation, Conceptualization.

Rand Abdulrahman, Panida Punnabhum, Robin Capomaccio, Kevin Treacher, Yvonne Perrie, Zahra Rattray. *Frit-inlet asymmetric flow field-flow fractionation for the analysis of lipid nanoparticle-protein interactions*. Journal of Chromatography A. Volume 1743. 2025. ISSN 0021-9673. https://doi.org/10.1016/j.chroma.2025.465663
Rand Abdulrahman: Writing – review & editing, Writing – original draft, Methodology, Investigation, Formal analysis, Data curation, Conceptualization.

Callum G Davidson, **Rand Abdulrahman**, Panida Punnabhum, Robin Capomaccio, Kevin Treacher, Yvonne Perrie, Zahra Rattray. *The use of orthogonal analytical approaches to profile lipid nanoparticle physicochemical attributes*. Nano Futures. Volume 8. 2024. https://doi.org/10.1088/2399-1984/ad70e6
Rand Abdulrahman: Writing – review and editing, Investigation, Methodology, Data curation.

Rand Abdulrahman, Huda Ibrahem, Amna Mahmood, Kevin Treacher, Robin Capomaccio, Catherine Vasey, Yvonne Perrie, Zahra Rattray. *Lipid nanoparticle protein corona formation and cytocompatibility*. British Journal of Pharmacy. Volume 8. 2023. https://doi.org/10.5920/bjpharm.1398
Rand Abdulrahman: Writing – review & editing, Writing – original draft, Methodology, Investigation, Formal analysis, Data curation, Conceptualization.

Conference contributions

Oral presentations

Abdulrahman, R., Punnabhum, P., Perrie, Y., Treacher, K., Vasey, C., Capomaccio, R., Rattray, Z. *The use of low to high resolution techniques to separate lipid nanoparticles and simple protein corona complexes*. *AstraZeneca Research Day*. 2024. Macclesfield, UK.

Abdulrahman, R., Punnabhum, P., Daramy, K., Davidson, C., Treacher, K., Capomaccio, R., Vasey, C., Perrie, Y., Rattray, Z. *Investigating the critical quality attributes of lipid nanoparticle prototypes in protein containing media*. *The Federation of Analytical Chemistry and Spectroscopy Societies (FACSS) and the SciX*. 2023. Nevada, USA.

Abdulrahman, R., Punnabhum, P., Perrie, Y., Treacher, K., Vasey, C., Capomaccio, R., Rattray, Z. *Investigating the physicochemical properties of lipid nanoparticles in protein containing media. International Flow Field Flow Fractionation (IsFFF2024)*. 2024. Nantes, France.

Poster presentations

Abdulrahman, R., Davidson, C., Perrie, Y., Treacher, K., Vasey, C., Capomaccio, R., Rattray, Z. *Stability study of Poly(A) lipid nanoparticles stored under different conditions based on the evaluation of their critical quality attributes. United Kingdom and Ireland Controlled Release Society Symposium* 2023. London, UK.

Abdulrahman, R., Davidson, C., Perrie, Y., Treacher, K., Vasey, C., Capomaccio, R., Rattray, Z. *Physicochemical characterisation of poly(A) lipid nanoparticles: effect of cryoprotectant and temperature storage conditions*. in *European Platform for Technology Network on Nanomedicine Symposium*. 2023. Liverpool, UK.

Abdulrahman, R., Ibrahem, H., Mahmood, A., Treacher, K., and R. Capomaccio, Vasey, C., Perrie, Y., Rattray, Z. *Assessing lipid nanoparticle protein corona formation and cytocompatibility. The Academy of Pharmaceutical Sciences*. 2023. Reading, UK: British Journal of Pharmacy.

Abdulrahman, R., Punnabhum, P., Perrie, Y., Treacher, K., Vasey, C., Capomaccio, R., Rattray, Z. *The use of low to high resolution techniques to separate lipid nanoparticles and simple protein corona complexes. AstraZeneca Research Day*. 2024. Macclesfield, UK.

Internship

Alterations in protein conformation following adsorption on lipid nanoparticles; characterisation using asymmetric flow field flow fractionation and circular dichroism. 2024. New Modalities Product Development, Pharmaceutical Technology & Development, Operations, AstraZeneca, Macclesfield, UK.

List of Teaching Activities

Demonstrator in Pure and Applied Chemistry as well as SIPBS teaching laboratories at the University of Strathclyde, providing support to undergraduate students in chemistry and biomedical science laboratories across the first and second semesters of 2023 and 2024.

Contributed to postgraduate research training by supporting the projects of two MSc in Cancer Research students (June-August 2023) and one MRes student (December-April 2024). This involved providing technical guidance, assisting with experimental design and laboratory techniques, and offering feedback on data analysis and interpretation.

Table of Contents

List of Abbreviations

AF4	Asymmetric Flow Field-Flow Fractionation
Apo	Apolipoprotein
ALC-0159	Methoxypolyethyleneglycoloxy(2000)-N,N-ditetradecylacetamide
ALC-0315	(4-hydroxybutyl)azanediyl)bis(hexane-6,1-diyl)bis(2-hexyldecanoate)
ASGPR	Asialoglycoprotein Receptor
ASO	Antisense Oligonucleotide
ASTM	American Society for Testing and Materials
BSA	Bovine Serum Albumin
COVID-19	Coronavirus Disease 2019
CQA(s)	Critical Quality Attributes
CRISPR-Cas9	Clustered Regularly Interspaced Short Palindromic Repeats And CRISPR-Associated Protein 9
Cryo-TEM	Cryogenic Transmission Electron Microscopy
D	Diffusion coefficient
DF	Detector Flow
DLin-MC3-DMA	4-(dimethylamino)-butanoic acid, (10Z,13Z)-1-(9Z,12Z)-9,12-octadecadien-1-yl-10,13-nonadecadien-1-yl ester
DLS	Dynamic Light Scattering
DMG-PEG 2000	1,2-dimyristoyl-rac-glycero-3-methoxypolyethylene glycol-2000
DMG-pSar	1,2-dimyristoyl-sn-glycero-3-succinyl-N-polysarcosine
DOE	Design of Experiments
DOPE	Dioleoylphosphatidylethanolamine
DOPC	1,2-dioleoyl-sn-glycero-3-phosphocholine
DOTAP	1,2-Dioleoyl-3-trimethylammoniumpropane (chloride
DSPC	1,2-distearoyl-sn-glycero-3-phosphocholine
EDL	Electric Double Layer
EDTA	Ethylenediaminetetraacetic Acid
EE	Encapsulation Efficiency
EMA	European Medicines Agency
EUNCL	European Nanomedicine Characterization Laboratory

FDA	Food and Drug Administration
FFF	Field-Flow Fractionation
FI-AF4	Frit-Inlet Asymmetrical Flow Field-Flow Fractionation
FLD	Fluorescence Detector
FLuc	Firefly Luciferase
FRR	Flow Rate Ratio
F/T	Freeze-Thaw
FWHM	Full Width at Half Maximum
GalNAc	N-acetylgalactosamine
GMP	Good Manufacturing Practice
H_{II}	Hexagonal II
hATTR	Hereditary Transthyretin Amyloidosis
HDL	High-Density Lipoprotein
HSA	Human Serum Albumin
ICP-MS	Inductively Coupled Plasma Mass Spectrometry
IDL	Intermediate-Density Lipoprotein
IgA	Immunoglobulin A
IgG	Immunoglobulin G
IgM	Immunoglobulin M
IM	Intramuscular
ISO/TS	International Organization for Standardization Technical Specification
IV	Intravenous
JRC	Joint Research Centre of the European Commission
kDa	Kilodaltons
LC-MS	Liquid Chromatography-Mass Spectrometry
LDL	Low-Density Lipoprotein
LNP	Lipid Nanoparticle
MALAT1	Metastasis Associated Lung Adenocarcinoma Transcript 1
MALS	Multi-Angle Light Scattering
MWCO	Molecular Weight Cut-Off
mRNA	Messenger Ribonucleic Acid
MPS	Mononuclear Phagocyte System

NIBS	Non-Invasive Backscatter
N/P	Nitrogen/Phosphate
NTA	Nanoparticle Tracking Analysis
PBS	Phosphate-Buffered Saline
PEG	Polyethylene Glycol
PEG-c-DMA	Polyethylene Glycol-carbamate-Dimyristoyl-sn-glycerol
PDI	Polydispersity Index
PES	Polyethersulfone
Poly(A)	Polyadenosine
PVDF	Polyvinylidene Fluoride
QbD	Quality by Design
RC	Regenerated Cellulose
RES	Reticuloendothelial System
RMSE	Root Mean Square Error
R_g	Radius of Gyration
R_h	Hydrodynamic Radius
RI	Refractive Index
RSD	Relative Standard Deviation
SARS-CoV-2	Severe Acute Respiratory Syndrome Coronavirus 2
SAXS	Small-Angle X-ray Scattering
SDS PAGE	Sodium Dodecyl Sulfate-Polyacrylamide Gel Electrophoresis
SF	Shape Factor
SHM	Stagged Herringbone Micromixer
siRNA	Small Interfering RNA
SEC	Size-Exclusion Chromatography
SM-102	8-[(2-hydroxyethyl)[6-oxo-6-(undecyloxy)hexyl]amino]-octanoic acid 1-octylnonyl ester
SPR	Surface Plasmon Resonance
TBS	Tris-Buffered Saline
TE	Tris-EDTA
TEM	Transmission Electron Microscopy
TFR	Total Flow Rate
TFF	Tangential Flow Filtration

UV	Ultraviolet
VLDL	Very Low-Density Lipoprotein
XF	Cross Flow
ζ-potential	Zeta Potential

Chapter 1: General Introduction

1.1 Lipid Nanoparticles (LNPs) for Drug Delivery

Lipid-based nanoparticles (LNPs) have emerged as a non-viral, versatile and clinically validated platform for drug delivery, offering significant advantages in the encapsulation, protection, and targeted transport of therapeutic agents. Their unique physicochemical properties enable efficient delivery of small molecules, nucleic acids, and biologics across various biological barriers. The first lipid-based formulation was a liposomal formulation in 1995, Doxil® (doxorubicin) indicated for Kaposi's sarcoma, marking a new era in lipid-based drug delivery systems [1]. However, liposomes face key limitations including the limited ability to deliver large and charged payloads like nucleic acids. The encapsulation of mRNA into a liposomal aqueous core is inefficient and often requires multiple steps that still yield low encapsulation efficiencies [2]. These challenges have resulted in a shift in drug delivery focus from liposomes to LNPs in recent years, particularly due to their proven track record of success in messenger RNA (mRNA)-based vaccines and small interfering RNA (siRNA) therapeutics.

LNPs consist of a lipid core surrounded by a lipid layer composed of (1) an ionizable lipid (2) a phospholipid (3) cholesterol and (4) a polyethylene glycol (PEG)-conjugated lipid (**Figure 1.1**). This unique composition enables LNPs to efficiently complex with and protect their nucleic acid cargo from *in vivo* degradation by nucleases in blood plasma and intracellular nucleases following cellular uptake *in vivo*. LNPs incorporate ionizable lipids which form cationic charges at low pH, promoting encapsulation of negatively charged nucleic acids and facilitate endosomal escape upon internalization, enhancing intracellular delivery of genetic material, a feature not enabled by traditional liposomes [3, 4]. The spatial distribution of lipids in LNPs depends on the molecular structure and composition of lipids as well as the physicochemical properties of their cargo [5]. It remains unclear how different lipids assemble in the LNP complex relative to the mRNA encapsulated in the core. Viger-Gravel *et al.* studied the spatial arrangement of different lipids within the LNP structure. They proposed a model in which 1,2-distearoyl-sn-glycero-3-phosphocholine (DSPC) phospholipid and PEG-lipid were at the surface of the LNP; whereas the cholesterol and ionizable lipid are in the core close the mRNA cargo [6]. Conversely, Kulkarni *et al.* showed that DSPC-Cholesterol forms crystals, which reside in the outer monolayer surrounding the LNP core [7].

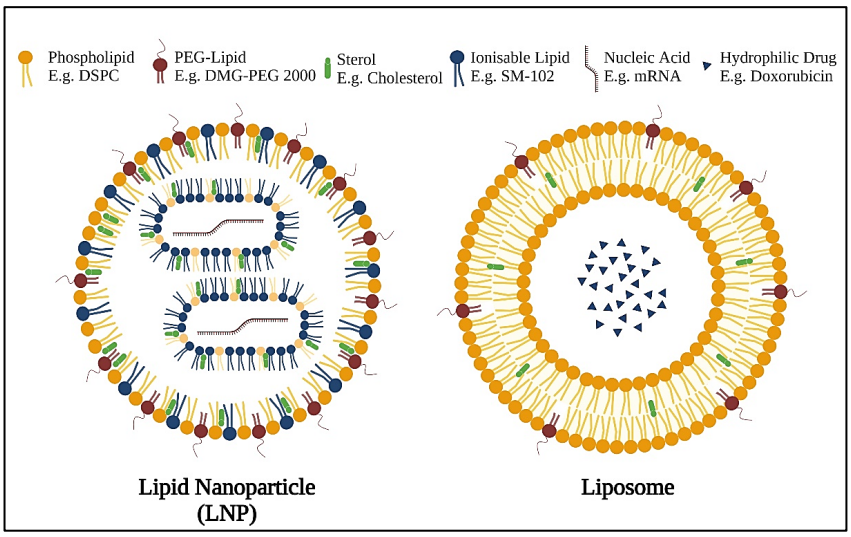

Figure 1.1 Liposome and LNP structure. The different components include cholesterol, DSPC (1,2-distearoyl-sn-glycero-3-phosphocholine), SM-102 (8-[(2-hydroxyethyl)[6-oxo-6-(undecyloxy)hexyl]amino]-octanoic acid, DMG-PEG 2000 (1,2-dimyristoyl-rac-glycero-3-methoxypolyethylene glycol-2000), messenger RNA (mRNA). Created with BioRender.com.

LNPs represent a rapidly expanding delivery technology in the biopharmaceutical sector. The global market was estimated at USD 786.4 million in 2024 and is projected to approximately double (to USD ~1.54 billion) by 2030 [8]. The rapid development and mass administration of mRNA-LNPs during the COVID-19 pandemic (combating severe acute respiratory syndrome coronavirus 2 (SARS-CoV-2)) increased their interest in subsequent years and established their scalability, and transformative potential. Progress in LNP technology has expanded their application across multiple fields, including oncology [9], gene therapy [10], gene editing tools e.g., clustered regularly interspaced short palindromic repeats (CRISPR)-Cas9 [11], infectious disease [12-14], glaucoma (QPI-100 and SYL040012 in clinical trials [15]), and additional therapeutic areas. By the time of writing this thesis there are five LNP therapeutics approved for clinical use (Onpattro® [16], Spikevax® [17], Comirnaty® [18] mNEXSPIKE® [19] and mRESVIA® [12]). As of 2025, there are >150 RNA-LNP formulations in clinical trials [20]. Collectively, the availability of licensed LNP-based therapeutics and the breadth of candidates progressing through clinical development highlight the significant and sustained advancement of LNP-based technology.

Despite this significant clinical progress, the effective use of LNPs still depends on their ability to traverse various biological barriers prior to reaching target cells and tissues. The first biological barrier encountered upon systemic administration is degradation by serum nucleases, which rapidly cleave nucleic acid-based therapeutics [21]. Further, the innate

immune system poses a barrier to mRNA delivery, as serum opsonins can adsorb onto mRNA molecules, promoting phagocytic clearance [22].

In instances when nucleic acid drugs evade degradation and immune clearance, they must traverse vascular endothelia by transcellular or paracellular routes to access target sites. Efficient intracellular delivery remains a formidable challenge for mRNA delivery by virtue of mRNA physicochemical properties. LNPs have enabled delivery of nucleic acids with highly diverse molecular sizes and mechanisms of action. For instance, nucleic acid therapeutics, including vaccines, are designed to exploit cellular translation machinery to produce functional proteins. COVID-19 vaccines encapsule mRNAs which are typically large molecules (the mRNA in Comirnaty® vaccine has a molecular weight of approximately 1,388 kDa [23]). In comparison, siRNA encapsulated in LNPs are smaller compared to mRNA (the siRNA in Onpattro®, patisiran sodium, has a molecular weight of 14.3 kDa [24]). Collectively, these examples illustrate the versatility of LNPs as a non-viral delivery platform capable of accommodating a broad spectrum of nucleic acid cargos and overcome transport barriers.

In addition, LNPs offer protection against enzymatic degradation, facilitate cellular uptake, and enable endosomal escape of RNA payloads. Key merits of LNPs as delivery systems are summarised in **Table 1.1.**

Table 1.1 Relative merits of LNP formulations.

Advantages	Explanation
Protection of labile therapeutics	Ionizable lipids within LNPs electrostatically bind negatively charged mRNA, encapsulating it within a protective lipid matrix that shields mRNA from nuclease degradation.
Non-viral gene delivery	Avoids risks associated with viral vectors (i.e., long-term immunogenicity) [25].
Ability to cross biological barriers	The use of pH-responsive ionizable lipids [26]. LNPs remain neutral at physiological plasma pH (~7.4), minimizing nonspecific biomolecule interactions and prolonging blood circulation, while becoming protonated in the acidic endosomal environment (pH 4-5). This protonation promotes electrostatic interactions with endosomal membranes, facilitating membrane destabilization and endosomal escape of the nucleic acid cargo.
Biocompatible lipids reducing long-term toxicity	Lipids used in LNPs are Food and Drug Administration (FDA) and European Medicines Agency (EMA) approved [7].
Surface modification for targeted delivery	Ligand-modified LNPs have been used to target hepatocytes or tumour cells with improved specificity (e.g. GalNAc ligands for liver targeting [27]).
Prolong circulation time and reduction in immune recognition	Modifications to the LNPs (e.g. PEGylation) help avoid immune recognition and prevent rapid clearance [28].
Large-scale manufacturing	Spikevax® vaccine was manufactured at commercial scale using GMP-compliant microfluidic mixing [29].
Versatility for different therapeutics	Different cargos can be encapsulated inside LNPs e.g. siRNA (Onpattro® [7]), mRNA (COVID-19 vaccines [14, 30]) and CRISPR-Cas9 components [31].
Flexibility in formulation components	Various lipid alternatives can be used (e.g. phospholipids, cholesterol, PEG-lipids) to alter properties.

1.2 Constituents of mRNA-LNPs

LNPs are composed of a mRNA payload encapsulated within the core as a result of electrostatic interactions with LNP constituent lipids [32]. The formulation typically includes four key lipid components: **(1)** an ionizable lipid, which facilitates the encapsulation of the negatively charge nucleic acid and endosomal escape, **(2)** a phospholipid, that contributes to membrane structure, **(3)** cholesterol, which enhances stability and fluidity; and (4) a polyethylene glycol (PEG)-lipid, which confers steric stability and increases circulation time. Together, these components form a protective drug delivery system that shields the mRNA from nucleases and supports its intracellular delivery. Each of these lipid constituents plays a distinct and essential role in the LNP formulation.

1.2.1 Lipid-based Components of LNP formulations

Each of the lipid components constituting the LNP confer distinctive features to the LNP. To be used in clinical applications, all lipids used in LNP production must be biocompatible, yield particles in the nanoscale size range, be biodegradable, and stable at storage temperatures to minimize degradation (4, -20, or -80 ^{o}C), with desirable encapsulating efficiency of the target mRNA [33]. The formulations of LNPs may contain different ratios of constituent ionizable lipid, phospholipid, cholesterol, and PEG-lipid (**Table 1.2**).

Table 1.2 Five RNA-LNP-based products on the market and their composition.

Product name	Route of administration	RNA	Therapeutic indication	Lipid				Excipients
				Ionizable Lipid (molar ratio %)	Phospholipid (molar ratio %)	PEG-Lipid (molar ratio %)	Sterol (molar ratio %)	
Onpattro® (Alnylam Pharmaceuticals) [16]	Intravenous (IV) infusion	Patisiran (siRNA)	Hereditary transthyretin-mediated (hATTR) amyloidosis	DLin-MC3-DMA (referred as MC3) (50)	DSPC (10)	DMG-PEG 2000 (1.5)	Cholesterol (38.5)	• Disodium hydrogen phosphate, heptahydrate • Potassium dihydrogen phosphate, anhydrous • Sodium chloride • Water for injections
Spikevax® (Moderna)[17]	Intramuscular (IM) injection	mRNA-1273	Prevention of SARS-CoV-2 infection	SM-102 (50)	DSPC (10)	DMG-PEG 2000 (1.5)		• Trometamol • Trometamol hydrochloride • Sodium acetate trihydrate • Sucrose • Water for injections
mNEXSPIKE® (Moderna) [19]		mRNA-1283	Prevention of SARS-CoV-2 infection					
mRESVIA® (Moderna) [34]		mRNA-1345	Respiratory Syncytial Virus (RSV)					
Comirnaty® (Pfizer-BioNTech) [35]		BNT 162b2	Prevention of SARS-CoV-2 infection	ALC-0315 (46.3)	DSPC (9.4)	ALC-0159 (1.6)	Cholesterol (42.7)	• Trometamol • Trometamol hydrochloride • Sucrose • Water for injections

1.2.1.1 Ionizable cationic lipids

Ionizable lipids are amphiphilic molecules composed of a hydrophilic head group, often bearing a tertiary amine headgroup connected to a long hydrophobic tail (**Figure 1.2**). Current commercial LNPs use ~50 mol % ionizable cationic lipids by composition (**Table 1.2**).

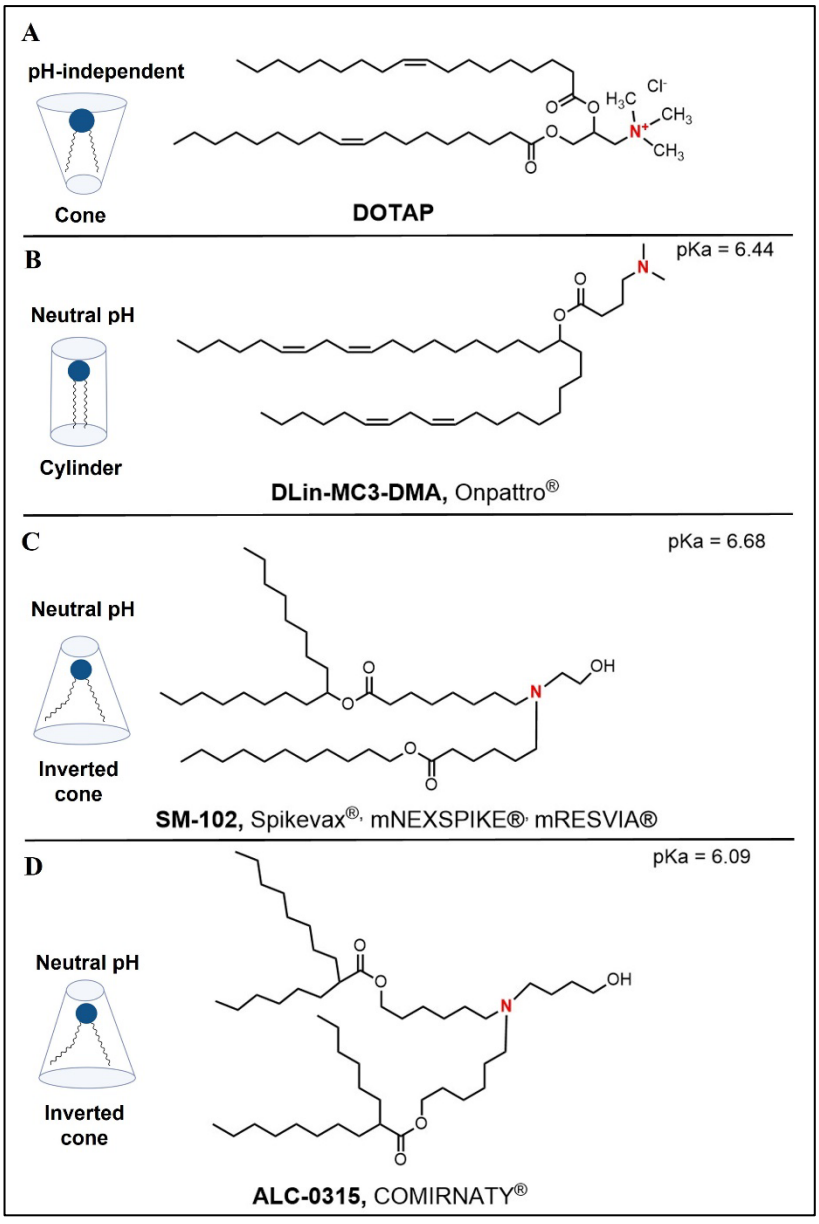

Figure 1.2 Chemical structure of cationic/ionizable lipids used in LNPs and their molecular geometry (cone, inverted cone and cylinder) adopted at neutral pH environments. Created with Biorender.com.

One example of a permanently cationic lipid is DOTAP (1,2-dioleoyl-3-trimethylammonium-propane) that contains a quaternary positively charged ammonium group. DOTAP forms strong electrostatic interactions with negatively charged nucleic acids, promoting high

encapsulation efficiency. However, the cationic nature of DOTAP is associated with elevated cytotoxicity and reduced biocompatibility, due to strong interaction with negatively charged lipids in plasma membranes resulting in membrane disruption and immune activation [36].

To overcome these inherent limitations, ionizable lipids with pH-dependent charge properties have been developed (pKa 6-7), which are widely used in mRNA vaccines (**Figure 1.2**). Examples include heptadecan-9-yl 8-((2-hydroxyethyl)(6-oxo-6-(undecyloxy)hexyl)amino)octanoate (SM-102), (6Z,9Z,28Z,31Z)-heptatriaconta-6,9,28,31-tetraen-19-yl-4-(dimethylamino)butanoate (DLin-MC3-DMA) and [(4-hydroxybutyl)azanediyl]bis(hexane-6,1-diyl)bis(2-hexyldecanoate) (ALC-0315). These lipids exhibit pH-dependent ionisation (pH (4.5 – 6) < pKa), which is critical for efficient nucleic acid encapsulation and intracellular delivery. The evolution from DOTAP to ionizable lipids reflects significant advancements in the suitability of lipids for clinical applications, particularly in the context of mRNA vaccine platforms.

During LNP formulation, nucleic acids are dissolved in a low pH buffer (sodium citrate, pH 4-5). When mixed with an organic phase containing lipids dissolved in ethanol, ionizable lipids with a pKa >4, undergo protonation of their tertiary amine headgroups in the acidic aqueous environment according to the Henderson-Hasselbalch equation [37] (**Equation 1.1**)**.** This enhances electrostatic interactions between the positively charged lipids and negatively charged nucleic acids, thereby promoting efficient encapsulation of the nucleic acid within the LNP [38].

$$\boldsymbol{pH = pKa + log_{10}\frac{[unprotonated\ head\ group]}{[protonated\ head\ group]}} \qquad \textbf{Equation 1.1}$$

Subsequently, ethanol and citrate buffer are eliminated through dialysis or an alternative buffer exchange technique, using a physiologically relevant buffer, which mimics blood pH. Adjusting the pH to 7.4 (>pKa of ionizable lipids) lowers the LNP surface charge. This stabilizes the LNP structure and ensures prolonged systemic circulation by preventing rapid sequestration by reticuloendothelial system (RES). The pKa of LNPs should be sufficiently high to allow protonation within acidic environments (endosome) and low enough to confer a slightly positive surface charge at physiological pH, facilitating electrostatic interactions with the negatively charged cell membrane.

LNPs are subsequently internalized by cells through various endocytic pathways (clathrin-mediated endocytosis and micropinocytosis) and are initially trapped within endosomes

[39]. Within the endosomal environment (pH 5.5-6.5), ionizable lipid headgroups become protonated, acquiring a positive charge. This facilitates electrostatic interactions with the negatively charged endosomal membrane, leading to destabilisation of the LNP structure and the cell membranes promoting the formation of non-bilayer structures, such as the inverted hexagonal (H_{II}) phase [40, 41]. This effectively releases the nucleic acid cargo into the cytoplasm and the interaction with other cellular components. Studies have indicated that 2-3 % of nucleic acids encapsulated in LNPs escape the endosome and reach the cytoplasm [39, 42]. The optimal pKa of the amino head group in ionizable lipid for efficient protein expression is ~6.5. In contrast, lipids with pKa values of ≤5.4 exhibit reduced transfection efficiency [43, 44]. These findings highlight the importance of balancing the use of pH-sensitive ionizable lipids in LNP formulations, as the pKa of the head group plays a critical role in facilitating endosomal escape [43].

In addition to pKa, the effectiveness of ionizable lipids is influenced by their molecular geometry under varying pH conditions. At physiological pH (pH 7.4), these lipids are predominantly uncharged and adopt a more cylindrical shape (DLin-MC3-DMA) and cone shaped (SM-102 and ALC-0315) geometry depending on their tail branching [45] (**Figure 1.2**). The cylindrical-shape geometry minimizes electrostatic interactions with serum proteins and cell membranes, enhancing circulation time and reducing cytotoxicity. In contrast, the cone-shape geometry is incompatible with cell membrane bilayers, inducing the formation of non-bilayer phases such as the inverted hexagonal (H_{II}) phase [46]. Moreover, the cone geometry of these ionizable lipids also promotes the formation of inverted micelle-like structures, in which the ionizable lipids surround and stabilise the nucleic acid payload within the LNP core (**Figure 1.2)**.

The choice between branched and non-branched lipid chains must be tailored to the functional role of each lipid within the LNP formulation. Branched lipids can improve lipid biodegradability and reduce toxicity by facilitating rapid elimination *in vivo* and reduce accumulation in tissue [47, 48].

1.2.1.2 Phospholipids

Phospholipids, exemplified by Dioleoylphosphatidylethanolamine (DOPE), Dioleoylphosphatidylcholine (DOPC), and Distearoylphosphatidylcholine (DSPC), are integral components of the LNP. These lipids, also termed ‘helper’ lipids, are zwitterionic at

physiological pH (pH 7.4), which mimics the plasma membrane lipids ensuring biocompatibility. Phospholipids provide structural stability to the LNP by facilitating the intercalation into bilayer structures and contributing to the stabilization of LNPs. Phospholipids also promote membrane fusion, facilitating cellular uptake, and endosomal

release [49, 50]. Current commercial LNPs use ~10 mol% single phospholipid component. Differences in phospholipid chemistries result in different LNP characteristics [51]. Changes in the chemical composition and concentration of phospholipids influence the surface charge of LNPs, subsequently impacting their tissue distribution and therapeutic efficacy [52].

The molecular geometries of phospholipids (cone, inverted cone and cylinder) also affect the endosomal escape of the nucleic acid cargo, which is determined by the ratio of the area occupied by the hydrophobic tails *versus* the hydrophilic head. DOPC and DOPE contain an unsaturated acyl chain in the lipid tail (**Figure 1.3**). The two unsaturated chains have a kinked structure, which increases the spatial area occupied for the hydrophobic tail adopting a cone geometry [53-55]. The unsaturated acyl chains results in lower melting points (**Figure 1.3**) and increased fluidity, which reduces LNP stability.

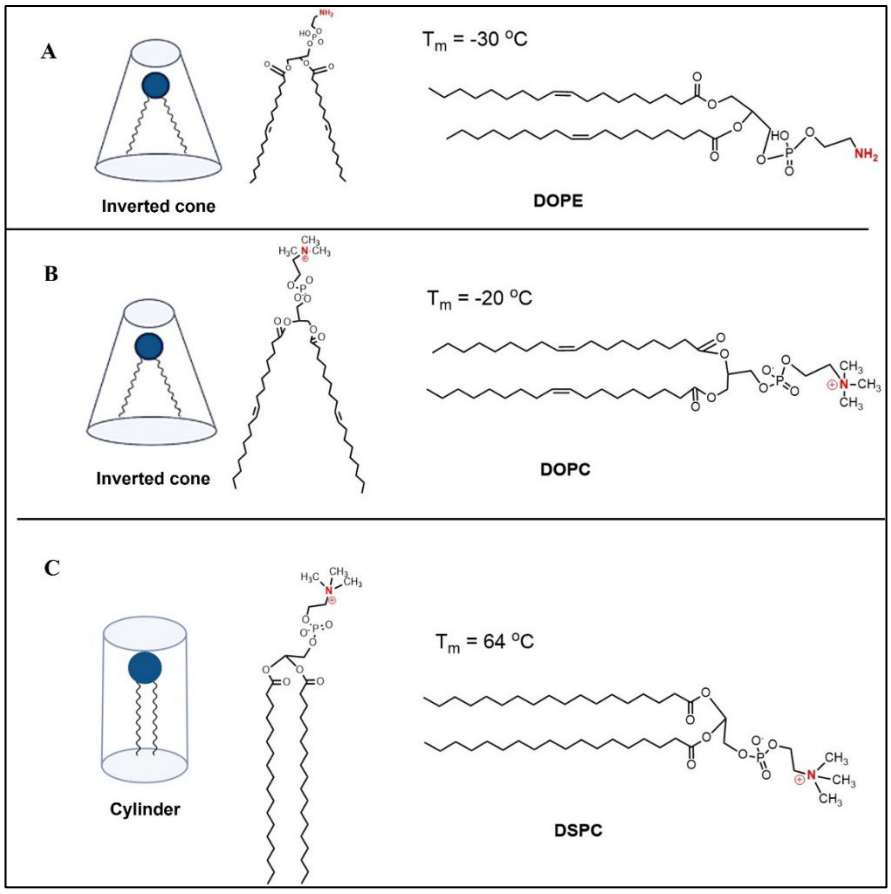

Figure 1.3 Chemical structure, geometry (inverted cone and cylinder) and melting temperature (T_m) of phospholipids (A) Dioleoylphosphatidylethanolamine (DOPE) (B) Dioleoylphosphatidylcholine (DOPC) and (C) 1,2-Distearoyl-sn-glycero-3-phosphocholine (DSPC). Created with Biorender.com.

Conversely to DOPC and DOPE phospholipids, DSPC (used in Onpattro® and all four mRNA vaccines) contains two saturated acyl chains in the lipid tail and a relatively larger

phosphocholine head group (quaternary amine with 3 methyl groups), which forms a cylinder-shaped geometry. This lipid shows a relatively high melting temperature (T_m = 64 °C), which prevents LNP degradation in biological systems and during storage and handling, improving their thermal and structural stability [56, 57]. However, DSPC can hinder LNP fusion with endosomal membranes, inhibiting endosomal escape and nucleic acid cargo release [58].

1.2.1.3 Sterols (Cholesterol)

Cholesterol incorporated in the lipid layer of LNPs can influence LNP stability, membrane rigidity, and endosomal fusion [59]. Cholesterol constitutes the second most abundant component in LNP formulations, accounting for ~38.5 mol% of the total lipid content (**Table 1.2**). Cholesterol is a sterol compound distinguished by its characteristic structure, comprising four fused hydrocarbon rings, a hydrocarbon tail, and a hydroxyl group. When incorporated into phospholipid bilayers, cholesterol occupies the interstitial gaps between phospholipid molecules, reducing the membrane fluidity by reducing lateral mobility [60]. Similar to phospholipids, cholesterol is also termed a 'helper' lipid, as it is planar and rigid, facilitating intercalation into bilayer structures and contributing to the stabilization of LNPs (**Figure 1.4**) [61]. This structural integration plays a critical role in minimising the leakage of nucleic acid cargo. Cholesterol was first introduced in Doxil®. The inclusion of cholesterol served two primary purposes of **(1)** its exchangeable nature allows for accumulation within the liposome during systemic circulation [62] and **(2)** it enhances LNP circulation half-life by preventing LNP interactions with biomolecules leading to prolonged circulation time [63].

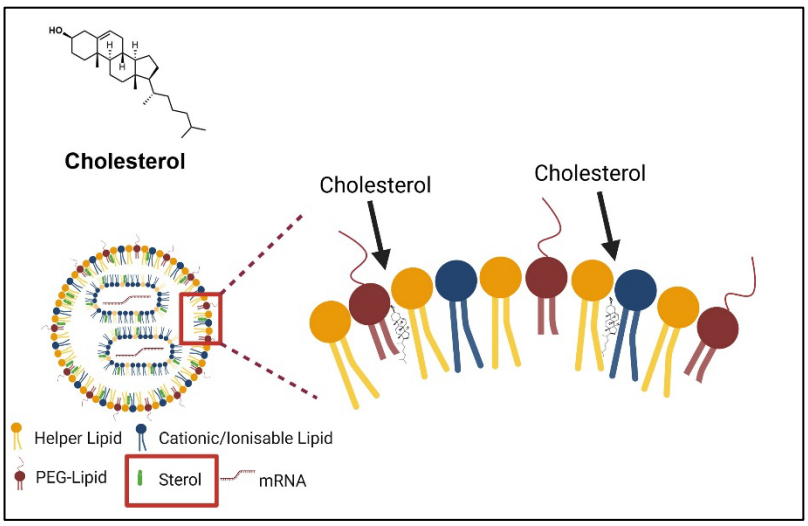

Figure 1.4 Chemical structure of cholesterol embedded in the lipid layer of the LNP. Created with Biorender.com.

LNP formulations do not retain high levels of cholesterol in a soluble state [59, 64]. Cholesterol exhibits relatively low aqueous solubility in circulation, with a reported solubility of 1.8 µg/mL [65]), and consequently tends to accumulate on LNP surfaces. This enrichment

of cholesterol on the LNP surface can influence endosomal fusion since cholesterol also constitutes ~30 % of the mammalian plasma membrane [66]. Furthermore, a reduction in the cholesterol molar percentage of mRNA-LNPs from 40 mol% to 20 mol% and 10 mol% resulted in diminished protein expression in the liver, indicating that cholesterol content plays a critical role in facilitating efficient mRNA delivery and translation *in vivo* [67].

1.2.1.4 PEG-Lipids

Polyethylene glycol (PEG)-lipid is a critical component in LNP formulation performance and stability. This lipid constitutes the lowest molar percentage of the LNP formulations (~1.5 mol%) (**Table 1.2**). PEG-lipids are composed of a hydrophobic lipid anchor covalently linked to a repeating ethylene glycol (-CH_2CH_2O-) unit, terminating in a hydroxyl group (-OH). The length of the PEG chain determines its molecular weight and influences its physicochemical characteristics. The PEG-lipids commonly incorporated into LNP therapeutics include ALC-0159 and DMG-PEG 2000. ALC-0159 contains an amide linkage, which is designed to exchange out of the LNPs, meaning that the PEGylated lipid can shed gradually from the LNP once in systemic circulation. PEG shedding is a crucial step for the effective delivery of LNPs, as this removes the steric shielding effect of LNPs enhancing cellular uptake and endosomal escape [68].

PEG-lipids adopt a distinct orientation in LNPs due to their amphiphilic structure, with the hydrophobic lipid tail anchoring in the lipid layer (**Figure 1.5**). The hydrophilic PEG chain extends into the aqueous environment, forming a stealth effect around the LNP surface. PEG stealthing reduces opsonisation by serum proteins and subsequent clearance by the mononuclear phagocyte system (MPS). Consequently, PEGylated LNPs exhibit prolonged circulation times, enhancing their potential for extravasation through leaky tumour vasculature and accumulation within tumour tissue [69]. Beyond improving LNP pharmacokinetics, PEGylation contributes to particle physicochemical stability by reducing particle size, inhibiting LNP aggregation during storage, and extending shelf-life [10].

Despite their advantages, PEG-lipids also present certain limitations in LNP formulation. The steric barrier created by the PEG chains impedes membrane destabilisation during LNP fusion with target cells, limiting endosomal escape and intracellular delivery efficiency [70]. PEGylation with weak or short bilayer linkers (e.g. cholesterol, 3-N-[(ω-methoxypoly(ethylene glycol)2000)carbamoyl]-1,2-dimyristyloxy-propylamine (PEG-C-DMA)) undergo gradual dissociation during circulation (PEG shedding) that facilitates interaction between LNPs and cell membranes [71-73].

PEG immunogenicity presents another limitation, which can elicit anti-PEG IgG and IgM antibody responses. Instances of anaphylaxis have been reported with the Pfizer-BioNTech-Comirnaty® vaccine in individuals with a confirmed PEG allergy [74]. To mitigate this, replacing a PEG with polypeptoides, such as polysarcosine (pSar) (analogs of polypeptides) in LNPs yielded LNPs with physicochemical characteristics similar to DMG-PEG 2000 LNPs, while retaining *in vitro* and *in vivo* mRNA delivery efficiency [75].

Beyond immunogenicity, PEG-lipids are susceptible to structural changes during long-term storage, forming blebs [76]. Blebs are protrusions on the surface of the LNP [77] consisting of an aqueous compartment surrounded by a lipid bilayer [32]. An additional challenge associated with PEG-lipids is their susceptibility to oxidative degradation due to their unsaturated fatty-acid chains. PEG-lipids may undergo oxygen-initiated degradation due to the nature of protons at α-carbon atoms of the ether bond [78]. Oxidative pathways are further accelerated by environmental stressors including heat, aeration, humidity, and light exposure. However, few publications offer information on the oxidative stability of such complex lipid formulations [79].

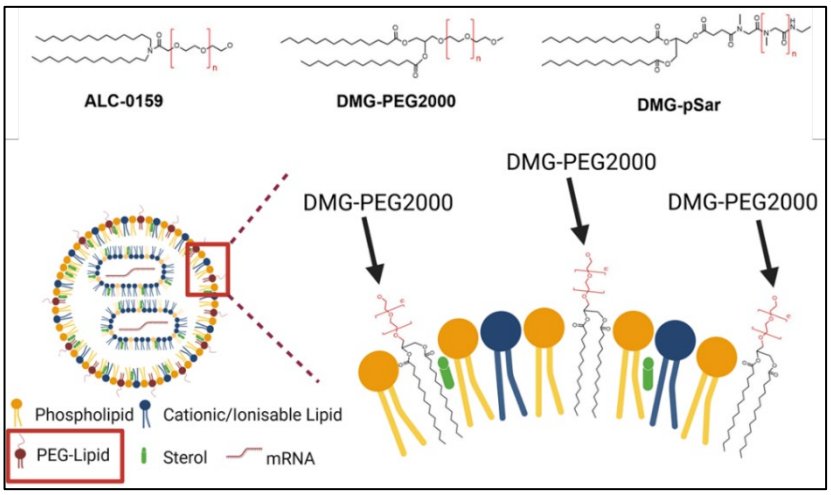

Figure 1.5 Chemical structure of three PEG-lipids acting as stealth for LNPs 2-[(Polyethylene glycol)-2000]-N,N-ditetradecylacetamide (ALC-0159), 1,2-Dimyristoyl-rac-glycero-3-methoxypolyethylene glycol-2000 (DMG-PEG2000) and 1,2-dimyristoyl-sn-glycero-3-phosphoethanolamine-poly(sarcosine) (DMG-pSar). Created with Biorender.com.

An important consideration for the translational potential of LNPs, particularly in the context of global health, is the cost and scalability of lipid components. Ionisable lipids such as MC3 and SM-102, can represent a significant proportion of formulation costs, especially at early stages of development where LNP design, development and synthesis is complex and production volumes are limited. The development of ionisable lipids via efficient multicomponent reactions has attracted increasing interest in recent years [80]. Miao *et al.* demonstrated the application of the three-component Ugi reaction (Ugi-3CR) to generate a

combinatorial library of ionisable lipids, facilitating early-stage screening for high-performance mRNA vaccines [81]. Improved synthetic efficiency and the adoption of standardised, high-throughput production methods contribute to reducing per-dose costs to levels compatible with broader access. Affordability is therefore likely to be achieved when LNP formulations can be produced reproducibly at high volume using scalable and streamlined manufacturing processes. Continued innovation in lipid design [82], alongside efforts to expand manufacturing capacity and enable technology transfer will be critical to ensuring equitable access in low- and middle-income settings.

1.2.2 Messenger RNA (mRNA) Cargo

The broad range of RNA applications is possible due to current advancements in rapid RNA production, and the potential for their deployment as personalised medicines. LNPs enable the delivery of multiple nucleic acid modalities, including siRNA (e.g., patisiran in Onpattro®) and mRNA (e.g., Comirnaty® and Spikevax® COVID-19 vaccines). They are also being developed for next-generation applications such as gene editing (e.g., CRISPR/Cas9 [11]). This thesis focuses on the design of LNPs for mRNA encapsulation.

MRNA payloads have a high molecular weight (~2,000-4,000 mers) and are negatively charged because of their phosphate groups in the phosphodiester backbone [83]. The large size prevents mRNA from crossing cell membranes *via* passive diffusion, and the negative charge causes electrostatic repulsion from the anionic cell membranes.

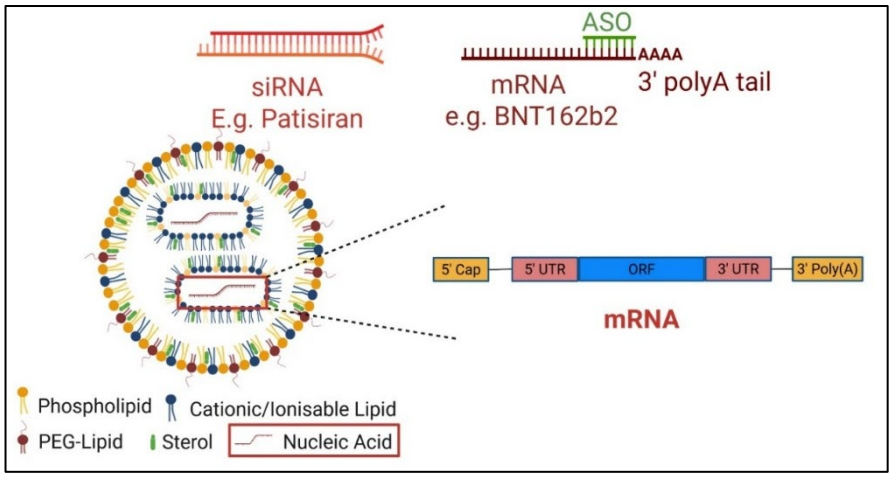

Figure 1.6 mRNA structure encapsulated in an LNP. Abbreviations: mRNA messenger RNA, siRNA small interfering RNA, ASO antisense oligonucleotide, Poly(A) Polyadenosine, UTR untranslated region. Created with BioRender.com.

MRNA is synthesised through RNA polymerase *via* Watson-Crick base pairing to form a complementary RNA sequence [84]. MRNA consists of a single-stranded nucleic acid molecule containing five structural elements: **(1)** a 5′ cap which protects the transcript from nucleolytic degradation and facilitates ribosome binding, **(2)** a 5' untranslated region (UTR), plays a role in translation regulation, **(3)** an open reading frame (ORF) which determines the amino acid sequence of the target protein, **(4)** a 3' UTR which promotes ribosomal recognition of the mRNA, and **(5)** a 3′ poly(A) tail added by poly(A) polymerase, which enhances mRNA stability and translation [85] (**Figure 1.6**).

MRNA therapeutics rely on the host cellular machinery to translate the encoded mRNA information into a protein, restoring the expression of functional target protein *in vivo*. However, to function *in vivo*, mRNA must evade multiple biological barriers. Initially, mRNA needs to be protected from nucleases, since it can undergo degradation by ribonucleases (RNases) in physiologic fluids [49, 86]. Secondly, mRNA must bypass the MPS and clearance by renal glomerular filtration. Thirdly, the mRNA needs to be internalised by target cells. Finally, once mRNA is internalised, endosomal escape is needed to reach the cytoplasmic target for initiation of translation. The endosomal membrane presents a physical barrier due to the inefficiency of endosomal disruption or fusion.

The use of LNP formulations enhances intracellular delivery to target cells and protects mRNA from degradation. Current mRNA vaccines are designed to express a specific protein (antigen) that will trigger an immune response. The Comirnaty® (Pfizer-BioNTech) and Spikevax® (Moderna) COVID-19 vaccines use mRNA encoding a stabilized spike (S) protein from SARS-CoV-2 [14]. In the case of mRESVIA® [34] by Moderna, nucleoside-modified mRNA encodes the RSV prefusion (F) glycoprotein. The new Moderna COVID-19 vaccine, mNEXSPIKE®, contains nucleoside-modified mRNA encoding a refined version of the SARS-CoV2 spike protein [87].

1.2.3 Buffers and cryoprotectants

During the initial formulation of LNPs, a slightly acidic environment (pH 4-5) is used to promote protonation of ionizable lipid headgroups, which facilitates efficient encapsulation of mRNA by forming electrostatic interactions between the positively charged tertiary amine group of the ionizable lipid and negatively charged phosphate group (PO_4^-) in the ribose-phosphate backbone of mRNA [88]. The rapid shift to a physiologic pH during dialysis prevents prolonged exposure of the mRNA to acidic conditions, minimizing the risk of acidic hydrolysis of the phosphodiester bonds along the mRNA sequence [89]. mRNA degradation through hydrolysis is the major culprit for chemical degradation of mRNA impacting its biological activity [5].

MRNA degradation *via* hydrolysis is a key challenge impacting downstream biological activity [5]. To preserve integrity, mRNA vaccines rely on buffers, stabilisers and cold-chain logistics. For example, Spikevax® uses sodium acetate buffer, while Comirnaty® uses sodium citrate and sodium phosphate to maintain formulation stability. Citrate buffers are preferred for their ability to chelate metal ions and inactivate nucleases [90, 91]. Sucrose acts as a cryoprotectant during freezing [92], and alternative buffers, lactate and malic acid, have also been explored [93]. LNPs formulated in acetate or lactate buffers exhibited a smaller mean hydrodynamic diameter (~100 nm) compared to those prepared in malate or citrate buffers (~150 nm), though encapsulation efficiency and polydispersity remained consistent [93].

1.3 The Manufacture, Purification and Storage of mRNA-LNP Formulations

The primary objective in manufacturing LNP formulations is to control process parameters to consistently achieve optimal critical quality attributes (CQAs) and biological performance [94]. Efficient nanofabrication of mRNA-LNPs (<100 nm) typically involves microfluidics or bulk mixing techniques that promote rapid self-assembly of the ionizable lipid, phospholipids, cholesterol, and PEG-lipids around the mRNA. Following synthesis, purification processes such as dialysis, spin-column centrifugation or tangential flow filtration (TFF) are employed to remove organic solvents ensuring product purity and safety. Stability of mRNA-LNP formulations is a critical factor for clinical translation, with optimized storage conditions required (**Table 1.4)** to maintain structural integrity, prevent aggregation, and preserve bioactivity over time.

1.3.1 Microfluidics for LNP Production

The choice of synthesis technique is the initial step in determining the LNP CQAs, including stability, encapsulation efficiency and performance. Various methods used to formulate LNPs including pipette mixing [95], vortex mixing [95, 96], thin-film hydration followed by extrusion [97], ethanol injection [98] and microfluidics [99]. The aim of each method is to synthesise stable LNPs with controlled CQAs such as of uniform size, narrow size distribution and morphology, while ensuring scalability and reproducibility (**Section 1.6**). CQAs are defined by the European Medicines Agency (EMA) guideline '*Guideline on the quality aspects of mRNA vaccines'* [100].

Microfluidics is the most-widely used method for formulating LNPs [101], offering precise control over nanoparticle size and uniformity (**Table 1.3**). Critical process parameters in microfluidics manufacture of LNPs include the geometry of the micromixer used, and the operating conditions that govern fluid behaviour within the channels. Typical mixing devices

include Staggered Herringbone Mixer (SHM) (NanoAssemblr™ Benchtop) [102] and Toroidal mixer (NanoAssemblr™ Ignite) [103] (**Figure 1.7)**. The micromixer geometry and dimensions strongly influence the mixing of the aqueous and lipid component in the formation of LNPs. The efficiency of mixing and the resulting characteristics of LNPs, such as size, PDI and morphological attributes can be affected by the micromixer design [104]. Precise control of microfluidics parameters is essential, as the CQAs of LNPs directly influence their therapeutic efficacy and biodistribution. The LNPs synthesized in this thesis were prepared using a Toroidal mixer (NanoAssemblr™ Ignite).

Table 1.3 Different manufacturing methods for LNPs.

Pipette mixing	Vortex mixing	Thin-film hydration followed by extrusion	Ethanol injection	Microfluidics
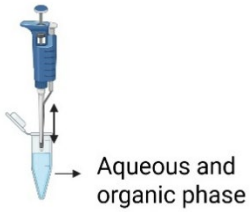 Phases are mixed through up and down rapid pipetting [95].	 Phases are vigorously mixed using a vortex mixer [95, 96].	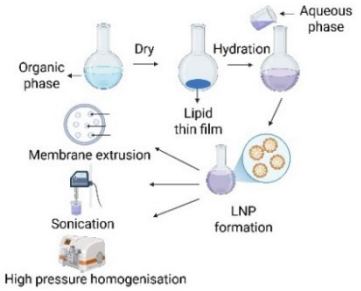 Thin film formation followed by extrusion, sonication and high-pressure homogenization [97].	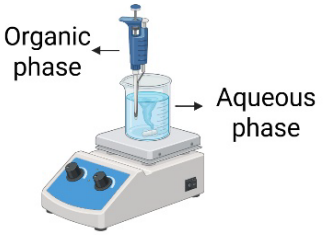 Phases are mixed while stirring [98].	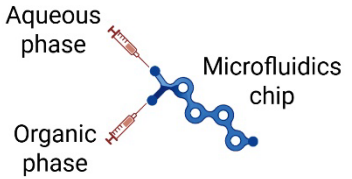 Phases are mixed in the microfluidic device [99].
Advantages				
• Time effective. • Low equipment and operational cost.	• Time effective. • Low cost.	• Low cost.	• Time effective. • Low cost.	• High control of CQAs. • Fast processing time.
Disadvantages				
• Poor reproducibility due to manual speed of mixing and pipetting.	• Poor scalability. • Poor reproducibility.	• Long time to evaporate the organic solvent. • Poor scalability.	• Limited control over CQAs due to stirrer speed and injection rate of the organic phase.	• Narrow channels are susceptible to blockages. • High cost of single use cartridges.

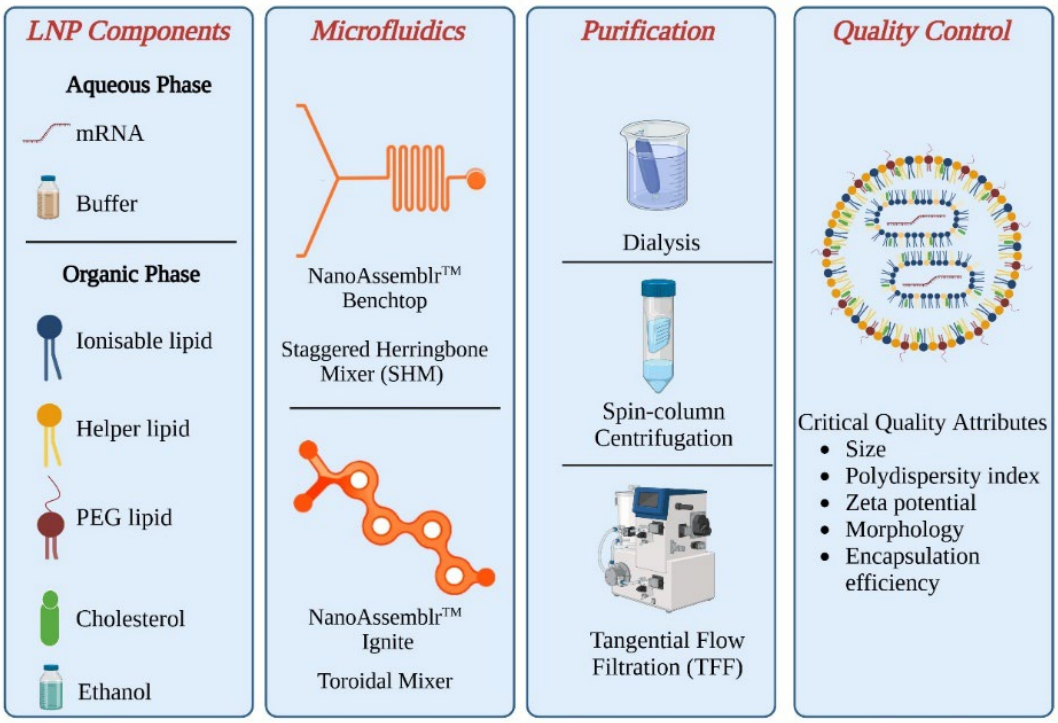

Figure 1.7 Microfluidics for LNP synthesis. The organic phase (lipids in ethanol) and the aqueous phase (mRNA in aqueous buffer) are injected at different streamlines using the microfluidic mixers Staggered Herringbone (SMH) or Toroidal. LNPs are collected for downstream processing. Created with BioRender.com.

Using microfluidics, the different phases (aqueous and organic phase) are introduced at different entry points and mixed at flow rates ranging from 1-20 mL/min. The mixer functions *via* a chip design consisting of joined circular structures. As the fluid travels through the channels, both phases are combined and divided several times which creates rapid mixing [104, 105]. The ethanol and water mixing rapidly causes a sudden decrease in lipid solubility. The ionizable lipids form electrostatic interactions with the nucleic acid forming a core-shell structure leading to nanoprecipitation of LNPs.

The microfluidics operating parameters Flow Rate Ratio (FRR) and the Total Flow Rate (TFR) play a key role in determining LNP formulation characteristics, such as size and stability [102]. The FRR (**Equation 1.2**) is the volumetric ratio between the aqueous phase (contains the nucleic acid) to the organic phase (contains the lipids) [106]. The TFR (**Equation 1.3**) is the overall speed of the microfluidic process [107]. Both parameters describe the movement of the of fluids in the microfluidic chip [108].

$$\textbf{Flow Rate Ratio } (FRR) = \frac{\textbf{Flow rate of aqueous phase}}{\textbf{Flow rate of organic phase}} \qquad \textbf{Equation 1.2}$$

$$\textbf{Total Flow Rate } (TFR) = \textbf{Flow rate of aqueous phase} + \textbf{Flow rate of organic phase} \qquad \textbf{Equation 1.3}$$

A high FRR, ranging 3:1 - 5:1 aqueous: organic, results in LNPs with a higher particle size (60 *versus* 50 nm respectively) [102]. Roces *et al.* showed that a low TFR increased the LNP manufacturing time and slowed the dilution of the solvent, which result in the manufacture of larger-sized LNPs. Conversely, a higher TFR (i.e., 20 mL/min) results in smaller nanoparticles due to insufficient time for proper particle formation and stabilization [102].

Microfluidics technologies offer distinct advantages over conventional formulation methods in achieving high encapsulation efficiency of nucleic acid and uniform particle size distributions [71, 109]. Mixing of the organic phase (containing lipids) and the aqueous phase (containing nucleic acid) is controlled by adjusting flow rates (TFR and FRR), hence avoid manual mixing. However, microfluidics also has limitations associated with high-cost of single-use chips, a requirement for downstream processing of LNP formulations to remove residual ethanol, and a high risk of micromixer channel clogging due to lipid precipitation or LNP aggregation [110].

1.3.2 Purification

Three examples of downstream processing methods used in LNP formulation are dialysis, centrifugation-based ultrafiltration and TFF **(Figure 1.7)**. McMillan *et al*. compared spin-column centrifugation and dialysis [111]. The study concluded that although spin columns slightly reduced the size of SM-102 and ALC-0159 LNPs, other CQAs were unaffected by the choice of downstream processing methods [111].

1.3.3 Storage

Following LNP purification, LNPs need to retain their target specification CQAs during storage. Factors such as the choice of storage temperature (refrigerated, frozen, or lyophilized), cryoprotectant content (sucrose, trehalose or mannitol), and formulation buffer significantly influence LNP formulation stability [112, 113]. Moderna COVID-19 vaccine Spikevax® uses tris-HCl-buffered saline (TBS; with 8 % *w/v* sucrose) stored at -20 °C for up to 6 months [133], while the Pfizer-BioNTech COVID-19 vaccine Comirnaty® uses phosphate buffered saline (PBS) as the solvent (with 20 % *w/v* sucrose) stored at -70 °C for up to 6 months [134] (**Table 1.4**).

Studies on LNP long term stability are still undergoing. Despite the remarkable success of the COVID-19 vaccines, challenges related to their long-term stability persist. Spikevax® requires stringent cold chain management, typically at temperatures around -50 °C to -15 °C for 9-month shelf life to maintain mRNA efficacy over time [114]. A more recently developed candidate in 2025, Moderna marketed mNEXSPIKE® COVID-19 vaccine highlighting the ongoing need for advancements in formulation and storage conditions [87].

Table 1.4 Storage conditions of clinically available mRNA therapeutics.

Product name	**Company**	**Storage conditions**		
		Unopened vial in freezer	**Unopened vial after thawing**	**Refrozen after thawing**
Onpattro® [16]	Alnylam Pharmaceuticals	Not stored in the freezer.	2°C to 8°C for 3 years or 8°C to 25°C for < 14 days.	Formulation not frozen.
Spikevax® [17]	Moderna	- 50 ºC to -15 ºC for <9 months.	2 ºC to 8 ºC for < 30 days.	Not recommended.
mNEXSPIKE® [115]	Moderna	- 50 ºC to -15 ºC (duration not indicated).	2 ºC to 8 ºC for <90 days or 8 °C to 25 °C for <24 hours.	
mRESVIA® [34]	Moderna	-40 °C to -15 °C for <12 months.	2 ºC to 8 ºC for <31 days or 8°C to 25°C for <24 hours.	
Comirnaty® [35]	Pfizer-BioNTech	-90 °C to -60 °C for <18 months.	2 ºC to 8 ºC <31 days or 8 °C to 25 °C for <12 hours.	

Comparison of siRNA-LNP therapeutic (e.g., Onpattro®, short-term storage at ambient temperature (8-25 ºC for <14 days)) and mRNA-LNP vaccines (e.g., COVID-19 vaccines, 8-25 °C for <12-24 hours) (**Table 1.4**) highlights a key difference in storage stability due to the physicochemical properties of the nucleic acid cargo. SiRNA is a double-stranded oligonucleotide that is relatively conformationally rigid and chemically robust, making it less prone to unfolding and structural changes during storage. In contrast, mRNA is a long, single-stranded transcripts that adopt complex secondary and tertiary structures and are more susceptible to chemical degradation pathways, including hydrolysis and oxidation which reduced its biological activity [5].

Orthogonal analytical workflows can sensitively detect early changes in LNP particle size distributions, morphology and nucleic acid integrity, providing a stability-indicating framework to support formulation development towards improved storage robustness.

Addressing these stability limitations is critical for improving vaccine accessibility, especially in resource-limited settings where ultra-cold storage is impractical. Therefore, enhancing the storage conditions of mRNA vaccines remains a key area of research to ensure broader and more effective immunization strategies worldwide.

1.4 LNP Mechanism of Action and Cellular Fate

The cellular uptake and mechanism of action of LNPs are illustrated in **Figure 1.8**. Following intramuscular (IM) administration, LNPs distribute within the interstitial space of the muscle and are taken up by multiple resident cell populations, including myocytes, fibroblasts, and antigen-presenting cells such as dendritic cells and macrophages. Cellular internalization of LNPs occurs *via* endocytic pathways, clathrin-dependent and clathrin-independent endocytosis mechanisms such as micropinocytosis [116, 117]. The initial step is possible because the head group of the ionizable lipids are positively charged and *via* electrostatic interaction interact with the negatively charged cell membrane. As the pH in the endosomes decreases (pH 4-5), this leads to the protonation of the ionizable lipids. The protonation results in the destruction of the membranes of the lysosome (into a hexagonal H_{II} non-bilayer structure), which leads to the release the cargo into the cytoplasm (endosomal release). Following this release, the mRNA in the cytoplasm is translated into the target protein.

Together, these coordinated uptake and intracellular processing steps define the mechanism of action of mRNA-LNP vaccines delivered IM (e.g., Comirnaty® and Spikevax®) and intravenously (IV) for siRNA-LNP therapeutics (Onpattro®). The endosomal release of mRNA is a critical step in the mechanism of action of LNPs because the payload needs to be released into the cytoplasm to exert a therapeutic effect. If this process is inefficient, the mRNA can undergo degradation during lysosome maturation, with only few mRNA released in the cytoplasm.

The efficient delivery of therapeutic cargo depends on multiple factors. Key factors include **(1)** the choice of the pH-dependent ionizable lipid: optimal pKa of ionizable lipid for optimal delivery efficiency is 6.2 to 6.5 for hepatic gene silencing [118] which renders LNPs with a neutral surface charge at physiologic pH (pH 7.4) and positively charged under the acidic conditions in the endosomes, **(2)** the geometry of the ionizable lipid is also a cofactor for transfection efficiency - ionizable lipids with cone geometry are more likely to adopt a hexagonal phase [119], **(3)** selection of mRNA: the high molecular weight of mRNAs can render in having more negative surface charges and is more tightly bounds to lipids which makes it more difficult to release from the endosomes, **(4)** surface target ligand: targeting-

ligand strategies can be adopted so that LNPs travel to specific target cells and tissues and be taken up intracellularly over there [120], **(5)** PEG-lipids: PEG forms a stealth layer on the LNP surface which affects the cellular uptake pathways [121], **(6)** biomolecular corona formation (discussed in **section 1.5**).

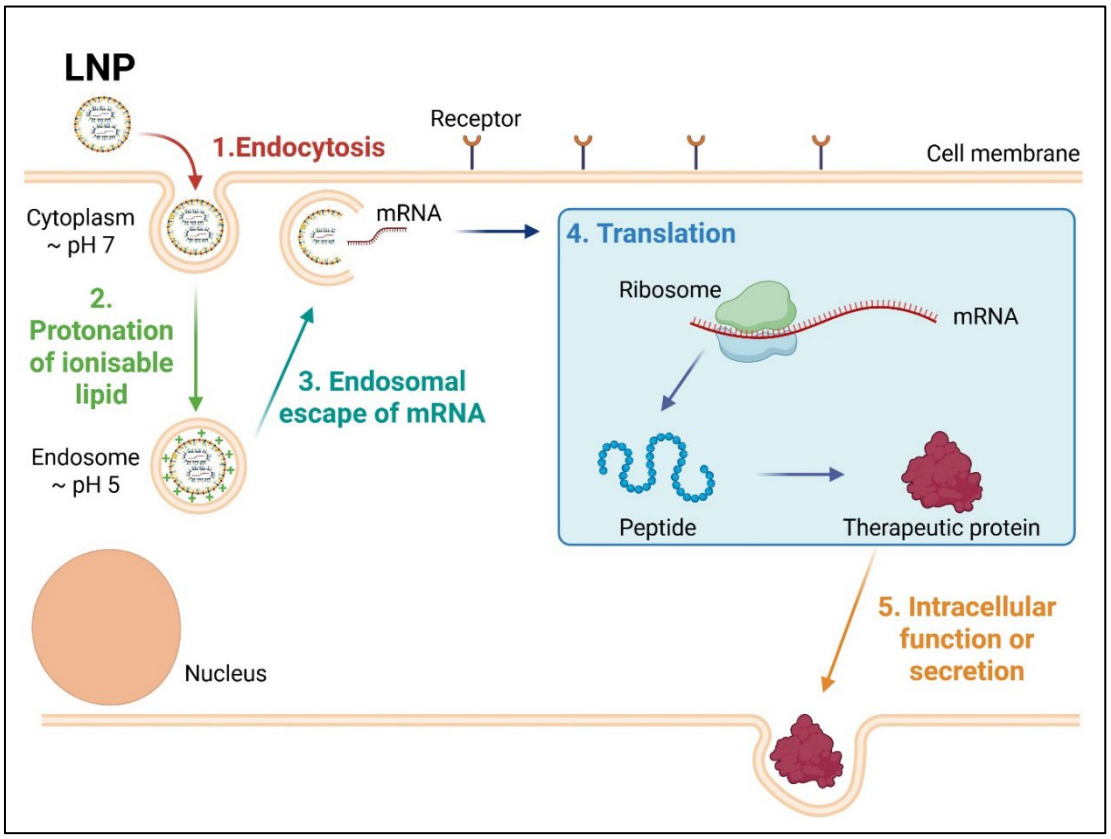

Figure 1.8 Lipid nanoparticles (LNPs) for mRNA delivery. Schematic represents cellular uptake of LNPs *via* endocytosis, endosomal escape, and mRNA release followed by mRNA translation into a therapeutic protein.

1.5 The LNP Biomolecular Corona

The concept of nanoparticle interaction with biomacromolecules was first introduced by Tyrrell *et al.* who investigated the effect of protein adsorption on liposome surfaces and its subsequent impact on cellular uptake [122]. This phenomenon was later referred to as the 'biomolecular corona', reflecting the layers of proteins and biomolecules that adsorb onto nanoparticle surfaces following exposure to biological media [123].

While proteins typically dominate the biomolecular corona, other components such as lipids, sugars, and nucleic acids may also be present, depending on the biological matrix to which nanoparticles are exposed, and nanoparticle physicochemical properties [124]. The

composition of the biomolecular corona is dynamic and influenced by several factors, including the relative abundance of biomolecules in the medium, their binding affinities, and competitive adsorption effects. However, Gharibi *et al.* showed that 51 of these proteins were consistently identified in nanoparticle protein corona studies across 17 proteomics core facilities [125]. Proteins identified in protein or biomolecular coronas include those found in **Table 1.5** and other non-abundant proteins such as glycoprotein, hemoglobin, ficolin-3, spectrin alpha chain and vitamin D-binding protein [125].

Table 1.5 Top 10 abundant proteins in human adult plasma. Information is provided by Universal Protein Resource (UniProt) [126].

No.	Protein name	Typical concentration in human plasma (mg/mL)	Function
1	Albumin	35 - 50 [127]	Regulation of the colloidal osmotic pressure of blood.
2	Immunoglobulins (IgG, IgA, IgM)	IgG 7 - 16 IgM 0.4 - 2.3 IgA 0.7 - 4 [128]	They function as B-cell receptors that, upon binding their specific antigen, drive clonal expansion and differentiation of the B lymphocytes into antibody-secreting plasma cells.
3	Fibrinogen	2 - 4.5 [129]	Promote the elimination of antigens following their binding.
4	Alpha-2-Macroglobulin	2.1 [129]	Inhibits all four classes of proteinases.
5	Apolipoproteins (ApoA1 and ApoA2 in HDL, ApoB in LDL, VLDL, and IDL)	ApoA1 1.1 - 2.05 [130] ApoA2 0.25 - 0.4 [131] ApoB 0.55 - 2.2 [130]	Mediate in the transport of cholesterol from tissues to the liver for excretion.
6	Transferrin	2.04-3.60 [132]	Mediates iron transport from areas of intestinal absorption and heme degradation to tissues responsible for iron storage and utilization.
7	Complement components (C3, C4)	C3 0.9-1.8 [133] C4 0.2-0.5 [133]	Involved in the complement pathways of series of protein that facilitate pathogen clearance through phagocytosis and enhancing signalling pathways that support adaptive immune responses.
8	Haptoglobin	0.45-1.650 [134]	Binds free haemoglobin in plasma, enabling hepatic heme iron recycling and protecting the kidneys from haemoglobin-induced damage.
9	Alpha-1-Antitrypsin	1.0-2.0 [135]	Primary inhibitor of the protease elastase.
10	Gelsolin	0.15-0.3 [136]	Actin-regulating protein that binds to actin monomers or filaments, thereby preventing the exchange of actin subunits.

Spontaneous formation of the biomolecular corona is the initial assembly formed between LNPs and apolipoproteins, albumins, immunoglobulins, coagulation factors, and many other biomolecules [137]. The corona bestows the nanoparticle with a 'new identity' due to the difference in physicochemical properties (surface charge, size, colloidal stability) and pharmacokinetic profile [138-140]. Prior to delving into the effect of the biomolecular corona on the biological fate of the LNP, it is worthwhile describing the surface chemistry involved in these interactions. Interaction forces involve non-covalent interactions (e.g. hydrogen bonds, electrostatic interactions, hydrophobic interactions) between two surfaces: the surface of the LNP and the surface of the biomolecule. The strength of these non-covalent intermolecular interactions affects the binding affinity between the nanoparticles and the biomolecule (**Figure 1.9**).

The 'Vroman effect' first described in 1962, detailed the desorption/adsorption of biomolecules on a solid surface [141]. When a biomolecule at low affinity approaches close to the nanoparticle (soft corona), this will be replaced a biomolecule of higher affinity which eventually changes the corona composition. This phenomenon supports the formation of the hard corona formed over with a long time with high affinity biomolecules remaining on nanoparticle surface [142-144]. The 'Vroman effect' [145] was later challenged by the notion that the hard corona on polystyrene and silica nanoparticles forms rapidly (<0.5 min), with subsequent changes arising mainly in the amount rather than the identity of bound proteins.

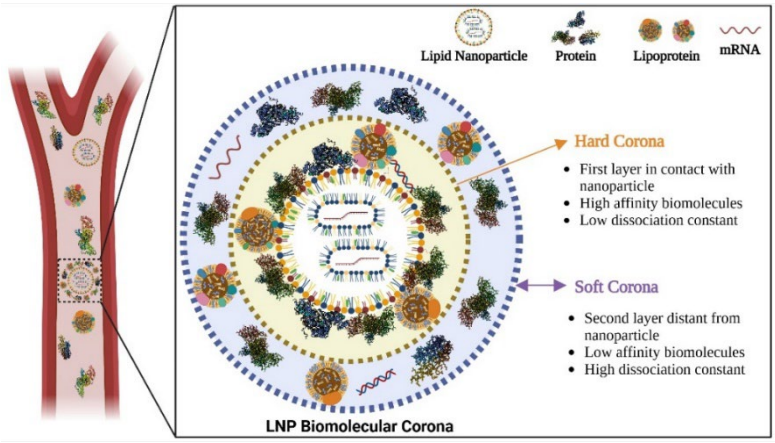

Figure 1.9 Schematic representation of the 'soft' and 'hard' lipid nanoparticle (LNP) corona. The hard corona consists of strongly bound biomolecules, which adsorb on nanoparticle surface when in direct contact with biological media. In contrast, the soft corona consists of loosely bound biomolecules covering the hard corona which exchange rapidly with higher affinity biomolecules. Created with BioRender.com.

Characterizing nanoparticle morphology is essential for understanding biomolecular corona formation. For example, a study comparing human serum albumin (HSA) adsorption onto branched and spherical nanoparticles demonstrated that HSA exhibited a three-fold higher affinity for spherical particles in comparison to branched nanoparticles [146]. Xia *et al*. examined how nanoparticle surface roughness influences corona composition, showing that 150 nm sized gold nanoparticles with rough surfaces bound bovine serum albumin (BSA) more weakly than smooth-surfaced counterparts, highlighting the role of surface texture in protein-nanoparticle interactions [147].

Surface charge further dictates protein adsorption by influencing both binding affinity and conformational changes upon biomolecule-nanoparticle association. Although albumin, which is negatively charged at physiological pH (isoelectric point 4.7-4.9 [148]), would be expected to preferentially bind to positively charged nanoparticles through electrostatic interactions, Lai *et al.* demonstrated that proteins could adsorb to both negatively and positively charged surfaces, indicating that electrostatic interactions alone cannot fully explain corona formation [149]. Other determining factors in studying the LNP biomolecular corona are highlighted in (**Table 1.6**).

Table 1.6 Factors driving the LNP biomolecular corona composition.

Factor	**Role**
Biomolecule abundance	High-abundance proteins are more likely to adsorb simply due to availability in plasma.
Affinity to surface	Low-abundance biomolecules can outcompete abundant ones if they have higher binding affinity to the nanoparticle surface.
Kinetics and exchange rates	The 'Vroman effect'.
LNP properties	Surface charge, size, and shape.
Environment	Biological environment (plasma, serum) and aqueous medium (pH, hydrophilicity).

1.5.1 Impact of the Biomolecular Corona on Biological Fate

When LNPs are introduced into biological fluids, cells do not encounter them in their pristine form. Instead, they interact with nanoparticles coated by a biomolecular corona. Consequently, it is the LNP bimolecular corona complex rather than the intrinsic CQAs of the pristine LNPs that governs their biological behaviour, fate, and therapeutic performance [150]. These interactions confer a new biological identity upon the LNPs, highlighting the importance of

assessing how CQAs are modified upon exposure to biological environments, as physicochemical properties can be significantly altered under such conditions.

Although research on the LNP biomolecular corona is limited at the time of this thesis, studies on gold [151], silica [145], polystyrene [152] and non-pegylated liposomal [153] nanoparticles have shown that surface-adsorption of opsonin proteins promotes immune recognition and uptake by macrophages of the MPS, thereby reducing their circulation time. Conversely, the presence of dysopsonins such as albumin or apolipoprotein E (ApoE) within the corona can impart a "stealthing" to LNPs, enabling immune evasion and prolonging circulation time [154].

The biomolecular corona also influences targeting efficiency. Salvati *et al.* demonstrated that nanoparticles lose their targeting abilities in the presence of the biomolecular corona [155]. When LNPs are functionalized with targeting ligands, exposure to biological fluids can result in biomolecule surface adsorption, which blocks interactions between the functionalised ligand and cell surface receptors, potentially resulting in off-target accumulation. Despite significant advancements in the design of novel nanoparticles for tumour-targeted delivery, most systemically administered LNPs predominantly accumulate in the liver rather than reaching the tumour site. This highlights a considerable knowledge gap in understanding how LNP physicochemical characteristics influence their biological behaviour following biomolecular corona formation [156].

Conversely, the biomolecular corona can confer targeting abilities to nanoparticles [157, 158]. One such example is the preferential hepatic accumulation of Onpattro® due to the abundance of ApoE in the biomolecular corona [159]. Ionizable lipids promote LNP targeting to hepatocytes by interacting with ApoE, which in turn binds low-density lipoprotein (LDL) receptors [160]. For Onpattro®, this mechanism is essential because hepatocytes are the primary target cells, and uptake occurs *via* LDL receptors [161]. To overcome the challenge of extrahepatic LNP targeting, LNP formulation composition can be tailored to minimise ApoE surface-adsorption [162, 163]. Lipid modifications (such as LNP PEGylation) have been used as an approach to effectively shield LNPs from surface adsorption [145, 164]. The configuration of PEG chains on the LNP surface is also critical in hindering formation of the biomolecular corona, with optimal configuration adopting a ‘mushroom’ or ‘brush’ configuration [165]. Another approach of predicting *in vivo* performance involves the addition of targeting ligands, which can be introduced by attaching targeting moieties during *in situ* conjugation. A liver-directed exogenous targeting approach was investigated by Akinc *et al.* for siRNA delivery by incorporating an external ligand featuring a multivalent N-

acetylgalactosamine (GalNAc)-PEG lipid cluster which can bind with high affinity to asialoglycoprotein receptor (ASGPR) expressed on hepatocytes [156].

Current understanding of how LNP biomolecular interactions dictate *in vitro* and *in vivo* biological fate remains elusive. Pre-screening LNPs under conditions that more closely mimic the *in vivo* environment can offer valuable early insights into their biological behaviour, including their tendency to agglomerate in complex biorelevant media and the identity of the dominant biomolecules that form the corona. Establishing such pre-clinical biorelevant testing frameworks helps anticipate stability issues and biomolecule-LNP interactions that may influence biodistribution or efficacy *in vivo*. For example, lab-on-a-chip systems provide a useful intermediary platform, allowing controlled microfluidic environment for plasma-LNP interaction [166]. This assessment can bridge the gap between pre-clinical development to clinical studies.

Although *in vitro* studies aim to closely replicate physiological conditions, significant discrepancies remain between *in vitro* and *in vivo* experimental settings in downstream effects on target expression. *In vitro* models are typically oversimplified, lack dynamic shear flow conditions *in vivo*, and allow for easier recovery of materials [167]. This disparity is largely attributed to the overlooked transitions in extracellular fluid composition between different organs. Further, more physiologically representative assays are increasingly important given the frequent discrepancies observed between human responses and preclinical model predictions. These inconsistencies can result in unreliable predictions of human drug metabolism, therapeutic performance, and potential toxicities, meaning that interventions showing promise in animal studies may ultimately lack efficacy or present safety risks in clinical settings [168].

1.5.2 Pipelines for Biomolecular Corona Analysis

Incubation of the biomolecular corona can be performed with individual biomolecules, such as purified proteins or lipids, to study specific binding affinities and competitive adsorption under well-controlled experimental conditions (**Figure 1.10**). Alternatively, LNPs may be incubated in complex biological media (e.g., serum, plasma, or cell-conditioned media), to replicate the heterogeneous environments encountered *in vivo* [150, 169]. Incubation times typically range from minutes for early adsorption kinetics to 30-60 minutes to capture equilibrium hard-corona formation, and several hours when mimicking prolonged physiological exposure. Experimental setups may involve static incubation, where LNP-biomolecule interactions occur without mechanical disturbance, or dynamic incubation, in

which samples are agitated, rotated, or exposed to flow to reproduce shear forces present in circulation [170]. Most studies are performed at 37 °C, reflecting physiological temperature.

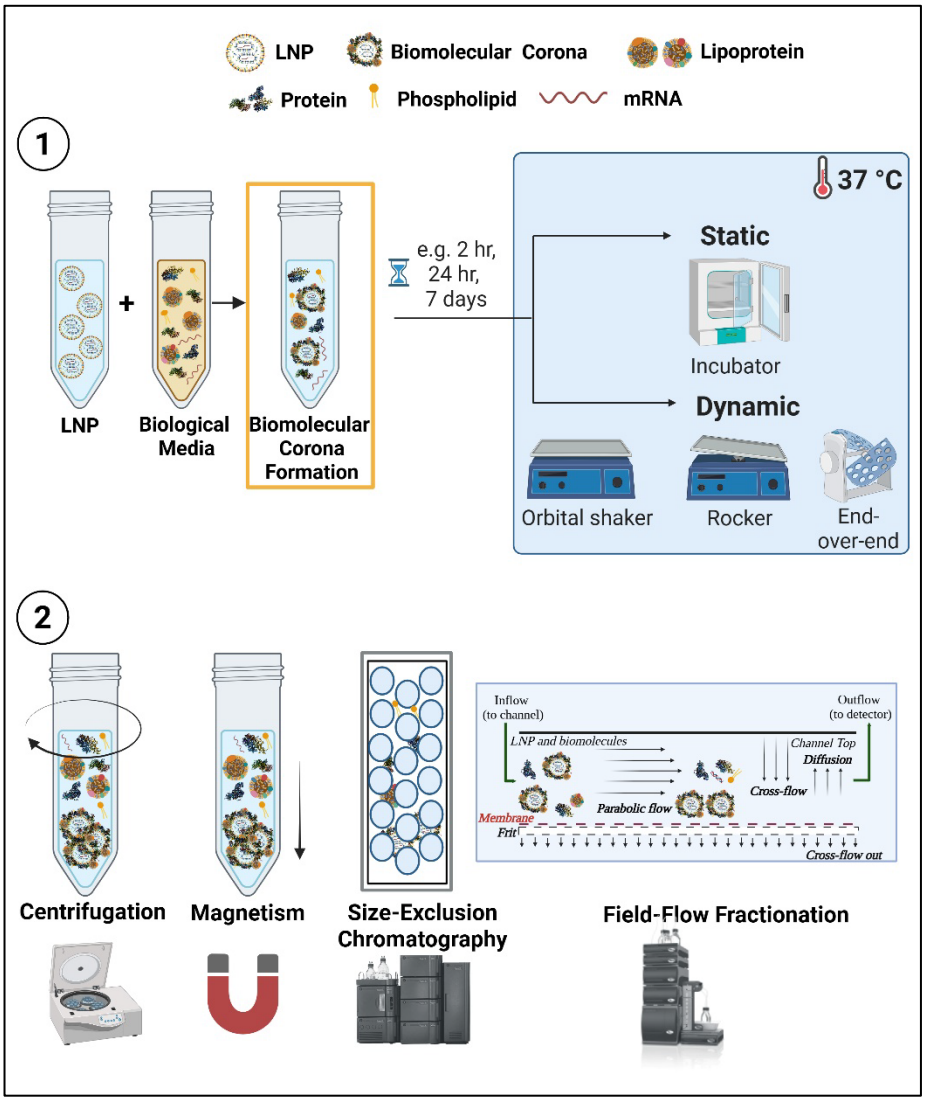

Figure 1.10 Workflow of the lipid nanoparticle (LNP) biomolecular corona studies currently employed. Figures represent (1) formation of LNP biomolecular corona using different incubation conditions and (2) methods for isolating the LNP biomolecular corona. Created with BioRender.com.

The use of different methods developed to isolate the biomolecular corona from the different matrices for subsequent downstream analysis of the isolated corona are highlighted in **Figure 1.10**. A survey of the literature indicates that centrifugation-resuspension separation remains the most common technique implemented for the isolation of nanoparticle-biomolecular corona complexes from biological media. Centrifugation is based on separation according to size and density, separating the LNP corona forced in biological complex media (plasma or

serum) may further pose a challenge since the size of naturally-occurring nanoparticles (lipoproteins; chylomicrons 75-1200 nm, lipoproteins; 7-80 nm, extracellular vesicles 30-1000 nm [171]) may sediment at the same rate as the biomolecular corona complexes. Centrifugation cannot be applied to soft nanomaterials due to its potential to alter corona composition and physical stability, may induce drug leaking from LNPs and can result in biased recovery that favours the high binding affinity proteins.

Magnetic separation has emerged as an effective separation methodology for isolating and purifying LNPs, offering a selective alternative to the centrifugation technique. This method works by the functionalising the LNPs with magnetic ligands, enabling their capture in the presence of an external magnetic field. Since the surface chemistry of LNPs is changed by specific magnetic carriers, LNPs with desired physicochemical properties (size, surface charge, ligand functionalization) can be separated. This reduces the shear forces that compromise LNP integrity during centrifugation. The separation of iron oxide- LNP corona complexes from unbound serum proteins using magnetic separation offered a milder and more selective alternative to traditional centrifugation methods [169].

Size-exclusion chromatography (SEC) is another separation-based method employed in biomolecular corona recovery pipelines, which separates analytes according to their size, with larger species eluting earlier and smaller species eluting later [172]. In the case of LNP and biomolecule mixtures, LNPs possessing a larger particles size compared to biomolecules will elute in the early fractions, while smaller biomolecules are retained longer on the column matrix [169]. Although compared to centrifugation, SEC is less destructive. However, particles of similar sizes will co-elute with LNPs (80-100 nm) and lipoproteins (8- >250 nm). Proteins may co-elute with LNPs, or minor losses of LNPs can occur due to non-specific interactions with the SEC column stationary phase [173]. SEC coupled with multi-angle light scattering (SEC-MALS) has been used to quantitatively assess mRNA-LNP stability in human plasma and serum [174]. By achieving separation of LNPs from plasma biomolecules, SEC allowed for the precise temporal measurement of nanoparticle degradation without interference from biological matrix components [174].

Asymmetric Flow Field-Flow Fractionation (AF4) represents another separation method for isolating the LNP biomolecular corona. The principle of this separation technique is discussed in **section 1.6.3**. Unlike traditional SEC, which is associated with shear stress or co-elution of similarly sized nanoparticles, AF4 preserves nanoparticle integrity. This makes AF4 particularly suitable for analysing the LNP biomolecular corona following incubation in a biologically relevant matrix. Recent studies have demonstrated the ability of AF4 coupled with

MALS to characterise the LNP biomolecular corona in biological fluids with high sensitivity and reproducibility [175, 176]. AF4 can also be multiplexed to other detectors (ultraviolet (UV) [177], refractive index (RI) [178], dynamic light scattering (DLS), fluorescence and small angle X-ray scattering (SAXS) [179]) to simultaneously separate and acquire comprehensive data on size, morphology, molecular weight, composition, and chemical properties. Such in-depth characterization is crucial for understanding the role of the biomolecular corona in determining LNP behaviour and biodistribution within biological systems. Further, the advantage of this emerging technique which is useful for the LNP biomolecular corona is the absence of the stationary phase which could alter the biomolecular corona properties. The native biomolecular corona can be preserved, allowing for accurate downstream analysis.

1.6 Analysis of LNP CQAs and Biomolecular Corona Attributes

During the development of new LNP formulations encapsulating different cargo, a range of LNP physical and chemical formulation-related parameters are analysed. The EMA 'Guideline on the quality aspects of mRNA vaccines' (2025) [180] defined the typical CQAs for LNPs including LNP particle size and morphology, LNP polydispersity index (PDI), potency relevant to RNA (RNA content, mRNA integrity), LNP surface properties (e.g., zeta potential), content of individual lipids, 5-cap and Poly(A) tail content and the functionality of the LNPs. These attributes need to be measured to understand LNP physicochemical properties and biological performance [181]. Different alterations in the LNP formulation composition will result in differences in the measured attributes [182], hence, designing the nano-formulation whilst considering each attribute is essential for an efficient and translatable LNP product from research to clinic.

A major challenge in the measurement of LNPs is the absence of a single analytical technique capable of comprehensively characterizing all CQAs. As a result, analysts require training across multiple analytical platforms to comprehensively assess the full range of CQAs. Comprehensive characterization relies on the use of orthogonal techniques, many of which may be inaccessible due to the high cost of specialized instrumentation (e.g., cryogenic transmission electron microscopy (Cryo-TEM) and liquid chromatography-mass spectrometry (LC-MS)). Given that LNPs are multicomponent systems, comprehensive characterization requires the measurement of attributes at multiple levels, including the encapsulated cargo, each individual lipid component, and the assembled LNP as a multiplexed entity. In addition, there are currently no harmonized regulatory specifications defining acceptable limits for

individual CQAs. As a result, laboratories often employ different analytical protocols, making cross-study comparisons and standardization particularly challenging.

Beyond analysis of their physicochemical properties in their pristine state, LNPs should also be screened for their biomolecular interactions within complex biological matrices [175]. Alterations in LNP formulation composition and the different incubation media used results in differences in measured LNP and LNP biomolecular corona attributes, hence, designing the nano-formulation whilst considering each attribute is essential for an efficient and translatable LNP product from research to clinic.

The focus of the thesis is the physicochemical analysis of LNPs, which is vital for pre-clinical characterization during early-stage development and optimization of LNPs. Though a single technique can provide comprehensive information on a specific LNP attribute, there remains the need to rely on orthogonality within the analysis of the same physicochemical variable [183]. This provides robust information on LNP attributes, and confidence in the data provided for each attribute.

Significant gaps remain in the comprehensive profiling of the LNP biomolecular corona. Studies on LNPs continue to focus on the characterisation of pristine LNPs, which fails to reflect the complexity and dynamic nature of the biological environments encountered *in vivo*. As the biomolecular corona governs the biological identity of LNPs, its physicochemical attributes should be systematically evaluated. Several parameters commonly used to characterise pristine LNPs including particle size, PDI, surface charge, and morphology are also applicable to the assessment of LNP biomolecular corona.

1.6.1 Particle Size and Polydispersity Index

LNP particle size is a critical parameter influencing LNP transfection efficiency, biodistribution, pharmacokinetics, and overall biological fate [184]. For most nanocarriers, a 10-100 nm size range is desirable to achieve prolonged circulation time and ensure efficient delivery of therapeutic agents to the target site at therapeutically-relevant concentrations [181]. Since LNPs are primarily intended for parenteral administration, the control of particle size is critical. Aggregated LNPs >5-6 µm can obstruct capillaries and cause embolism. After systemic circulation, LNPs must traverse endothelial cells to access target tissues. Under pathological conditions such as inflammation or cancer, endothelial integrity is compromised, increasing intercellular gaps and facilitating nanoparticle penetration [185, 186]. LNPs sized 50-150 nm are more likely to passively accumulate in tumour tissues *via* these gaps, while avoiding rapid renal clearance and uptake by the reticuloendothelial system.

DLS (**Figure 1.11**) measures the hydrodynamic diameter of a particle in the 0.3 nm-10 µm size range [187]. Particles undergoing Brownian motion [188] encounter an incident laser beam, and scatter light in all directions based on their shape, diffusion coefficient, solvent temperature and viscosity. Time-dependent fluctuations in the scattering intensity are used to construct the autocorrelation function from which the diffusion coefficient (D) is derived.

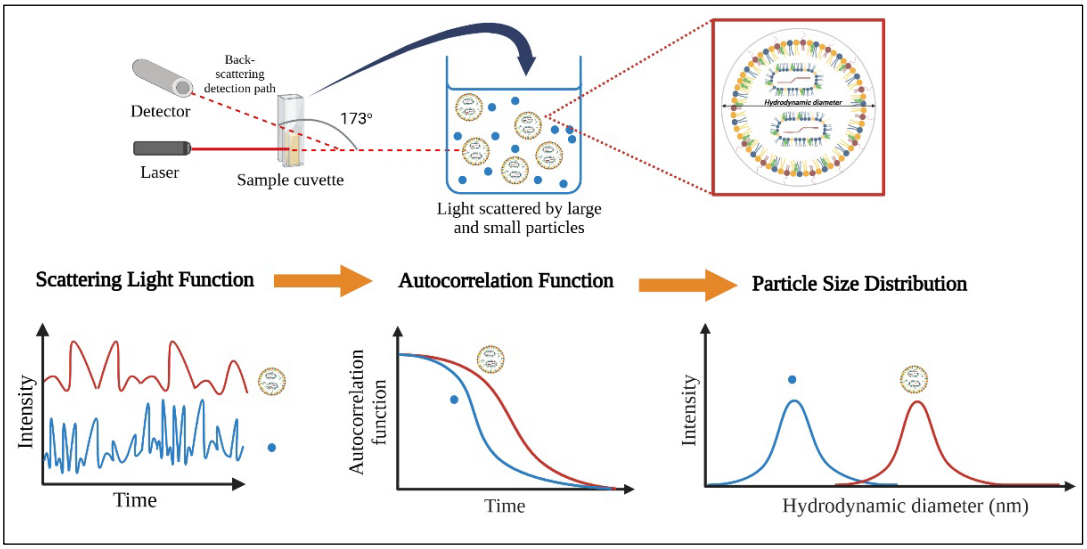

Figure 1.11 Schematic showing the setup of dynamic light scattering (DLS). A laser light is directed to the sample placed in a cuvette. Particles scatter light in all directions, the angle of detection in this case a back-scatter of 173° in which light is detected only at this angle over time. The output signal by the detector will determine the particle size and diffusion coefficient using the Stokes-Einstein equation. Created with BioRender.com.

Using the Stokes-Einstein equation [188], hydrodynamic diameter may be determined from diffusion coefficient as follows:

$$\mathbf{D} = \frac{\mathbf{k_B T}}{\mathbf{6\pi\eta D_H}} \qquad \textbf{Equation 1.4}$$

where D is the diffusion coefficient (m^2/s), k_B is the Boltzmann's constant (1.38×10^{-23} J/K), T is temperature (K) and η is the viscosity (Pa.s) of the medium in which the particle is dispersed and D_H is the hydrodynamic diameter (nm).

The Stokes-Einstein equation (**Equation 1.4**) relates indirectly to the speed of particle diffusion in the buffer and the particle size, such that smaller particles move faster. Polydisperse samples containing particles of varied sizes will scatter light at different angles. The angle of scattering can be either forward scattering or back scattering. Non-Invasive Back

Scattering (NIBS) at a 173° angle is a DLS technique that uses a short path length to minimize multiple scattering effects [189]. In the case of LNPs, NIBS is more useful since the interest is to detect small particles coexisting in solution with minimal interference from dust particles.

Parameters derived from DLS include mean hydrodynamic size (Z-Average, intensity weighted mean diameter), and polydispersity index (PDI). Distribution analysis, which uses a different mathematical analysis of the correlation function compared to the cumulant analysis, provides greater insight into the number of particle populations within a polydisperse sample based on the intensity of scattered light.

DLS also provides information on the width of the particle size distribution through the PDI (**Equation 1.5**), which ranges from 0-1. A PDI value near 0 indicates a highly monodisperse particle population, whereas values approaching 1 suggest a high degree of polydispersity, often due to nanoparticle aggregation. Typically, a PDI of < 0.1 is considered indicative of a monodisperse system [190]. In the field of nanomedicine, polydispersity is measured by the DLS technique whereby it measures the size distribution and the heterogeneity of the particles [191].

$$\mathbf{PDI} = \left(\frac{\boldsymbol{\sigma}}{\mathbf{D_H}}\right)^{\mathbf{2}} \qquad \textbf{Equation 1.5}$$

where σ is the standard deviation of the mean and D_H is the mean hydrodynamic diameter (nm) obtained from the Stokes-Einstein equation.

PDI is another essential parameter used as a surrogate to establish the homogeneity of LNP size. Vogelaar *et al.* discuss the control of LNP production process parameters to achieve monodisperse size distribution [192]. A polydisperse sample results in heterogeneity of the LNPs, which increases the particle size distribution consequently hindering LNP cellular uptake [193]. Although an ISO standard specifying acceptable PDI values for LNPs does not exist at this time, FDA guidelines for liposomes suggest that PDI should remain <0.3 [194]. Generally, a PDI <0.2 is desirable and indicates a narrow and highly uniform size distribution and a PDI >0.3 suggests a heterogeneous distribution.

In addition to DLS, Nanoparticle Tracking Analysis (NTA) is used to measure the size of LNPs. NTA measures particles in the 30-1,000 nm size range [195]. The concept of NTA is similar to that of DLS, whereby the system tracks the random movement of particles by Brownian motion which determines the diffusion coefficient. The principles of NTA are illustrated in **Figure 1.12**. Light scattered by particles undergoing Brownian motion is captured through a microscope and directed onto a camera, which captures the motion of

individual particles [196]. The mean squared displacement determined from measuring particle motion tracks from different frames is used to measure the diffusion coefficient which is then converted to a hydrodynamic diameter using the Stokes-Einstein equation (**Equation 1.4**).

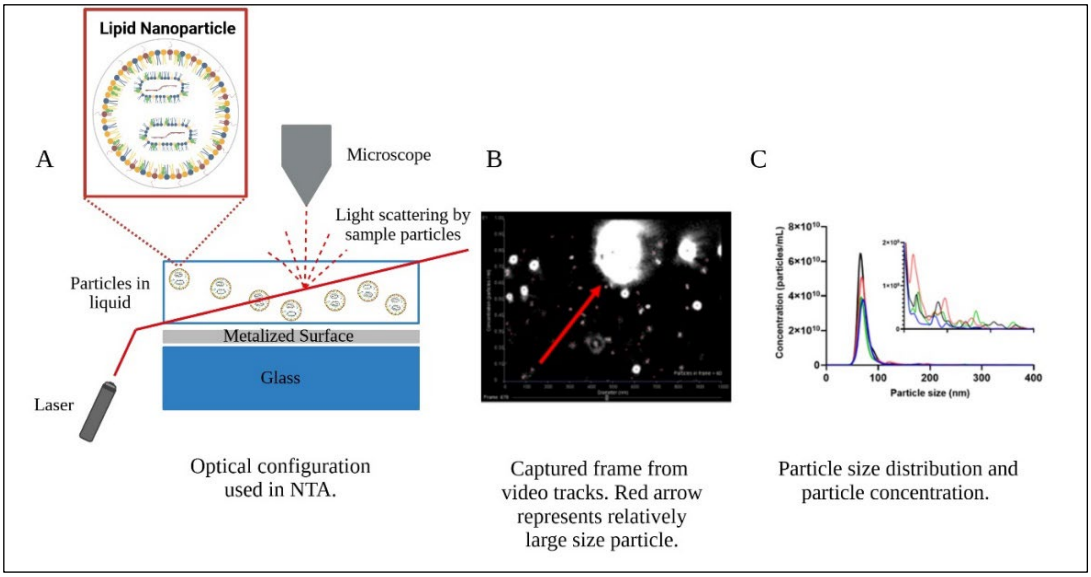

Figure 1.12 Illustration of (A) nanoparticle tracking analysis (NTA) measurement principle (B) video frame and (C) particle concentration (particles/mL) versus particle size (nm) profile. Created with BioRender.com.

DLS does not make use of the particle displacement and particle tracking, it is an ensemble technique, whereas NTA is a single particle high resolution technique. In addition, DLS reports particle size distributions in terms of intensity (%) against size (nm), whereas NTA provides size distributions based on particle concentration (particles/mL) and their respective size (nm) thereby enabling simultaneous measurement of both particle size and concentration within the sample.

Both DLS and NTA often require sample dilution. Dilution, in the case of DLS, is necessary to avoid multiple scattering and excessively high-count rates. For NTA, samples must typically be diluted to achieve particle concentrations in the optimal range of 10^7-10^9 particles/mL, enabling the capture of approximately 20-60 particle tracks. The hydrodynamic diameter measured by DLS and NTA can be influenced by the formulation buffer's salt concentration and pH. Variations in buffer properties can lead to nanoparticle change in colloidal stability which results in aggregation and increased polydispersity [197]. The viscosity of the medium also plays a critical role since both DLS and NTA measures size based in Brownian motion. Higher viscosity slows particle diffusion, yielding a lower diffusion coefficient and,

consequently, a larger apparent particle size according to the Stokes-Einstein equation (**Equation 1.4**).

1.6.2 Surface Charge

The surface charge of LNPs plays a critical role in governing interparticle interactions within the formulation and, importantly, facilitates their adsorption onto negatively charged cell membranes, a key step required for effective cellular internalisation [45]. LNPs with neutral or negative surface charges face greater challenges in achieving efficient intracellular delivery compared to their positively charged counterparts. A zeta potential value ranging from -10 to 10 mV is considered neutral [198]. The surface charge of LNPs also influences their circulation half-life, as it affects interactions with serum biomolecules and clearance by the MPS. Alexis *et al.* concluded that neutral and positively charged LNPs have prolonged systemic circulation time due to the low adsorption of LNPs to plasma proteins and reduced cellular uptake at the target site [199].

LNP composition including the surface charge of ionizable lipids (e.g., MC3, SM-102) dictates the net charge of the LNP effected by the surrounding environment pH and ionic strength [200]. In the case of DOTAP, which is a cationic lipid, its zeta potential is not significantly affected by the pH of the dispersing medium because it has a quaternary amine with a permanent positive charge [201].

The zeta potential of LNPs can be quantified by Electrophoretic Light Scattering (ELS). Electrophoresis is the movement of a charged particle relative to the liquid it is suspended in under the influence of an applied electric field [202]. The LNP is surrounded by a double layer of ions in aqueous media under an electric field referred to as the Electric Double Layer (EDL) (**Figure 1.13**) The inner layer (stern layer) is the layer in contact with the nanoparticle surface and is composed of oppositely charged ions. The second layer (slipping plane) is the outermost diffusive layer consisting of both same charged ions, and counterions. The zeta potential is the potential at this slipping plane, which is the electrophoretic mobility of the charged particles and the fluid interface [203].

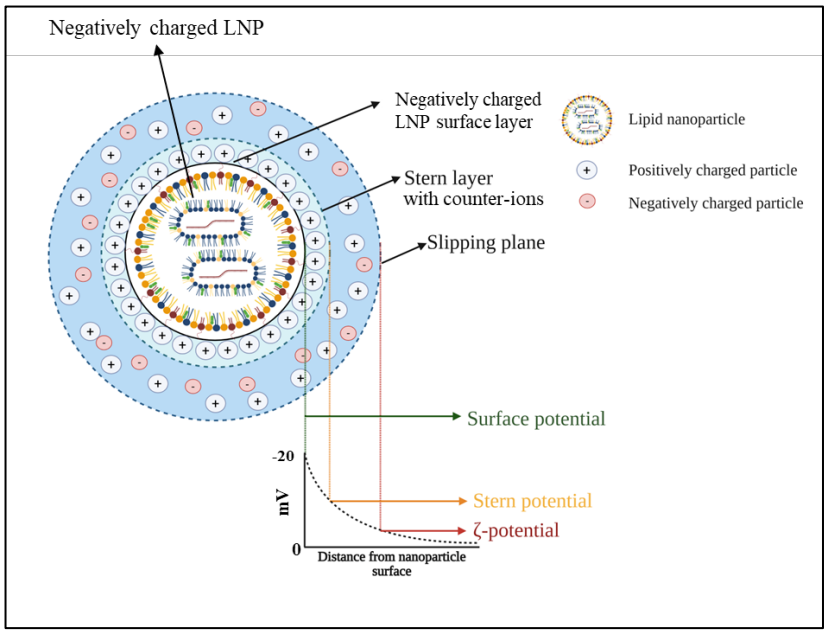

Figure 1.13 Schematic representation of zeta (ζ) potential of a negatively charged LNP showing surface potential, zeta potential, and stern potential. Created with BioRender.com.

Electrophoretic mobility can be calculated using the Henry's equation (**Equation 1.6**) which converts the electrophoretic mobility of LNP into zeta potential [204].

$$\mu_e = \frac{2\varepsilon_r\varepsilon_0\zeta f(Ka)}{3\eta} \qquad \textbf{Equation 1.6}$$

where μe is the Electrophoretic Mobility (μm·cm / V·s), ε_r is the Dielectric Constant, ζ is the Zeta Potential (V), $f(Ka)$ is the Henry's or Helmholtz-Smoluchowski function and η is Viscosity (Pa.s).

Since zeta potential is the electrophoretic mobility between the charged nanoparticle and the formulation buffer, the ionic strength and the pH of the medium are important parameters to control when measuring the zeta potential of the final LNP formulation [205]. Changing the ionic strength of the medium from 0.01-0.03 mol/L NaCl resulted in a zeta potential change from -45 mV to -32 mV. These changes in zeta potential can be attributed to protonation of the amines on the lipids [198]. However, stability of LNPs in aqueous media does not necessarily translate to biological stability in physiological fluids. A number of components present in the blood including electrolytes, lipids, amino acids, plasma proteins and cells adsorb to the LNP surface and form the LNP biomolecular corona [206]. Overall, zeta potential can be used to predict interactions with blood components, the degree of opsonisation, and aid prediction of nanoparticle circulation time *in vivo*.

1.6.3 Asymmetric Flow Field-Flow Fractionation

Asymmetric Flow Field-Flow Fractionation (AF4) is designed for the fractionation of complex macromolecules, colloids and particles ranging from 1-1000 nm [207]. Unlike conventional chromatography, which relies on continuous interaction between the analyte and a tightly packed column, AF4 is considered a gentle separation method as the absence of a stationary phase reduces the risk of analyte degradation or denaturation [208].

The principle underpinning AF4 technique is simple. Following injection, analytes are introduced into the channel and concentrated on the membrane (**Figure 1.14)**. The channel is subjected to an external field perpendicular to the longitudinal parabolic flow, driving analyte into the thin channel [207]. The cross-flow pushes the particles to the centre of the channel to encounter parabolic laminar flow, which results in different channel flow velocities, highest in the centre of the channel and slowest at the walls. Separation occurs through the balance between the field force pushing the samples to the accumulation wall, and the particles acting against the field force by diffusion. According to Stokes-Einstein equation, smaller particles will have a higher diffusion coefficient and will diffuse further to the center of the channel (high velocity) in comparison to larger particles which will accumulate on the elution wall. Hence, small components elute first, followed by larger ones.

In a simple approach, retention time relies on the liquid flow within the channel and the molecular diffusion of the particles and can be measured according to:

$$\mathbf{t_R = \frac{w^2}{6D_i} \ln\left(1 + \frac{F_C}{F_{OUT}}\right)} \qquad \textbf{Equation 1.7}$$

where t_R is the retention time (min), w is the height of channel (μm), D_i is the diffusion coefficient of the analyte (m^2/s) and F_C is the flow which passes through the membrane referred as the cross flow (mL/min) F_{OUT} is the flow which flows in the axial direction along the channel, referred as the channel flow (mL/min).

In this thesis, AF4 has been used for the separation and characterisation of LNPs. AF4 utilises an asymmetric channel design, consisting of an impermeable upper channel and a lower semi-permeable channel membrane supported on a channel frit. AF4 consists of two modalities according to channel configuration: conventional AF4 (AF4) and frit-inlet AF4 (FI-AF4). The difference between AF4 and FI-AF4 modality is the need for a focusing step for conventional AF4. The focusing step concentrates the sample in a thin band within the channel, which can promote sample aggregation and promote membrane interaction. Conversely, in FI-AF4, the sample spreads uniformly along the accumulation wall without a focusing step. AF4 is used

for a variety of analytes while FI-AF4 is preferred for soft particles (e.g. LNPs [113, 177, 209] and exosomes [210]).

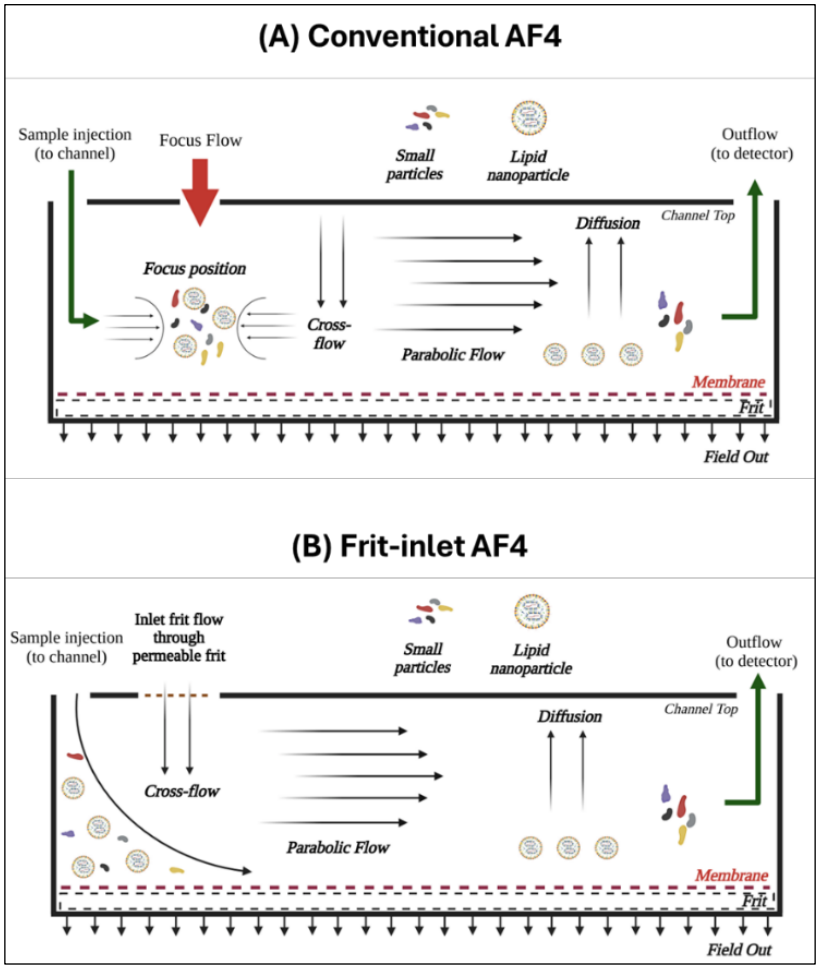

Figure 1.14 Schematic illustration of the principles of asymmetric flow-field flow fractionation (AF4) for the fractionation of a mixture of lipid nanoparticles and smaller particles. The illustration compares (A) conventional AF4 and (B) Frit-inlet AF4 with main difference in the focus flow present in conventional AF4 but absent in frit-inlet AF4. Created with BioRender.com.

1.6.3.1 AF4 multiplexation with online detectors

A major strength of AF4 is that it can be coupled to various detectors such as UV, DLS and MALS, which aids in obtaining complementary multiparametric information about the analyte [211] (**Table 1.7**). The coupling of AF4 to different detectors can be used to detect sub-populations such as smaller nanoparticles and larger aggregates which would be otherwise challenging with batch-mode DLS and NTA.

Table 1.7 The different detectors can be coupled to AF4. Abbreviations: UV: ultraviolet, MALS: multi-angle light scattering, DLS: dynamic light scattering.

Feature	MALS	UV	DLS
Principle	Rayliegh scattering (**Equation 1.8**).	Beer-Lambert Law (**Equation 1.9**).	Stokes-Einstein (**Equation 1.4**).
Image	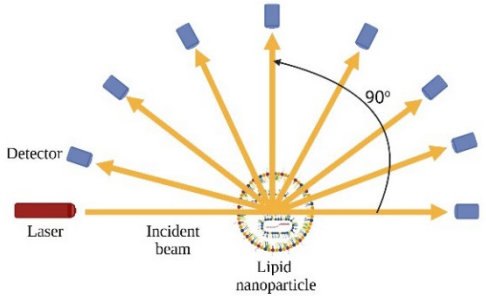	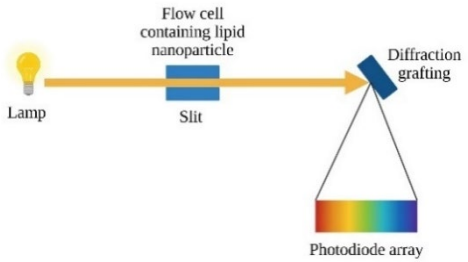	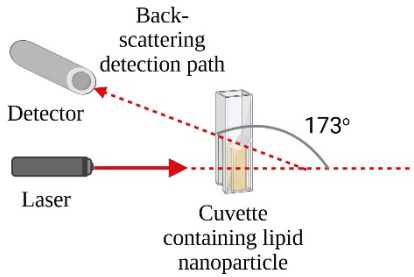
Parameter	Molecular weight, R_g, conformation determined if coupled to DLS detector (R_g/R_h).	Concentration.	R_h, size distribution, conformation determined if coupled to MALS detector (R_g/R_h).
Size Range	10-500 nm.	All size ranges.	1-1000 nm
Analyte requirement	Scattering particles.	The analyte must be a chromophore.	Scattering particles
Limitations	Isotropic scattering for particles <10 nm or small aggregates can distort scattering. Approximate conformation of the particle is required for MALS scattering model selection.	No information on conformation. Cannot detect non-UV absorbing analytes (e.g., lipids) Requires information about Extinction Coefficient (ε) and UV absorption wavelength. Signal can be affected by impurities which also absorb UV.	Sensitive to aggregates and polydispersity.

The MALS detector operates by measuring light scattered by particles at multiple angles (7°-164°) as they traverse the laser beam. The intensity of scattered light in static light scattering is influenced by both particle size and molecular weight. LNPs produce sufficient light scattering to enable accurate analysis by the MALS detector as described by the Rayleigh theory (**Equation 1.8**) [212].

$$\frac{Kc}{R_\theta} = \left(\frac{1}{Mw} + 2A_2c\right)\frac{1}{P_\theta} \qquad \textbf{Equation 1.8}$$

where K is the optical constant, c is the sample concentration, R_θ is the Rayleigh ratio (measured scattering intensity at angle θ), M_w is the weight-average molecular weight, A_2 is the second virial coefficient, P_θ is the form factor.

MALS can be used to measure molecular weight and radius of gyration (R_g). R_g reflects how the mass of the nanoparticles is distributed around the center of mass. In the case of LNPs, a small R_g reflects compact spheres, while larger R_g indicates extended chains around the LNP. Relatively small samples (10-15 nm radius) are isotropic scatterers, scattering light uniformly in all directions within a plane perpendicular to the incident beam [213]. In the case of larger particles (>15 nm), the intensity of scattered light is angular dependent which results in the molecular weight calculated based on the angle of the detector.

To obtain an accurate measurement of R_g, the appropriate scattering model based on the particle size and morphology needs to be selected. This is because different light scattering models (e.g. coated sphere, Zimm, Debye, or Berry models) (**Table 1.8**) are selected based on the anticipated geometry of the particle, such as a random coil, rod, or coated sphere. Selecting an inappropriate model can result in inaccurate estimation of R_g. Therefore, understanding the structural characteristics of the nanoparticle is essential before performing data fitting in MALS analysis.

Table 1.8 Light scattering models in MALS analysis, detailing their target radius of gyration (R_g) size ranges, and applications.

Model	Particle size	Uses
Zimm	10 - 30 R_g <50 nm [214].	Small particles, as the model assumes angular dependence e.g., peptides, proteins, polymers.
Debye	R_g >100 nm [214].	Random coils, polymers, globular aggregates, non-spherical aggregates.
Berry	R_g >50 nm [215].	Conjugated polymers, branched nanoparticles.
Coated Sphere	10-500 nm [216].	Well-defined core-shell, spherical, rigid particles.

The UV absorbance detector often connected to AF4 monitors the absorbance at a specific wavelength (260 nm for nucleic acids encapsulated within LNPs). The detection principle of the UV detector is through light absorbance using Beer-Lambert Law (**Equation 1.9**), providing a signal intensity for the analytes that absorb in the UV region such as proteins and nucleic acids.

$$\mathbf{A = \epsilon c l} \qquad \textbf{Equation 1.9}$$

where A is absorbance at a specific wavelength (nm), ε is the molar absorption coefficient (M/cm), c is the molar concentration (M), and l is the optical path length (cm).

The advantage of coupling the UV detector to AF4 is the elution of different UV-absorb analytes and their concentration at a specific time in the elution profile. Implementing the Beer-Lambert principles, the UV detector can be used as a concentration input to the MALS analysis. DLS multiplexed to AF4, measures hydrodynamic radius (R_h) of analytes in the 0.5-300 nm range. The ratio of the particle radius R_g (MALS) and R_h (DLS) is used to determine the particle shape factor. The shape factor (ratio R_g/R_h) is characteristic of particle morphology, with a value ~0.775 suggesting a solid spherical structure, while shape factors >1.5 indicate extended conformations (flexible coils or rod-like structures) [217]. Shape factor can provide an indication of morphological changes in response to formulation processes, composition, or biomolecular corona effects on LNP architecture [218]. Since biomolecule adsorption occurs at the nanoparticle's surface, any additional mass is deposited externally. Since R_g measures how mass is distributed relative to the center, this peripheral addition increases R_g more than R_h, leading to a higher shape factor [219].

Despite its versatility and ability to separate a wide particle size range in the absence of a stationary phase, AF4 has several limitations. AF4 is time-consuming due to required optimisation of cross-flow rates, focusing times, and carrier liquid composition for different samples. The operation of AF4 instrumentation can be complex and requires specialized expertise, limiting routine adoption. Sample recovery may be incomplete, particularly for positively-charged LNPs that exhibit adsorption onto the negatively-charged channel membrane (e.g., commonly used negatively-charged Regenerated Cellulose (RC) membrane).

Concentrated samples require dilution prior to analysis, and LNPs are subsequently diluted into the running buffer, which may alter sample concentration affecting nanoparticle size [220]. Although an advantage of AF4 is the ability to collect eluted fractions for downstream analyses, a significant limitation is that sample dilution during elution can complicate downstream analyses and reduce sensitivity. This is especially problematic for low-abundance

components, such as weakly scattering aggregate fractions or low levels of the LNP biomolecular corona fraction. The need to concentrate diluted AF4 fractions prior to analysis can introduce variability and potential sample loss, highlighting the importance of optimizing fraction collection and detection strategies to ensure reliable characterization of these minor components.

1.7 Overall Outlook

Although LNPs as a drug delivery system have demonstrated success over the past years, there remains a gap in the standardisation of LNP formulation attributes and the analytical methods for their characterisation. Standardisation is essential to ensure reproducibility, enable comparability across laboratories and manufacturing sites, support regulatory evaluation, and ultimately accelerate the development and market approval of medicines. At the time of this thesis there are no set guidelines for acceptable criteria for LNP formulation, necessitating the development of more standards by regulatory authorities on CQAs for LNPs. The international Organisation for Standardisation (ISO), the International Committee for Standardization (CEN), the American Society for Testing and Materials (ASTM) and other organisations still need to identify acceptable ranges for the measurement of LNP attributes, hence each characterisation technique should satisfy the vagueness of regulatory needs and accepted standards [221, 222]. The stringent characterisation requirements for nanomedicine requires substantial data provision for it to be standardised, which is a focus of current efforts by the Nanotechnology Characterisation Laboratory of the National Cancer Institute (US) and the European Nanomedicine Characterization Laboratory (EUNCL). Having analytical methods and CQAs standardised in LNP early and late-stage development would add measurable value to the field of nanomedicine.

The importance of studying the LNP biomolecular corona is well established, however, there remains a significant gap in the literature, largely due to its inherently polydisperse nature and complex composition. Traditional analytical techniques, such as batch-mode DLS, NTA, bulk UV-Vis spectroscopy or fluorescence spectroscopy, often provide only ensemble-averaged measurements that obscure subtle but functionally important differences in size distribution and surface composition between pristine LNPs and their corona-coated state. The formation of a biomolecular corona in biological environments has direct clinical implications, as it governs interactions with biological systems, including biodistribution, clearance and therapeutic efficacy [223]. Enrichment of apolipoproteins in the corona has been linked to

enhanced hepatic uptake *via* LDL receptor pathways [159, 161], whereas opsonin binding facilitates rapid clearance by phagocytic cells, with LNPs being recognized and subsequently sequestered by Kupffer cells [223]. Further, multiple studies have demonstrated that variations in corona composition can lead to significant differences in targeting [155] and efficacy [150, 224].

Challenges in resolving pristine LNPs and their corona-coated state using ensemble-averaged measurements make it difficult to detect or quantify compositional and morphological changes reliably. In this context, advanced separation and characterization techniques such as AF4 coupled with MALS, DLS and UV offer critical advantages. Coupled detectors allow determination of key parameters such as R_g, R_h, and even insights into polydispersity through the fractogram profile and particle shape (*via* the R_g/R_h ratio).

1.8 Hypothesis, Aims and Objectives

At the start of this PhD, the number of studies addressing the CQAs of LNP formulations were limited, and the application of advanced analytical techniques, such as AF4, for their detailed characterization was still emerging. Beyond LNP formulation, characterizing LNPs without accounting for their interactions with biological media, offers only a partial view of their biological fate and downstream clinical performance. Therefore, a significant literature gap remained in comprehensive analysis of LNP biomolecular corona physicochemical attributes, including the use of a single workflow for *in situ* multiparametric analysis, while permitting sample recovery for downstream analytics. The development of such an integrated pipeline establishes a foundational framework streamlines both development and regulatory assessment of the physicochemical attributes of LNPs. This can be extended to inform later-stage development and accelerate clinical translation, a need highlighted by the rapid timelines demonstrated during the COVID-19 vaccine development campaign in 2020. Improved understanding of the biomolecular corona formed in biological environments can directly inform the rational design and optimisation of LNP formulations by linking physicochemical properties to *in vivo* behaviour. Such improvements rely on advancing our understanding of the fundamental roles of orthogonality in characterisation.

The LNPs used in the entire studies consisted of Poly(A) as a model payload, and composed of an ionizable lipid (DOTAP, MC3 or SM-102), a phospholipid (DSPC), cholesterol, and a

PEG-lipid (DMG-PEG 2000) at a ratio of 50:10:38.5:1.5 mol %, respectively. One of the aims of this thesis is to strengthen and standardise the analysis of existing LNP CQAs during product development phases, starting from post-formulation stability studies. **Chapter 2** provides data on the stability of DOTAP-LNPs by profiling different stability conditions post-formulation. LNPs were brought to market under accelerated timelines, and the urgency of their deployment constrained the thoroughness of stability evaluations. This chapter therefore focuses on assessing the impact of LNP formulation processing and its stability following production. Cationic LNPs were synthesised followed by their exposure to different conditions such as temperature, cryoprotectant and filtration followed by the analysis of their particle size, surface charge, polydispersity index, encapsulation efficiency and morphology. This starting point provides an ideal foundation for further studies aiming to develop ionizable LNP prototypes. AF4 coupled with multi-detection (AF4-MD) was used in profiling the physical parameters of the LNP during the different stability conditions.

Since LNP formulations are not always monodisperse, **Chapter 3** presents an in-depth analysis of the CQAs of heterogeneous nanoparticle mixtures (MC3-LNPs and BSA). This work underpins the development and standardisation of a robust AF4 method for characterising such polydisperse systems. The objectives of this chapter are to evaluate the limitations of the current ISO standard, CEN ISO/TS 21362:2021 'Analysis of nano-objects using asymmetrical-flow and centrifugal field-flow fractionation', and to determine whether its method-performance parameters can be effectively applied to polydisperse samples. To achieve this, a range of AF4 methods were explored, and multiple LNP CQAs were assessed, including particle size, light-scattering model fitting, run-to-run signal consistency, and particle morphology.

Most studies on LNPs have focused primarily on formulation and reporting their *in vitro* and *in vivo* outcomes, without providing detailed characterisation of LNPs prior to clinical studies. To address this gap in the literature and building on the AF4 method developed for LNPs, **Chapter 4** investigates the characterisation of two LNP prototypes (MC3 and SM-102) in the presence of BSA forming the biomolecular corona. The LNP biomolecular corona has been a persistent topic of debate, given the argument that its composition is highly individual-specific. In this work, I examine the differences in the LNP biomolecular corona formed around the two prototypes. AF4 was employed to separate LNPs from BSA.

Finally, I hypothesized that LNP interactions with biomolecules may be biomolecule-specific. **Chapter 5** addresses a biomolecular corona formed between SM-102-LNPs and HDL. Since blood contains a variety of biomolecules beyond albumin, this study aimed to investigate a

more complex biomolecule, HDL, in comparison to BSA, given HDL's content of apoproteins, phospholipids, cholesterol and triglycerides. HDL was selected because it is known to adsorb onto LNPs and mediate their delivery to the liver. However, for extrahepatic targeting of LNPs, it is necessary for LNPs to resist this adsorption. In **Chapter 5**, two different AF4 modalities were compared for their effectiveness in separating LNPs from HDL and to study the formation of the LNP-HDL complex. Additionally, I collected the separated fractions for downstream analyses, assessing protein molecular weight using SDS-PAGE, evaluating surface charge and particle size changes, and determining dilution factors following AF4 elution. These results can be compared to the findings in **Chapter 3**, which examined the same LNP prototype (SM-102 LNP) with a different biomolecule, thereby supporting the discussion that the LNP biomolecular corona is biomolecule-specific.

Chapter 6 presents a discussion of the overall findings of this thesis and outlines directions for future research.

Chapter 2: Profiling LNP Physicochemical Attributes Using Orthogonal Analytical Techniques

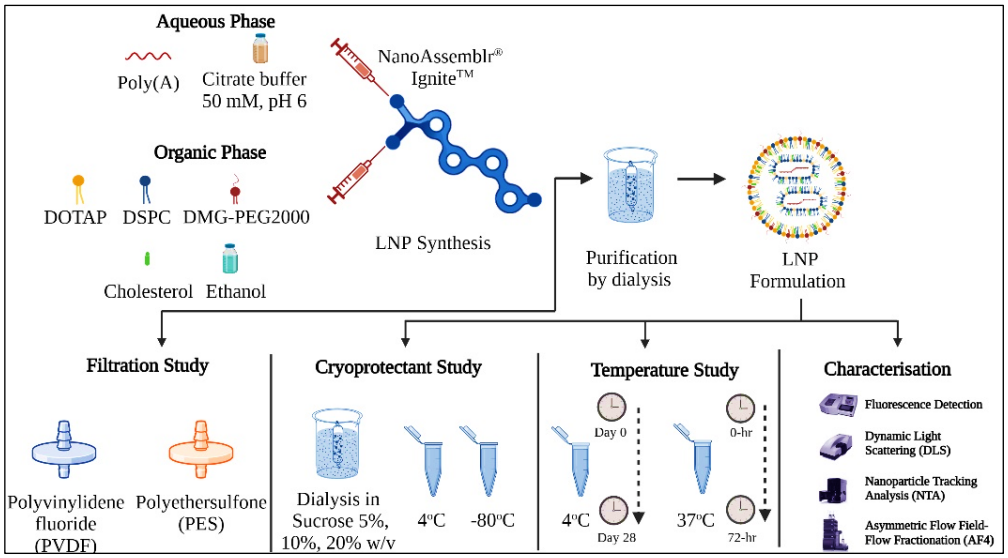

Findings from this work are published in Nano Futures.

Davidson CG, **Abdulrahman R**, Punnabhum P, Cairns M, Rattray NJ, Capomaccio R, Treacher K, Perrie Y, Rattray Z. The use of orthogonal analytical approaches to profile lipid nanoparticle physicochemical attributes. Nano Futures. 2024 Sep 6;8(3):035001. https://doi.org/10.1088/2399-1984/ad70e6

Abdulrahman R, author of this thesis, performed experimental work for the stability study across different time points, developed and conducted the AF4 method and experimental work for DOTAP-LNPs, and completed all data analysis presented in this chapter.

2.1 Introduction

LNPs represent an emerging therapeutic modality, necessitating research in their optimal storage conditions and the subsequent impact on their critical quality attributes (CQAs). To ensure clinical efficacy, LNPs must maintain stability throughout their intended shelf life. However, various environmental and formulation-related stimuli can compromise LNP stability, leading to mRNA leakage and nanoparticle aggregation, both of which reduce therapeutic efficacy. Despite their growing clinical relevance, gaps remain in our understanding of appropriate conditions for LNP transport and storage.

A key objective in LNP manufacturing is to maximize formulation stability over time while preserving efficacy and minimizing costs. Consequently, refrigerated (2-8 °C) and frozen (≤ -20 °C) storage temperatures are commonly used to slow degradation processes such as lipid oxidation and hydrolysis. Instability in mRNA-LNPs delivery systems can arise from both the nucleic acid cargo and the lipid components, which are sensitive to changes in pH, light, moisture, and other environmental factors [225]. Packer *et al*. have shown that oxidation and hydrolysis of LNP lipids can accelerate the degradation of encapsulated mRNA [226]. Given the multitude of factors influencing LNP stability and the susceptibility of their formulation components, maintaining long-term stability of LNP formulations remains a significant challenge.

Although LNPs as a drug delivery system have achieved remarkable success in recent years, there remains a gap in standardisation of the attributes and analytical techniques used to measure these. At the time of this thesis, there are no set guidelines for acceptable criteria for LNP size, PDI, zeta potential, morphology, total lipid concentration and encapsulation efficiency, necessitating the development of more certified reference materials and guidance on the measurement of quality attributes by regulatory authorities on CQAs for LNPs [227].

The analytical techniques outlined in this chapter (dynamic light scattering (DLS), nanoparticle tracking analysis (NTA) and asymmetric flow field-flow fractionation (AF4)) have been applied in numerous studies to characterize complex nanocarrier systems [228-230], including LNP formulations [209, 215, 231, 232]. However, a significant knowledge gap remains in the detailed understanding of CQAs. In particular, LNPs have not been comprehensively evaluated across the full manufacturing process, and their behaviours in physiologic conditions, from microfluidic production to purification, filtration, and storage under both physiologically relevant (37 ºC), refrigerated (8 ºC) and frozen (-80 °C) conditions.

In this work, frozen storage at -80 °C was selected because it matches the storage requirements of the Pfizer-BioNTech COVID-19 vaccine, representing the lowest standard commercial freezer temperature before liquid nitrogen storage. Incorporating final product storage conditions into early-stage LNP development and testing is crucial to confirm storage stability. Nevertheless, ultra-low temperature storage introduces logistical challenges for the supply chain, as highlighted during the large-scale distribution of LNP-based COVID-19 vaccines. In addition, studying LNPs at 37 °C allows to simulate *in vivo* conditions, assess potential aggregation, degradation, or changes in size distribution, and evaluate the impact on CQAs [233]. Such assessments are essential for predicting pharmacokinetics, bioavailability, and therapeutic efficacy, as well as for optimizing formulation design to ensure safety and effectiveness in clinical use.

This chapter emphasises the importance of employing high-resolution analytical approaches to characterize the physicochemical properties of LNP candidates during early stages of nanomedicine development, with the goal of supporting successful clinical translation. The cationic lipid used in this study for synthesising LNPs is 1,2-dioleoyl-3-trimethylammonium-propane chloride salt (DOTAP), owing to its permanently cationic nature. Poly(A) was used as a model messenger RNA (mRNA) payload for encapsulation within the LNPs. While both components are well established in the field, no previous studies have performed a comprehensive cross-comparison of analytical techniques using a workflow that integrates microfluidics-based manufacturing, downstream processing, and multi-detector AF4 analysis.

2.2 Aim and Objectives

The goal of this chapter is to evaluate how in-process manufacturing steps influence key physical parameters, using DOTAP-LNPs prototype as a model LNP. To achieve this aim, the objectives of this chapter were **(1)** to formulate DOTAP-LNPs loaded with Poly(A) as a model single stranded single-stranded RNA drug substance for due to its simple structure (chain of adenosine units) and its ability to mimic the biophysical properties of functional mRNA (e.g., surface charge) **(2)** characterise LNP CQAs following microfluidic synthesis, dialysis, and filtration using polyethersulfone (PES) and polyvinylidene fluoride (PVDF) syringe filters; **(3)** to assess LNP stability over 28 days under different storage temperatures 8 ºC, 37 ºC and -80 ºC followed by one cycle of freeze-thaw (1X F/T) in the presence of sucrose as a cryoprotectant; and **(4)** to develop and apply an AF4 method to characterise 1X F/T DOTAP-LNPs in the absence of sucrose.

2.3 Materials and Methods

2.3.1 Materials

Polyadenylic acid (Poly(A)), cholesterol, ethanol, and dialysis tubing cellulose membrane (molecular weight cut-off size (MWCO) 14 kDa) were purchased from Sigma-Aldrich (St. Louis, MO, USA). The cationic lipid 1,2-dioleoyl-3-trimethylammonium-propane chloride salt (DOTAP), helper lipids 1,2-distearoyl-sn-glycero-3-phosphocholine (DSPC), 1,2-dimyristoyl-rac-glycero-3-methoxypolyethylene glycol-2000 (DMG-PEG 2000) and were purchased from Avanti Polar Lipids (Alabaster, AL, USA). Invitrogen™ UltraPure™ DNase/RNase-Free Water, PVDF 0.22 µm filters, Quant-iT™ RiboGreen™ RNA Assay Quantitation Kit, sodium citrate dihydrate, phosphate-buffered saline (PBS) 10X salt solution pH 7.4 and lyophilised powder Bovine Serum Albumin (BSA) were acquired from Fisher Scientific (Loughborough, UK). PES 0.2 µm Acrodisc® filters were purchased from Pall Corporation.

2.3.2 Methods

2.3.2.1 Preparation of DOTAP-LNPs

Poly(A) DOTAP-LNPs were manufactured using the NanoAssemblr® Ignite Precision NanoSystems (Vancouver, BC, Canada) using the NxGen™ single-use microfluidic cartridge. Lipid stocks were prepared in ethanol at a molar ratio of DOTAP: DSPC: Cholesterol: DMG-PEG2000 (50:10:38.5:1.5 mol%, respectively), which is based on the lipid ratio composition of Onpattro® (Alnylam Pharmaceuticals) [234] and Comirnaty® (Pfizer-BioNTech) [235]. The aqueous phase consisted of initial Poly(A) stock of 1.5 mg/mL dissolved in 50 mM sodium citrate buffer (pH 6.0). The Total Flow Rate (TFR) was set at 15 mL/min, and an aqueous-to-organic Flow Rate Ratio (FRR) of 3:1 was used with a final lipid concentration of 1.25 mg/mL and Poly(A) of 0.055 mg/mL. The N:P (N for lipid nitrogen and P for nucleic acid phosphate) was 6:1. Initial and final waste volumes were set at 0.35 and 0.05 mL, respectively. Resultant suspensions were dialysed (MWCO 14 kDa, Sigma-Aldrich, St. Louis, MO, USA) into 1X PBS (pH 7.4) (200X dialysate ratio) under magnetic stirring for 1 hour at 25 ºC to remove residual ethanol and citrate buffer. For all studies, Day 0 denotes the day of LNP synthesis. **Table 2.1** summarises the target specifications of the synthesised DOTAP-LNPs.

Table 2.1 Target critical quality attributes (CQA) for DOTAP-LNPs. PDI: polydispersity index, ZP: zeta potential, EE: encapsulation efficiency.

CQA	Specification
Z-Average (nm)	≤ 100
PDI	PDI ≤ 0.2
ZP (mV)	+ 10 > ZP > -10
EE (%)	≥ 90

2.3.2.2 LNP stability

Filtration

Following dialysis, LNPs were filtered using a 0.2 µm pore-sized syringe filter equipped with either PES or PVDF membranes to compare their impact on LNP CQAs. These membranes were selected due to their established use as sterilizing-grade, single-use filters in pharmaceutical applications. Filtration was performed under gentle manual pressure. Prior to use, all filters were pre-rinsed with PBS to condition the membrane and remove potential contaminants. Unfiltered LNPs served as control.

Refrigeration

Following dialysis, unfiltered LNPs were stored under refrigerated conditions (4 °C) in glass vials for 28 days representing the maximum duration over which the LNPs would be used for further studies. At predefined time points (**Table 2.2**) LNPs were withdrawn for analysis of CQAs.

Table 2.2 Stability time-points and measured critical quality attributes (CQAs) for DOTAP-LNPs. PDI: polydispersity index, ZP: zeta potential, EE: encapsulation efficiency.

CQA	Stability time-point (days)
Z-Average	0, 1, 2, 3, 4, 7, 10, 14, 21, 28
PDI	0, 1, 2, 3, 4, 7, 10, 14, 21, 28
ZP (mV)	0, 7, 10, 14, 21, 28
EE (%)	0, 7, 10, 14, 21, 28

Use of cryoprotectant at ultra-low temperature

LNPs were tested for their stability using sucrose as a cryoprotectant at different concentrations, 5 %, 10 % and 20 % (*w/v*) sucrose. Sucrose was dissolved in PBS to prepare the buffer, and buffer exchange was performed *via* dialysis under magnetic stirring for 1 hour at 25 °C to replace citrate and ethanol with the sucrose-containing PBS solution. Sucrose 0 % (*w/v*) (consisting of PBS only) served as the control. All LNP samples were analysed on the

day of LNP synthesis (day 0) and following 1X F/T cycle. The 1X F/T cycle involved storage at -80 °C for 24 hours followed by thawing to ambient temperature (25 °C).

Physiologically relevant temperature

Following dialysis, unfiltered LNP formulations were stored at 37 °C control room in sealed glass vials under static conditions. At predefined time points (24, 48, and 72 hours), LNPs were withdrawn for analysis of CQAs.

2.3.2.3 Particle size

Z-average and PDI were measured by DLS using Zetasizer Nano ZS system (Malvern Panalytical, Worcestershire, UK). Parameters were set at 25 °C using non-invasive backscatter (NIBS, 173°) at a dilution of 1:10 in 10 mM PBS (pH 7.4) to achieve a final theoretical lipid concentration of 125 µg/ mL (corresponding theoretical Poly(A) concentration 5.5 µg/mL). The refractive index (RI) and viscosity of the aqueous buffer (PBS) were set at 1.34 and 1.02 cP, respectively. All measurements were performed in three independent replicates consisting of at least two technical replicates.

2.3.2.4 Surface charge

The LNP zeta potential was measured by electrophoretic light scattering (ELS) using Zetasizer Nano ZS system. Unless otherwise stated, all measurements were performed at 25 °C and at a 1:10 dilution in DNase/RNase-free water established in [102]. The RI and viscosity of DNase/RNase-free water were set at 1.33 cP and 0.89 cP, respectively. All zeta potential measurements were performed in three independent replicates consisting of at least two technical replicates.

2.3.2.5 Particle size distribution and particle concentration

Particle size distribution and estimated concentration were measured by NTA using a NanoSight NS300 system (Malvern, Worcestershire, UK), equipped with sCMOS camera for video captures, a low-volume flow cell, a 488 nm laser and an automated syringe driver. All samples were diluted in 10 mM PBS (pH 7.4) prior to analysis with NTA. Dilutions, camera level and detection threshold varied between 20 to 80 particles per video capture (**Table 2.3**). All measurements were performed at 25 °C and injected into the flow cell using a syringe driver set at 50 arbitrary units (AU). The corresponding NTA data acquisition parameters were five replicate videos of 60 s duration. All data were analysed in the NTA 3.4.003 program. Three independent replicate measurements consisting of five technical replicates each were performed for each sample.

Table 2.3 NTA optimised experimental parameters for DOTAP-LNPs. PES: polyethersulfone, PVDF: polyvinylidene fluoride, F/T: freeze-thaw.

Sample	Dilution	Detection Threshold	Camera Level
Post-Microfluidics	X10000	5	15
Post Dialysis (Day 0)	X4000		
Post PES-Filtration			
Post 1X F/T			
Post PVDF-Filtration	X100		
Post 37 ºC incubation at 24, 48, 72 hours	X4000	5	16

2.3.2.6 Encapsulation Efficiency (EE)

Quant-iT™ RiboGreen RNA Assay Quantitation (Invitrogen™, Thermo Fisher Scientific, UK) was used for the quantification of Poly(A) encapsulation in DOTAP-LNPs as per manufacturer's instructions. LNPs were serially diluted in Tris and Ethylenediaminetetraacetic acid (TE buffer) in the presence and absence 2 % *v/v* Triton X-100 in a 96-well plate. The plate was incubated at 37 °C for 15 minutes, followed by the addition of two dilutions of 1X Ribogreen Reagent (500-fold and 200-fold) to wells containing TE buffer and Triton X-100, respectively. Fluorescence was measured using a GloMax® Microplate Reader (Promega Corporation, UK) with an excitation of 475 nm and emission 500-550 nm wavelength. EE% (**Equation 2.1**) was determined by constructing standard calibration curves using naked Poly(A) solutions prepared both in the absence and presence of Triton X-100. These standard curves allowed for accurate quantification of free and total Poly(A) in the LNP samples, enabling calculation of EE% by comparing the amount of encapsulated Poly(A) to the total Poly(A) content.

$$\mathbf{EE}\ (\%) = \frac{\mathbf{Poly(A)_{total} - Poly(A)_{free}}}{\mathbf{PolyA_{total}}} \mathbf{x\ 100} \qquad \textbf{Equation 2.1}$$

where $Poly(A)_{total}$ is the total Poly(A) concentration (µg/mL) in wells containing Triton-TE buffer, $Poly(A)_{free}$ the concentration (µg/mL) of the unentrapped Poly(A) for wells containing TE buffer.

2.3.2.7 Frit-Inlet Asymmetric Flow Field-Flow Fractionation (FI-AF4)

2.3.2.7.1 Radius of Gyration (R_g), Hydrodynamic Radius (R_h) and Shape Factor (R_g/R_h) by FI-AF4 in-line with Multiple Detectors (UV, MALS and DLS)

FI-AF4 (AF200 Postnova Analytics, Landsberg, Germany) was used for characterising DOTAP-LNPs for their R_g (FI-AF4-MALS), R_h (FI-AF4-DLS) and R_g/R_h. The system was configured with tip and pressure pumps, a degasser, and autosampler. The system was equipped with an online UV-Vis (PN3242, λ = 280 nm, Postnova Analytics), 21-angle Multi-angle Light Scattering (MALS-PN3621, Postnova Analytics) and online Zetasizer Nano ZS (Malvern Panalytical, Malvern, UK) detector. The frit-inlet channel configuration included the use of a 10 kDa MWCO size amphiphilic regenerated cellulose (RC) membrane, a spacer thickness of 350 µm, and 10 mM PBS (pH 7.4) as the carrier liquid.

DLS measurements were obtained using a Malvern quartz flow cell (ZEN0023), with a flow rate of 0.3 mL/min at 25 °C at three-seconds intervals. The measurement position was set at 4.2 mm with the attenuator set at 11. The FI-AF4 parameters for separation are in **Table 2.4.** Due to the positive charge of DOTAP-LNPs and an amphiphilic membrane used, membrane pre-conditioning with triplicate injections was carried out using BSA (5 mg/mL) and 6 injections of fresh DOTAP-LNPs. For the analysis, DOTAP-LNPs were injected at technical replicates of three and diluted to total lipid concentration of 0.5 mg/mL. The intensity of the scattered light using the MALS detector was calculated for angles 36° to 148° and the MALS sphere fit model was used for the R_g measurement.

Table 2.4 Corresponding FI-AF4 parameters for applied cross-flow.

Time (min)	Cross-flow (mL/min)	Type	Exponent	Detector flow (mL/min)	Injection volume (µL)	Injection flow rate (mL/min)
20	0.75	Constant	0	0.3	20	0.2
60	0.75	Exponential Power Decay	0.2			
5	0	Constant	0			

2.3.2.7.2 Sample recovery by FI-AF4

The recovery (R %) of the samples for was calculated using the following equation:

$$\mathbf{R}\ (\%) = \frac{\mathbf{Ac}}{\mathbf{A}}\ \mathbf{x\ 100} \qquad \textbf{Equation 2.2}$$

Where A_c is the area under the peak of LNPs under a cross flow, and A the area under the peak of the unfractionated LNP *via* direct sample injection (without an applied cross-flow).

Table 2.5 depicts the parameters for direct injection. Absorbance was measured at 280 nm using a UV detector. Fractions eluting after the cross-flow stops (0 mL/min for 5 minutes) were not included in the fractogram integration. A criteria to establish optimal methodology was based on a sample recovery of ≥70 % (CEN ISO/TS 21362:2021 [236]). Recovery was calculated for LNPs at day 0.

Table 2.5 Corresponding FI-AF4 parameters for direct injection.

Time (min)	Cross-flow (mL/min)	Type	Exponent	Detector flow (mL/min)	Injection volume (µL)	Injection flow rate (mL/min)
10	0	Constant	0	0.3	20	0.2
5	0	Linear				

2.3.2.8 Statistical Analysis

All data were analysed using GraphPad Prism 10 (GraphPad Software Inc). The mean ± standard deviation (SD) was calculated for all experiments with three independent replicates and at least two technical replicates. Normality of all datasets was assessed using Shapiro-Wilk test. One-way analysis of variation (ANOVA) followed by Tukey's multiple comparisons test was used for normally distributed data. For non-normally distributed data, non-parametric analysis was carried out using Kruskal-Wallis test followed by Dunn's multiple comparison test. Statistical significance was considered at *p-value* < 0.05, *p < 0.05, **p < 0.01, ***p < 0.001, ****p < 0.0001.

2.4 Results

2.4.1 The effect of dialysis and filtration on LNP CQAs

Initially, the effect of the manufacturing process (microfluidics) on key attributes of the LNPs was investigated. This analysis was conducted on samples taken at various stages, including initial microfluidics production, formulation purification by dialysis, and sterile filtration using two commonly used membrane types, PES and PVDF. Sub-populations of relatively high concentrations for DOTAP-LNPs pre-dialysis (**Figure 2.1A** and **Figure 2.1B**) show the importance of dialysis to exchange ethanol following microfluidics. NTA showed different particle size subpopulation at > 100 nm (**Figure 2.1B**). This signifies the advantage of NTA over DLS. NTA tracks the movement of single particles illuminated by a laser under a microscope whereas DLS is an ensemble technique. NTA does not average signals over the

entire sample, rather analyses particles individually. In addition, DLS calculates the *Z*-average by intensity-weighted average whereas NTA measures the hydrodynamic diameter by number-weighted distribution of the valid tracks.

The *Z*-average for LNP averaged 57.0 (± 3.2) nm for pre-dialysis and 55.9 (± 0.9) nm post-dialysis (**Figure 2.1C**). DLS revealed a slightly lower *Z*-average following dialysis and PES-filtration (56.9 (± 1.2) nm post-PES filtration) compared to a non-significant higher *Z*-average following PVDF filtration (115.7 (± 45.5) nm) (**Figure 2.1C**). Despite a reduction in *Z*-average size observed *via* DLS post-dialysis, NTA measurements indicated an increase in the hydrodynamic diameter of the LNPs post-dialysis (**Figure 2.1C**). The differences can be attributed to the fundamental differences in the measurement principles of DLS and NTA.

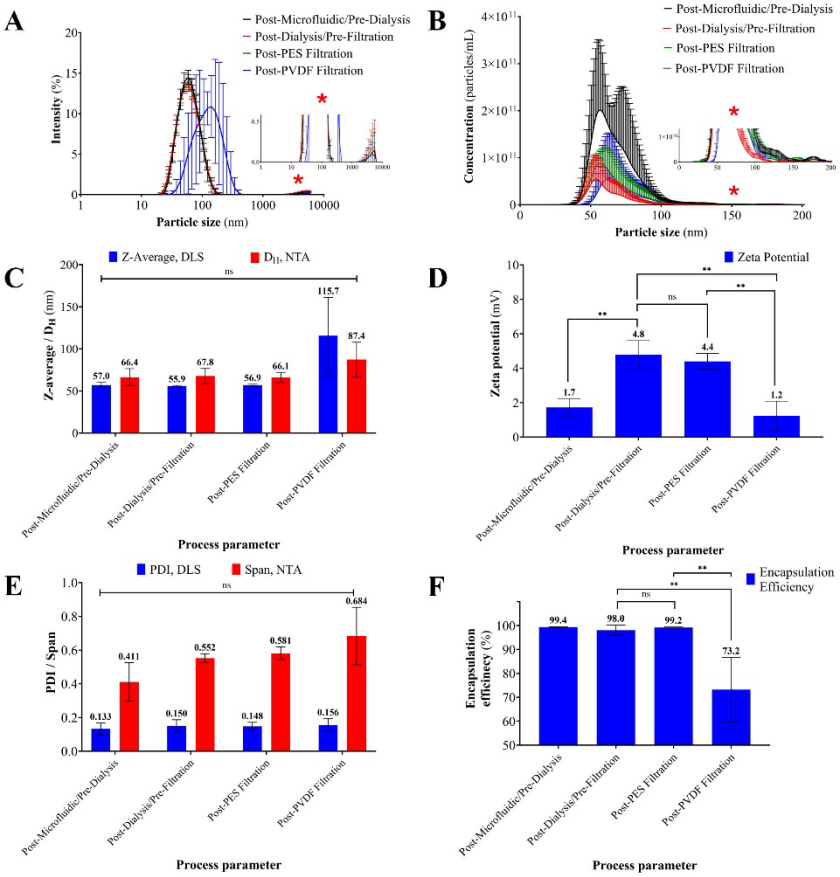

Figure 2.1 Physicochemical trend analysis of the impact of process parameters on DOTAP-LNPs. Plots represent (A) intensity-based size distribution obtained by DLS (B) particle size per concentration obtained by NTA (C) *Z*-average obtained by DLS and hydrodynamic diameter (DH) obtained by NTA (D) zeta potential (E) PDI and span (D90-D10)/D50) and (F) encapsulation efficiency. Error bars represent ± S.D mean of 3 independent replicates. Statistical analysis was performed using one-way ANOVA followed by post-hoc Tukey's test, **$p < 0.01$, ns; not significant.

The integration of CQAs with a comparative analysis of the post-dialysis and PES/PVDF filtration stages suggests that the increase in *Z*-average for PVDF filtration may have led to the loss of electrostatic complexes between the DOTAP lipid and Poly(A) nucleic acid. This is likely due to adsorption onto the membrane surface, which in turn promoted particle aggregation and self-association, resulting in a 110 % increase in particle size (56.9 nm to 115.7 nm for post-PES and post-PVDF filtration respectively). Filtration steps demonstrated a slightly higher polydispersity for PVDF filtration compared to PES (PDI 0.148 (± 0.024) and 0.156 (± 0.037) for PES- and PVDF-filtration respectively) whereas span calculated using NTA indicated a higher polydispersity compared to PDI (0.581 (± 0.038) for PES- and 0.684 (± 0.170) for PVDF-filtration respectively) (**Figure 2.1E**). The size distributions observed after dialysis (pre-PES filtration) and post-PES filtration remained comparable, supporting the suitability of PES membranes for LNP purification following dialysis. The buffer exchange by dialysis resulted in an increase in PDI (**Figure 2.1E**). This increase suggests the emergence of detectable sub-populations at various stages, relative to the post-microfluidic baseline, an expected outcome as citrate buffer and ethanol are removed and filtration (*via* dialysis) introduces mechanical stress that may affect LNP stability.

LNPs undergoing PVDF filtration showed the lowest values for surface charge (1.2 (± 0) mV) (**Figure 2.1D**) and encapsulation efficiency (73.2 (± 13.5) %) (**Figure 2.1F**). The surface charge was lower for pre-dialysis compared to post-dialysis (1.7 (± 0) mV and 4.8 (± 0) mV respectively) indicates the presence of ethanol and citrate buffer in the formulation affecting the exposed charges of the LNP. The buffer used to dissolve Poly(A) is citrate buffer (pH 6). At pH 6, citrate carries two negative charges due to deprotonation of its carboxyl groups [237], which can interact electrostatically with the positively charged surfaces of LNPs. This interaction masks the LNP surface charge, leading to lower zeta potential readings. Additionally, some unencapsulated Poly(A) may remain loosely attached to the LNP surface following microfluidic synthesis, further reducing the apparent surface charge. Immediately after formation, some lipid components (e.g. DOTAP) may not be fully organized or protonated as they would be under physiological pH conditions or require additional time for self-assembly. Upon removal of citrate buffer and ethanol *via* dialysis and exchanged with PBS, surface charge measurements are increased, likely due to the detachment of loosely bound Poly(A) which was masking the surface lipid and the complete self-assembly of LNPs. This suggests that dialysis introduces detectable changes in LNP CQAs such as heterogeneous size distribution and increase in zeta potential.

2.4.2 The effect of short-term stability on LNP CQAs

The physical stability of DOTAP-LNPs was assessed over a 28-day period by monitoring CQAs using DLS, NTA, and Quant-iT™ RiboGreen assay at different time-points for each CQA investigation. Formulations were analysed post-dialysis without filtration and stored in glass vials under refrigerated conditions to allow direct comparison with samples subjected to filtration. Throughout the 28-day stability study, all measured CQAs exhibited time-dependent changes (**Figure 2.2)**. The size-based distribution revealed an initial LNP population followed by particles of > 1000 nm hydrodynamic diameter **(Figure 2.2A).** The average particle Z-average increased by 14.1 nm from day 0 to day 28 (measured using DLS) and an increase in the hydrodynamic diameter of 9.5 nm (measured using NTA) (**Figure 2.2C**). Statistical significance was seen between Day 0 and Day 14 in the case of DLS and between Day 0 and Day 10 in the case of NTA. The observed changes in *Z*-average are likely influenced by DLS sensitivity to larger particles, which tends to skew measurements toward higher values. Despite the increase in size, the PDI has remained ~ 0.2 and a span ~ 0.6 across the 28-days (**Figure 2.2E**).

The NTA data exhibited variability throughout the stability study period with concentration against particle size (**Figure 2.2B**) revealed increased particle aggregates concentration with time (particles > 100 nm), suggesting the formation of sub-populations. Measurements taken at later time points (days 14, 21, and 28) showed no trend in *Z*-average or hydrodynamic diameter (**Figure 2.2E**). Further, along the 28 days storage period, PDI range between (0.163-0.227) and span (0.623-0.746). Statistical difference are shown between *Z*-average (measured using DLS) and hydrodynamic diameter (measured using NTA) and also between PDI (measured using DLS) and span (measured using NTA) (**Figure 2.2C** and **Figure 2.2E**). While DLS data showed statistically significant changes in particle size and PDI across time points, NTA analysis did not yield comparable statistical differences. These discrepancies between low-resolution and high-resolution techniques highlight the importance of employing more sensitive analytical methods for accurate CQA characterization.

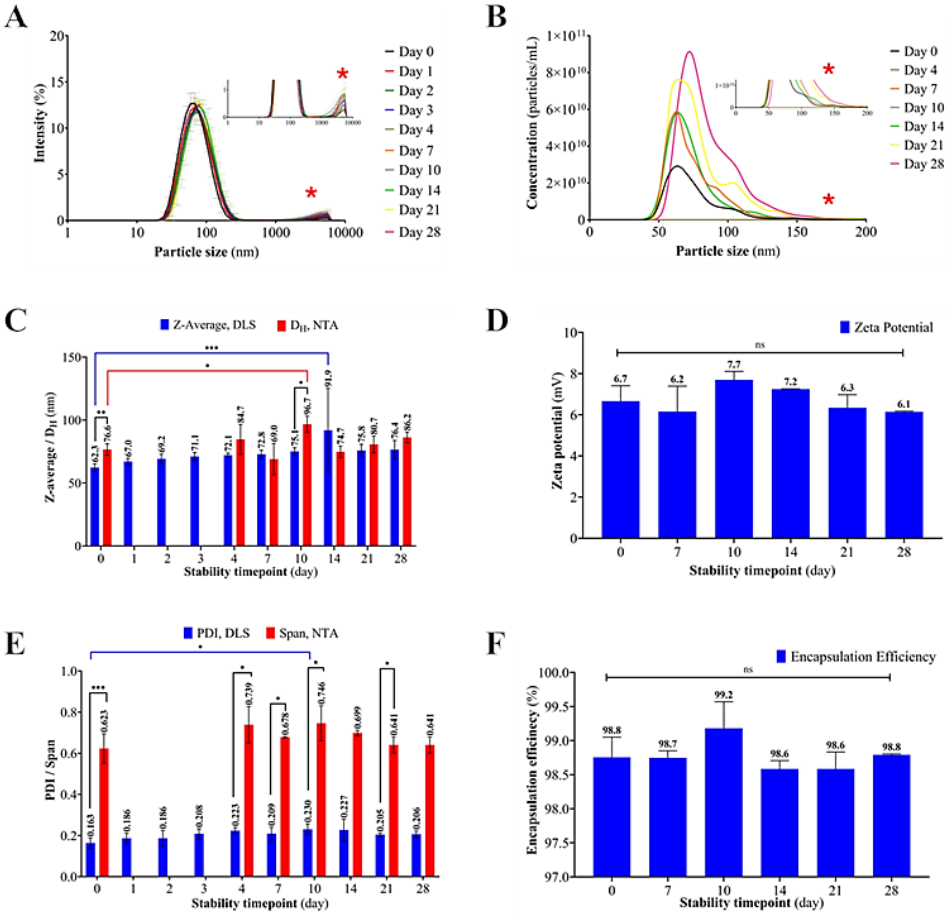

Figure 2.2 Physicochemical trend analysis of the impact of 28-days storage of DOTAP-LNPs at 4 ºC. Plots represent (A) intensity-based size distribution (B) particle size per concentration (C) *Z*-average and hydrodynamic diameter (DH) (D) zeta potential (E) PDI and span and (F) encapsulation efficiency. Error bars represent ± S.D mean of 3 independent replicates. Statistical analysis was performed using one-way ANOVA followed by post-hoc Tukey's test comparing between different days, *p < 0.05, ***p < 0.001, ns; not significant. The peaks marked with a red asterisk (*) show enlarged trace.

The zeta potential remained slightly positive, ranging between +6 to +8 mV, with no significant fluctuations observed across the different time points (**Figure 2.2D**). Variations in surface charge may result from the DOTAP lipid gradually repositioning itself within the LNP outer monolayer to achieve a more thermodynamically stable orientation on the LNP surface This led to minor differences in zeta potential compared to day 0 values. Further, the adsorption/desorption of ions (in the PBS buffer) onto the surface of the LNPs may contribute to minor fluctuations in surface charge at specific time points. Poly(A) encapsulation efficiency remained above 98 % throughout the 28-day study, indicating that no significant

leakage occurred and that Poly(A) remained stably encapsulated within the LNP structure (**Figure 2.2F**).

2.4.3 The effect of 72-hr incubation at 37 ºC on DOTAP-LNP CQAs

The physicochemical stability of DOTAP-LNPs over a 72-hr incubation period at physiologically relevant temperature (37 ºC) was evaluated. Results revealed time-dependent changes across multiple CQAs.

DLS intensity based on intensity-weighted measurements (**Figure 2.3A**) indicates minimal shifts in the particle size distribution profile over time, with highest intensity for day 0 suggesting a higher particle size at day 0, and shrinkage of LNP following incubation. The non-significant difference in intensity (overlapping SD) suggests overall colloidal stability of LNP. However, NTA revealed noticeable changes (**Figure 2.3B**), particularly with the emergence of larger particle sub-populations after 48-hr and 72-hr (highlighted by red asterisks in **Figure 2.3B**). The hydrodynamic diameter measured using NTA remained relatively stable up to 48-hr incubation (65-67 nm) before a significant increase at 72-hr (91.6 (± 3.4) nm), suggesting particle aggregation or fusion of LNPs. DLS has shown a significant reduction in *Z*-average between day 0 and 24-hr followed by a gradually increase up to 72-hr time point.

PDI and span remained consistent up to 48 hrs, but both exhibited significant increases at 72 hrs, particularly the span which reached 1.142 (± 0.121) (**Figure 2.3E**). This highlights a substantial increase in heterogeneity, confirming the formation of sub-populations and aggregates as evident in the particle size differences. The zeta potential of LNPs significantly increased from + 3.0 (± 0.5) mV (0 hr) to + 6.3 (± 0.6) mV (24 hr), followed by a gradual decline to 5.2 (± 0.6) mV (48 hr) and 5.9 (± 0.3) mV (72 hr) (**Figure 2.3F**). This initial increase may be attributed to temperature-dependent conformational reorganization of lipids with the LNP which affects the distribution of the surface charges of lipids. Minor significant fluctuations in encapsulation efficiency were shown over the 72-hr incubation with a peak at (101.1 %) (24-hr) before returning to baseline (99.0 % by 72-hr) (**Figure 2.3G**). These changes were statistically significant and may reflect slight shifts in the partitioning of Poly(A) during incubation, although no major Poly(A) release was indicated.

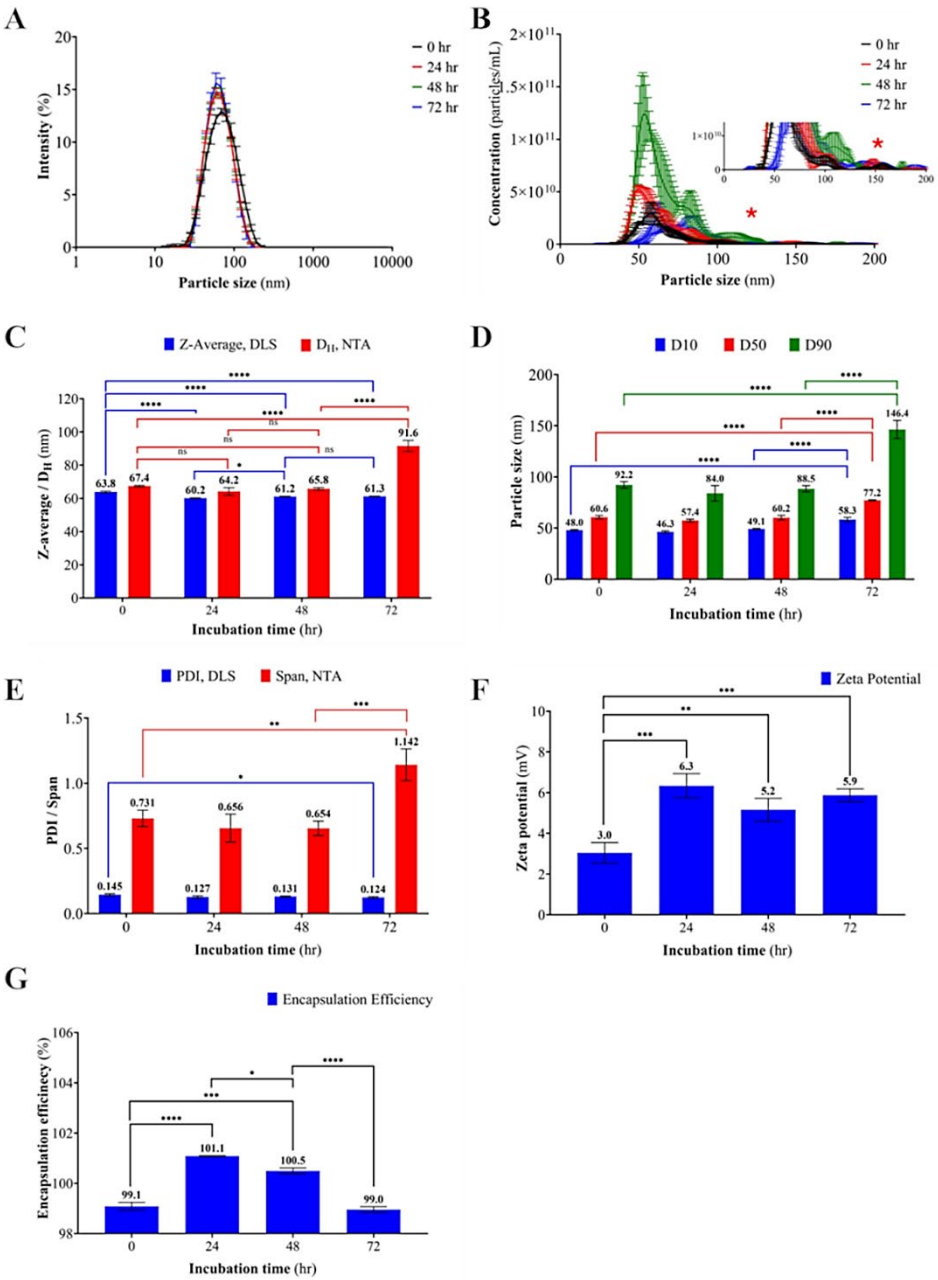

Figure 2.3 Physicochemical trend analysis of the impact of 72-hour incubation of DOTAP-LNPs at 37 ºC. Plots represent (A) intensity-based size distribution (B) particle size per concentration (C) *Z*-average and hydrodynamic diameter (DH) (D) particle size distribution D10, D50, and D90 corresponding to 10 %, 50 %, and 90 % respectively of LNPs under the reported particle size (E) PDI and span (F) zeta potential and (G) encapsulation efficiency. Error bars represent ± S.D mean of 3 independent replicates. Statistical analysis was performed using one-way ANOVA followed by post-hoc Tukey's test comparing between different time-points, *p < 0.05, **p < 0.01, ***p < 0.001, ****p < 0.0001 ns; not significant. The peak marked with a red asterisk (*) show enlarged trace.

2.4.4 The effect of frozen-storage physicochemical stability on LNP CQAs

Given the wide range of cryoprotectants available for preserving LNPs during frozen storage, this study focused on sucrose, which is also utilised in the formulations of the Moderna and Pfizer-BioNTech COVID-19 vaccines. LNPs were prepared and subsequently dialysed into PBS (pH 7.4) containing varying concentrations of sucrose (5 %, 10 % and 20 % *w/v*) followed by the storage at -80 °C.

Overall, incorporating sucrose during dialysis and in the storage buffer resulted in changes in the CQAs of the DOTAP-LNPs. Sucrose disrupted the formation of ice crystals as evident from the significantly lower particle Z-average in the absence and presence of sucrose, 731.8 (± 392.7) nm and 154.7 (± 31.1) nm, 109.8 (± 9.1) nm, 153.5 (± 58.4) nm for 5 %, 10 % and 20 % *w/v* sucrose following a single F/T (**Figure 2.4A** and **Figure 2.4C**). NTA measurement of particle size and concentration also showed heterogeneity in hydrodynamic diameter for LNPs subjected to F/T stress (>100 nm) (**Figure 2.4B**). There was no trend in PDI with increase in sucrose concentration following a single F/T with (**Figure 2.4D**). Poly(A) encapsulation efficiency remained reproducible (~99 %) (**Figure 2.4F)**. The surface charge remained consistent at day 0 between 5 % (4.8 (± 0.7) mV) and 10 % (4.8 (± 0.9) mV) *w/v* sucrose but increased with 20 % *w/v* sucrose (5.2 (± 0.4) mV). Relating to a single F/T, there was a significant reduction between 0 % *w/v* sucrose (5.6 (± 0.2) mV) and 10 % *w/v* sucrose (4.8 (± 0.7) mV), but no significant reduction between 0 % *w/v* sucrose and 10 % or 20 % *w/v* sucrose (6.5 (± 0.3) mV) (**Figure 2.4E**).

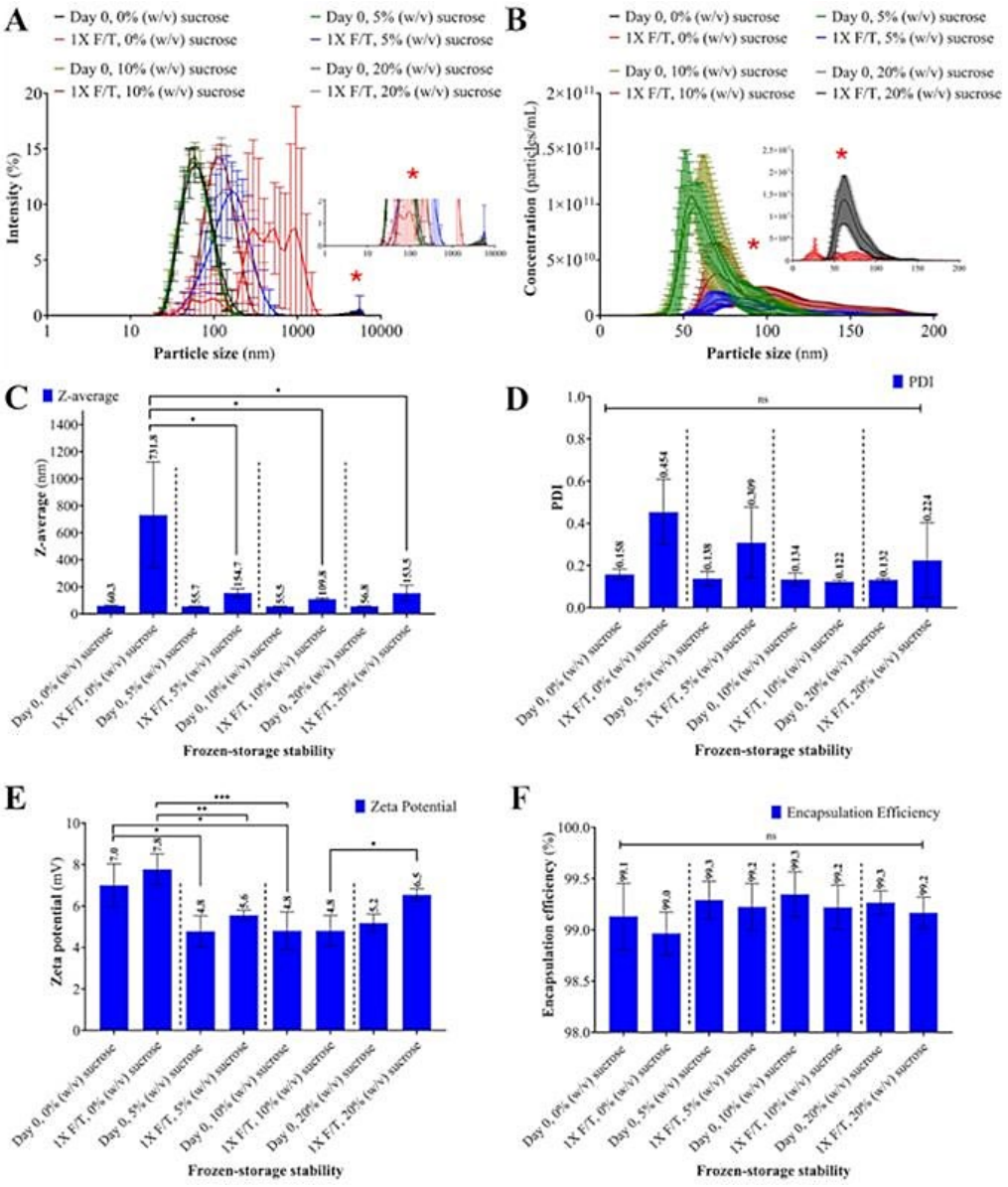

Figure 2.4 Physicochemical trend analysis of the freeze-thaw (F/T) and sucrose percentage (0, 5, 10 and 20 % *w/v* in the LNP formulation) on the stability of DOTAP-LNPs. Plots represent (A) intensity-based size distribution (B) particle size per concentration (C) *Z*-average (D) PDI and (E) zeta potential and (F) encapsulation efficiency. Error bars represent ± S.D mean of 3 independent replicates. Statistical analysis was performed using one-way ANOVA followed by post-hoc Tukey's test comparing between different sucrose concentration and day 0 and 1X F/T for each sucrose concentration, *p < 0.05, **p < 0.01, ***p < 0.001, ****p < 0.0001 ns; not significant. The peak marked with a red asterisk (*) show enlarged trace.

A comparison between DLS and NTA after subjecting LNPs to F/T stress (**Figure 2.4**) revealed significant discrepancies in the results and measured CQAs, emphasizing the

importance of using advanced, high-resolution analytical techniques for thorough evaluation. To investigate colloidal stability in the absence of a cryoprotectant, I developed and applied a multi-dimensional analytical approach using FI-AF4 coupled with in-line UV-MALS-DLS detection to assess the effects of F/T stress on LNP characteristics.

2.4.5 FI-AF4 method development of DOTAP-LNPs

Method development of LNPs using FI-AF4 was initiated using 5 mg/mL BSA (dissolved in 10 mM PBS at pH 7.4) for RC membrane pre-conditioning and MALS detector equilibration in triplicate injections (reps 1-3) (**Figure 2.5A** and **Figure 2.5B**). BSA UV absorbance (280 nm) and MALS (90°) showed a symmetric and narrow peak eluting ~7 min, indicating a consistent retention time and reproducible elution profile (**Figure 2.5A** and **Figure 2.5B)**. The peak intensities are closely aligned across replicates with a signal relative standard deviation (RSD) of 7 % for both the UV and MALS detectors. Following 10 min, the UV and MALS signal return to baseline and remain at 0 mV signal intensity for the rest of elution method, indicating no large particle size components or system contamination present.

DOTAP-LNPs elute between ~15-26 min (UV and MALS fractogram). The position of the peaks is consistent across all runs, indicating good reproducibility in retention time (**Figure 2.5C** and **Figure 2.5D)**. The intensities increased for DOTAP-LNPs injections from replicate injections1-6, ranging from 0.6-1.1 mV (UV signal) with 0.18 % RSD and 5.6-8.6 mV (MALS signal) with 0.17 % RSD (**Supplementary Table S2.1**). The gradual increase in detector intensities suggests a higher concentration reaching the detector and minimal adsorption to the membrane by the 6th injection. Both UV and MALS fractograms show that following DOTAP-LNP elution, the signal does not plateau indicating the presence of low concentration of LNP fractions of a larger particle size which have not eluted (**Figure 2.5C** and **Figure 2.5D)**.

To assess the resolution and polydispersity of the main LNP population, the Full Width at Half Maximum (FWHM) of the primary UV absorbance peak (15-25 min region) was compared across the six runs (**Supplementary Figure S2.1**). The FWHM ranged between 6.6-7.7 min, however increasing with replicate runs (**Supplementary Table S2.2**). This is corresponding to the peak areas ranging 3.33-6.44 VMin. A smaller FWHM typically indicates a more monodisperse formulation. In contrast, the increase in peak broadness can reflect heterogeneity or aggregation of DOTAP-LNPs (**Figure 2.5C** and **Figure 2.5D)**. LNP recoveries >97 % obtained by FI-AF4-UV suggest minimal particle-membrane interactions and demonstrate compliance with ISO (ISO/TS 21362) performance criteria for AF4 methods (**Supplementary Table S2.3).**

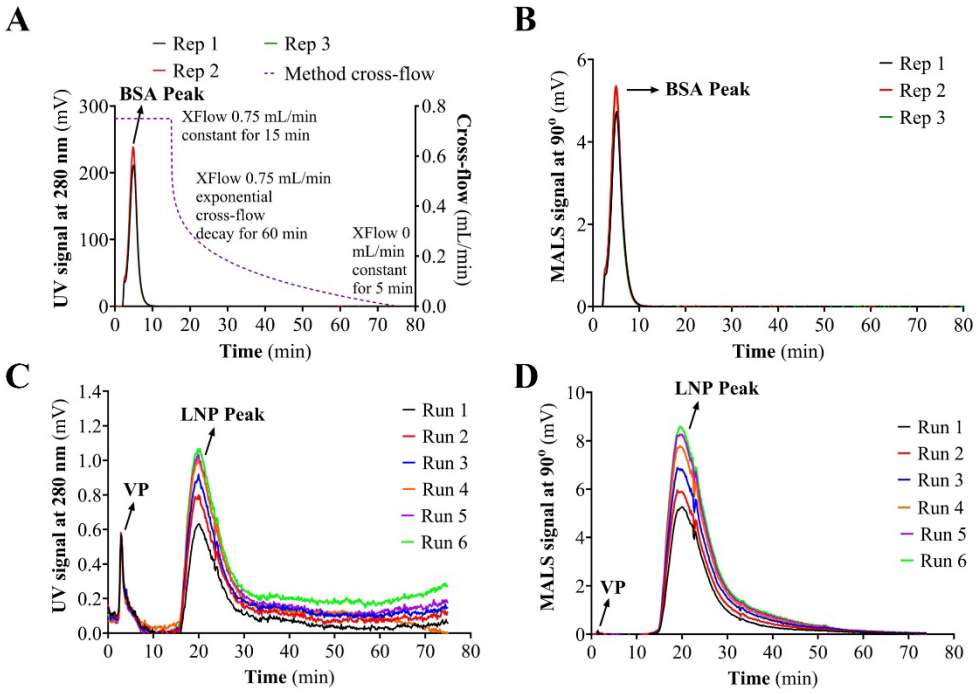

Figure 2.5 FI-AF4 evaluation of DOTAP-LNPs post-dialysis and Bovine Serum Albumin (BSA). Plots represent (A) UV elution profile at 280 nm wavelength and (B) MALS (90°) for membrane pre-conditioning with BSA (C) UV elution profile at 280 nm wavelength and (D) MALS (90°) for DOTAP-LNPs. Error bars represent ± S.D mean of triplicate injections. Dashed line in Figure (A) indicates FI-AF4 elution profile. VP: void peak.

The FI-AF4 UV and MALS profile of the initial batch of LNPs (batch 1) was compared with a second batch of DOTAP-LNPs (batch 2) (**Figure 2.6**). Both LNPs (batch 1 and batch 2) showed two peaks in the MALS and UV trace eluting at 20 min (batch 1) and 25 min (batch 2) (**Figure 2.6A** and **Figure 2.6B**). A higher signal was evident for batch 2 compared to batch 1 for both UV and MALS detectors indicating larger particles present in batch 2 compared to batch 1 as large particles scatter more light. Both batches showed increasing R_h (17-30 nm (batch 1) and 18- 38 nm (batch 2)) and increasing R_g over time (18-48 nm (batch 1) and 28-51 nm (batch 2)) suggesting larger particles eluting later over time (**Figure 2.6C** and **Figure 2.6D**). Batch 1 exhibited higher variability (higher SD) overall in shape factor compared to batch 2, with shape factor values frequently exceeded 1.5 in the early phase of the elution time (15-20 min) and showing a pronounced increase in shape factor (> 2) after 28 min (**Figure 2.6E**). These findings suggest that batch 2 possesses higher overall morphological consistency relative to batch 1, supporting better formulation homogeneity and potentially improved batch quality.

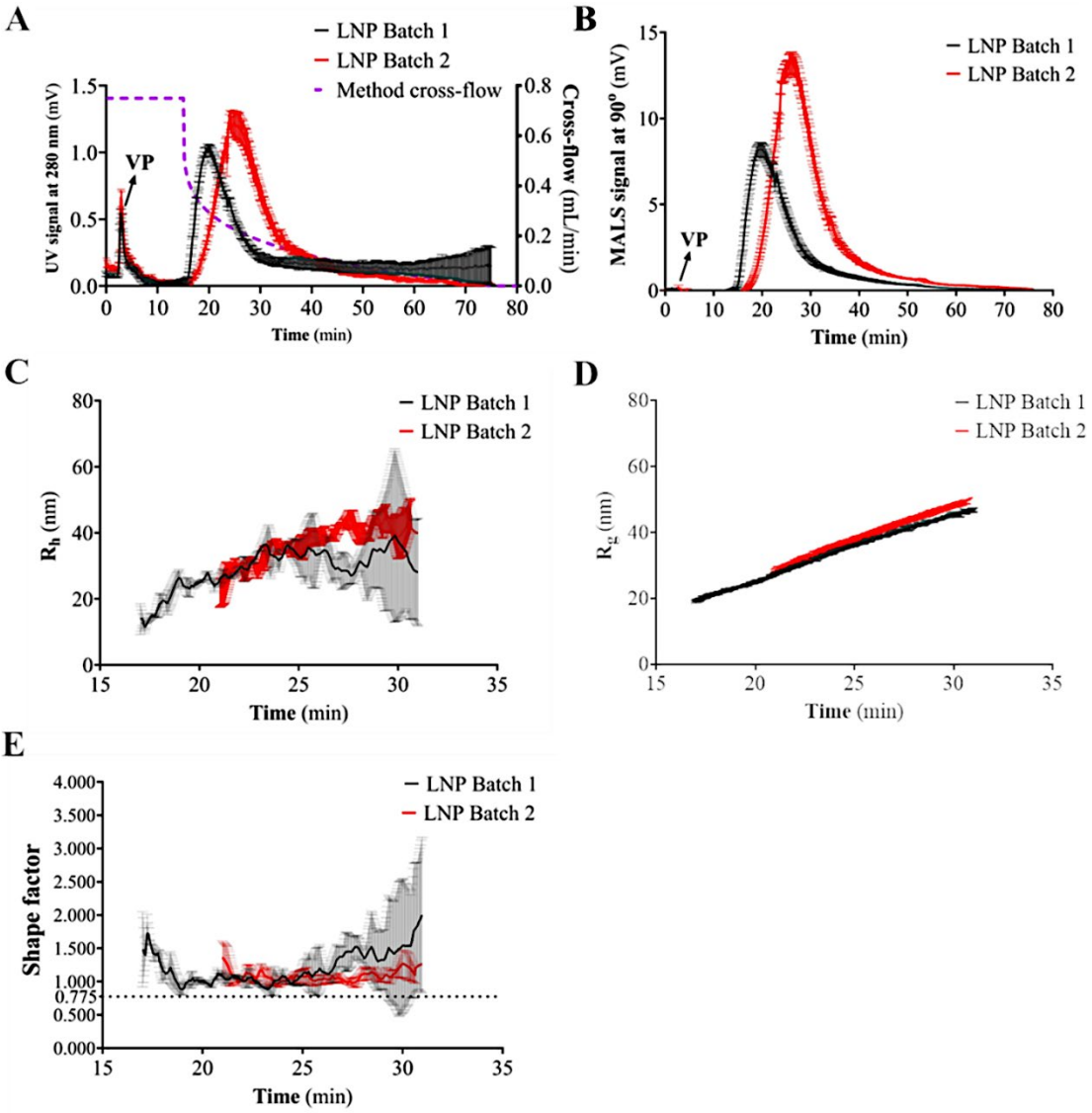

Figure 2.6 FI-AF4 evaluation of batch 1 and batch 2 DOTAP-LNPs post-dialysis. Plots represent (A) UV elution profile at 280 nm wavelength (B) MALS (90º) elution profile (C) hydrodynamic radius (R_h) (D) radius of gyration (R_g) and (E) shape factor (R_g/R_h). Error bars represent ± S.D (n = 3), mean of triplicate injections. Dashed line in plot (A) represent the FI-AF4 elution profile. Dashed line in plot (E) marks 0.775 which is the shape factor value for a sphere.

DOTAP-LNPs (0 % *w/v* sucrose) stored at -80 °C were thawed to room temperature prior to analysis by FI-AF4 coupled with UV, MALS, and DLS detection. These samples displayed a retention time ~56 min (**Figure 2.7A** and **Figure 2.7B**). The UV detector produced a minimal signal (~0.2 mV), which was lower than the void peak signal (~1 mV) (**Figure 2.7A**) and the MALS detector recorded a signal ~0.4 mV, indicating that aggregated LNPs scatter less light compared to freshly prepared LNPs (**Figure 2.7B**). F/T-stressed LNPs exhibited pronounced aggregation (R_g and R_h increased with increase in elution time), consistent with DLS and NTA

data. F/T samples also showed increased visual turbidity and precipitation. F/T replicate injections showed largest average R_h (9259 (± 1524.7) nm) reaching up to 15,000 nm by the end of the elution profile (**Figure 2.7C**). In contrast, replicates 1 and 2 maintained much lower and relatively stable R_h measurements throughout the elution profile (average 406.2 (± 88.6) nm and 625.6 (± 131.8) nm for replicate 1 and replicate 2, respectively. At diameters greater than 1 μm (R_h 500 nm), particles are prone to clustering and sedimentation. This contributes to the total scattering intensity, making larger particles unsuitable for accurate DLS detection [238]. Variability in R_g between replicates is shown in **Figure 2.7D**, with R_g ranging from 150-500 nm. Replicate 1 exhibited the highest overall R_g (300-500 nm) and greater fluctuations across the measured interval, suggesting the formation of larger or more polydisperse aggregates following F/T.

Fresh LNPs (batches 1 and 2) exhibited R_g/R_h 1.21 (± 0.15) and 1.08 (± 0.06) respectively (**Figure 2.7E)**. F/T LNP replicates showed variability in R_g/R_h with replicate 2 showing a relatively higher R_g/R_h (> 0.77 between 40-46 min). These findings highlight variability in aggregation within technical replicates. The high variability between FI-AF4 technical runs, along with R_h, R_g, and R_g/R_h were employed to characterize changes in DOTAP-LNP CQAs and assess the resulting impact on FI-AF4 analysis.

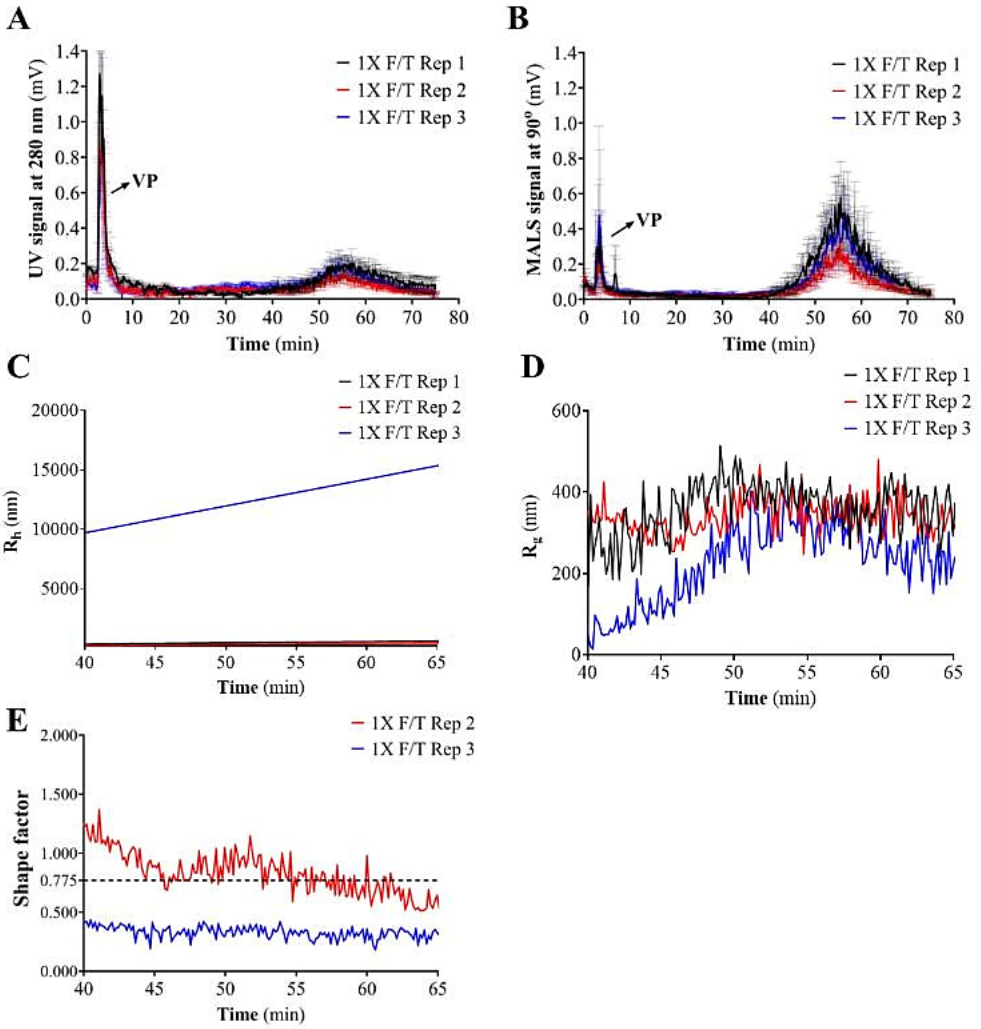

Figure 2.7 FI-AF4 evaluation of DOTAP-LNPs post-one cycle of freeze-thaw (1X F/T) for three replicate injections (reps 1-3). Plots represent (A) UV elution profile at 280 nm wavelength (B) MALS (90°) elution profile (C) hydrodynamic radius (R_h) (D) radius of gyration (R_g) and (E) shape factor (R_g/R_h) along the MALS (90°) elution profile. Error bars in plots (A) and (B) represent ± S.D mean of triplicate (n=3). Dashed line in plot (E) marks 0.775 which is the shape factor value for a sphere.

2.5 Discussion

In this chapter, I applied low to high resolution analytical methodologies to characterize the physicochemical properties of DOTAP-LNPs prototype during early-stage prototype development, with the goal of facilitating their clinical application. DOTAP-LNPs encapsulating Poly(A) as a payload were used as a model LNP system. I examined how manufacturing process parameters, purification steps and storage conditions influenced LNP

physical characteristics. LNP physicochemical stability under both refrigerated, physiologic temperature and frozen storage conditions were investigated using complementary, high-resolution analytical approaches. These advanced methods provide valuable insights into LNP CQAs, supporting improved control and promoting successful clinical translation.

The effect of process parameters on LNP CQAs

Analysis of process conditions revealed that exchanging the manufacturing buffer for the formulation storage buffer after dialysis led to unmasking of surface charges. This change increased the LNP particle size distribution by promoting sub-population formation. The findings underscore the critical role of filter membrane selection. Both PES and PVDF membranes used in the study are hydrophilic and low-protein-binding, making them generally appropriate for aqueous biological formulations. However, PVDF membranes contain electronegative fluoride groups [239], whereas PES membranes have sulfone moieties [240]. Filtration through PVDF membranes resulted in 73 % encapsulation efficiency, while PES membranes achieved 99 % encapsulation. This proved that the PES filter membranes are more compatible with the DOTAP-LNP formulation than PVDF, as its less electronegative sulfone groups are less disruptive to cationic lipid (DOTAP) and Poly(A) electrostatic interactions. Roces *et al*. [102] similarly observed an increase in *Z*-average from post-manufacturing to post-dialysis stages, along with a PDI increase from <0.2 to >0.2. While their study did not further filter Poly(A)-DOTAP-LNPs, they used a lower DOTAP molar ratio and different manufacturing conditions (TFR 5, 10, and 20 mL/min and FRR 1:1, 3:1, and 5:1 of organic to aqueous phase), which could explain the observed differences. Ma *et al*. [241] also evaluated two and three-component DOTAP-based LNP formulations with mRNA payloads, reporting *Z*-averages >200 nm and zeta potentials ~ -25 mV [241].

The changes on CQAs during DOTAP-LNP long-term stability

The 28-day stability study under refrigerated conditions underscored challenges in establishing specifications based on the CQAs of LNPs. DLS measurements showed a gradual increase in *Z*-average over 28 days. However, the DLS technique's intrinsic bias toward larger particles led to overall higher apparent sizes. In contrast, NTA measurements did not show significant size differences across time points. The DLS total scattering intensity increases proportionally with size, making DLS sensitive to larger particles [238]. The Zetasizer PDI values rose significantly on days 10 and 14, while the NTA span values remained consistent throughout the study. The absence of span changes suggests that the overall size distribution remained equivalent, with a uniform shift toward larger particle sizes. No further significant size changes were detected at later time points. Overall, these stability assessments provided

valuable insights into formulation changes over 28 days. Literature on LNP stability details differing prototype formulations and conditions which have led to conflicting reports, some describing size increases over time [242], while others observe stable particle sizes throughout the evaluation period [243, 244].

Exploring the use of FI-AF4 methodology for the resolution of DOTAP-LNPs

FI-AF4 offers analytical capabilities beyond the resolution limits of DLS and NTA, providing a gentle separation approach for evaluating size and morphological distributions when coupled with in-line multi-detectors. In this chapter, I described the development of an FI-AF4-UV-MALS-DLS method. The FI-AF4 protocol was designed in line with ISO guidelines (ISO 21362), delivering a robust and reliable method. The method demonstrated high LNP recovery after separation and detection, along with acceptable selectivity and resolution.

Prior to using FI-AF4 for the characterisation of DOTAP-LNPs, pre-conditioning of the RC membrane in AF4 was performed. This is a crucial step to ensure consistent separation, ensure there is equal interactions between the LNPs and the RC membrane along the entire channel length and reduce nonspecific adsorption of DOTAP-LNPs components onto the membrane surface. At pH 7.4, deprotonation of cellulose hydroxyl groups occurs hence the membrane yields a slight net negative surface charge. This negative surface charge can promote electrostatic interactions with permanently cationic DOTAP-LNPs, which carries a positive charge at pH 7.4. The positive charge of DOTAP-LNPs is attributed to the quaternary ammonium group of DOTAP lipid (**Figure 1.2**).

Effective membrane pre-conditioning contributed to improved resolution and recovery, supporting reliable characterization of LNP size distributions and CQAs. Even though BSA was used for membrane pre-conditioning, pre-conditioning of the membrane was also carried out with DOTAP-LNPs (six replicate injections). DOTAP-LNPs can still interact with the RC membrane, leading to adsorption of DOTAP-LNPs, hence necessitating further pre-conditioning of the membrane with DOTAP-LNPs. With each subsequent injections, the pores of the membrane become increasingly saturated with DOTAP-LNPs, reducing nonspecific binding and allowing more of the sample to elute and be detected, hence increase the signal with replicate injections.

Despite variations in peak height and post-peak baseline, all runs demonstrated a consistent elution profile with a well-defined primary peak. This suggests the FI-AF4 method reliably resolves the main LNP fraction while revealing subtle differences between the runs. The LNPs

themselves acted as a secondary conditioning agent. Early injections 'coat' the RC membrane, thus increasing UV and MALS signal.

On day 0, analysis showed two LNP batches with sizes of 58 nm (LNP batch 1) and 79 nm (LNP batch 2). Each batch produced different UV and MALS detector responses, with batch 2 generating higher signal intensities than batch 1. Given the AF4 high recovery observed for both batches (~97 %), these differences were attributed to variations in post-dialysis concentration, any subsequent dilution during equivalent FI-AF4 sample preparation would further lower sample concentration and detector signal intensity. Although both batches followed the same formulation protocol, uncontrolled variables such as differences in ambient laboratory temperature and lighting may have affected components solubility, stability, and miscibility between the organic and aqueous phases, leading to batch-to-batch variability. Subjecting samples to F/T stress generated additional sub-populations, as evidenced by fragmented and noisy detector signals in both UV and MALS fractograms. Prior to FI-AF4 analysis, F/T LNP suspensions appeared visibly turbid, further supporting the conclusion that aggregation and precipitation during stress contributed to the poor overall recovery.

Changes in DOTAP-LNP particle size and geometry in response to F/T stress

This observed variability in R_g and R_h for F/T samples underscores the sensitivity of LNP size and morphology to F/T conditions and highlights the challenge of achieving consistent physical stability across a single batch. The broad range and fluctuations in R_g suggest that F/T stress induces heterogeneous aggregation due to the formation of ice crystals which exerts mechanical stress and increase the LNP size. Ball *et al*. [242] has also demonstrated the increase in particle hydrodynamic diameter of lipidoids following F/T using sucrose as the cryoprotectant. Previous studies have demonstrated the use of trehalose, and mannitol as cryoprotectants to improve the stability of LNPs [245, 246].

Although size is a prominent indicator of nanoparticle stability, morphology should also be considered an important parameter. The results indicate that freshly prepared LNPs exhibited a rod-like morphology (shape factor >1). Ideally, the initial synthesis of LNPs should result in a spherical morphology (~0.775), as supported by previous literature [209, 247]. The inclusion of sucrose reduced the shape factor to closer to 0.775, indicating a shift toward a more spherical shape. A deviation from spherical shape toward a rod-like structure may reflect improper self-assembly of Poly(A) and lipid components during formulation. Cheng *et al*. [77] demonstrated the presence of bleb-like structures in LNPs using cryo-TEM. These blebs appear as protruding vesicular structures attached to the LNP surface, consisting of an aqueous core enclosed by a lipid bilayer, and may represent a morphological irregularity associated

with instability [248]. Maintaining a spherical morphology is critical for LNPs, as nanoparticles particle shape significantly influences the transfection efficiency and distribution within tissues [249]. Heterogeneity in particle size and morphology may complicate downstream processing and formulation development, reinforcing the need for robust cryoprotectant strategies and process controls. Such outlier behaviour highlights the sensitivity of LNP formulations to subtle variations in handling or composition (addition of a cryoprotectant) and underscores the risk of batch-to-batch variability in physical stability under stress conditions.

Using analytical methods of increasing resolution, from DLS to NTA to FI-AF4, demonstrated that stress-induced sub-populations were detectable with NTA and multidetector FI-AF4 but not with DLS alone. Moreover, the results emphasize the value of high-resolution techniques like FI-AF4-MALS-DLS for detecting subtle differences in size and morphology that are not readily captured by lower-resolution methods.

Limitations and next steps

One limitation of this study is the use of a single LNP prototype (DOTAP-LNPs). DOTAP is a permanently cationic lipid, which differs from clinically relevant ionisable lipids such as MC3 and SM-102. Consequently, the CQAs observed across processing steps including dialysis, filtration, physiologically relevant incubations (37 ^{o}C), refrigerated (4 ^{o}C), and ultra-low temperature storage (-80 °C) may not be directly generalisable to other LNP prototypes. In particular, differences in lipid composition, especially the ionisable lipid component which typically constitutes the highest molar fraction (50 mol%), are likely to influence LNP physicochemical properties [250]. Future studies should therefore extend this work to additional LNP formulations to comprehensively evaluate the impact of in-process manufacturing steps on LNP properties.

Further, although ultra-low temperature storage was assessed in the presence of a cryoprotectant, the formulation was not subjected to freeze-drying to replicate the conditions commonly employed for mRNA vaccines. Freeze-drying removes water by sublimation under vacuum at low temperatures which stabilised the mRNA-LNP in the presence of a cryoprotectant [251]. Future studies should explore lyophilization and evaluate its impact on LNP formulation stability and physicochemical properties in the presence of cryoprotectants. Incorporating such approaches would support the development of a more robust formulation and characterisation pipeline that better reflects clinically relevant and industrial practices.

Chapter 3: Multi-Detector Frit-Inlet Asymmetric Flow Field-Flow Fractionation Method Development for Nanoparticle Mixtures: Deeper Analysis Beyond ISO Quality Standards

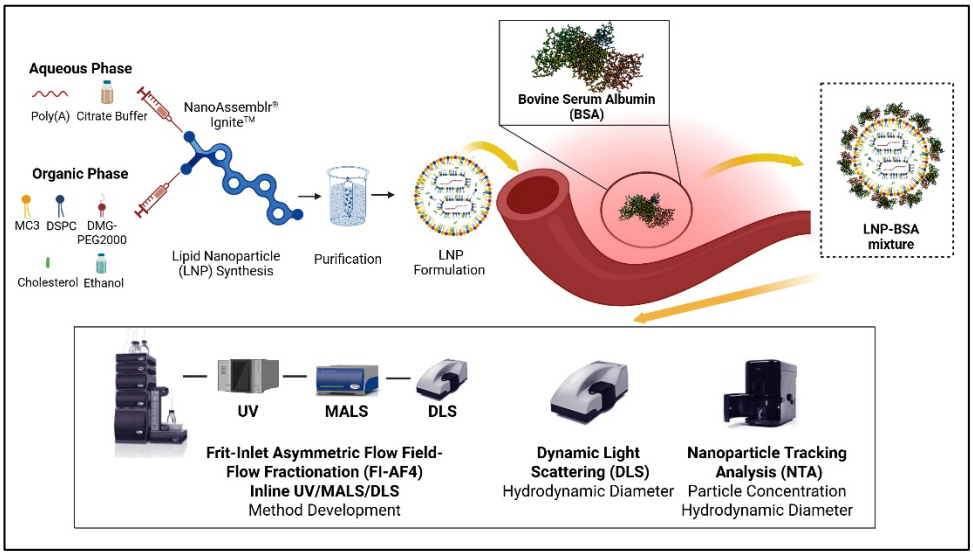

Findings from this work are published in Analytical Methods.

Abdulrahman R, Punnabhum P, Van Den Driest L, Rattray N, Capomaccio R, Treacher K, Perrie Y, Rattray Z. Multi-detector frit-inlet asymmetric flow field-flow fractionation method development for nanoparticle mixtures: deeper analysis beyond ISO quality standards. Analytical Methods. https://doi.org/10.1039/D5AY01758K

Abdulrahman R, author of this thesis, performed all the experimental work and completed all data analysis (except R^2 and RMSE for MALS fitting models) presented in the publication and this chapter.

3.1 Introduction

Lipid nanoparticles (LNPs) have emerged in recent years as a promising nanocarrier-based delivery system for a diverse therapeutic payload, with several formulations incorporating small molecule drugs and nucleic acid-based drugs (e.g. siRNA, mRNA) against target therapeutic indications of unmet clinical need. With such an acceleration in the industry uptake of LNPs, comes the need for analytical pipelines to profile their formulation and biological attributes. This need for novel analytical approaches has introduced challenges in the context of analytical method reliability and reproducibility due to the dynamic and complex nature of LNPs.

To date, there are five RNA LNP-based therapeutics on the market, siRNA drug Onpattro® (Alnylam Pharmaceuticals) [16] for the treatment of hereditary transthyretin-mediated amyloidosis (hATTR), three mRNA vaccines against SARS-CoV2 , Spikevax® (Moderna) [14], mNEXSPIKE® [19] and Comirnaty® (Pfizer-BioNTech) [235] and mRESVIA® (Moderna) mRNA vaccine against respiratory syncytial virus (RSV) in 2023 [12]. The clinical success of these LNP-based therapeutics has drawn attention to the analytical methodologies used to characterise these drug delivery systems.

LNPs are typically composed of four primary lipid components: (1) *ionizable lipids*, that facilitate the encapsulation of negatively-charged nucleic acid payload and promote endosomal escape, enabling cytosolic release of nucleic acid [28], (2) *phospholipids* and (3) *cholesterol* both of which support stability during storage and improves circulation time [252] and (4) *polyethylene glycol (PEG)-conjugated lipids* that prolong LNP circulation time by reducing opsonisation and clearance [253].

While considerable research focus has been invested in establishing the role of each lipid in the LNP structure [7, 68, 252-255] and modulating LNP immunogenicity [81, 256-260], comparatively less attention has been given to the pre-clinical characterisation of LNPs using advanced analytical techniques. A major regulatory challenge lies in the accurate quantification of LNP-based formulation Critical Quality Attributes (CQAs). Comprehensive understanding and control of these CQAs is critical for successful translation, and the safety and efficacy of LNP-based products in clinical applications.

While suitable for a quality control setting, lower resolution techniques such as Dynamic Light Scattering (DLS) and Nanoparticle Tracking Analysis (NTA) offer limited information on LNP CQAs, including formulation heterogeneity, degradation, and morphology. These limitations necessitate the use of high-resolution orthogonal techniques that can generate reproducible data and detect subtle inter-batch variations. However, the high cost and complexity of these methods can be prohibitive. Compounding these issues is the current lack of regulatory guidelines and harmonization of analytics specifically tailored to LNPs, which contributes to inconsistency, ambiguities and a lack of standardization across analytical practices. At present, these gaps are being addressed by various institutions and initiatives (e.g. European Nanomedicine Characterisation Laboratory (EUNCL) [214], International Organization for Standardization (ISO) [236], American Society for Testing and Materials (ASTM) [261], SINTEF and LNE [262] and Joint Research Centre of the European Commission (JRC) [263].

The application of Asymmetric Flow Field-Flow Fractionation (AF4) has recently gained prominence for evaluating the impact of manufacturing processes on LNP formulation attributes [264], measuring particle size [177, 265-271], and profiling LNP nano-bio interactions [177]. AF4, multiplexed with online detectors can simultaneously perform separation and analysis of sub-populations within a polydisperse sample. By virtue of its low shear stress in comparison to chromatographic approaches, AF4 is a non-disruptive and powerful separation technique widely used for the analysis of nanomedicine physicochemical attributes [177, 265-271]. In principle, analytes are introduced into the AF4 channel and concentrated on the accumulation wall. An external force field is applied perpendicular to the parabolic flow of the channel mobile phase, resulting in size-based separation under diffusion [207].

Unlike traditional chromatographic methods, the absence of a stationary phase compared to traditional chromatographic techniques and lower system pressures, offers a minimally disruptive means of separating polydisperse nanoparticle mixtures due to a lack of nanoparticle adsorption on the stationary phase in chromatography columns, and minimal high shear forces. This gentle separation allows for the analysis of complex nanoparticle mixtures that are otherwise challenging to analyse using conventional techniques [272].

Method development for AF4 remains a complex and nuanced process, requiring the careful optimisation of many parameters, including the choice of membrane, selection of the appropriate cross-flow, focus flow (AF4), and detector flow rates, choice of channel geometry

and dimensions, accounting for sample surface charge characteristics, sample injection volume and composition of the carrier liquid. Despite the growing interest in AF4, there is a distinct lack of method development literature on AF4 applications for LNP separation and analysis [272], where publishing method development protocols can significantly benefit the community in implementing robust and reproducible pipelines for profiling nanomedicines during early discovery efforts.

The International Organization for Standardization / Technical Specification ISO/TS 21362:2021 guideline 'Nanotechnologies - Analysis of nano-objects using asymmetrical-flow and centrifugal field-flow fractionation' addresses the requirements of analytical characterisation of nanomaterials using AF4 [236]. While this guideline addresses most nanomaterials, its practical application for complex nanoparticle mixtures due to their inherent polydisperse nature is often challenging. The frit-inlet AF4 (FI-AF4) protocol demonstrated improved run-to-run repeatability and provided superior resolution of polydisperse populations in the sample, enabling the accurate separation and characterisation of sub-population that maybe overlooked by the current available guidelines. The protocol also incorporates multi-angle light scattering (MALS) fit-model reporting, ensuring that the assumption and parameters used in data interpretation are reproducible and comparable across repeated studies. In addition, the FI-AF4 protocol addresses the occurrence of sample recoveries of >100 %, which are not addressed by previous FI-AF4 guidelines leaving uncertainty in data interpretation. Hence, the parameters established in this work represent the best practices that can serve as a foundation for future FI-AF4 guidelines and standardisation efforts.

Multiple detectors can be multiplexed with FI-AF4 to measure nanoparticle CQAs, that include MALS [209, 269, 273] (measuring Radius of Gyration (R_g) and molecular weight), ultraviolet (UV) [175, 274-276] and refractive index (RI) (measuring concentration) [113, 177, 229, 276-281] and DLS (measuring Hydrodynamic Radius (R_h) [271, 275, 278, 282-285]. Particle structure and morphology can be inferred from combining readout from both MALS and DLS detectors and obtaining R_g/R_h [228, 229, 276, 281, 286, 287]. Differences in R_g/R_h ratio provide insights into nanoparticle geometry, with values near 0.77 indicative of an ideal hard sphere [288] whereas shape factor value of ~1.22 suggests a rod-like geometry [289]. Particle morphology is essential for quality control as it reveals the presence of aggregates in the formulation, a factor that strongly influences product stability and LNP potency [290, 291]. Analysis of MALS data requires a consideration of various experimental parameters, including the light scattering angles selected and the fit models applied to each sample component.

Further, theoretical model fits for optimal approximation of R_g remain limited in the literature. It becomes questionable whether calculation of R_g and R_g/R_h is a correct approximation in the absence of using optimal scattering angles and a lack of standardisation of fit models. Such unpublished details and key parameters of FI-AF4 analysis may hamper interlaboratory harmonisation efforts in standardising FI-AF4 analytical pipelines for nanomedicines [43].

Sample recovery is a critical parameter in FI-AF4 to ensure the accurate quantification and representative characterisation of the analyte. ISO/TS 21362 recommends a recovery of ≥70 % as acceptable for nanoscale particles. While this metric refers to the sample recovery of the entire sample, selecting a single appropriate detection wavelength becomes challenging for heterogenous samples, particularly when various sample components absorb light at different wavelengths (e.g. nucleic acids and proteins absorb light at 260 and 280 nm, respectively) [292, 293]. Sample loss may arise from poor selection of membrane pore size as molecules may penetrate through the pores, attractive interactions occurring between sample and the membrane, retention within tubing or channel edges, and solvent incompatibility. Conversely, inadequate method optimisation can lead to apparent recoveries of >100 % due to mass overloading [294-296].

The selection criteria used in method development were based on minimal overlap between peaks, acceptable signal intensity (distinguishable analyte peak from baseline noise), sample recovery (≥70 %) and optimal fit to MALS scattering fit models (R^2 >0.9 and Root Mean Square Error (RMSE) <1). The data generated will complement the ISO/TS 21362:2021 method performance criteria for FI-AF4 method development on heterogenous samples. The sample mixture used for FI-AF4 data analysis consists of LNP and Bovine Serum Albumin (BSA). This mixture was used since the nature of the nanoparticles are different hence the FI-AF4 respective analysis in the case of nanoparticle mixtures is explained (**Figure 3.1**).

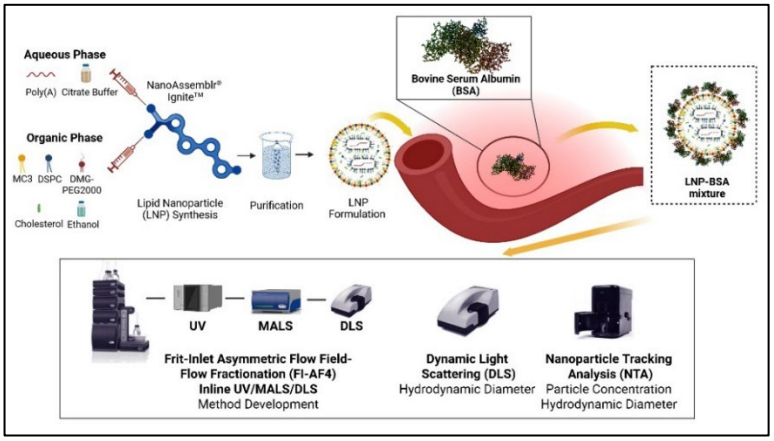

Figure 3.1 Schematic procedure of MC3-LNPs synthesis, formation of the protein corona with BSA and characterisation using DLS, NTA and FI-AF4 coupled to ultraviolet (UV), multi-angle light scattering (MALS) and DLS detectors.

3.2 Aims and Objectives

The aim of the study is to develop a robust analytical method based on a FI-AF4 hyphenated to multiple detectors, for the separation, characterisation of nanoparticle mixtures, beyond the method performance criteria identified by ISO/TS 21362. To achieve this aim, the objectives were **(1)** encapsulate Poly(A) mRNA into the ionizable MC3-LNPs **(2)** incubate MC3-LNPs with BSA at 37 °C for 24 hours to form MC3-LNP-BSA nanoparticle mixtures; **(3)** develop a detailed, step-by-step protocol for the analysis of polydisperse nanoparticle mixture MC3-LNP-BSA focusing on reproducibility and accuracy across analytical techniques and **(4)** develop a FI-AF4 method based on minimal overlap between peaks, acceptable signal intensity (distinguishable analyte peak from baseline noise), sample recovery (≥70 %) and optimal fit to MALS scattering fit models (coefficient of determination (R^2) >0.9 and Root Mean Square Error (RMSE) <1).

3.3 Materials and Methods

3.3.1 Reagents and Materials

Polyadenylic acid (Poly(A)), cholesterol, sodium citrate dihydrate, ethanol, and dialysis tubing cellulose membrane (MWCO 14 kDa) were purchased from Sigma-Aldrich (St. Louis, MO, USA). Helper lipids 1,2-distearoyl-sn-glycero-3-phosphocholine (DSPC), 1,2-dimyristoyl-rac-glycero-3-methoxypolyethylene glycol-2000 (DMG-PEG 2000) were purchased from Avanti Polar Lipids (Alabaster, AL, USA). The ionizable lipid (6Z,9Z,28Z,31Z)-Heptatriaconta-6,9,28,31-tetraen-19-yl 4-(dimethylamino)butanoate (D-Lin-MC3-DMA) was purchased from BroadPharm (San Diego, CA, USA). Lyophilised powder BSA, Invitrogen™

UltraPure™ DNase/RNase-free water and phosphate-buffered saline (PBS) 10X salt solution pH 7.4 was acquired from Fisher Scientific (Loughborough, UK).

3.3.2 Methods

3.3.2.1 Synthesis of MC3-LNP formulations

Poly(A) LNPs were manufactured using the NanoAssemblr® Ignite Precision NanoSystems (Vancouver, BC, Canada) using the NxGen microfluidic cartridge. Lipid stocks were prepared in ethanol at molar ratios 50:38.5:10:1.5 for d-Lin-MC3-DMA: Cholesterol: DSPC: DMG-PEG 2000, which is based on the lipid compositions of Onpattro® and Comirnaty® [177]. The aqueous phase consisted of initial Poly(A) stock at 1.5 mg/mL dissolved in 50 mM citrate buffer (pH 4.0). The N:P ratio (N for lipid nitrogen and P for nucleic acid phosphate) was 6:1. The Total Flow Rate (TFR) was set at 15 mL/min, and an aqueous-to-organic Flow Rate Ratio (FRR) of 3:1 was used with a final lipid concentration of 1.25 mg/mL and Poly(A) of 0.055 mg/mL. The resultant suspension was dialysed at 4 ºC (MWCO 14 kDa, Sigma-Aldrich, St. Louis, MO, USA) into 1X PBS (pH 7.4) (500X dialysate ratio) to remove ethanol and citrate buffer. LNP formulations were syringe filtered through a 0.2 µm pore-sized Supor® membrane (Pall Corporation, USA) and stored at 4 ºC until further use.

3.3.2.2 Preparation of the LNP-BSA corona

The MC3-LNP formulation was incubated with BSA to form LNP-BSA mixture. The LNP was incubated at a 1:1 (volumetric ratio) with BSA (35 mg/mL in PBS, representing physiologically-relevant levels of BSA) for 24 hours at 37 ºC. The control sample included an equal volume of PBS and LNP formulation.

3.3.2.3 Particle size and polydispersity determination

LNP formulation sample attributes were analysed using a Zetasizer Nano ZS (Malvern Panalytical, Malvern, Worcestershire, UK) to obtain particle size and Polydispersity Index (PDI) for LNPs (LNP in PBS) at 0 hour-time point (control) and control (LNP-PBS) and treated (LNP-BSA) at 24 hour-time point. All measurements were performed using non-invasive backscattering (NIBS, 173°) at a dilution of 1:10 in PBS (pH 7.4). The Refractive Index (RI) and viscosity of the buffer (PBS) were set at 1.34 and 1.02 cP, respectively. All DLS measurements were performed in three independent measurements consisting of at least three technical replicates.

3.3.2.4 Zeta potential determination

To measure zeta potential, Electrophoretic Light Scattering (ELS) of LNP-control was measured using the Smoluchowski approximation. All measurements were performed at a

dilution of 1:10 in DNA/RNA free water. The RI and viscosity of the medium (DNA/RNA free water) were set at 1.33 cP and 0.89 cP, respectively. ELS measurements were performed at a measurement temperature of 25 ºC, and material RI and absorbance were set at 1.45 and 0.001, respectively. All zeta potential measurements were performed in three independent measurements consisting of at least three technical replicates.

3.3.2.5 Particle size distribution and particle concentration determination

Nanoparticle Tracking Analysis (NTA) was used to perform *in situ* analysis of LNPs incubated with BSA, studying changes in LNP size in response to BSA surface-adsorption. All NTA measurements were performed using a NanoSight NS300 system (Malvern Panalytical, Malvern, Worcestershire, UK), configured with a 488 nm laser and a sCMOS camera. LNP samples were diluted in PBS (pH 7.4) and analyzed with a syringe driver set at 50 AU. All measurements were performed at 25 ºC with five successive videos of 60 second duration captured, with a camera level of 14 and a detection threshold of 5 for all measurements. Particle dilutions were by a factor of 2 x 10^3. The span of particle size distribution, as measured using NTA, was calculated using the ratio (D90-D10)/D50). The mean and standard deviation for parameters were determined from three independent replicate measurements consisting of five technical replicates.

3.3.2.6 Encapsulation Efficiency (EE)

Quant-iT™ RiboGreen RNA Assay (Invitrogen™, Thermo Fisher Scientific, UK) was used for the quantification of Poly(A) encapsulation in LNPs as per manufacturer's instructions.

LNPs were serially diluted in Tris and Ethylenediaminetetraacetic acid (TE buffer) in the presence and absence 2% *v/v* Triton X-100 in a 96-well plate. The plate was incubated at 37 °C for 15 minutes, followed by the addition of two dilutions of 1× Ribogreen Reagent (500- and 200-fold) to wells containing TE buffer and Triton X-100, respectively. Fluorescence was measured using a GloMax® Microplate Reader (Promega Corporation, UK) with an excitation of 475 nm and emission 500-550 nm wavelength. EE was calculated using the following equation:

$$\mathbf{EE}\ (\%) = \frac{\mathbf{Poly(A)_{total} - Poly(A)_{free}}}{\mathbf{PolyA_{total}}} \mathbf{x\ 100} \qquad \textbf{Equation 3.1}$$

Where $Poly(A)_{total}$ is the total Poly(A) concentration (µg/mL) in wells containing Triton-TE buffer, $Poly(A)_{free}$ the concentration (µg/mL) of the unentrapped Poly(A) for wells containing TE buffer.

3.3.2.7 Frit-Inlet Asymmetric Flow Field-Flow Fractionation

3.3.2.7.1 Radius of Gyration (R_g), Hydrodynamic Radius (R_h) and Shape Factor (R_g/R_h) by Frit-Inlet Asymmetric Flow Field-Flow Fractionation (FI-AF4) in-line with Multiple Detectors

FI-AF4 (AF200 Postnova Analytics, Landsberg, Germany) was used for characterising MC3-LNPs for their R_g, R_h and R_g/R_h. The system was configured with tip and pressure pumps, a degasser, and autosampler. The system was equipped with an online UV (PN3242, ʎ = 260 nm and 280 nm, Postnova Analytics), 21-angle Multi-angle Light Scattering (MALS-PN3621, Postnova Analytics) and online Zetasizer Nano ZS (Malvern Panalytical, Malvern, UK) detector. The frit-inlet channel configuration included the use of a 10 kDa MWCO size amphiphilic regenerated cellulose (RC) membrane, a spacer thickness of 350 µm, and 10 mM PBS (pH 7.4) as the carrier liquid. Online DLS measurements were obtained using a Malvern quartz flow cell (ZEN0023), with a flow rate of 0.2 mL/min at 25 ^{o}C at three-seconds intervals. The measurement position was set at 4.2 mm with the attenuator set at 11.

FI-AF4 method development included the optimisation of detector flow, and exponential decay cross-flow. A total of four methods were simulated (**Table 3.1**). Method development was initiated with the LNP-BSA incubated sample at the 24-hour time-point to determine separation efficiency of the two sub-populations. Method development was based on the flowchart in **Figure 3.2**.

Membrane pre-conditioning with triplicate injections was carried out using BSA (5 mg/mL). The intensity of the scattered light using the MALS detector was calculated for angles 36^{o} to 148^{o} and the sphere fit model for all samples was used for the R_g measurement. LNP samples were analysed in technical triplicates without additional dilution, at a theoretical LNP lipid concentration of 0.625 mg/mL and a BSA concentration of 35 mg/mL.

Table 3.1 Corresponding FI-AF4 parameters for four methods.

Method	Time (min)	Cross-flow (mL/min)	Type	Exponent	Detector flow (mL/min)
1	20	0.75	Constant	0	0.2
	60	0.75	Power	0.2	
	10	0	Constant	0	
2	20	1.0	Constant	0	0.2
	60	1.0	Power	0.2	
	10	0	Constant	0	
3	20	1.5	Constant	0	0.2
	60	1.5	Power	0.2	
	10	0	Constant	0	
4	20	1.5	Constant	0	0.3
	60	1.5	Power	0.2	
	10	0	Constant	0	

3.3.2.7.2 FI-AF4-MALS-fit models for R_g measurement

The MALS detector was normalized using BSA and the laser power set to 80 %. Four different model fit transformations for light scattering (Zimm, Coated Sphere, Random Coil and Debye) were examined for extracting the R_g based on the data obtained from Nova FFF software (version 2.2.0.1, PostNova Analytics, Landsberg, Germany). The Zimm model assumes isotropic scattering from small particles (R_g <50 nm), best suited from near-spherical nanoparticles as the model assumes angular dependence is minimal [214]. The coated sphere model accounts for a dense core surrounded by a shell-layer. The Debye model describes the scattering from Gaussian random coils and is particularly applicable for flexible polymers or proteins [297]. The random coil model is an extension of the Debye model. Whereas the Debye model uses a polynomial function, the random coil model fits the angular light scattering data using the formula for a theoretical random coil [214].

The normalised RMSE (**2** and **3)** and R^2 (**4**) were obtained using Python 3.12.4 by comparing the actual and the predicted values for the model from the slope (R_θ/Kc against $\sin^2(\theta/2)$ plot) for the predicted values. The actual and predicted values were obtained from Nova FFF software. Curve fitting was performed using scattering angles between 36°-148° for all methods investigated.

$$\mathbf{RMSE} = \sqrt{\frac{\sum(\hat{y}_i - y_i)^2}{N}} \qquad \textbf{Equation 3.2}$$

$$\mathbf{Nomalised\ RMSE} = \frac{\mathbf{RMSE}}{\bar{y}} \qquad \textbf{Equation 3.3}$$

Where $\hat{y}_i$ is the predicted value for R_θ/Kc from the MALS model-fit used (Zimm, coated sphere, random coil and Debye), y_i is the actual value for R_θ/Kc and N is the number of

parameters for $\sin^2(\theta/2)$ and $\bar{y}$ is the mean of the actual R_θ/Kc values. R_θ/Kc and $\sin^2(\theta/2)$ are obtained from Nova FFF software.

$$\mathbf{R^2 = 1 - \frac{\Sigma(y_i - \hat{y}_i)^2}{\Sigma(y_i - \bar{y})^2}} \qquad \textbf{Equation 3.4}$$

Where $\hat{y}_i$ is the predicted value for R_θ/Kc from the MALS model-fit used (Zimm, coated sphere, random coil and Debye), y_i is the actual value for R_θ/Kc and $\bar{y}$ is the mean of the actual R_θ/Kc values.

Shape factor measurements were calculated using the equation below:

$$\boldsymbol{\rho = \frac{R_g}{R_h}} \qquad \textbf{Equation 3.5} \text{ [218]}$$

where ρ is the shape factor, R_g represents the radius of gyration (nm) obtained from MALS detector, R_h represents the hydrodynamic radius (nm) obtained from DLS detector.

3.3.2.7.3 Sample recovery by FI-AF4

The recovery (R %) of the samples for was calculated using the following equation:

$$\mathbf{R(\%) = \frac{Ac}{A} \times 100} \qquad \textbf{Equation 3.6}$$

Where A_c is the area under the peak of LNPs under a cross flow, and A the area under the peak of the unfractionated LNP *via* direct sample injection (without an applied cross flow). The parameters for the direct injection (**Table 3.2**). Absorbance was measured at 260 nm and 280 nm using a UV detector. Fractions eluting after the cross-flow stops (0 mL/min for 10 minutes) were not included in the fractogram integration. A criteria to establish optimal methodology was based on a sample recovery of ≥70 %.

Table 3.2 Corresponding AF4 parameters for direct injection.

Time (min)	Cross-flow (mL/min)	Type	Exponent	Detector flow (mL/min)	Injection volume (µL)	Injection flow rate (mL/min)
10	0	Constant	0	0.2	20	0.2
5	0	Linear				

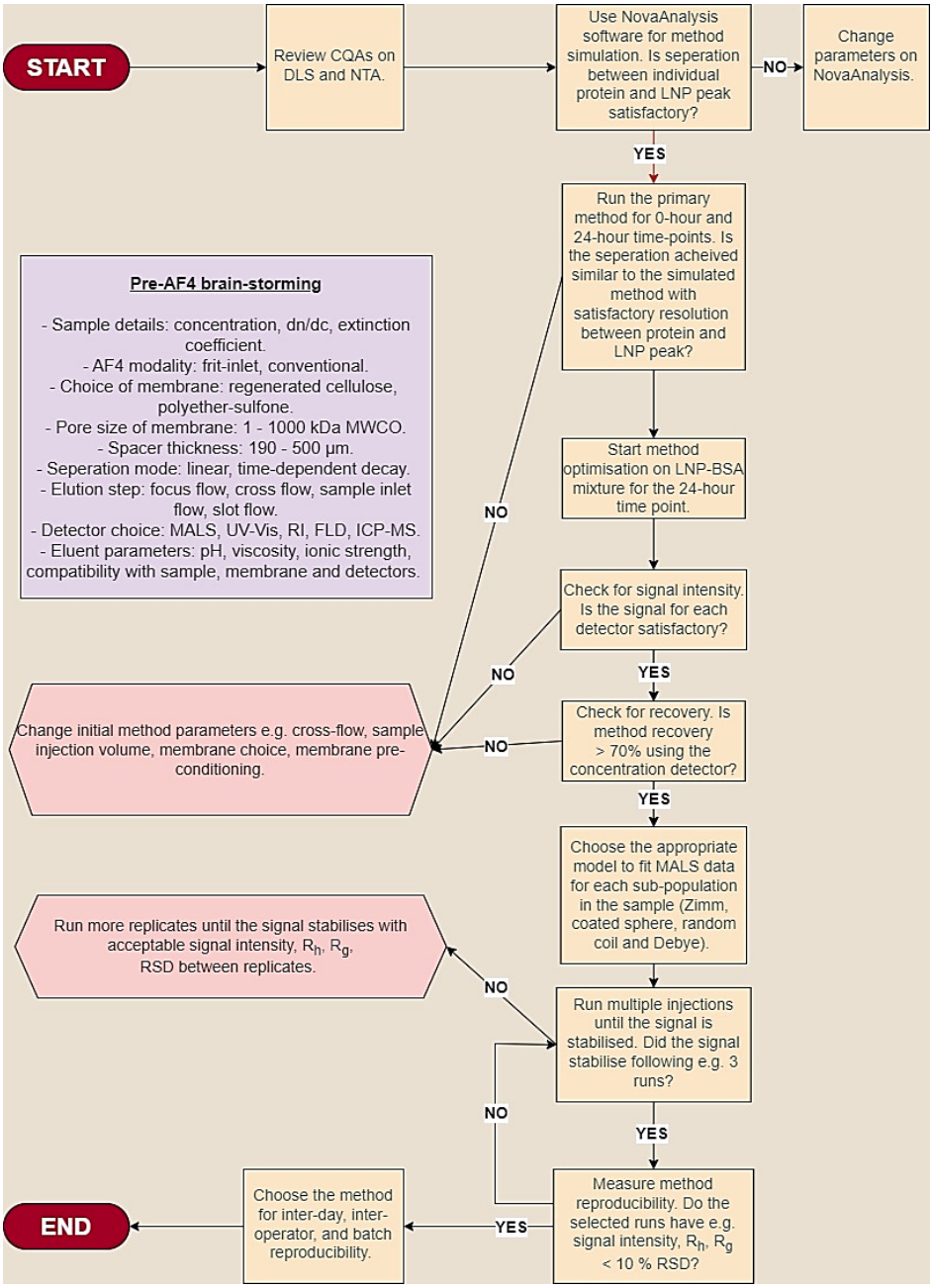

Figure 3.2 Protocol adopted for method optimisation on FI-AF4 for nanoparticle mixtures. Abbreviations: FLD Fluorescence Detector, ICP-MS Inductively Coupled Plasma Mass Spectrometry, RSD Relative Standard Deviation. Method performance criteria used for the selection of the optimal method were guided by the ISO/TS 21362:2021 standards [20]. Criteria included a recovery (R %) of ≥70, retention $0.03 \leq R \leq 0.2$ and resolution Rs >1.5 in the case of Gaussian peak and non-overlap peaks in case of non-Gaussian peaks.

3.3.2.8 Statistical Analysis

Normality of all datasets was assessed using Shapiro-Wilk test. One-way analysis of variation (ANOVA) followed by Tukey's multiple comparisons test was used for normally distributed data. For non-normally distributed data, non-parametric analysis was carried out using Kruskal-Wallis test followed by Dunn's multiple comparison test. Statistical significance was considered at *p-value* < 0.05; *p < 0.05, **p < 0.01, ***p < 0.001, ****p < 0.0001. All data were analyzed using GraphPad Prism 10.4.2 (GraphPad Software Inc) and are expressed as mean ± SD (n = 3) or stated otherwise.

3.4 Results

3.4.1 Baseline analysis of particle size using DLS and NTA

The CQAs of MC3-LNP formulation are shown in **Table 3.3**. LNPs were incubated with BSA and examined for their particle diameter using distribution algorithm analysis, size distribution profile, polydispersity and particle concentration. Initial LNP CQAs were measured using DLS (*Z*-average and PDI), ELS (zeta potential) and encapsulation efficiency before corona formation with BSA and fractionation using FI-AF4. LNPs manufactured had a mean *Z*-average of 75.9 (± 4.6) nm, a PDI <0.2 and a zeta potential of -3.6 (± 4.2) mV. The encapsulation efficiency in all cases was measured as >95 %.

Table 3.3 Baseline Critical Quality Attributes (CQAs) for MC3-LNPs. *Z*-average and Polydispersity Index (PDI) were measured using DLS cumulant algorithm analysis. Data are shown as mean ± SD, N=3 independent replicates, n=3 technical replicates.

DLS Parameters	MC3-LNP
Z-average (nm)	75.9 (± 4.6)
PDI	0.152 (± 0.039)
Zeta potential (mV)	-3.6 (± 4.2)
Encapsulation efficiency (%)	98 (± 2)

Following LNP incubation with BSA, the different sub-populations could not be compared using the *Z*-average cumulant analysis due to the high PDI 0.540 (± 0.049) on DLS and a span of 0.61 (± 0.04) using NTA (**Figure 3.3** and **Table 3.4**) occurring as a result of excess unadsorbed BSA contained in the incubation media (peak 1). Comparing particle size distribution for the BSA-control and the LNP-control to the LNP-BSA mixture, peak 1 and peak 2 occurring at a particle diameter of 7.5 (± 0.2) nm and peak 2 of 92.7 (± 2.9) nm were

identified as free BSA (BSA-control) and LNP bound to BSA (LNP-BSA) respectively (**Figure 3.3A and Supplementary Table S3.1**). Peak 3 for all samples (BSA-control 0-hour, LNP-control 0-hour and 24-hour and LNP-BSA 24-hour) are defined as aggregates.

Size measurements by NTA followed a similar trend to that of DLS. Comparing changes in the NTA-measured LNP-BSA complex, concentration distribution profiles did not show distinct peaks corresponding to BSA and LNP however it showed a polymodal size distribution (**Figure 3.3B**). An increase in concentration resulted from 2.4 x 10^{11} (± 2.0 x 10^{11}) particles/mL (LNP-PBS at 24-hour) to 1.4 x 10^{12} (± 5.9 x 10^{11}) particles/mL which is attributed to the presence of BSA (**Supplementary Table S3.1**). The incubation of LNP with BSA for 24 hours resulted in a shift in the mean particle diameter 96.1 (± 9.4) nm for LNP-control and 80.7 (± 1.8) nm for LNP-BSA.

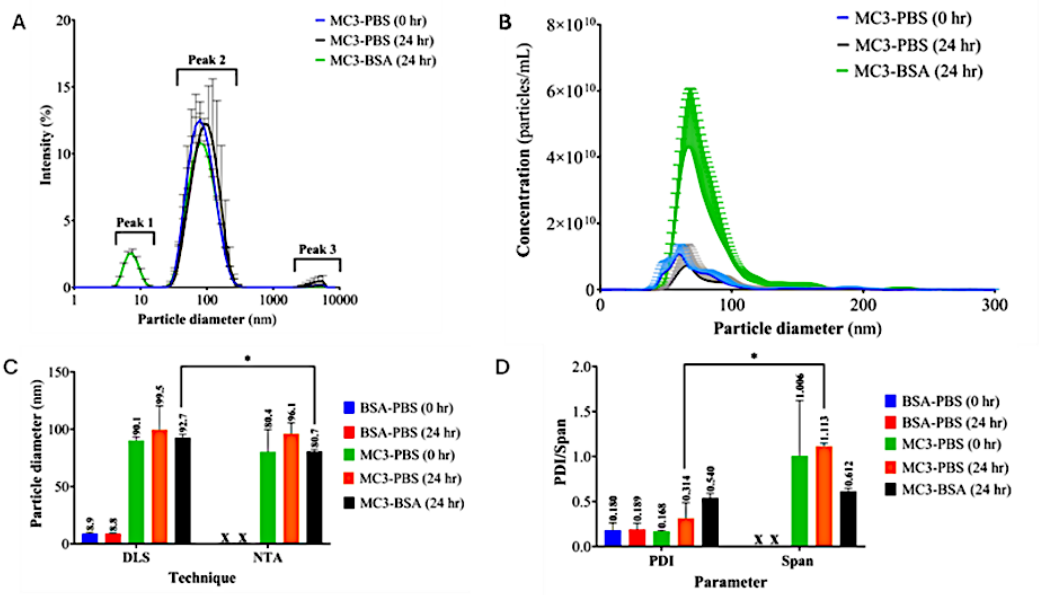

Figure 3.3 Particle size analysis using DLS and NTA for MC3-LNPs incubated in PBS (control) and 35 mg/mL Bovine Serum Albumin (BSA) at 0 hour (control) and 24 hours incubation at 37 ºC. Plots represent (A) particle size distribution by DLS cumulative algorithm analysis (B) NTA particle size distribution (C) comparison of particle diameter obtained using DLS and NTA and (D) polydispersity index (PDI) measured by DLS and span using NTA. Results are shown as mean ± S.D, N=3 independent replicates, n=3. 'X' in plots (C) and (D) refer to samples not measured due to the polydispersity of the BSA. Peak 1 indicates BSA peak, peak 2 indicates LNP peaks and peak 3 refers to aggregate particles. *p < 0.05 as determined by a two-tailed paired t-test.

Table 3.4 Physiochemical attributes describing hydrodynamic particle diameter (particle size) and Polydispersity Index (PDI) measured by DLS distribution algorithm analysis for BSA (control), MC3 incubated in PBS (control) and in 35 mg/mL BSA. Results are shown as mean ± S.D, n= 3 independent replicates. Measurement values indicate 0 hour (control) and 24 hours incubation at 37 °C. Peak 1 indicates BSA peak, peak 2 indicates LNP peak and Peak 3 are aggregate particles. Peaks 1, 2 and 3 are labelled in **Figure 3.3A**.

			Particle diameter (nm)			
Sample	**Time-Point**	**Sample**	**Peak 1**	**Peak 2**	**Peak 3**	**PDI**
BSA	0 hr	BSA-PBS	8.9 (± 1.0)	665.3 (± 0.0)	2597.3 (± 1466.6)	0.180 (± 0.009)
	24 hr		8.8 (± 0.5)	358.1 (± 0.0)	3074.8 (± 873.3)	0.189 (± 0.070)
MC3-LNPs	0 hr	MC3-PBS	-	90.1 (± 3.1)	1538.7 (± 66.5)	0.168 (± 0.012)
	24 hr		-	99.5 (± 20.9)	2928.7 (± 2537.1)	0.314 (± 0.173)
	24 hr	MC3-BSA	7.5 (± 0.2)	92.7 (± 2.9)	518.0 (± 897.2)	0.540 (± 0.049)

3.4.2 Optimisation of FI-AF4 parameters for the separation of LNP-BSA complexes from bulk incubation media

The superior separation power of FI-AF4 allows for the high-resolution separation of free BSA from LNP-BSA corona complexes, which was otherwise difficult to measure using batch-mode DLS and NTA due the highly polydisperse nature of these mixtures. Multi-detector hyphenation enabled determination of the signal intensities, particle size and morphology (combining DLS and MALS detectors to measure R_g/R_h) for the different particle sub-populations within these complex mixtures. FI-AF4 method development increases in complexity with mixtures of heterogeneous nanoparticles with varying material compositions.

Here, I used MC3-LNPs and BSA in the mixture to form MC3-BSA corona complexes (BSA was present in excess concentration at a physiologically-relevant concentration of 35 mg/mL), followed by the separation of free BSA from the MC3-BSA corona. The cross-flow (0.75, 1 and 1.5 mL/min), detector flow (0.2 and 0.3 mL/min) and UV detector wavelength (260 nm and 280 nm) were varied between methods, while maintaining all other run parameters constant. Initially, NovaAnalysis software was used to simulate the fractograms for LNP-BSA mixture (**Figure 3.4** and **Supplementary Figure S3.1**).

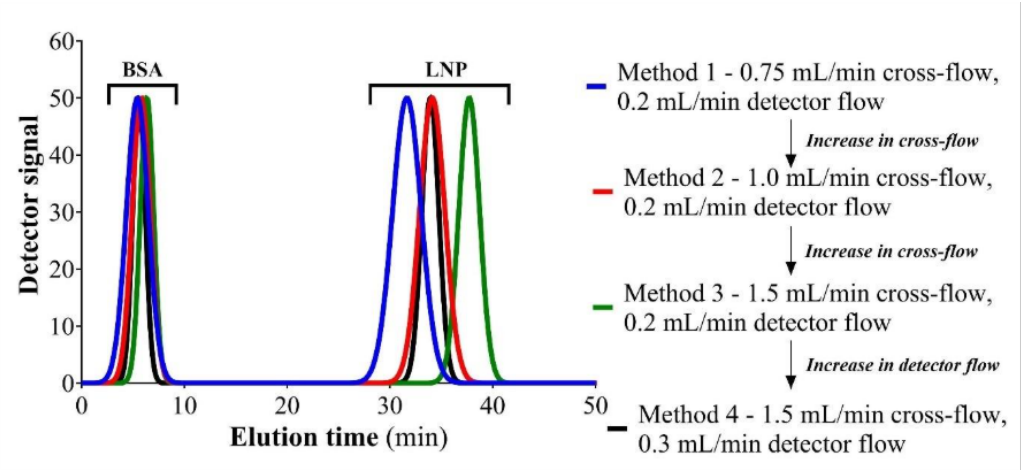

Figure 3.4 FI-AF4 method simulation for MC3 LNP- Bovine Serum Albumin (BSA) mixture using the NovaAnalysis software. The simulated fractogram shows that all methods tested can separate BSA and LNP(BSA) peaks, with a shift in elution time following the application of different exponential decay cross-flow and detector flow profiles. The parameters inputted on the software at % v:v ratio of 50%:50% (BSA:LNP), hydrodynamic radius (R_h) of 3.8 nm and 46.4 nm (BSA and LNP respectively). These parameters were inputted following the particle sizes obtained using DLS for the MC3 LNP-BSA mixture.

Ideally, the fractograms for the different detectors exhibit a narrow Gaussian distribution and minimal overlap between free BSA and LNP-BSA corona complex peaks. Prior to method optimisation, the control for BSA and LNPs were carried out using method 1 to identify and assign peaks accurately (**Figure 3.5**). Each fractogram shows an initial BSA peak eluting at ~5 min, followed by two LNP sub-populations, LNP peak 1 and peak 2 eluting after 20 min.

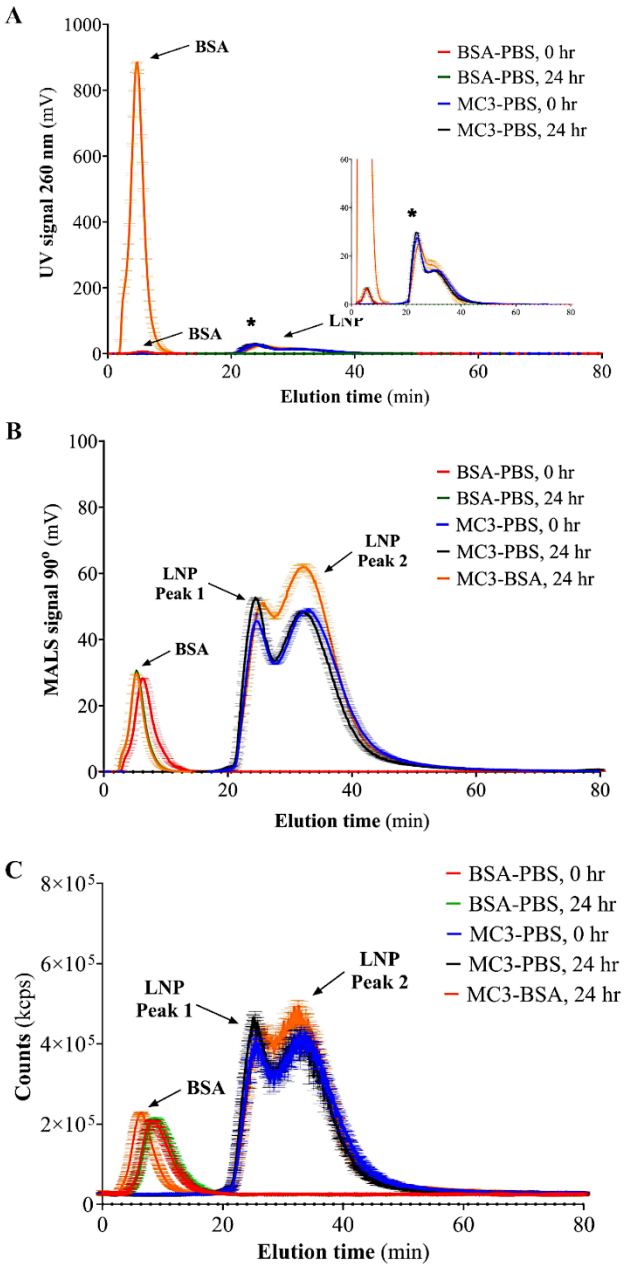

Figure 3.5 Fractograms for (A) FI-AF4-UV at 260 nm (B) FI-AF4-MALS (90°) (C) FI-AF4-DLS for Bovine Serum Albumin (BSA) (control), LNPs (control) and MC3-LNPs incubated in 35 mg/mL BSA. Time-points indicate 0 hour (control) and 24 hours incubation at 37 °C. The arrows in each fractogram represent BSA, LNP peak 1 and LNP peak 2 eluting at different time-points of the elution profile. Error bars represent ± S.D mean of triplicate injections, BSA-PBS (24 hr) using FI-AF4-DLS represent duplicate injections. The peaks marked with a black asterisk (*) show enlarged peaks.

3.4.3 Analysis of LNPs using FI-AF4-UV

The intensity of the BSA and LNP UV signals were measured at 280 nm and 260 nm, respectively (**Figure 3.6**). **Figure 3.6A** and **Figure 3.6B** represent a well-defined peak for BSA (eluting at ~5 min). The LNP shows different sub-populations eluting at different time-point in the UV fractogram elution profile. **Figure 3.6A** and **Figure 3.6B** showed measured signal for BSA ~50-fold higher than that of LNP. The increased signal for BSA at 280 nm is attributed to Tryptophan (Trp) and Tyrosine (Tyr) residues, which absorb at 280 nm [298]. LNP absorbance at 260 nm is attributed to the aromatic chromophore of the aromatic base adenine in the mRNA (Poly(A)) encapsulated in the LNP [272].

Methods 1, 2 and 3 were run at progressively higher cross-flow (0.75, 1.0 and 1.5 mL/min respectively), however this did not result in a consistent increase in elution time accross all sub-populations within the sample. Method 1 had two LNP sub-peaks eluting without sufficient resolution at 25.5 (± 0.1) min (peak 1) and 32.5 (± 0.5) min (peak 2) (**Figure 3.6B**). The higher cross-flow applied in method 2 eluted the first LNP subpopulation at 30 (± 0.1) min and the second sub-population at 53.5 (± 0.3) min. However, methods 3 and 4 produced the longest elution times for the first LNP sub-population, with method 3 yielding 33.2 (± 0.1) min and a shorter elution time for method 4 for the same sub-population (29.5 (± 0.1) min). The UV absorbance for LNPs arises from the encapsulated nucleic acid (Poly(A)), which maybe distributed unevenly across the elute fractions. Hence, LNP peak 3 can be identified as larger LNPs (due to a longer elution time). However, a lower intensity for LNP peak 3 might indicate that the Poly(A) content encapsulated per particle is lower or might have leaked from the LNP when the aggregates formed or during the elution time period of the method. Methods 3 and 4 exhibited substantial tailing and fractionated larger sized particles in the sample.

In FI-AF4, increasing the cross-flow rate (while maintaining other parameters constant) decreases the detector signal intensity. This trend was not observed for BSA and LNP peaks (**Figure 3.6C** and **Figure 3.6D**). Increasing the cross-flow rate from 0.75 mL/min to 1.0 mL/min increased the signal intensity from 598 (± 0) % to 986 (± 0) % (**Figure 3.6C** and **Figure 3.6D**). This can be attributed to the saturated peak intensity shown by the peak capping in methods 2 and 3 due to the BSA concentration (35 mg/mL) used. The LNP peaks showed statistically significant differences in intensities across all four methods, both for LNP peak 1 and LNP peak 2 with no statistical significance in the case of LNP peak 3. Statistically significant differences were observed between intensities measured across all four different methods (LNP peak 1 and LNP peak 2) (**Figure 3.6D**).

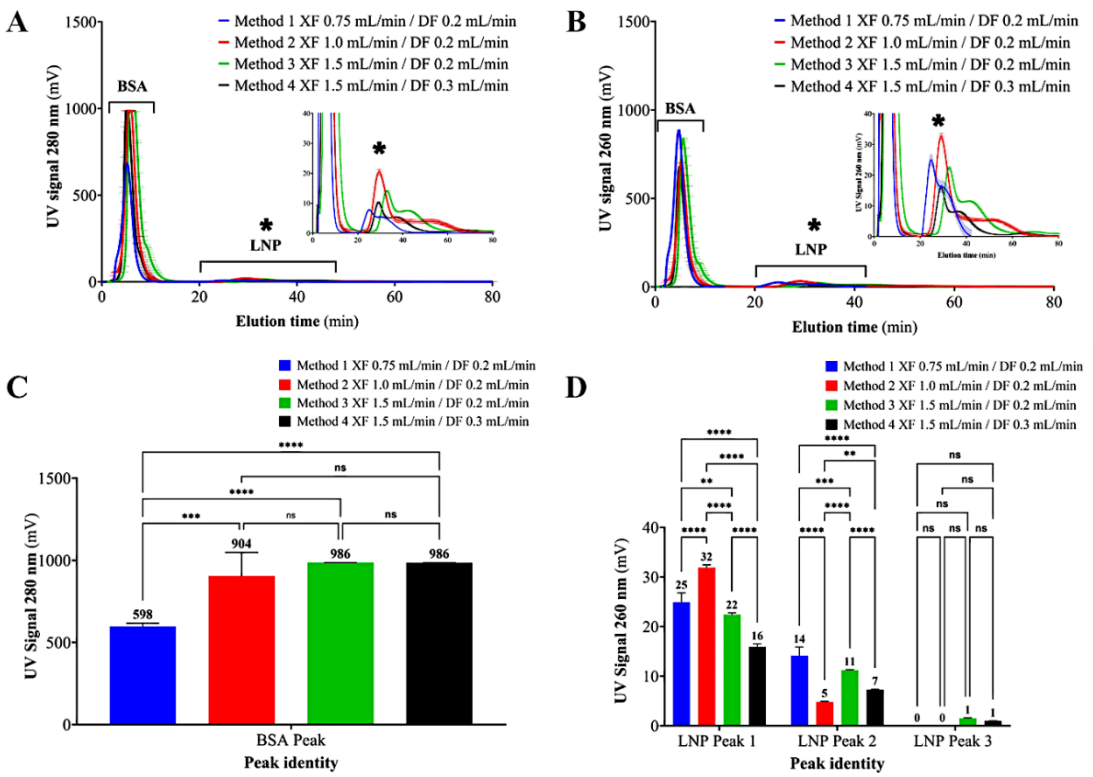

Figure 3.6 The use of UV detector coupled to FI-AF4 for determining the differences between signal intensities between methods 1-4 with different cross-flow rate (XF) and detector flow rates (DF). Plots represent MC3-LNP incubated in 35 mg/mL Bovine Serum Albumin (BSA) at 37 ºC for 24 hours. Figures represent (A) FI-AF4-UV fractogram profile at 280 nm (B) 260 nm (C) signal intensities measured for UV detection at 280 nm (D) 260 nm. Error bars represent ± S.D mean of triplicate injections. The peaks marked with asterisks (*) show enlarged peaks. Statistical analysis was performed using one-way ANOVA followed by post-hoc Tukey's test. *$p < 0.05$, **$p < 0.01$, ****$p < 0.0001$, ns non-significant. Refer to **Figure 3.7** for BSA and LNP peaks 1-3 identifications.

3.4.4 Method repeatability

The repeatability of the cross-flow profile for each method was tested by three replicate injections under identical conditions (**Figure 3.7** and **Supplementary Table S3.2**), and the RSD of UV signal intensity calculated for each method for a polydisperse sample (LNP-BSA mixture).

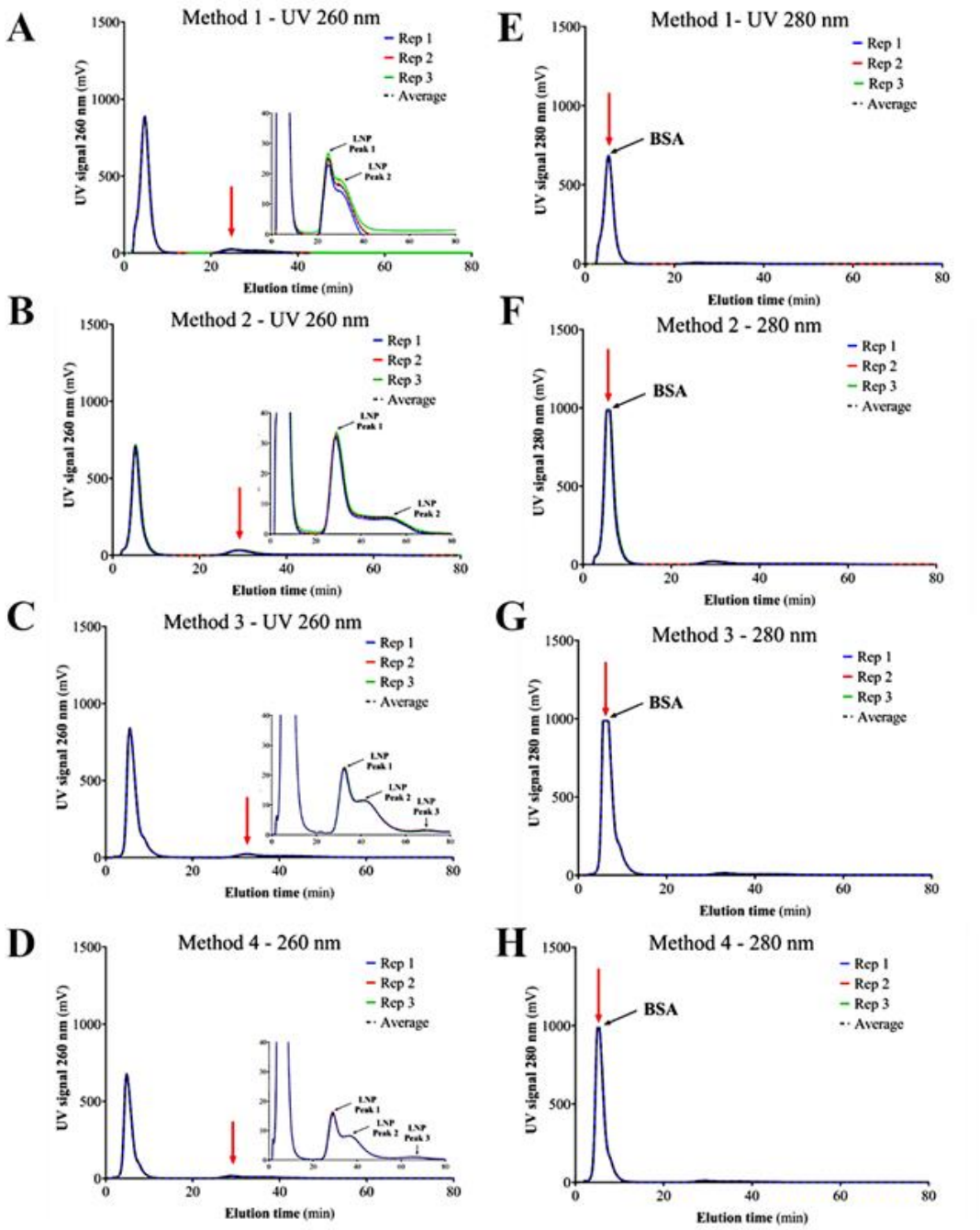

Figure 3.7 UV detector coupled to FI-AF4 Flow-mode for MC3-LNPs incubated in 35 mg/mL Bovine Serum Albumin (BSA) for 24 hours at 37 °C. Plots (A) to (D) represent methods 1 to 4 respectively for UV detector absorbance at 260 nm for investigating LNP (LNP peaks 1-3 depicting the different LNP subpopulations). Plots (E) to (H) represent methods 1 to 4 respectively for UV detector absorbance at 280 nm for investigating BSA. The red arrows represent the peak of interest for the specific UV absorbance wavelength (260 nm or 280 nm). Reps 1-3 represent triplicate injections with an average calculated.

Figure 3.8 and **Supplementary Figure S3.2** illustrates the RSD of peak intensities across the four FI-AF4 methods. Method 4 had the lowest RSD for LNP Peaks 1-3 (1-4 %). Method 1 showed a clear trend in increased RSD with higher particle size (3-13 %). Method 2 showed the highest variabiliy for the BSA peak (16 %) indicating low injection precision for the protein. In the case of LNP peaks, methods 1 and 3 exhibit signal intensities (> 5 %) between replicate injections, whereas methods 2 and 4 maintain variability within the acceptance criteria of ISO/TS 21362 (<5 %). These findings demonstrate that increasing the cross-flow rate (0.75-1.5 mL/min) does not inherently enhance run-to-run repeatability, and in some cases may contribute to variability. An optimized cross-flow to detector-flow ratio (method 4) contributed to consistent retention behaviour for each component in the sample across three replicate runs.

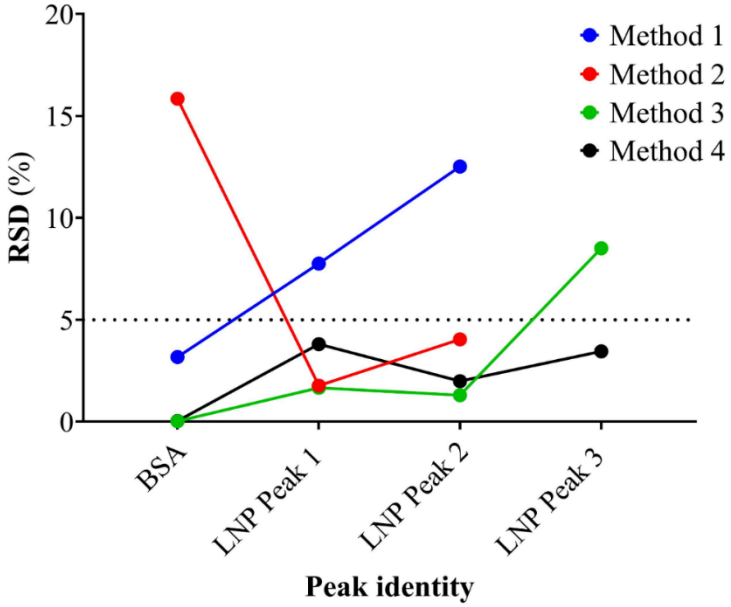

Figure 3.8 Relative standard deviation (% RSD) of UV signal intensities of LNP-BSA (Bovine Serum Albumin) sample across three replicate runs for four FI-AF4 methods. The signal intensities were measured using the UV detector at 260 nm and 280 nm wavelength for LNP and BSA respectively. Refer to **Figure 3.7** for FI-AF4-UV fractograms for peak identification and run-to-run replicates and **Supplementary Table S3.2** for UV 260 and 280 nm signal intensities. Dotted horizonal line indicates 5 % RSD.

3.4.5 Contribution of UV detector at 260 nm and 280 nm signal intensity for percentage sample recovery

The presence of analyte mixtures with different optical characteristics (i.e. BSA and LNP) renders the quantification of sample recovery at a single UV detector wavelength challenging. Method 3 exhibited a more prominent truncation of the BSA peak relative to the other methods, while method 4 showed incomplete elution of LNP peak 3 (**Figure 3.7C-D**), resulting in non-representative recovery data. Therefore, methods 1 and 2 were selected for determining sample recovery. Methods 1 and 2 achieved an acceptable sample recovery level of ≥ 70 %. Method 1 resulted in no statistically significant difference in recovery dermined using 260 nm and 280 nm (105 % for 260 nm and 96 % for 280 nm) detection wavelengths but a significant difference was noted for method 2 (102 % for 260 nm and 127 % for 280 nm) (**Figure 3.9**). An increased concentration of the sample can improve detection using FI-AF4 but it can also cause overloading (recovery of >100 %). Marioli *et al*. observed higher retention times, peak broadening, and fronting peaks with overloaded fractograms [299]. To mitigate these artefacts, samples should be diluted to fall within the lower and upper limits of the detector with sample loading to be adjusted to avoid channel saturation. The type of protein, membrane protein permeability [299], carrier liquid composition [299], spacer dimensions [300] and sample viscosity [299] may also impact sample recovery. The analysis found that comparing methods 1 and 2 for the same wavelength with an increase in cross-flow rate, exhibited a non-significant reduction for 260 nm, but a significant increase for the 280 nm signal. Generally, higher cross-flow rates result in lower recovery rates, which may be explained by sample constituents being pushed close to the membrane by the channel perpendicular cross-flow, which increases interactions between sample analytes and the membrane [299]. This trend was observed with the UV 260 nm wavelength (**Figure 3.9**). The non-significant increase at 280 nm was attributed to increased saturation of the UV detector at 280 nm due to high BSA concentrations (35 mg/mL).

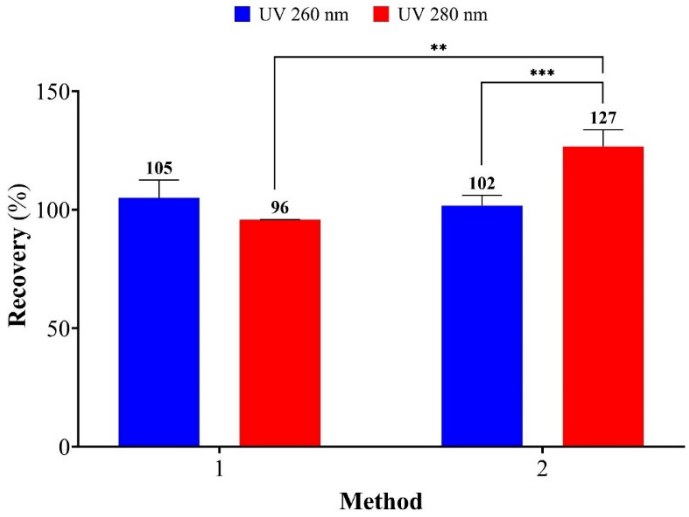

Figure 3.9 Sample recovery of LNP-BSA mixture incubated for 24-hour at 37 °C. Methods 1 and 2 have a cross-flow rate of 0.75 mL/min and 1.0 mL/min respectively. Detector flow rate for both methods is 0.2 mL/min. Statistical analysis was performed using one-way ANOVA followed by post-hoc Tukey's test. Error bars represent ± S.D mean of triplicate injections, **p < 0.01, ***p < 0.001.

3.4.6 MALS scattering for fit-models precision

The FI-AF4-MALS fractograms for the four methods are presented in **Figure 3.10**. Coupling UV and MALS detectors to FI-AF4 enabled the detection of sub-populations eluting at identical retention times, indicating appropriate flow path alignment between detectors, and suggesting that methods 1-4 did not induce aggregation and exhibited minimal sample interaction with the FI-AF4 RC membrane. The principles underlying light scattering are well-established [301, 302], with scattered intensity directly related to the R_g of the particles. Accordingly, in the case of LNP-BSA mixture, BSA, which has a smaller particle size as confirmed by batch-mode DLS (batch-mode DLS hydrodyanmic diameter (7.5 (± 0.2) nm) (**Figure 3.3A)**, exhibited lower light scattering intensity in comparison to larger-sized LNPs (batch-mode DLS hydrodyanmic diameter (92.7 (± 2.9) nm). Methods 1 and 2 yielded a monomodal peak for BSA indicating a homogeneous population. In contrast, methods 3 and 4, with a higher cross-flow rate of 1.5 mL/min, revealed two unresolved BSA sub-populations, consistent with the presence of oligomeric forms. These sub-populations were more clearly shown in the FI-AF4-MALS fractograms (**Figure 3.10**). For LNPs, methods 3 and 4 indicated the presence of a third, higher-size sub-population (LNP peak 3) further demonstrating the resolving power of the FI-AF4-MALS approach.

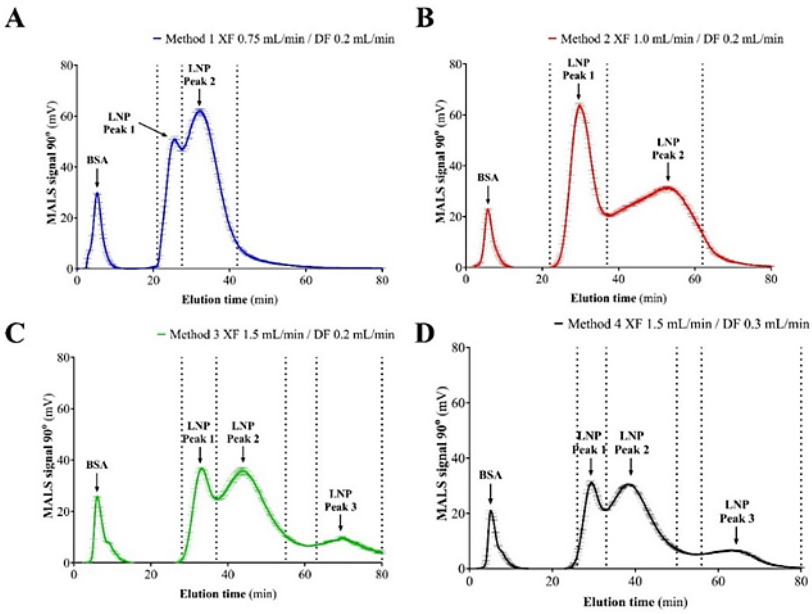

Figure 3.10 FI-AF4-MALS fractograms for MC3-LNP incubated in 35 mg/mL Bovine Serum Albumin (BSA) for 24 hours at 37 °C. Methods 1-4 represent differences in cross-flow (XF) and detector flow (DF) rate. Plots represent (A) Method 1 (B) Method 2 (C) Method 3 (D) Method 4. The peaks represent an initial BSA peak and peaks 1-3 represent different LNP sub-populations. Error bars represent ± S.D mean of triplicate injections. Vertical dashed lines indicate peak region of interest.

Four different MALS scattering fit models were compared (Zimm, coated sphere, random coil and Debye) to dermine the R_g for each nanoparticle fraction in the fractogram profile. The four fit models relate to the different relations of scattering intensity to $\sin^2(\theta/2)$ [303]. Mathematical equations and first principles for each mathematical transformation of R_g from the fit models are described elsewhere [304]. **Figure 3.11** shows MALS best fit models using two key statistical metrics, the R^2 and the RMSE.

R^2 measures the proportion of variance in the actual data that is explained by model predictions, with values closer to 1 indicating a stronger fit [305]. Conversely, RMSE quantifies the average magnitude of the prediction errors, representing how closely the predicted values match the observed measurements in absolute terms [306]. For the purpose of this study, the R^2 and RMSE were used to accurately characterise the R_g. **Figure 3.11** and **Supplementary Table S3.3** depicts the R_g as determined from light scattering data for Nova FFF software version 2.2.0.1 (Postnova Analytics, Landsberg, Germany) for each fitting model. Results suggest that BSA (R_g ~ 4-8 nm amongst all methods and model fits) has the least best-fit (R^2 ranging between 0.22-0.59) among the diffferent fits and methods. Small

molecules (<10 nm) have no angle-dependent light scattering, and scatter light isotropically, making it difficult to extract meaningful information about R_g even though the appropriate method parameters are chosen. The Zimm model fit for BSA and LNP peaks 1-3 demonstrated a zero gradient, indicating the scattering intensity is independent of the scattering angle. This exhibits unsuitability of the Zimm approximation for the LNP size. Therefore, the derived R_g for LNP subpopulations (peaks 1-3) for the Zimm model is unreliable. Furthermore, the RMSE for BSA using the coated sphere, random coil and Debye models resulted in a relatively low RMSE and low R^2. Hence, even though RMSE is low suggesting a low prediction error, the model may not capture variance in the data. Correlating the variance with FI-AF4, this can be attributed to non-uniform flow profile of BSA where the BSA particles are interacting with the RC AF4 membrane.

For LNP peak 1, the coated sphere and the random coil had the highest R^2 and lowest normalised RMSE values (R^2 0.95-0.98 and normalised RMSE 0.006-0.011 for coated sphere and R^2 0.95-0.98 and normalised RMSE 0.004-0.011 for random coil) (**Figure 3.11**). This was comparable to LNP peak 2, which also resulted in the coated sphere and the random coil as best fits. For larger sized particles in the case of LNP peak 2, the coated sphere, random coil and Debye resulted in the highest R^2 (R^2 0.981, 0.976 and 0.932, respectively). Larger nanoparticles, in the case of LNP peak 3, had the lowest RMSE for the random coil fit (0.075 (± 0.010) and 0.072 (± 0.020) for method 3 and method 4, respectively).

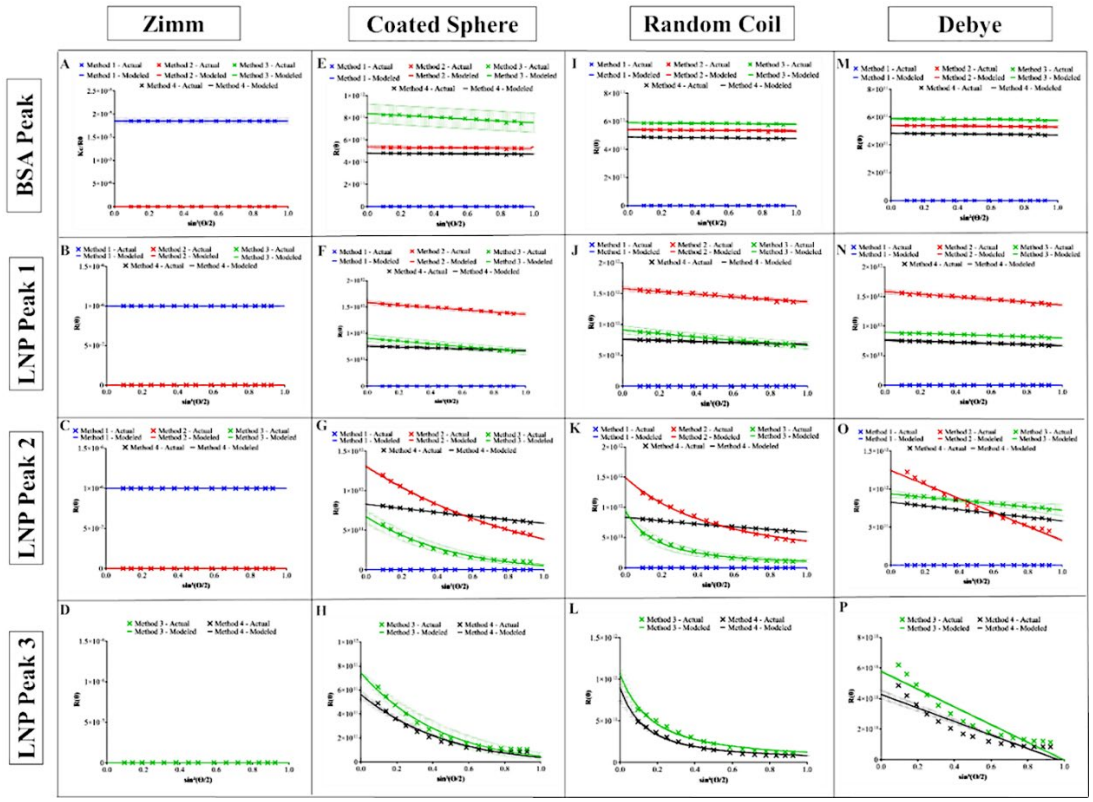

Figure 3.11 Plots for the predicted and actual values for MALS scattering fit models (Zimm, coated sphere, random coil and Debye). Plots (A) to (D) represent the Zimm model, (E) to (H) coated sphere, (I) to (L) random coil and (M) to (P) Debye model for BSA and LNP peaks 1-3. Refer to **Supplementary Table S3.3** for the Coefficient of Determination (R^2) and normalised Root Mean Square Error (RMSE) for the predicted and actual values.

In relation to comparing R_g between the different FI-AF4 methods, method 4 having the highest cross-flow and the highest detector flow resulted in the largest R_g for BSA and LNP peaks 1-3. However, there was no trend of particle size with increased cross-flow (methods 1-3) for the same nanoparticle fraction. Method 2 has resulted in the largest R_g for both LNP peaks 1 and 2 (20.9 (± 0.1) nm - 21.4 (± 0) nm for LNP 1 and 47.4 (± 0.5) nm - 72.7 (± 1.3) nm for LNP 2). **Figure 3.12** shows an indirect correlation between the R_g and the cross-flow, the R_g does not increase with an increase in cross-flow. This is evident for all the methods among the coated sphere, random coil and Debye fit models. However, results show that an increase in detector flow results in an increase in R_g (method 3 versus method 4), which was consistent with coated sphere, random coil and Debye fit models (in the case of LNP peak 1, coated sphere model 31.1 (± 0.7) nm for method 3 to 32.1 (± 0.7) nm for method 4, random coil 18.1 (± 0.8) nm method 3 to 19.9 (± 0.3) nm method 4 and 17.6 (± 0.7) nm to 19.2 (± 0.3) nm). This can be attributed to the poor resolution in the seperation of particles and a broader

R_g with increased detector flow. Methods 3 and 4 (cross-flow of 1.5 mL/min) had higher fractionation power for the same elution profile as the other methods. Both methods resulted in the third LNP fraction (LNP peak 3) (>50 nm). Comparing all methods, the Debye model gave the lowest values of R_g for LNP peaks 1-3 . The Debye model tends to underestimate R_g for particles >70 nm. This underestimation arises because the model assumptions do not adequately account for the structural complexities of larger particles [307].

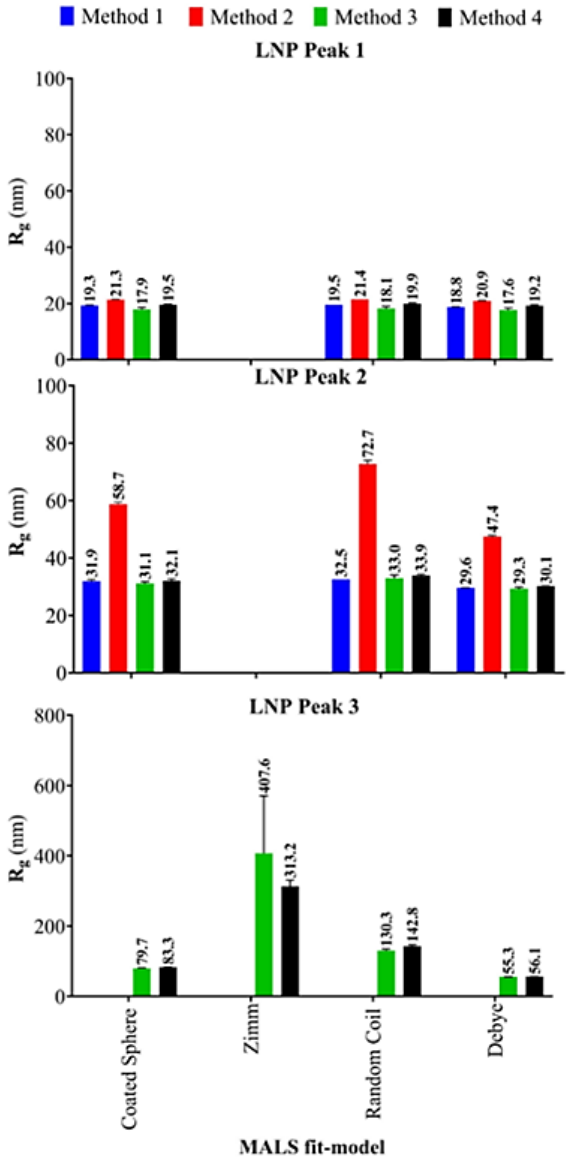

Figure 3.12 Comparison of Radius of Gyration (R_g) obtained from the different MALS fit models (coated sphere, Zimm, random coil and Debye) for FI-AF4 methods 1-4 for LNP peaks 1-3. Data are shown as ± S.D mean of at least two injections. Refer to **Figure 3.10** for definition of the LNP peaks 1-3.

3.4.7 FI-AF4-DLS demonstrated significant differences in Hydrodynamic Radius (R_h) among the four methods

The DLS detector (in flow-mode) coupled in-line to FI-AF4 provides a high-resolution measurement of R_h for each component in a sample (**Figure 3.13**). The R_h obtained by coupling FI-AF4 to DLS can be compared with batch-mode DLS for the BSA particle in MC3-BSA mixture (**Table 3.5**). In the case of batch-mode DLS, this has shown a single monomodal peak in the particle size distribution (R_h 3.8 (± 0.2) nm). In the case of FI-AF4 coupled to DLS, the broader distribution of R_h (methods 3 and 4 at cross-flow of 1.5 mL/min) for BSA suggests the resolving oligomeric forms. Similarly, whereas batch-mode DLS resulted in a single LNP peak at R_h of 46.4 (± 2.9) nm, in-line FI-AF4-DLS showed distinct populations of the LNP in the LNP-BSA mixture. The R_h obtained for LNP peak 1 ranged between (24.3 (± 0.1) nm to 27.1 (± 0.3) nm), LNP peak 2 (38.4 (± 0.2) nm to 63.9 (± 0.9) nm) and LNP peak 3 (67.3 (± 7.2) nm to 71.1 (± 2.0) nm). Method 2 has resulted in the highest R_h compared to the other methods. This is similar to R_g for method 2 obtained using MALS detector. Despite an increase in cross-flow between methods 1-3, there was no trend in increase in R_h which was in-line with results obtained for the R_g. An increase in detector flow (methods 3 and 4), resulted in a significant increase in R_h for LNP peaks 1 and 2, but no significant decrease for LNP peak 3.

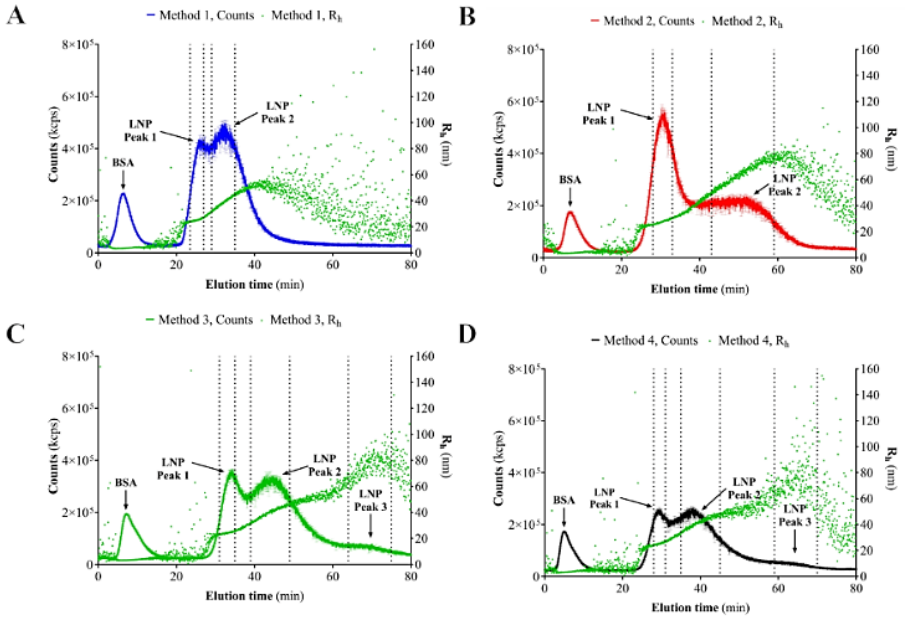

Figure 3.13 Flow-mode (FI-AF4-DLS) for MC3-LNPs incubated in 35 mg/mL Bovine Serum Albumin (BSA) for 24 hours at 37 °C. Plots represent (A) Method 1, (B) Method 2, (C) Method 3, (D) Method 4. The peaks represent an initial BSA peak and peaks 1-3 represents different LNP sub-populations of increasing R_h with elution time. Error bars represent ± S.D mean of triplicate injections. Vertical dashed lines indicate peak region of interest.

Table 3.5 Hydrodynamic Radius (R_h) obtained from batch-mode Dynamic Light Scattering (DLS) and FI-AF4 coupled to DLS detector (FI-AF4-DLS) for methods 1-4. Data is shown as ± S.D mean of three replicate injections (n=3). A hyphen (-) indicates no peak identified.

Sample	Constituents	Batch-mode DLS R_h (nm)	FI-AF4-DLS, R_h (nm)			
			Method			
			1	2	3	4
MC3-BSA	BSA	3.8 (± 0.2)	3.4 (± 0.0)	3.4 (± 0.0)	3.7 (± 0.0)	4.2 (± 0.1)
	LNP	46.4 (± 2.9)	**Peak 1** 25.3 (± 0.1) **Peak 2** 38.4 (± 0.2) **Peak 3** -	**Peak 1** 27.1 (± 0.3) **Peak 2** 63.9 (± 0.9) **Peak 3** -	**Peak 1** 24.3 (± 0.1) **Peak 2** 40.0 (± 0.2) **Peak 3** 71.1 (± 2.0)	**Peak 1** 26.2 (± 0.7) **Peak 2** 42.3 (± 0.5) **Peak 3** 67.3 (± 7.2)
	Aggregates	259.0 (± 897.2)	-	-	-	-

3.4.8 Combined contributions of FI-AF4 multiplexed with MALS and DLS for determining particle morphology

The combine use of both MALS and DLS detectors enables determination of particle morphology through calculation of the shape factor, defined as the ratio of R_g/R_h (**Equation 3.5**). The effect of varying FI-AF4 parameters on shape factor has not previously been reported. To gain insights into potential differences between shape factor values among different LNP sub-populations under different cross-flow and detector flow conditions, we evaluated the shape factor between distinct eluting sub-populations. R_g was extrapolated for the coated sphere fit model for light scattering data from the MALS detector for LNP peaks 1-3. The shape factor for an ideal sphere is ~ 0.77 [218]. Oblong or rod-shaped particles have a ρ value of >1 [308]. Significant differences in the shape factor values of each LNP sub-population between different methods were observed (**Figure 3.14** and **Supplementary Table S3.4**). Shape factor values ranged between 0.709-0.793 (LNP peak 1), 0.765-0.853 (LNP peak 2) and 1.069-1.263 (LNP peak 3) (**Figure 3.14**). The differences in the shape factor values

between the different sample constituents can be attributed to the interaction of BSA with LNP forming the protein corona [177, 219]. A small increase in shape factor typically suggests minimal protein association with the nanoparticle surface, whereas a larger increase indicates substantial protein adsorption [309]. **Figure 3.14** shows that particle morphology is not constant amongst the different resolved sample subpopulations. Assuming BSA adsorption occurs at the surface of the LNP, the R_g increases more than the R_h leading to an elevated shape factor.

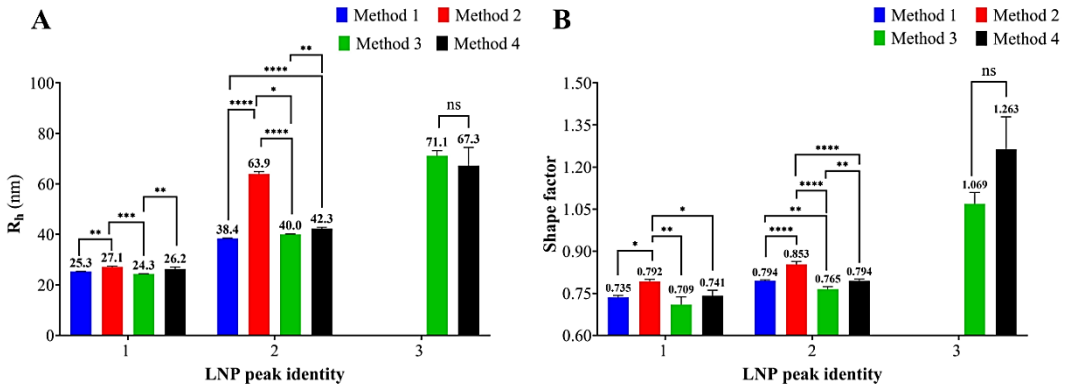

Figure 3.14 Contribution of different detectors coupled to FI-AF4 for determining (A) Hydrodynamic radius (R_h) obtained by FI-AF4-DLS (B) Shape factor (R_g/R_h) obtained by FI-AF4-MALS-DLS. Characterisation was carried out for different sub-populations of LNP (peak 1-3). Refer to **Figure 3.13** for DLS distribution plots and **Figure 3.10** for MALS (90°) signal and LNP peak identities. Statistical analysis for LNP Peak 1 and Peak 2 were performed using one-way ANOVA followed by post-hoc Tukey's test. Statistical analysis for LNP peak 3 was carried out using un-paired t-test. Error bars represent ± S.D mean of triplicate injections, *p < 0.05, **p < 0.01, ****p < 0.0001, ns; non-significant.

These findings indicate that LNPs examined span a morphological spectrum ranging from coated spheres to rod-like structures, with measurable changes in morphology occurring throughout the FI-AF4 elution profile. The applied cross-flow and detector flow conditions in FI-AF4 altered nanoparticle morphology likely due to particle alignment with flow and the force pushing particles towards the accumulation wall. The external forces and nanoparticles interactions with the accumulation wall and channel surfaces alter nanoparticle R_g and R_h, consequently altering the shape factor (R_g/R_h). Monitoring the shape factor is valuable, as it distinguishes the main particle population from additional sub-populations, such as aggregates or particles bearing a protein corona (shape factor > 0.77). The shape factor parameter also provides critical insights into formulation stability and biomolecular interactions that would

not be apparent from particle size measurements alone. DLS and NTA used for the initial characterisation of the LNP sample did not provide information on the morphology or heterogeneity of the different subpopulations. In contrast, AF4-MALS-DLS enabled assessment of particle morphology across the elution profile, as evidenced by analysis of the shape factor. Previous work by Davidson *et al.* [310] and Roamcharern *et al.* [311], established direct correlations between AF4-derived shape factor (~0.7) values and particle morphologies determined by negative-stain transmission electron microscopy (TEM) and scanning electron microscopy (SEM) imaging, demonstrating strong agreement between AF4 measurements and imaging-based approaches. Marassi *et al*. [312], similarly reported a shape factor value of 1.2 for aggregated human amniotic mesenchymal stromal cell–derived extracellular vesicles (hAMSC-EVs), further supporting the interpretation that elevated shape factor values are indicative of aggregated or non-spherical species.

3.5 Discussion

In this study, I presented a detailed methodological and analysis framework for implementing FI-AF4 coupled to online detectors UV, MALS and DLS to separate and characterize polydisperse nanoparticle mixtures comprising of LNPs and BSA. FI-AF4 is a powerful and adaptable technique for separating and characterizing complex nanoparticle mixtures. Unlike conventional chromatographic technique, FI-AF4 operates without a stationary phase, thereby minimizing shear forces that could otherwise alter nanoparticle conformation or induce aggregation, effects that may misrepresent the native state of the sample. One of the key strengths of the FI-AF4 technique is its ability to resolve broad and heterogeneous particle size distributions such as proteins (e.g. BSA) and LNPs and the presence of large aggregates, capabilities that outperform conventional analytical techniques. Methods utilizing elevated cross-flow rates (e.g. 1.0 and 1.5 mL/min) improved the resolution of larger aggregates, further highlighting FI-AF4's advantages in analysing complex mixtures.

Despite its strengths mentioned above, the FI-AF4 technique is not without limitations. One of the challenges lies in the complexity of method development. Moreover, there is considerable variation in the published literature on what constitutes a 'satisfactory' AF4 method, with one such example being the satisfactory RSD between replicate runs, the threshold for acceptable resolution and context-dependent percentage sample recovery. Resolution is defined as "two adjacent eluting peaks representing two monodisperse populations", however the presence of polydisperse populations hinders the calculation of the resolution factor [236]. The key contribution of this work is the development of FI-AF4 protocol that directly addresses the several limitations in the current ISO/TS 21362 guideline.

Parameters such as cross-flow rate, detector flow-rate and membrane equilibration must be finely tuned for optimal separation and minimal disruption of the material. In this study, FI-AF4 method development revolves around separating BSA fraction from the LNP using the method performance criteria (recovery, selectivity, retention and resolution [236]). The method developed was according to protocol developed by the lab and the ISO/TS 21362 standards for characterisation of nanomedicine using AF4 [236]. Although the ISO guidelines might be implicated for most of nanomedicine, it was difficult to follow these for LNPs and protein corona complexes due to their polydispersity nature; the MC3-LNP fractogram has shown two unresolved peaks (**Figure 3.5** and **Figure 3.6**), hence the resolution values cannot be calculated reliably for a non-Gaussian distribution.

Parameters that require optimization in AF4 method development are the cross-flow and detector flow rates. Both parameters influence the resolution, recovery, and structural integrity of the analyte. The cross-flow refers to the perpendicular flow applied across the channel, opposing the longitudinal parabolic flow. This flow directs analytes toward the accumulation wall, establishing the separation field that fractionates the particles based on their diffusion coefficients. While increasing cross-flow can enhance resolution by tightening the separation band, excessively high cross-flow may lead to analyte loss due to membrane permeation. This occurs when particles are driven too forcefully toward the membrane, increasing the likelihood of pore penetration, adsorption to the membrane surface, and reduced recovery or may result in protein denaturation due to high pressure. Qureshi *et al.* [313] and Marioli *et al.* [299] have shown that a high cross-flow rates reduce recovery. Moreover, higher cross-flow rates can result in a shift in retention times and peak broadening [281]. This relationship between cross-flow and retention time is considered to be linear according to the first order linear approximation [314] equation (**Equation 3.7**).

$$\mathbf{t_R = \frac{\pi \eta w^2 t^0 d_H}{2 k_B T V^0} . V_x} \qquad \textbf{Equation 3. 7}$$

where t_R is the retention time, η is the solvent viscosity, w is the channel height, t^0 is the time required for the carrier solution to pass through the channel (void time), k_B is the Boltzmann constant, T is the temperature, and V^0 is the geometric volume of the channel, V_x is the cross-flow.

In addition to the limitations associated with high cross-flow, practical experimental challenges must also be considered. Elevated cross-flow rates can lead to increased system backpressure and, in some cases leakage, particularly in sensitive or older instruments. Therefore, optimizing the cross-flow rate requires a balance between achieving sufficient

separation resolution, maintaining sample retention, and ensuring acceptable recovery. While higher cross-flow rates can enhance resolution by prolonging particle elution, this also extends the total run time of the method. This presents logistical constraints, especially when multiple replicates are required or when solvent consumption must be minimized. As such, determining an optimal cross-flow rate involves not only theoretical considerations of separation efficiency, but also practical limitations related to instrument performance.

Optimization of the detector flow rate is also essential in FI-AF4 method development, as it determines the rate at which eluted species exit the frit-inlet channel and proceed to the coupled detectors. Detector flow directly influences retention time and resolution. Lower detector flow rates are generally associated with improved resolution, as analytes spend more time within the separation channel, allowing better separation. In contrast, higher detector flow rates reduce analyte residence time, potentially compromising resolution. Kogej *et al*. demonstrated that lower detector flow rates (0.2 mL/min) yielded more accurate R_h measurements compared to higher flow rates (0.5 mL/min and 1.0 mL/min) [315]. Additionally, detector flow rate impacts signal intensity; elevated flow rates often lead to dilution effects and reduced signal response [316].

The measurement of R_g (FI-AF4 coupled to MALS detector) is critical for LNPs and bio nano-interactions specifically if coupled with R_h (FI-AF4 coupled to DLS detector) to obtain the shape factor value. Choosing the optimal method will have an excellent estimate to the size of LNP-control and LNP-BSA. The results obtained for R_g for LNP-control and the biomolecular corona are far smaller than values obtained by the other orthogonal techniques. As published by Kerker *et al*. [317], it had mentioned whether R_g is of any use or any added measurement which is meaningful to obtain the scattering data for complex, non-homogenous spheres. This concluded that R_g is a useful measurement obtained for small simple structured particles.

Literature repletes from publishing data for AF4-MALS fit models and subsequent fits results for the MALS fit model selected. There is not yet sufficient published literature on method optimization and theoretical model fits for optimal approximation of R_g for LNPs. It becomes questionable whether the particle morphology (R_g/R_h) is a correct approximation when the optimal scattering angles and fit models for LNPs is not standardized. Several publications reported the use of coated sphere model amongst other fittings as it gave the best MALS fit angles data with lowest fit errors [318, 319]. Other studies made use of the Zimm model [175, 320], Berry model [303, 321] and random coil algorithm [322, 323]. These studies show that the MALS model applied in AF4-MALS analysis is inherently material-independent, as it relies on fundamental light scattering principles rather than specific material properties.

Crucially, the shape and structure of the scattering profile are influenced by the particle's R_g and morphology, not its chemical composition. As a result, the MALS model can be applied universally to a wide range of analytes, whether polymeric, colloidal, lipid-based nanoparticles, proteins or inorganic material.

There remains a significant gap in validated methodologies tailored to this application of AF4 to heterogeneous nanoparticle mixture. The lack of standardized protocols presents a challenge not only for routine characterization but also for regulatory acceptance and cross-laboratory comparability. Furthermore, the field of LNPs characterisation using AF4 is hindered by the absence of certified reference materials for LNPs, limiting the ability to benchmark performance or validate results. Current literature also reveals a shortage of dedicated method development studies focused specifically on mixture of nanoparticles, underscoring the need for systematic research that addresses particle heterogeneity, stability, and complex formulations. Advancing AF4-based characterization of nanoparticle mixtures will require both methodological refinement and the development of appropriate reference standards to support robust and reproducible analyses.

The findings in this chapter underscore the importance of careful method selection as a critical first step in bionanomaterial FI-AF4 characterization, directly influencing detector signal, resolution, light scattering model fit, the accurate determination of particle size (R_g and R_h) and morphology (shape factor, R_g/R_h ratio). While the results presented here focus on LNPs and proteins, the protocol and analytical considerations are broadly applicable to a wide range of heterogeneous nanoparticle systems. Furthermore, I emphasize the value of extracting and critically analysing raw FFF data, rather than relying solely on automated software outputs, to guide robust method development and improve reproducibility in the characterization of complex nanomaterials.

Limitations and next steps

This study investigated the separation of a single protein (BSA) and a single LNP prototype (MC3-LNPs), which is appropriate for initial method development and the establishment of a robust protocol for separating heterogeneous particle mixtures. However, the study did not extend to complex biological media (e.g., serum or simulated intestinal fluid). The increased compositional complexity and heterogeneity of such media may affect method repeatability, sample recovery, and the accuracy of MALS model fitting, as well as influence measured physicochemical attributes, including R_h, R_g, and particle morphology.

Furthermore, this study investigated the effect of two FI-AF4 parameters (cross-flow and detector flow). However, other key parameters such as channel membrane selection (including membrane pore size), elution buffer composition, and spacer thickness were not explored. Evaluating the influence of these variables on FI-AF4 performance could provide further insight into method optimisation and may be systematically addressed through a design of experiments (DoE) approach.

Chapter 4: Frit-Inlet-Asymmetric Flow Field-Flow Fractionation for the Comparative Analysis of the Biomolecular Corona Formation of Two LNP Prototypes (MC3-LNP and SM-102-LNP)

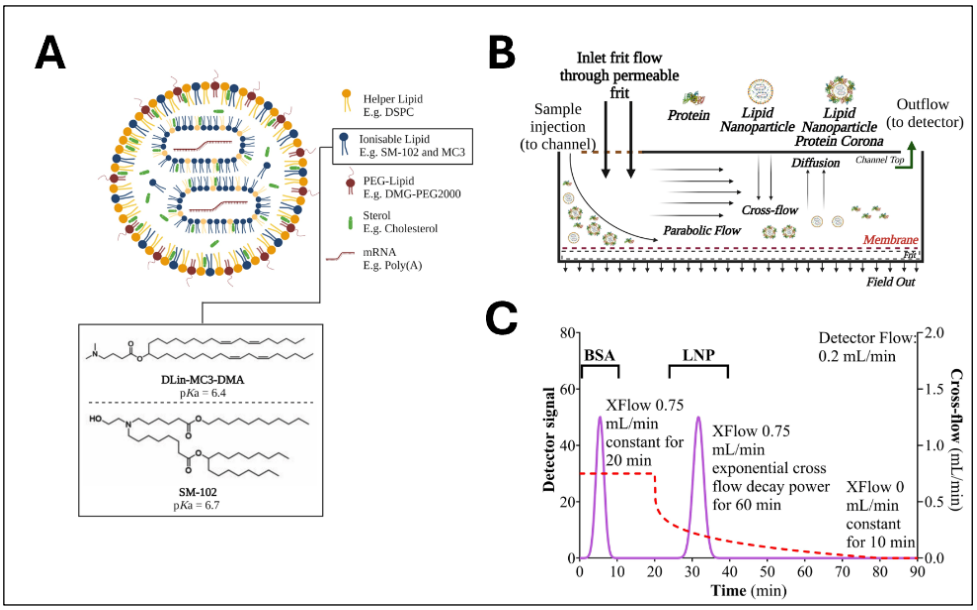

Findings from this work are published in Journal of Chromatography A.

Abdulrahman R, Punnabhum P, Capomaccio R, Treacher K, Perrie Y, Rattray Z. Frit-inlet asymmetric flow field-flow fractionation for the analysis of lipid nanoparticle-protein interactions. Journal of Chromatography A. 2025 Feb 22;1743:465663. https://doi.org/10.1016/j.chroma.2025.465663

Abdulrahman R, author of this thesis, performed all the experimental work and completed all data analysis presented in the publication and this chapter.

4.1 Introduction

mRNA-based therapies, which target disease-related proteins to alter their expression and function, have gained traction as a strategy for treating diseases [324]. While lipid nanoparticles (LNPs) have proven to be an effective drug delivery system, particularly highlighted by their success in COVID-19 immunisation efforts, the interactions between LNPs and biological systems have not been thoroughly explored. Following administration, depending on the route of administration, various proteins from the subcutis interstitial fluid and blood serum spontaneously adsorb onto the LNP surface, forming a complex termed the 'protein corona' [325-327]. This protein corona is critical in determining how LNPs interact with biological systems. The formation of the protein corona can alter the LNP surface, impacting its biological activity including its biophysical characteristics in the presence of surface-adsorbed biomolecules. These changes can affect LNP physical properties, organ biodistribution, physicochemical stability, cellular uptake and circulation time. As a result, the behaviour and effectiveness of LNPs can significantly vary [223, 328-331].

The fate of LNPs is influenced by the composition of surface-adsorbed proteins, and the physicochemical changes induced by the biomolecular corona can be correlated with different LNP constituents (**Figure 4.1**). Ionizable lipids are particularly important for LNP function. Efforts to optimise these ionizable lipids for siRNA delivery have led to the development of novel lipids that are now incorporated into clinically approved LNPs [28, 156]. DLin-MC3-DMA (referred as MC3) (heptatriaconta-6,9,28,31-tetraen-19-yl-4-(dimethylamino)butanoate) and SM-102 (heptadecan-9-yl 8-((2-hydroxyethyl) (6-oxo-6-(undecyloxy) hexyl) amino) octanoate) are two clinically-approved ionizable lipids used in Onpattro® (Alnylam Pharmaceuticals) and Spikevax® (Moderna), respectively [114, 234].

Asymmetric Flow Field-Flow Fractionation (AF4) is emerging as a valuable technique in the field of nanomedicine due to its low-stress and non-disruptive separation capabilities [207]. AF4 can be coupled with multiple detectors to analyse various LNP Critical Quality Attributes (CQAs) such as particle size, polydispersity and molecular weight [209, 273, 335]. Multi-angle light scattering (MALS) is used to measure the molar mass and size of particles, often expressed as the radius of gyration (R_g) [336]. In conjunction with R_g, the Stokes radius or hydrodynamic radius (R_h) can be determined using in-line dynamic light scattering (DLS). The combination of these measurements allows for the assessment of particle shape factor (R_g/R_h) [209, 218]. A key advantage of AF4 for protein corona analysis is its ability to

characterise particles *in situ* without the need for prior separation of unbound proteins. This avoids potential alterations to nanoparticle parameters that may occur with commonly used methods such as centrifugation-resuspension [170, 337].

Although emerging publications demonstrate the use of AF4 for analysing LNP formulation stability, there is a notable lack of studies focusing on AF4 applications for the separation and online analysis of LNPs in biological media. This study aims to understand different interactions of two model LNP prototypes with different ionizable lipid composition (MC3 and SM-102) with Bovine Serum Albumin (BSA) as a model protein contained in biological media. This work lays the foundation for future studies on LNP biomolecule-nanomaterial interactions using a high-resolution characterisation and gentle separation technique which is extremely critical for soft LNP materials.

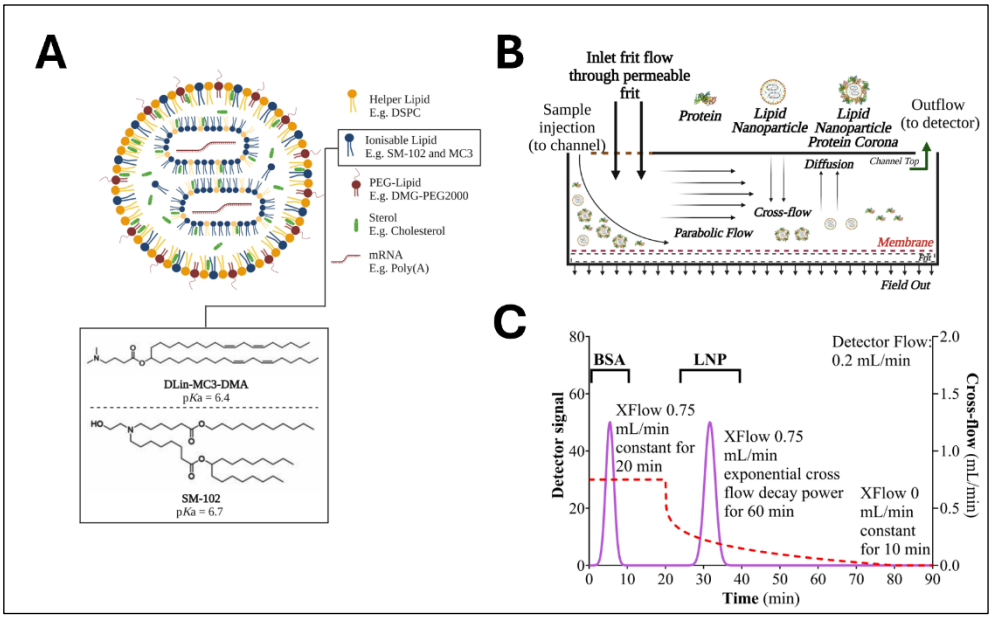

Figure 4.1 Schematic showing formation (A) Lipid nanoparticles (LNP) components with difference in ionizable lipids (D-Lin-MC3-DMA referred as MC3 and SM-102), (B) Side-view of frit-inlet AF4 (FI-AF4) channel with protein, LNP and LNP-protein corona in the channel and (C) a representative simulated FI-AF4 profile of Bovine Serum Albumin (BSA) and LNP with the applied cross-flow (XFlow) and detector signal. Figures (A) and (B) created with BioRender.com and (C) NovaAnalysis software.

4.2 Aim and Objectives

This study investigates the applicability of Frit-Inlet (FI-AF4) for the separation of MC3- and SM-102-based LNPs from BSA and the high-resolution characterization of the resulting LNP-BSA complex. LNP formulation differences including changes in ionisable lipid geometry (cylinder and inverted cone shape for MC3 and SM-102 lipid respectively) can result in variable affinities for BSA, influencing LNP-biomolecule interactions. To achieve this aim, the objectives were **(1)** encapsulate Poly(A) mRNA into the ionizable MC3-LNPs and SM-102-LNPs; **(2)** incubate MC3-LNPs and SM-102-LNPs with BSA at 37 °C for 24 hours to form MC3-LNP-BSA and SM-102-LNP-BSA corona, respectively; **(3)** characterise LNPs-control and LNP-BSA particle size (R_g), (R_h) and morphology (R_g/R_h) by coupling FI-AF4 to multiple detectors (UV, MALS and DLS) and **(4)** determine the particle size and morphological distributions of LNP-control and LNP-BSA samples and evaluate the significant changes of the MC3-LNP-BSA and SM-102-LNP-BSA.

4.3 Material and Methods

4.3.1 Reagents and Materials

Polyadenylic acid (Poly(A)), cholesterol, sodium citrate dihydrate, ethanol, and dialysis tubing cellulose membrane (molecular weight cut-off (MWCO) 14 kDa) were purchased from Sigma-Aldrich (St. Louis, MO, USA). Helper lipids 1,2-distearoyl-sn-glycero-3-phosphocholine (DSPC), 1,2-dimyristoyl-rac-glycero-3-methoxypolyethylene glycol-2000 (DMG-PEG 2000) were purchased from Avanti Polar Lipids (Alabaster, AL, USA). The ionizable lipids (6Z,9Z,28Z,31Z)-Heptatriaconta-6,9,28,31-tetraen-19-yl 4-(dimethylamino)butanoate (D-Lin-MC3-DMA) and 8-[(2-hydroxyethyl)[6-oxo-6-(undecyloxy)hexyl]amino]-octanoic acid, 9-Heptadecanyl 8-((2-hydroxyethyl)[6-oxo-6-(undecyloxy)hexyl]amino) octanoate (SM-102) were purchased from BroadPharm (San Diego, CA, USA). Lyophilised powder Bovine Serum Albumin (BSA), Invitrogen™ UltraPure™ DNase/RNase-free water and phosphate-buffered saline (PBS) 10X salt solution pH 7.4 was acquired from Fisher Scientific (Loughborough, UK).

4.3.2 Methods

4.3.2.1 Preparation of SM-102-LNPs and MC3-LNPs

Poly(A) LNPs were manufactured using the NanoAssemblr® Ignite Precision NanoSystems (Vancouver, BC, Canada) using the NxGen single-use microfluidic cartridge. Lipid stocks were prepared in ethanol at molar ratio of MC3/SM-102 : DSPC: Cholesterol: DMG-PEG2000

(50:10:38.5:1.5 mol% respectively) which is based on the percentage composition of Onpattro® (Alnylam Pharmaceuticals) [234] and Comirnaty® (Pfizer-BioNTech) [235]. The aqueous phase consisted of initial Poly(A) stock of 1.5 mg/mL dissolved in 50 mM sodium citrate buffer (pH 4.0). The Total Flow Rate (TFR) was set at 15 mL/min, and an aqueous-to-organic Flow Rate Ratio (FRR) of 3:1 was used with a final lipid concentration of 1.25 mg/mL and Poly(A) of 0.055 mg/mL. The N:P (N for lipid nitrogen and P for nucleic acid phosphate) was 6:1. LNPs were purified by dialysis to remove ethanol and acidic citrate buffer. Initial and final waste volumes were set at 0.35 and 0.05 mL, respectively. The volume of LNPs prepared was 4 mL. Resultant suspensions were dialysed (MWCO 14 kDa, Sigma-Aldrich, St. Louis, MO, USA) into 1X PBS (pH 7.4) (500X dialysate ratio, 2 mL of LNPs in 1000 mL of PBS) under magnetic stirrer for 6 hours at 4 ºC to remove ethanol and citrate buffer. The dialysate was replaced with fresh PBS after 1 hour and 3 hours from the start of dialysis. All formulations were syringe-filtered through 0.2 µm pore-sized Supor® membrane (Pall Corporation, USA) and stored at 4 °C until further use.

4.3.2.2 Preparation of LNP-BSA corona

MC3 and SM-102 LNPs were incubated with BSA, which was used as a model protein to study LNP-BSA corona formation. MC3 and SM-102-LNPs were incubated at a 1:1 (volumetric ratio) with BSA (35 mg/mL in PBS (pH 7.4) corresponding to the physiological serum albumin concentration in humans [338]). Final theoretical LNP lipid concentration was 0.625 mg/mL. The mixture was incubated for 24 hr at 37 °C in Protein LoBind eppendorfs under static conditions. Control samples included an equal volume of PBS and LNP.

4.3.2.3 Particle size and polydispersity determination

Particle size (*Z*-average) and the Polydispersity Index (PDI) were measured by DLS using Zetasizer Nano ZS system (Malvern Panalytical, Worcestershire, UK). Parameters were set at 25 ºC using non-invasive backscattering (NIBS, 173°) at a dilution of 1:10 in 10 mM PBS (pH 7.4). Final measured sample concentrations were theoretical lipid concentration of 125 µg/ mL and Poly(A) concentration of 5.5 µg/mL. The refractive index (RI) and viscosity of the buffer (PBS) were set at 1.34 and 1.02 cP, respectively. *Z*-Average and PDI were measure using DLS cumulant algorithm analysis. All measurements were performed in three independent replicates consisting of at least three technical replicates.

4.3.2.4 Zeta potential determination

The zeta potential of LNP-control (LNP-PBS) at 0 hr was measured by Electrophoretic Light Scattering (ELS) at 25 °C and the Smoluchowski approximation was used. Measurements were performed at 25 ºC and at a 1:10 dilution in DNase/RNase-free water established in [102].

The RI and viscosity of the medium (DNase/RNase-free water) were set at 1.33 cP and 0.89 cP, respectively. All zeta potential measurements were performed in three independent replicate measurements consisting of five technical replicates.

4.3.2.5 Particle size distribution and particle concentration

Nanoparticle Tracking Analysis (NTA) was used to perform the *in situ* analysis of LNPs incubated with BSA, studying changes in LNP size occurring in response to BSA surface-adsorption. All NTA measurements were performed using a NanoSight NS300 system (Malvern Panalytical, Malvern, Worcestershire, UK), configured with a 488 nm laser and a sCMOS camera. LNP samples were diluted in PBS (pH 7.4) and analyzed under a constant syringe driver set at 50 AU at 25 °C. Five successive videos of 60-second duration were captured with the camera level set at 14 (MC3-LNPs) and 12 (SM-102-LNPs), and a corresponding detection threshold of 5 (MC3 and SM-102 LNPs). Particle dilutions were by a factor of 2 x 10^3 (MC3-LNPs) and 4 x 10^4 (SM-102-LNPs). The span of particle size distribution, as measured using NTA, was calculated using the ratio (D90-D10)/D50). The mean and standard deviation for parameters were determined from three independent measurements consisting of five technical replicates.

4.3.2.6 Encapsulation Efficiency (EE)

Quant-iT™ RiboGreen RNA Assay Quantitation (Invitrogen™, Thermo Fisher Scientific, UK) was used for the quantification of Poly(A) encapsulation in LNPs as per manufacturer's instructions. LNPs were serially diluted in Tris and Ethylenediaminetetraacetic acid (TE buffer) in the presence and absence 2% *v/v* Triton X-100 in a 96-well plate. The plate was incubated at 37 °C for 15 minutes, followed by the addition of two dilutions of 1X Ribogreen Reagent (500-fold and 200-fold) to wells containing TE buffer and Triton X-100, respectively. Fluorescence was measured using a GloMax® Microplate Reader (Promega Corporation, UK) with an excitation of 475 nm and emission 500-550 nm wavelength. EE % (**1**) was determined by constructing standard calibration curves using naked Poly(A) solutions prepared both in the absence and presence of Triton X-100. These standard curves allowed for accurate quantification of free and total Poly(A) in the LNP samples, enabling calculation of EE % by comparing the amount of encapsulated Poly(A) to the total Poly(A) content.

$$\mathbf{EE}\ (\%) = \frac{\mathbf{Poly(A)_{total} - Poly(A)_{free}}}{\mathbf{PolyA_{total}}} \mathbf{x\ 100} \qquad \textbf{Equation 4.1}$$

where $Poly(A)_{total}$ is the total Poly(A) concentration (µg/mL) in wells containing Triton-TE buffer, $Poly(A)_{free}$ the concentration (µg/mL) of the unentrapped Poly(A) for wells containing TE buffer.

4.3.2.7 Frit-Inlet Asymmetric Flow Field-Flow Fractionation (FI-AF4)

4.3.2.6.1 Radius of Gyration (R_g), Hydrodynamic Radius (R_h) and Shape Factor (R_g/R_h) by FI-AF4 in-line with Multiple Detectors

FI-AF4 (AF200 Postnova Analytics, Landsberg, Germany) was used for characterising MC3 and SM-102 LNPs for their R_g, R_h and R_g/R_h. The system was configured with tip and pressure pumps, a degasser, and autosampler. The system was equipped with an online UV (PN3242, ʎ = 260 nm, Postnova Analytics), 21-angle MALS-PN3621, Postnova Analytics) and online Zetasizer Nano ZS (Malvern Panalytical, Malvern, UK) detector. The frit-inlet channel configuration included the use of a 10 kDa MWCO size amphiphilic regenerated cellulose (RC) membrane, a spacer thickness of 350 µm, and 10 mM PBS (pH 7.4) as the carrier liquid.

DLS measurements were obtained using a Malvern quartz flow cell (ZEN0023), with a flow rate of 0.2 mL/min at 25 °C at three-seconds intervals. The measurement position was set at 4.2 mm with the attenuator set at 11. The AF4 parameters for separation are in **Table 4.1**. Membrane pre-conditioning with triplicate injections was carried out using BSA (5 mg/mL). The samples were not diluted for AF4. The intensity of the scattered light using the MALS detector was calculated for angles 36° to 148° and the sphere fit model for all samples was used for the R_g measurement.

For the analysis, MC3 and SM-102 LNPs and their corresponding corona samples were analysed in technical triplicates without additional dilution, at a theoretical LNP lipid concentration of 0.625 mg/mL and a BSA concentration of 35 mg/mL.

Table 4.1 Corresponding AF4 parameters for applied cross-flow.

Time (min)	Cross-flow (mL/min)	Type	Exponent	Detector flow (mL/min)	Injection volume (µL)	Injection flow rate (mL/min)
20	0.75	Constant	0	0.2	20	0.2
60	0.75	Exponential Power Decay	0.2			
10	0	Constant	0			

4.3.2.6.2 Sample recovery by FI-AF4

The recovery (R %) of the samples for was calculated using the following equation:

$$\mathbf{R}(\%) = \frac{\mathbf{Ac}}{\mathbf{A}} \mathbf{x\ 100} \qquad \textbf{Equation 4.2}$$

Where A_c is the area under the peak of LNPs under a cross flow, and A the area under the peak of the unfractionated LNP *via* direct sample injection (without an applied cross flow). The parameters for the direct injection (**Table 4.2**). Absorbance was measured at 260 nm using a UV detector. Fractions eluting after the cross-flow stops (0 mL/min for 10 minutes) were not included in the fractogram integration. A criteria to establish optimal methodology was based on a sample recovery of ≥70 %.

Table 4.2 Corresponding FI-AF4 parameters for direct injection.

Time (min)	Cross-flow (mL/min)	Type	Exponent	Detector flow (mL/min)	Injection volume (µL)	Injection flow rate (mL/min)
10	0	Constant	0	0.2	20	0.2
5	0	Linear				

4.3.2.8 Calculation of LNP surface saturation with BSA

The number maximum number of BSA particles forming the corona layer around a single LNP assuming a close packed protein arrangement forming a BSA monolayer is given by the following expression:

$$\mathbf{N_{BSA} = 0.65\ x \left(\frac{(R_{tot}{}^3) - (R_{LNP}{}^3)}{(R_{BSA}{}^3)}\right)} \qquad \textbf{Equation 4.3 [339]}$$

where R_{LNP} is the radius of LNP, R_{BSA} is the radius of BSA, $R_{tot} = R_{LNP} + (2\ X\ R_{BSA})$. A filling factor of 0.65 is used for BSA hard sphere [340]. It was assumed that **(1)** each LNP is fully surface covered with BSA **(2)** both BSA and LNP have a spherical geometry with a filling factor of 0.65.

4.3.2.9 Statistical Analysis

All data were analysed using GraphPad Prism 10 (GraphPad Software Inc). The mean ± standard deviation (SD) was calculated for all experiments with three independent replicates and at least two technical replicates. Normality of all datasets was assessed using Shapiro-Wilk test. One-way analysis of variation (ANOVA) followed by Tukey's multiple comparisons test was used for normally distributed data. For non-normally distributed data, non-parametric analysis was carried out using Kruskal-Wallis test followed by Dunn's multiple comparison test. Statistical significance was considered at *p-value* < 0.05; *p < 0.05, **p < 0.01, ***p < 0.001, ****p < 0.0001.

4.4 Results

4.4.1 Characterisation: particle size, PDI, zeta potential, and encapsulation efficiency

Prior to incubation with BSA, the initial characterization of LNP prototypes was performed using batch-mode DLS. This included measurements of particle hydrodynamic diameter, PDI, and zeta potential, analysed using the DLS cumulant algorithm analysis in accordance with ISO 22412:2025 standards for particle sizing [341]. Both LNP formulations demonstrated *Z*-average diameters below 100 nm, specifically, 74.9 (± 2.6) nm for MC3-LNPs and 67.7 (± 0.6) nm for SM-102-LNPs (**Table 4.3**). The corresponding PDI values indicated a uniform size distribution, with MC3-LNPs at 0.152 (± 0.010) and SM-102-LNPs at 0.165 (± 0.069). LNP prototypes carried a negative surface charge, and their encapsulation efficiencies exceeded 95 %.

Table 4.3 Baseline Critical Quality Attributes (CQAs) quantified for MC3, SM-102 LNPs and Bovine Serum Albumin (BSA). Data are shown as mean ± SD, N=3 independent batches and n=3 technical replicates.

Sample	*Z*-Average (nm)	PDI	Zeta Potential (mV)	Enapsulation Efficiency (%)
BSA	7.5 (± 0.0)	0.180 (± 0.081)	-15.4 (± 5.0)	-
MC3-LNP	74.9 (± 2.6)	0.152 (± 0.010)	-7.6 (± 2.6)	98 (± 2)
SM-102-LNP	67.7 (± 0.6)	0.165 (± 0.069)	-5.6 (± 2.3)	96 (± 2)

Both LNP prototypes were incubated with BSA to examine the formation of corona complex, *in situ*. The PDI measured in the presence of BSA was 0.540 (± 0.049) for MC3-LNPs and 0.534 (± 0.061) for SM-102 LNPs, indicating a polydsiperse system in the presence of BSA (**Figure 4.2** and **Table 4.4**). Hence, following incubation of LNPs with BSA, LNP-corona mixture could not be compared using the *Z*-average cumulant analysis due to the high PDI (PDI >0.3) and polymodal distribution resulting from the presence of excess unadsorbed BSA in the sample (**Figure 4.2** and **Table 4.4**).

DLS distbution algorithm analysis was used for measuring particle size of the LNP-corona mixture (**Table 4.4**). The 24-hour incubation for MC3 and SM-102 LNPs with BSA showed 3 peaks (peak 1, peak 2 and peak 3) in the DLS particle size distribution (**Figure 4.2B** and **Figure 4.2C**). Comparing 24-hour incubations of LNPs in the absence and presence of BSA, particle hydrodynamic diameter for MC3-LNPs showed a reduction in the size of the main

peak corresponding to LNPs (MC3-PBS 99.5 (± 20.9) nm to MC3-BSA 92.7 (± 2.9) nm), whereas SM-102-LNPs showed an increase in size corresponding to LNP-BSA corona formation (SM-102-PBS 72.9 (± 2.2) nm to SM-102-BSA 81.8 (± 3.3) nm), however interestingly this difference was not significant (**Figure 4.2** and **Table 4.4**). SM-102-LNPs showed a more positive zeta potential in comparison to MC3-LNPs in the presence of BSA (a change from -6.5 (± 1.2) mV to -3.4 (± 1.1) mV for SM-102-PBS and SM-102-BSA respectively, and -6.3 (± 0.3) mV and -6.6 (± 0.8) mV for MC3-PBS and MC3-BSA respectively.

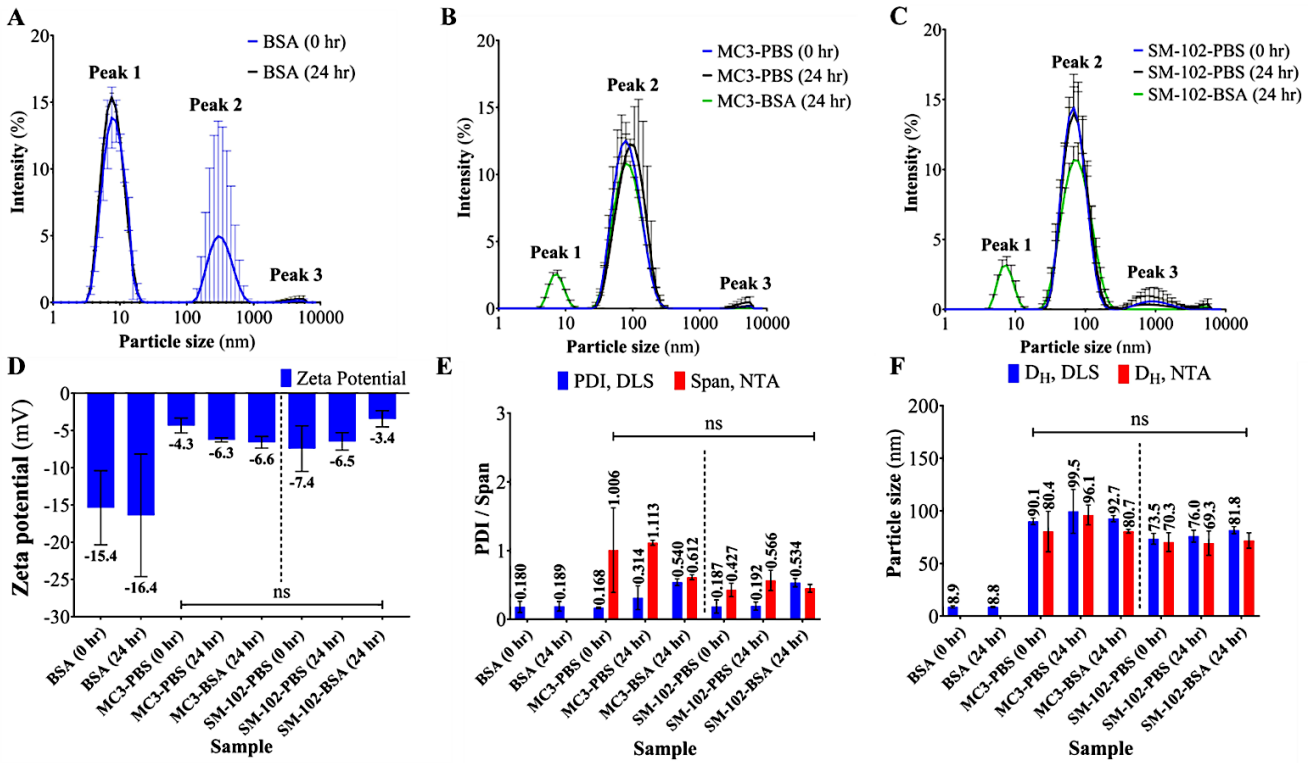

Figure 4.2 Critical Quality Attributes (CQAs) measured using different analytical techniques. Plots represent (A) DLS particle size particle size distribution for Bovine Serum Albumin (BSA) 35 mg/mL (control) (B) MC3-LNPs incubated in PBS (control) (MC3-PBS) and in 35 mg/mL BSA (MC3-BSA) (C) SM-102 LNPs (D) zeta potential (E) PDI and span (F) hydrodynamic diamter (D_H) measured using distribution algorithm analysis using DLS and mean D_H using NTA. Results are shown as mean ± S.D, N=3 independent replicates, n=3 technical replicates. All plots show 0 hour (control) and 24 hours incubation at 37 ºC for 24 hours. Peaks 1-3 in (B) and (C) correspond to BSA (peak 1), LNP-control or LNP-BSA (peak 2) and aggregates (peak 3). Statistical analysis was performed using Kruskal-Wallis followed by post-hoc Dunn's test for plots (D) and (E) and one-way ANOVA followed by post-hoc Tukey's test for plot (F). Stastical analysis was carried out comparing between LNP-PBS (control) at 24 hours and LNPs in 35 mg/mL BSA (LNP-BSA) at 24 hours between the same LNP protype. ns: non significance. The vertical dashed line in plots (E) and (F) distiguishes MC3 LNPs and SM-102 LNPs.

Table 4.4 Physiochemical attributes describing hydrodynamic particle diameter (particle size) measured by Dynamic Light Scattering (DLS) distribution algorithm analysis and Polydispersity Index (PDI). Samples represent MC3 and SM-102 LNPs incubated in PBS (control) and in 35 mg/mL BSA. Results are shown as mean ± S.D, N=3, n=3. Measurement values indicate 0 hour (control) and 24 hours incubation at 37 °C. The symbol (-) indicates unidentified peaks. Peaks 1, 2 and 3 are labelled in **Figure 4.2**.

			Particle hydrodynamic diameter (nm)				
	Time-point (hr)	**Sample**	**Peak 1**	**Peak 2**	**Peak 3**	**PDI**	**Zeta potential (mV)**
BSA	0	BSA-PBS	8.9 (± 1.0)	665.3 (± 0.0)	2597.3 (± 1466.6)	0.180 (± 0.081)	-15.4 (± 5.0)
	24		8.8 (± 0.5)	358.1 (± 310.0)	3074.8 (± 873.3)	0.189 (± 0.070)	-16.4 (± 8.2)
MC3-LNP	0	MC3-PBS	-	90.1 (± 3.1)	1538.7 (± 66.5)	0.168 (± 0.012)	-4.3 (± 1.0)
	24	MC3-PBS	-	99.5 (± 20.9)	2928.7 (± 2537.1)	0.314 (± 0.173)	-6.3 (± 0.3)
		MC3-BSA	7.5 (± 0.2)	92.7 (± 2.9)	518.0 (± 897.2)	0.540 (± 0.049)	-6.6 (± 0.8)
SM-102-LNP	0	SM-102-PBS	-	73.5 (± 5.1)	2853.0 (± 2760.5)	0.187 (± 0.096)	-7.4 (± 3.1)
	24	SM-102-PBS	-	72.9 (± 2.2)	4723.0 (± 66.6)	0.192 ± 0.060	-6.5 (± 1.2)
		SM-102-BSA	7.4 (± 0.3)	81.8 (± 3.3)	4671.9 (± 140.1)	0.534 (± 0.061)	-3.4 (± 1.1)

Size information obtained by NTA followed a similar trend to that of DLS. Comparing changes in NTA-measured LNP size following 24 hour incubation in BSA, a reduction in mean particle size was observed for MC3-LNPs (96.1 (± 9.4) nm for MC3-PBS and 80.7

(± 1.8) nm for MC3-BSA) and an increase in mean particle diameter for SM-102 LNPs (69.3 (± 11.5) nm for SM-102-PBS to 71.9 (± 7.3) nm for SM-102-BSA) (**Figure 4.2F**). Particle concentration varied between prototypes (**Figure 4.3**). NTA images indicated the presence of relatively larger particles in the LNP-corona mixture (**Figure 4.4**).

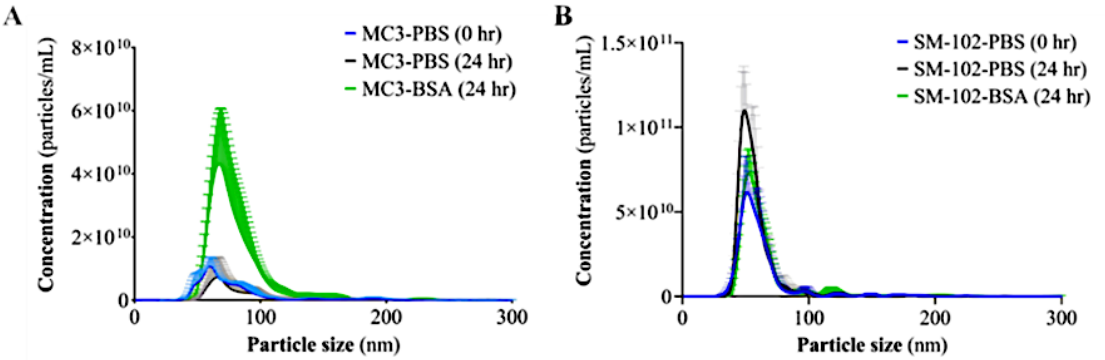

Figure 4.3 Particle concentrations obtained using NTA for (A) MC3-LNPs incubated in PBS (control) (MC3-PBS) and in 35 mg/mL Bovine Serum Albumin (BSA) (MC3-BSA) and (B) SM-102 LNPs. Time-points indicate 0 hour (control) and 24 hours incubation at 37 ºC. Error bars represent ± S.D, N=3, n=3.

Although particle tracks appear roughly circular in live NTA videos, this visual representation does not reflect actual morphology. Unlike cryo-electron microscopy (cryo-EM), which provides high-resolution structural detail, NTA does not offer morphological information. However, it can indicate the presence of particles with larger hydrodynamic diameters, suggesting potential aggregation or BSA adorption to LNPs. Since larger particles scatter more light, these appear brighter in the image. According to NTA, which is contradicting the PDI values obtained from DLS, at 24 hours the span is higher for MC3-PBS (1.11 (± 0.04)) compared to MC3-BSA (0.44 (± 0.04)), and similarly higher from SM-102-PBS at (0.61 ± 0.04) compared to SM-102-BSA (0.45 ± 0.06) (**Figure 4.2E**).

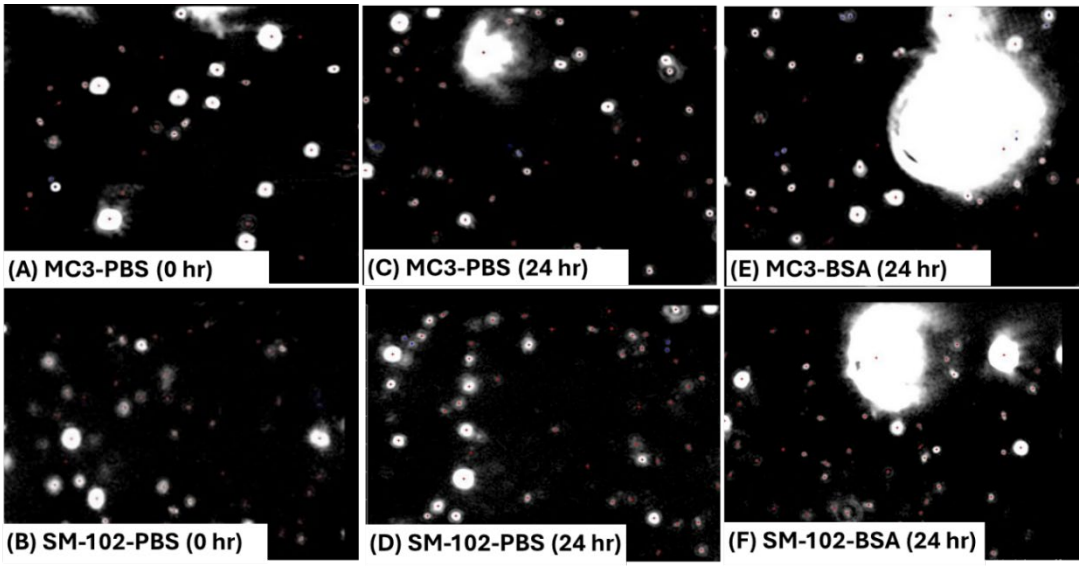

Figure 4.4 Live monitoring tracking images and particle concentration obtained using NTA for (A) MC3-LNPs incubated in PBS (control) (B) SM-102 LNPS (C) MC3-LNPs incubated in PBS (D) SM-102 LNPs (E) MC3-LNPs incubated in 35 mg/mL Bovine Serum Albumin (BSA) (MC3-BSA) and (F) SM-102 LNPs. Time-points indicate 0 hour (control) and 24 hours incubation at 37 ^{o}C.

4.4.2 Calculation of LNP surface saturation with BSA

The number maximum number of BSA particles forming the corona layer around a single LNP assuming a close packed protein arrangement forming a BSA monolayer was calculated.

4.4.2.1 MC3-BSA at 24 hours

Using **Equation 4.3**, where R_{LNP} is 37.5 nm (MC3-LNPs *Z*-average 79.4 nm), R_{BSA} is 3.4 nm, R_{tot} = 44.3 nm, this results in 566 BSA particles per 1 MC3-LNP at 24 hours.

The concentration of MC3-LNP is **1.6 x 10^{12} particles/mL** which indicates that there needs to be a maximum of **9.1 x 10^{14} particles/mL** of BSA for saturation of LNP surface with BSA.

Concentration of BSA used is 35 mg/mL with molecular weight of 66,500 g/mol, result in **5.3x 10^{-7} moles/mL** (0.035 g / 66500 g/mole) of BSA. Using Avogadro's number 6.02×10^{23} $moles^{-1}$, there are **3.2×10^{17} particles/mL BSA** ([5.3x 10^{-7}] moles x [6.02×10^{23}]), it indicates that MC3-LNP surface saturation has been reached, with free unbound BSA present with excess concentration of BSA of **~360X** ([3.2×10^{17}] / [9.0 x 10^{14}] particles/mL).

4.4.2.2 SM-102-BSA at 24 hours

Using **Equation 4.3**, where R_{LNP} is 33.9 nm (SM-102-LNPs *Z*-Average 67.7 nm) at 24 hours, R_{BSA} is 3.4 nm, R_{tot} = 40.7 nm resulting in 471 BSA particles per 1 SM-102-LNP. The concentration of SM-102 LNPs is **1.6 x 10^{12} particles/mL** measured using NTA which indicates that there needs to be a maximum of **7.5 x 10^{14} particles/mL** ([1.6 x 10^{12}] particles/mL x [469] BSA particles) of BSA for saturation of LNP surface with BSA.

Similar to MC3-LNP calculation, there are **3.2 × 10^{17} particles/mL BSA**. This indicates that LNP surface saturation has been reached with excess concentration of BSA of **~430X** ([3.2 × 10^{17}] / [7.5 x 10^{14}] particles/mL).

4.4.3 Frit-Inlet AF4 (FI-AF4)

Cryogenic transmission electron microscopy (cryo-TEM) analyses reported in earlier studies have confirmed that ionizable cationic LNPs typically exhibit a spherical morphology [32, 342, 343]. Based on this, and method development in chapter 3, a spherical model was used to fit the MALS data. The sphere fit for the MALS data for MC3 and SM-102 LNPs are shown in **Supplementary Figure S4.1**. Recovery assessments (**Supplementary Table S4.1**) demonstrated high initial recovery rates for the LNP formulations, with MC3-LNPs achieving 97 (± 2) % and SM-102-LNPs showing 111 (± 13) % recovery at t = 0.

4.4.3.1 Hydrodynamic Radius (R_h) and Radius of Gyration (R_g) in response to incubation with BSA

Although DLS was able to distinguish free BSA from the LNP-BSA mixture, the analysis was based on distribution particle analysis, which is not recommended by ISO standards due to its limitations in resolving polydisperse systems. To overcome this, a higher-resolution technique, FI-AF4 was used. FI-AF4 enabled the measurement of both the R_g and the R_h. Furthermore, previous analytical techniques did not provide insight into the morphology of LNP-BSA corona. By calculating the R_g/R_h ratio, FI-AF4 also allowed for the characterization of particle morphology, offering a more comprehensive understanding of the LNP-protein interactions.

MALS and UV analysis for both MC3-BSA and SM-102-BSA corona revealed a distinct BSA peak eluting at ~5 min, while both control LNPs and LNP-BSA complexes eluted between 25-30 min **(Figure 4.5**). In panels A and B (**Figure 4.5)** (LNP-BSA at 24 hours), a reduction in UV absorbance for the LNP peak was observed, attributed to the strong absorbance of BSA's

amino acid residues. Conversely, panels C and D (**Figure 4.5**) (LNP-BSA at 24 hours) showed a diminished MALS signal for BSA relative to LNPs, due to the inherently stronger light scattering properties of the larger LNP particles.

At 0 hours, MC3-LNPs displayed peak splitting, indicating two sub-populations with differing R_g and R_h. In contrast, SM-102-LNPs presented a single, well-defined peak across both UV and MALS channels (**Figure 4.5**). Notably, SM-102 LNPs showed a consistent MALS signal across incubations, with variations remaining below 10 %. Meanwhile, MC3-LNPs exhibited a marked increase in MALS signal intensity following 24 hours of incubation with BSA.

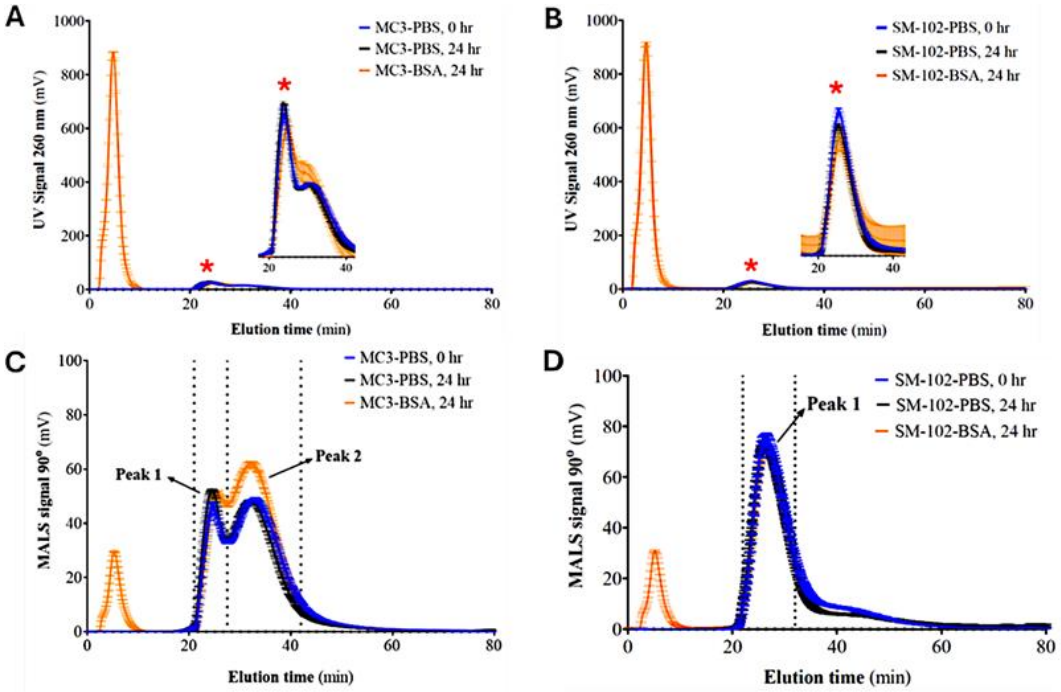

Figure 4.5 FI-AF4-UV-MALS fractograms for (A) MC3-LNPs (control) and MC3-LNPs incubated in 35 mg/mL Bovine Serum Albumin (BSA), (B) SM-102 LNPs, (C) MALS fractograms (90°) plotted for peak 1 and peak 2 for MC3-LNPs and (D) SM-102 LNPs. Time-points indicate 0 hour (control) and 24 hours incubation at 37 °C. Error bars represent ± S.D mean of triplicate injections. The peaks marked with a red asterisk (*) show enlarged peaks.

An increase in both R_g and R_h was observed along the elution profile for both LNP prototypes, with MC3-LNPs displaying a more pronounced increase than SM-102 LNPs, suggesting greater polydispersity in the MC3 formulation (**Figure 4.6A, Figure 4.6B and Supplementary Table S4.2**). The cumulative R_g distributions (RG10, RG50, RG90) are shown in **Figure 4.6C** and **Figure 4.6D**, while corresponding R_h values are presented in **Figure 4.6E** and **Figure 4.6F**.

A significant decrease in RH90 was noted for SM-102-LNPs following 24-hour incubation with BSA, dropping from 34.6 (± 0.4) nm in PBS to 33.3 (± 0.0) nm in the presence of BSA. However, no statistically significant changes were observed in R_g for the same conditions. Specifically, SM-102-BSA at 24 hours exhibited a slightly lower RG90 (26.3 (± 1.2) nm), though the overlapping error bars with SM-102-PBS indicate this difference was not statistically significant (**Figure 4.6D**). In contrast, MC3-LNPs showed subtle variations in cumulative distribution profiles following BSA exposure (**Figure 4.6C**).

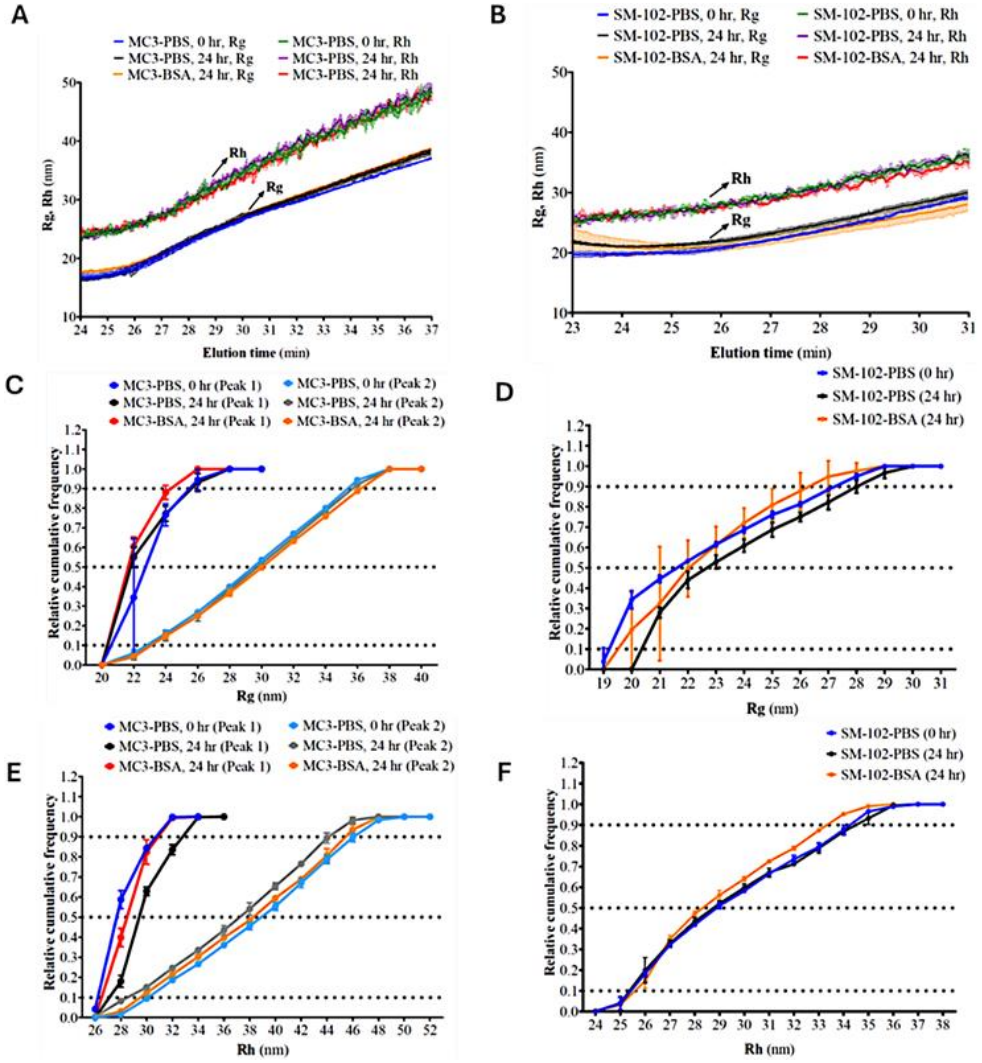

Figure 4.6 Radius of gyration (R_g) and hydrodynamic radius (R_h)obtained by obtained by FI-AF4-MALS-DLS for (A) MC3-LNPs incubated in 35 mg/mL BSA, (B) SM-102 LNPs (C) R_g distribution RG10, RG50, RG90 corresponding to the percentages 10 %, 50 % and 90 % respectively of MC3-LNPs under the reported R_g value, (D) SM-102 LNPs (E) R_h distribution RH10, RH50, RH90 corresponding to the percentages 10 %, 50 % and 90 % respectively under the reported R_h value for MC3-LNPs, (F) SM-102 LNPs. Time-points indicate 0 hour (control) and 24 hours incubation at 37 ºC. Error bars represent ± S.D mean of triplicate injections.

Further analysis of the average R_h and R_g values revealed that, after 24 hours, the second MC3-LNP subpopulation exhibited a significant decrease in R_h (from 39.8 (± 0.0) nm to 38.9 (± 0.2) nm for MC3-PBS and MC3-BSA, respectively), while peak 1 showed a significant increase in R_g (from 17.6 (± 0.4) nm to 19.0 (± 0.2) nm) (**Figure 4.7** and **Supplementary Table S4.2**). For SM-102-LNPs, a significant increase in R_g was observed over time for in PBS (22.9 (± 0.2) nm at 0 hr to 24.1 (± 0.3) nm at 24 hr), followed by a significant decrease upon BSA incubation (from 24.1 (± 0.3) nm to 23.0 (± 1.0) nm) (**Figure 4.7**).

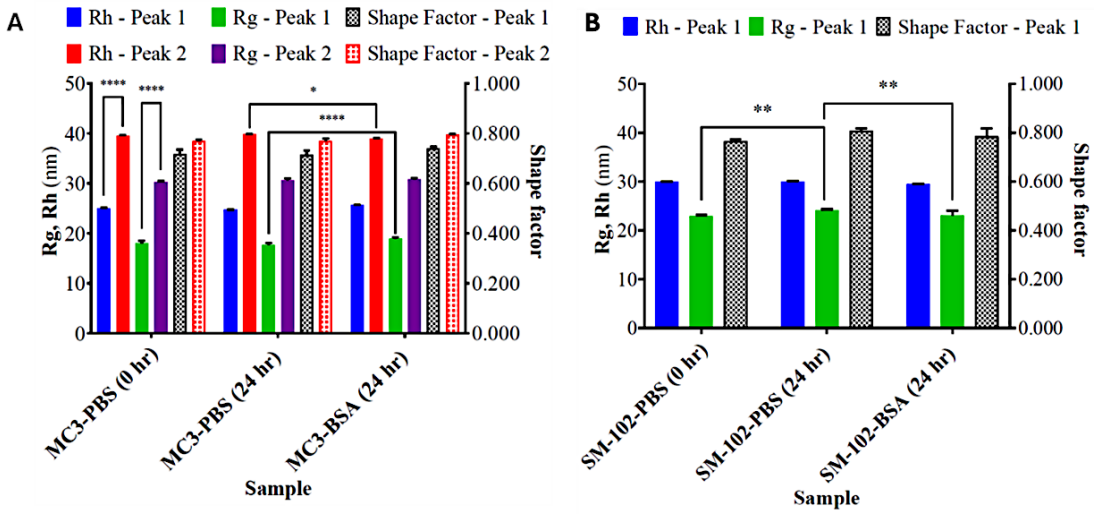

Figure 4.7 Average radius of gyration (R_g), hydrodynamic radius (R_h) and shape factor (R_g/R_h) calculated from peaks integrated in **Figure 4.6A-B**. Plots represent (A) MC3-LNPs incubated in PBS (control) and in 35 mg/mL Bovine Serum Albumin (BSA) (B) SM-102 LNPs. Time-points indicate 0 hour (control) and 24 hours incubation for 24 hours at 37 ºC. Statistical analysis was performed using one-way ANOVA followed by post-hoc Tukey's test. Error bars represent ± S.D mean of triplicate injections, *p < 0.05, **p < 0.01, ***p < 0.001, ****p < 0.0001. Peaks 1-2 are identified in **Figure 4.5**.

4.4.3.2 Quantification of MC3 and SM-102 LNP geometry in response to incubation with BSA

The theoretical shape factor for a perfectly solid sphere is approximately 0.775 [344]. Values exceeding this threshold typically suggest a deviation from ideal sphericity, often due to an asymmetric mass distribution concentrated toward the particle's surface. Following a 24-hour incubation with BSA, MC3-LNPs showed an increase in shape factor upon BSA exposure, particularly in the second sub-peak. Specifically, sub-peak 2 increased from 0.769 (± 0.011) (MC3-PBS) to 0.795 (± 0.004) (MC3-BSA), while sub-peak 1 increased from 0.713 (± 0.018) to 0.741 (± 0.006), respectively (**Figure 4.8A** and **Supplementary Table S4.2**). In contrast, SM-102-LNPs exhibited a slight reduction in shape factor, although the values remained relatively stable across the elution peak, measured at 0.806 (± 0.012) for SM-102-PBS and 0.783 (± 0.034) for SM-102-BSA both incubated at 24-hour. This change was not statistically significant (**Figure 4.8B**).

Cumulative distributions of the shape factor (SF) were also analysed, including SF10, SF50, and SF90 values (**Figure 4.8C** and **Figure 4.8D**). Although statistical tests indicated no significant differences between conditions (**Figure 4.8E** and **Figure 4.8F**), the observed variations are still considered meaningful. Notably, MC3-BSA exhibited higher SF90 values for both peak 1 (0.762 (± 0.007)) and peak 2 (0.804 (± 0.004)) compared to MC3-PBS at 24 hours (0.753 (± 0.006) and 0.780 (± 0.009)), respectively). On the other hand, SM-102-BSA showed a lower SF90 value (0.804 (± 0.045)) relative to SM-102 LNPs alone at 24 hours (0.823 (± 0.012)), suggesting a slight compaction or shape alteration after BSA incubation.

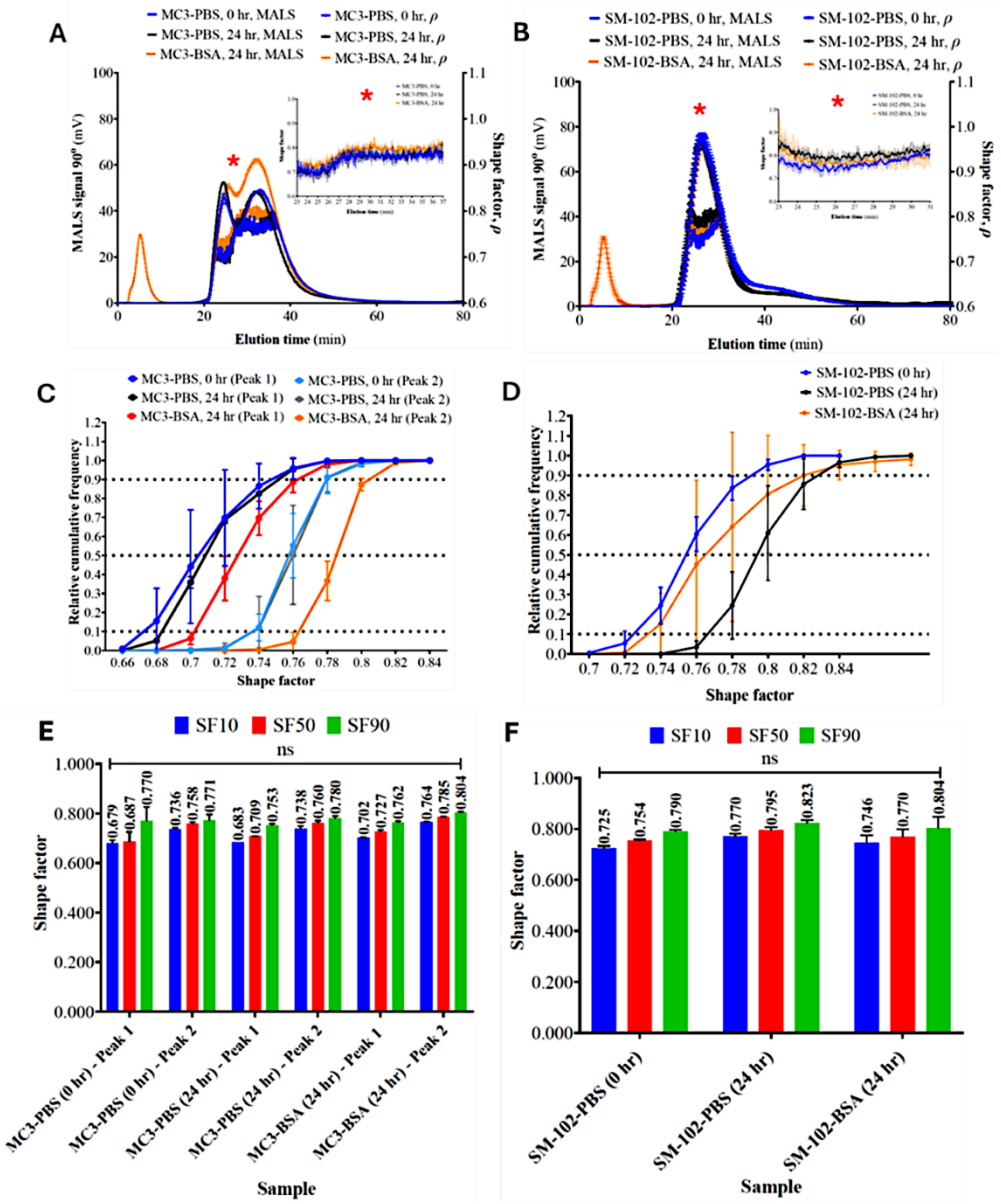

Figure 4.8 Shape factor obtained by FI-AF4-MALS-DLS. Plots represent (A) simultaneous MALS (90°) signal and shape factor for MC3-LNPs incubated in PBS (control) and 35 mg/mL BSA, (B) SM-102 LNPs, (C) shape factor distribution for shape factor (SF) SF10, SF50, SF90 corresponding to the percentages 10 %, 50 % and 90 % of LNPs under the reported shape factor value for MC3-LNPs, (D) SM-102-LNPs, (E) statistical analysis using one-way ANOVA followed by post-hoc Tukey's test comparing SF10, SF50 and SF90 between incubations, (F) SM-102 LNPs. Time-points indicate 0 hour (control) and 24 hours incubation at 37 °C. Error bars which represent ± S.D mean of triplicate injections. The peaks marked with a red asterisk (*) show enlarged shape factor trace. Abbreviation: ns: not significant.

4.5 Discussion

In this chapter orthogonal characterization techniques were used to investigate the surface adsorption of BSA on MC3 and SM-102 LNP prototypes. MC3 lipid constitutes Onpattro® (Alnylam Pharmaceuticals) LNP formulation [234] whereas SM-102 lipid constitutes Comirnaty® LNP formulation [342]. I used low resolution orthogonal technique DLS, followed by a higher resolution technique NTA to measure the surface-adsorption of BSA. This was followed by developing a FI-AF4 multidetector methodology for measuring corona formation using BSA as a model system. BSA has the advantages of high availability and low cost. Further, it has ~76 % similarity in structure and amino acid sequence to human serum albumin (HSA) [345]. The approach enabled the comprehensive analysis of subpopulations in the LNP-BSA heterogenous mixture of LNP-protein corona and unbound BSA unit. In addition to size effects, changes in LNP morphology, PDI and zeta potential were also measured. The analysis of the LNP-BSA protein-corona was carried out *in situ* with no prior separation (e.g. separation of free unbound BSA using centrifugation resuspension technique) [337]. Although this technique can be suitable for separating BSA from the protein corona due to the difference in densities of the BSA and the LNP prototypes being investigated, the centrifugation process may alter nanoparticle parameters such as particle size, zeta potential and disrupt the loosely-associated soft corona [170]. Further, the presence of the soft and hard corona and unbound protein adds further complexity to method development for resolving nanoparticle-protein complexes from biological media. Hence, in this chapter I explored the use of FI-AF4 as a gentle separation technique for isolating unbound proteins from LNP-protein complexes for in-line analysis.

The physicochemical parameters of the protein corona were not significantly different from the LNP. At a fundamental level, having BSA adsorbed on both sides of the LNP would increase the nanoparticle diameter by ~ 18 nm (one BSA particle binding to each side of the LNP) but this was not the case for DLS, NTA and FI-AF4 measurements. In addition, it is expected that an abundance of BSA on the LNP surface would alter the zeta potential which more closely resemble BSA zeta potential (~15 mV), but the zeta potential of the LNP-corona resembles the same zeta potential as that of the pristine LNP (~ -6.5 mV). LNPs incubated with BSA resulted in a high PDI value (>0.2) with a multi-modal distribution (peaks corresponding to BSA, LNP-BSA and aggregates). Due to the polydispersity of the analytes arising from the presence of multiple species (BSA, LNP, and LNP-BSA complexes) I demonstrated that the use of DLS for analysis of the LNP-BSA protein corona is not appropriate. The analysis of corona formation in more complex mixtures such as serum

becomes significantly more challenging due to the presence of proteins with different molecular weights.

Next, NTA was used to analyse LNP size following manufacture and its complexation with BSA under physiologically-relevant temperature. It is expected that the bulk BSA in the incubation media will not be detected by NTA (NTA lower detection limit is ~30 nm) [346] while the LNP and LNP-BSA complexes can be measured. Moreover, an additional advantage of using NTA as an orthogonal technique is measuring particle concentration, which can be used to track relative changes in particle sub-populations and can indicate aggregation or precipitation of LNPs in the presence of BSA [195]. The main limitation of NTA is that the LNP formulation is introduced into narrow manifolds in the flow cell in the presence of buffer under flow, which may disrupt the LNP-BSA corona. Batch-mode DLS and NTA detect the size of LNP heterogenous mixtures but results show that these two methods overestimate the size of large aggregate subpopulations as shown in the particle distributions for both LNP prototypes (**Figure 4.2** and **Figure 4.3).** In the case of polydisperse samples, the scattered light from the relatively large particles will dominate and records a large average hydrodynamic diameter. Hence, these techniques would be best suited for monodisperse samples. In practice, LNP formulations are polydisperse (PDI >0.2) with heterogeneity increasing in the presence of proteins [170].

LNP-BSA adsorption can also be explained by electrostatic forces. At pH 7.4 both BSA and LNPs carry a negative surface charge, leading to electrostatic repulsion between BSA and LNP, minimising BSA adsorption onto LNPs. However, the colloidal stability could be determined by the decrease span value observed using NTA. The incubation of LNP with BSA increased electrostatic repulsion between particles which in turn caused a narrow particle distribution; the monodispersity is BSA-induced. Wang *et al.* explained the incubation of BSA with solid lipid nanoparticles (SLNs) at pH 7.4 resulted in no drastic changes of surface properties even though BSA led to system aggregation; this is attributed to the balance in repulsive and attractive forces [347].

The shape factor, which reflects deviations from a spherical structure, proved especially informative in evaluating BSA binding [218, 273], as it helps distinguish whether the LNP retains a spherical form or exhibits mass redistribution toward its periphery. Under the assumption that protein adsorption mainly occurs on the surface, a greater increase in R_g compared to R_h would elevate the shape factor. This is based on the premise that BSA is denser than the overall LNP structure. For MC3-LNPs, both sub-peaks 1 and 2 showed increased shape factors after BSA binding, suggesting that protein association leads to a more spherical

morphology. In contrast, SM-102-LNPs displayed a reduced shape factor following BSA exposure, indicating internal reorganization and a denser core structure. This structural reconfiguration is also supported by marked shifts in mean radii and significant differences in the 90th percentile values of both R_g and R_h post-BSA adsorption. The cumulative distribution curves for R_g further highlight these differences between MC3 and SM-102-LNP formulations. The variations in shape factor values between MC3-BSA and SM-102-BSA are likely due to differences in the ionizable lipid structures: SM-102 lipid features a branched tail with extended aliphatic groups resembling multi-tail lipids, while MC3 lipid comprises unsaturated linear chains. These structural disparities lead to distinct molecular packing, cylindrical for MC3 and cone-shaped for SM-102 lipid, which in turn, influence surface chemistry and affect how the LNPs interact with BSA.

Fundamentally, following adsorption of opsonins on the LNP surface, they facilitate phagocytosis by the mononuclear phagocyte system (MPS) through hydrophobic interactions. PEG increases surface hydrophilicity and forms protrusions on the nanoparticle surface which is a critical role in hindering interactions between nanoparticles and opsonins [348]. This explains why the surface properties of LNPs were not significantly altered following the formation of LNP protein-corona [349]. Hence it can be hypothesized that the hydrophilic layer formed around the LNP surface caused a physical barrier to prevent protein adsorption to LNP surface as reported by previous studies [347, 350, 351]. Pioneering studies on pegylated nanoparticles led to the development of the first pegylated nano formulation Doxil® in the form of pegylated liposome [1]. This shows the importance of PEG as a key constituent in LNP formulations. Previous research has also shown that PEG detachment, or 'PEG-shedding' occurs after intravenous (IV) administration, facilitating fusion between LNPs and endosomal membranes to enable cargo release [348]. Additionally, PEG-shedding has been observed in response to anti-PEG immunoglobulin M (IgM) induction, providing a mechanism to modulate LNP interactions with cellular targets [352].

Proteins can experience conformational alterations when interacting with nanoparticles [353]. Their secondary structures, such as alpha-helices and beta-sheets, are stabilized by non-covalent interactions but may partially unfold when adsorbed onto LNP surfaces [354]. This structural disruption is influenced by surface characteristics of the nanoparticles, including hydrophilicity and surface charge. For instance, BSA may undergo unfolding, revealing its hydrophobic regions and regions of opposing charge upon contact with LNPs [355]. Therefore, it cannot be assumed that BSA retains its native folded state after adsorption, as unfolding could contribute to increase in both R_g and R_h of the protein corona.

Limitations and next steps

In this study, FI-AF4 was employed to characterize MC3 and SM-102 LNPs in the presence of BSA, serving as a method to isolate LNPs from physiologically-relevant environments. This approach provides valuable insights into how LNPs interact with biological matrices and supports future advancements in RNA-based drug delivery platforms. Although a single protein (BSA) was used as the model protein and only two LNP prototypes were examined (MC3-LNPs and SM-102 LNPs), the adaptability of AF4 makes it a suitable technique for analysing a broad range of LNP formulations and biomolecular interactions while maintaining sample integrity. The application of high-resolution and robust analytical methods in nanomedicine characterization sets the stage for evaluating emerging LNP components (e.g. lipids) and manufacturing technologies.

Furthermore, this study did not investigate potential changes in LNP internal lipid structure following protein adsorption. Future work should consider extending this approach to SM-102-based LNPs, given that SM-102 is a clinically relevant ionisable lipid used in Moderna mRNA vaccine (Spikevax) [14] and is characterised by an cone-shaped geometry lipid that facilitates endosomal membrane disruption [356]. In particular, coupling small-angle X-ray scattering (SAXS) with FI-AF4 would enable detailed investigation of lipid organisation and structural changes upon protein binding. SAXS is a powerful technique for characterising particle morphology and internal structure through analysis of X-ray scattering patterns, and its integration with separation methods offers significant potential for resolving structural heterogeneity [357]. At present, there remains a gap in understanding how LNP internal structure changes upon interaction with biological environments *in vivo*. Such morphological changes could be further validated through complementary techniques such as cryo-TEM, enabling direct visualisation of structural features and facilitating correlation with SAXS-derived results.

Chapter 5: The Use of Frit-Inlet and Conventional Asymmetric Flow Field-Flow Fractionation Modalities for the Separation, Isolation and Downstream Analyses of SM-102-LNP Prototype and High-Density Lipoprotein Biomolecular Corona

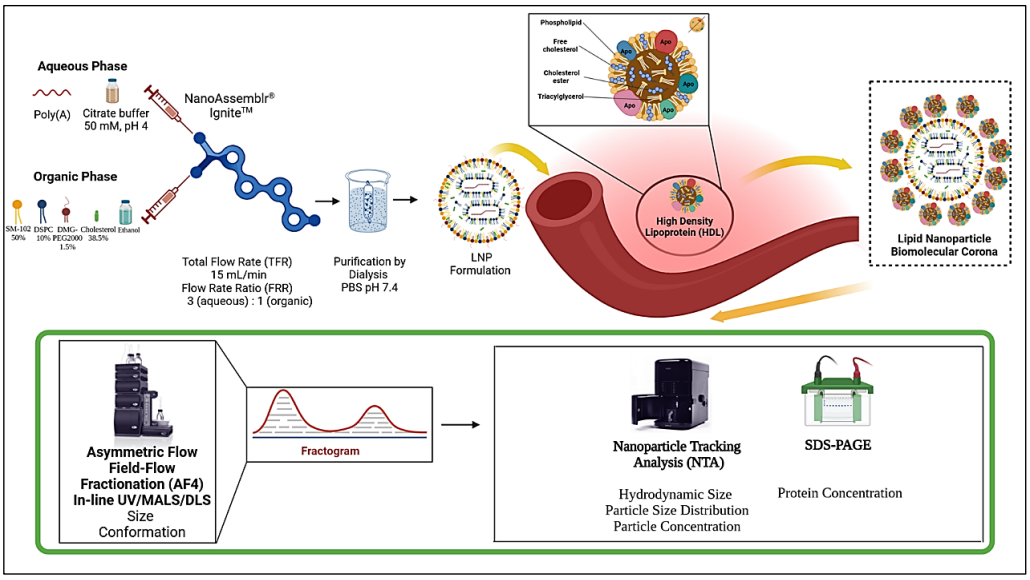

Abdulrahman R, author of this thesis, performed all the experimental work (except negative stain TEM) and completed all data analysis presented in this chapter.

5.1 Introduction

LNPs represent the leading nanocarrier platform for mRNA delivery. LNP formulations typically consist of ionizable cationic lipids, phospholipids, PEGylated lipid, and cholesterol by composition. The clinical success of the SARS-CoV-2 immunization programmes adopting the use of LNPs has propelled their application in the clinical domain. The focus of effort in LNP-based research to-date has largely been on the design and optimisation of novel lipid chemistries [358, 359] and refining the scalability of microfluidics-based manufacture [360]. In contrast, challenges such as poor *in vitro-in vivo* correlation in transfection efficiency and biodistribution has received comparatively less attention.

Despite their clinical impact, the broader application of LNPs in other therapeutic areas has been constrained by their predominant hepatic biodistribution. Following systemic administration, LNPs interact with apolipoproteins, which facilitates binding to Low-Density Lipoprotein Receptors (LDLR) [156, 160]. The liver exhibits high expression levels of LDLR, which facilitates the preferential accumulation of LNPs in hepatocytes [361]. While this preferential accumulation is beneficial for liver-targeted LNP therapies, it poses a major challenge for extrahepatic delivery, where off-target hepatic accumulation can compromise therapeutic efficacy and increase systemic toxicity.

Liver tropism has been demonstrated with Onpattro® (patisiran), the first FDA-approved siRNA LNP therapeutic. Preclinical studies reported that approximately 90 % of radiolabelled patisiran localised to the liver within 4 hours following intravenous (IV) administration in rats. Surface-adsorption of the patisiran LNPs with apolipoprotein E (ApoE) further enhanced LDLR mediated uptake, significantly restricting LNP distribution to extrahepatic tissues [16]. While this feature is beneficial for treating transthyretin-mediated (TTR) amyloidosis, since the liver is the primary site of TTR protein production, it presents a major limitation for therapies targeting non-hepatic tissues. Similarly, biodistribution studies of COVID-19 mRNA vaccines have shown that up to 21.5 % of the administered dose accumulates in the liver following intramuscular injection [12, 13].

One of the key contributors to this hepatic targeting is High-Density Lipoprotein (HDL), which readily adsorbs onto the surface of LNPs, potentially altering their physicochemical properties. HDL is an endogenous, water-soluble nanoparticle produced by the liver and intestines. Its spherical structure comprises a hydrophobic core of cholesterol esters and triglycerides, surrounded by a hydrophilic surface membrane containing apolipoproteins, free cholesterol and phospholipids [171, 362] (**Figure 5.1** and **Supplementary Table S5.1**).

Proteomic analyses revealed that apolipoproteins are highly abundant in the biomolecular corona of lipid-based nanoparticles, with Apo-AI being the most prominent, followed by Apo-CII and Apo-E [137]. Apo-E3 and Apo-AI bind with the highest affinity to LNPs, independent of their overall serum protein abundance [363]. Apo-AI and Apo-AII account for approximately 60-70 % and 20 %, respectively of the total protein content in HDL [364]. Notably, proteomics data suggest that LNPs preferably adsorb HDL-associated proteins, which is not reflective of plasma HDL abundance [224]. HDL, when enriched with Apo-AII and Apo-M, demonstrates a potent effect on LNP function. The modulation of the LNP-biomolecular corona offers a promising route to enhance their biodistribution. As the corona's composition critically shapes nanoparticle interactions with biological systems [150], strategies aimed at controlling or engineering this layer may enable more favourable pharmacokinetics and improved delivery to target tissues [365].

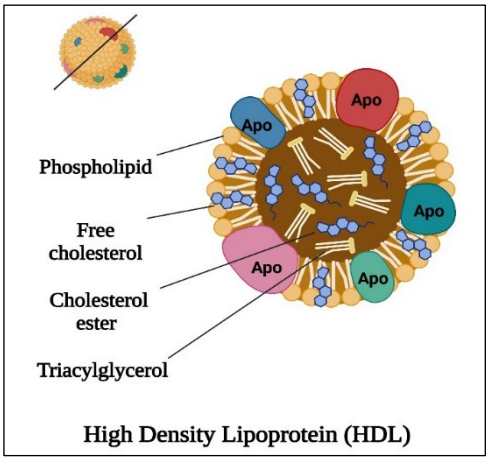

Figure 5.1 Structure of High-Density Lipoprotein (HDL). This core is surrounded by apolipoproteins (Apo) mostly Apo-AI and Apo-AII. Created with Biorender.com.

Isolation of the LNP-biomolecular corona remains technically challenging due to the compositional overlap between corona-associated biomolecules and free biomolecules. Conventional methods such as centrifugation or size-exclusion chromatography (SEC) often lack the resolution to separate intact LNP-biomolecular corona complexes at sufficient resolving power and may induce artefacts through mechanical stress which can change the attributes of the corona and promote LNP aggregation. Consequently, the isolated corona may not accurately represent the native corona present in biological fluids, and biomolecular corona characterisation can be affected by methodological artefacts. Magnetic separation of the biomolecular corona is also feasible, but its use is limited to magnetic LNPs, such as iron-oxide-loaded LNP formulations [169]. Asymmetric flow field-flow fractionation (AF4) offers

a promising solution, providing gentle, high-resolution separation of nanoparticles *in situ*. Unlike traditional chromatographic methods, AF4 operates without a stationary phase, thereby minimizing sample interaction with column materials and reducing shear-induced degradation. This makes AF4 particularly suitable for fragile or aggregation-prone biomolecules.

Two main modalities of AF4 are commonly employed, conventional AF4 (hereafter referred as AF4) and frit-inlet AF4 (FI-AF4). AF4 was first was introduced in the 1980s by Giddings and Wahlund [366] followed by the later introduction of FI-AF4 [367]. The FI modality is integrated into AF4 platforms with the main aim of mitigating the focusing step and improving the resolution for sensitive samples [367, 368]. Conventional AF4 requires a focusing step, in which a dedicated focus flow is applied to concentrate the sample at the head of the channel and establish a steady-state distribution. However, this focusing period can promote sample loss through interactions with the accumulation wall membrane or induce particle agglomeration [369, 370]. FI-AF4 eliminates the need for a focus flow. Instead, the sample undergoes hydrodynamic relaxation as it enters the channel through the porous frit [209]. Sample localisation is achieved by two opposing flows (downstream channel flow and perpendicular cross-flow, without the use of a focusing step). This reduces the direct exposure of particles to the membrane, minimising sample loss and aggregation [113, 177, 209, 228]. A further advantage of using FI-AF4 is the ability to use a higher injection mass while minimising the overloading effect [368]. Conventional AF4 may prevent the complete relaxation of the samples into to channel due to the focusing step resulting in an overloading effect [299]. FI-AF4-DLS has also been shown to provide enhanced resolution for the characterisation of dextran nanoparticles [228]. Comparable elution profiles have been reported between AF4 and FI-AF4 for the separation of nAg-extracellular polymeric substances (EPS) [274] and improved recovery of LNPs using FI-AF4-MALS [209]. However, Fuentes *et al*. showed poor sub-population resolution with FI-AF4 compared to AF4 [368]. Importantly, FI-AF4 is not widely and commercially available in laboratories. The preferred approach therefore depends on both the analytical priorities (aggregation, sample-membrane interaction, resolution and recovery) and on modality availability. Establishing whether both modalities produce consistent results therefore offers important evidence on their interchangeability for characterising the LNP-biomolecular corona.

Our previous study has demonstrated changes in SM-102 LNP formulation attributes upon interaction with Bovine Serum Albumin (BSA) using FI-AF4. This chapter investigates how the surface adsorption of HDL onto LNP surfaces influences the physicochemical attributes

of LNPs. HDL was selected as a physiologically relevant lipoprotein because previous findings showed that only HDL-augmented coronas enhanced cellular responses to LNP exposure [224]. This chapter tests the hypothesis that HDL binding alters key nanoparticle parameters such as size, shape, and surface characteristics. The use of two AF4 modalities, AF4 and FI-AF4 for simultaneous separation and in-depth characterisation whilst maintaining LNP and corona integrity is a method which, to our knowledge has not been used until today for and the analysis of the LNP biomolecular corona.

Given that very few studies have considered the interactions between lipoproteins and LNPs, in this chapter, AF4 was employed to isolate LNP-HDL complexes from unbound LNPs, free HDL particles, and other formulation components (e.g., free mRNA, dissociated HDL). Fractions were collected across the AF4 elution profile for downstream analysis, with particular attention to those corresponding to LNP-HDL complexes. By examining these changes in both binary systems (BSA protein) and more complex biological media (HDL), this work aims to provide fundamental insights into how LNPs behave in biological environments. Understanding these physicochemical transformations is critical, as they can significantly impact the *in vivo* fate of LNPs. These findings can, in turn, inform the rational design and engineering of LNP formulations to enhance their stability, targeting specificity, and overall delivery efficiency.

5.2 Aim and Objectives

This chapter aims to evaluate the use of AF4 and FI-AF4 as high-resolution separation techniques for isolating LNP-HDL complexes, followed by their subsequent downstream analysis. To achieve this, the objectives of this study were to **(1)** encapsulate Poly(A) mRNA into ionizable SM-102-LNPs **(2)** incubate SM-102-LNPs with HDL at 37 °C for 24 hours to form SM-102-LNP-HDL corona, **(3)** develop methods for two AF4 modalities for size-based separation and characterisation of the LNP-HDL corona from free LNPs and native HDL and **(4)** confirm the presence of HDL-associated LNPs following AF4 fraction collection using sodium dodecyl sulfate–polyacrylamide gel electrophoresis (SDS-PAGE) with silver staining, zeta potential measurements, and negative-stain transmission electron microscopy (TEM).

5.3 Materials and Methods

5.3.1 Materials and Reagents

Polyadenylic acid (Poly(A)), cholesterol, sodium citrate dihydrate, ethanol, and dialysis tubing cellulose membrane (14 kDa MWCO) and high-density lipoprotein (HDL, LP3) were purchased from Sigma-Aldrich (St. Louis, MO, USA). Helper lipids 1,2-distearoyl-sn-glycero-3-phosphocholine (DSPC), 1,2-dimyristoyl-rac-glycero-3-methoxypolyethylene glycol-2000 (DMG-PEG 2000) were purchased from Avanti Polar Lipids (Alabaster, AL, USA). The ionizable lipid 8-[(2-hydroxyethyl)[6-oxo-6-(undecyloxy)hexyl]amino]-octanoic acid, 9-Heptadecanyl 8-((2-hydroxyethyl)[6-oxo-6-(undecyloxy)hexyl]amino) octanoate (SM-102) were purchased from BroadPharm (San Diego, CA, USA). Invitrogen™ UltraPure™ DNase/RNase-free water and phosphate-buffered saline (PBS) 10X salt solution pH 7.4 was acquired from Fisher Scientific (Loughborough, UK).

5.3.2 Methods

5.3.2.1 Manufacture of Lipid Nanoparticles

LNPs were formulated using the NanoAssemblr® Ignite Precision NanoSystems (Vancouver, BC, Canada) using the NxGen microfluidic cartridge. Lipid stocks were prepared in ethanol at molar ratios 50:38.5:10:1.5 for SM-102: Cholesterol: DSPC: DMG-PEG 2000, which is based on the lipid compositions of Onpattro® and Comirnaty® [177]. The aqueous phase consisted of initial Poly(A) stock at 1.5 mg/mL dissolved in 50 mM citrate buffer (pH 4.0). The N:P ratio was (N for lipid nitrogen and P for nucleic acid phosphate) was 6:1. The Total Flow Rate (TFR) was set at 15 mL/min, and an aqueous-to-organic Flow Rate Ratio (FRR) of 3:1 was used with a final lipid concentration of 1.25 mg/mL and Poly(A) of 0.055 mg/mL. The resultant suspension was dialysed at 4 ºC (MWCO 14 kDa, Sigma-Aldrich, St. Louis, MO, USA) into 10 mM PBS (pH 7.4) (500X dialysate ratio) to remove ethanol and citrate buffer. LNP formulations were filtered through a 0.2 µm pore-sized Supor® membrane (Pall Corporation, USA) and stored at 4 ºC until further use.

5.3.2.2 Sample preparation

LNP formulation was incubated with HDL to form LNP-HDL mixture. LNP was incubated at a 1:1 (volumetric ratio) with HDL (0.4 mg/mL in PBS, representing physiologically-relevant HDL levels) for 24 hours at 37 ºC under static conditions. The control sample included an equal volume of PBS and LNP formulation.

5.3.2.3 LNP formulation particle size characterisation

Particle size and PDI were determined using a Zetasizer Nano ZS (Malvern Panalytical, Malvern, Worcestershire, UK) for pristine LNPs and HDL at 0-hours (control) and control (LNP-PBS and HDL-PBS) at 24 hours. LNP and HDL samples were diluted prior to measurement at 1:10 and 1:8 respectively in PBS (pH 7.4). The refractive index and viscosity of the buffer (PBS) were set at 25 °C, 1.34 and 1.02 cP, respectively. DLS measurements were performed at a measurement temperature of 25 °C, and material RI and absorbance were set at 1.45 and 0.001, respectively. Zeta potential was measured by electrophoretic light scattering (ELS) of LNP-PBS and HDL-PBS using the Smoluchowski approximation. Pre-AF4 samples were performed at a dilution of 1:10 in DNA/RNA free water. The RI and viscosity of the medium (water) were set at 1.33 cP and 0.89 cP, respectively. Fractions collected using AF4 were not diluted prior to zeta potential measurements. ELS was performed at 25 °C, and material RI and absorbance were set at 1.45 and 0.001, respectively.

Particle concentration and size distribution of samples were measured by nanoparticle tracking analysis (NTA, NS300, Malvern Panalytical, Worcestershire, UK), equipped with a 488 nm laser and a sCMOS camera. *In situ* analysis of SM-102 LNP-PBS at 0 hr and 24 hr pre-AF4 and post-AF4 was performed, studying changes in LNP size in response to AF4 fractionation and sample dilution. LNP samples were diluted in PBS (pH 7.4), with the syringe driver set at 100 AU. All measurements were performed at ambient temperature with five successive videos of 60 second duration captured. All samples were measured at camera level of 10 and detection threshold of 5. Particle dilutions are in **Supplementary Table S5.2**. The percent difference formula was used to determine the change in concentration between the pre-AF4 sample and the corresponding post-AF4 fraction.

$$\textbf{Concentration difference}\ (\%) = \frac{(\textbf{Pre} - \textbf{AF4}) - (\textbf{Post} - \textbf{AF4})}{[(\textbf{Pre} - \textbf{AF4}) + (\textbf{Post} - \textbf{AF4})] \div \textbf{2}} \textbf{ x 100}$$

Equation 5.1

where pre-AF4 is the concentration of LNP-PBS sample (particles/mL) before Asymmetric Flow Field-Flow Fractionation (AF4) and post-AF4 is the concentration of LNP-PBS sample (particles/mL) after AF4.

5.3.2.4 Quantification of Encapsulation Efficiency (EE)

mRNA encapsulation in LNPs was quantified using the Quant-iT™ RiboGreen RNA Assay (Invitrogen™, Thermo Fisher Scientific, UK) as per manufacturer's instructions. LNPs were serially diluted in Tris and Ethylenediaminetetraacetic acid (TE buffer) in the presence and

absence 2 % *v/v* Triton X-100. The plate was incubated at 37 °C for 15 minutes, followed by the addition of two dilutions of 1× Ribogreen Reagent (500- and 200-fold) to wells containing TE buffer and Triton X-100, respectively. Fluorescence was measured using a GloMax® Microplate Reader (Promega Corporation, UK) with an excitation of 475 nm and emission 500-550 nm wavelength. Encapsulation Efficiency (EE) was calculated using the following equation:

$$\mathbf{EE}\ (\%) = \frac{\mathbf{Poly(A)_{total} - Poly(A)_{free}}}{\mathbf{PolyA_{total}}} \mathbf{x\ 100} \qquad \textbf{Equation 5.2}$$

where $Poly(A)_{total}$ is the total Poly(A) concentration (µg/mL) in wells containing Triton-TE buffer, $Poly(A)_{free}$ the concentration (µg/mL) of the unentrapped Poly(A) for wells containing TE buffer.

5.3.2.5 Asymmetric Flow Field-Flow Fractionation (AF4)

Samples were analysed by AF4-UV-MALS-DLS using Postnova Analytics AF2000 asymmetric Flow Field-Flow Fractionation (AF4) (Landsberg, Germany). The system was configured with tip and pressure pumps, a degasser, and autosampler. Online UV–Vis (PN3242, 260 nm- Postnova Analytics) operated at wavelength of 260 nm and a 21-angle Multi-angle Light Scattering (MALS-PN3621, Postnova Analytics), and online Zetasizer Nano ZS (Malvern Panalytical, Malvern, UK) detectors were integrated into the system. Online DLS measurements were acquired using a Malvern quartz flow cell (ZEN0023), at a flow rate of 0.2 mL/min at 25 °C at three-second intervals. The measurement position was set at 4.2 mm with the attenuator set at 11.

The conventional AF4 channel (Postnova Analytics) was equipped with a rectangular shape (300 × 60 × 40 mm). The frit inlet (FI) AF4 channel (Postnova Analytics) was also rectangular with the same shape and dimensions as the conventional AF4 channel. The FI of the channel was 3.2 mm at the inlet end of the channel. The spacer had a nominal thickness of 350 µm with a sample inlet canal of 4.0 mm × 1 mm between the frit and sample flow.

The membrane used for both channels was a 10 kDa MWCO size amphiphilic regenerated cellulose (RC) membrane, with a 100 µL injection loop size and a 20 µL sample injection volume. PBS (10 mM, pH 7.4) was used as the carrier liquid. **Table 5.1** shows the corresponding detector flow (DF), and cross-flow (XF) settings for each channel.

Mass recovery for the LNP and LNP-HDL complex at 0 and 24 hr were determined using the below equation (UV signal at 260 nm):

$$\mathbf{R}\ (\%) = \frac{\mathbf{A_c}}{\mathbf{A}}\ \mathbf{x\ 100} \qquad \textbf{Equation 5.3}$$

Where A_c is the area under the peak of nanoparticles under a cross-flow, and A is the area under the peak of the unfractionated sample without an applied cross-flow *via* direct sample injection.

Corresponding shape factor was calculated using the following equation:

$$\boldsymbol{\rho} = \frac{\mathbf{R_g}}{\mathbf{R_h}} \qquad \textbf{Equation 5.4}$$

where ρ is the shape factor, R_g represents the radius of gyration (nm) obtained from MALS detector and R_h represents the hydrodynamic radius (nm) obtained from DLS detector.

NovaAnalysis Software was used to simulate the AF4 methods (AF4 and FI-AF4). The simulated methods also included the expected size of the different population according to the distinct particle populations obtained using batch-mode DLS. The AF4 method was simulated for the LNP-HDL sample which included unbound HDL particles, the LNP-HDL corona and relatively larger aggregated particles (**Supplementary Figure S5.1** and **Supplementary Table S5.4**).

In this study, conventional AF4 is referred to as AF4 and frit-inlet AF4 is referred as FI-AF4. LNP batches were synthesised for the use for conventional AF4 (batches 1 and 2) and FI-AF4 (batches 3 and 4). Method development of FI-AF4 to AF4 for SM-102 LNP-control is presented in **Supplementary Figure S5.2**.

Table 5.1 Corresponding Asymmetric Flow Field Flow Fractionation (AF4) and Frit-Inlet (FI-AF4) parameters.

Modality	**Focus Step**	**Elution Step**				**Detector flow (mL/min)**	**Injection volume (µL)**
	Time (min)	**Time (min)**	**Cross Flow (mL/min)**	**Type**	**Exponent**		
FI-AF4	-	20	1.0	Constant	0	0.2	30
		60	1.0	Power	0.2		
		10	0	Constant	0		
AF4	5	2	1.0	Constant	0		
		60	1.0	Power	0.2		
		10	0	Constant	0		

5.3.2.6 Sodium Dodecyl Sulfate-Polyacrylamide Gel Electrophoresis (SDS PAGE)-Silver Staining

SDS-PAGE was used to determine the presence and molecular weight of HDL following AF4 fractionation. AF4 fractions were concentrated using 1000 kDa spin columns and centrifuged at 1,000 x g for 1 minute. The recovered AF4 samples were mixed in equal volume with the sample buffer (consisting of 2X Laemmli and β-mercaptoethanol) (Bio-Rad Laboratories, UK) and heated at 95 ºC for 5 min. Samples were loaded (10 µL) onto separate well of a 4-20 % SDS-polyacrylamide Mini-PROTEAN® TGX™ Precast Gels (Bio-Rad Laboratories, UK). The electrophoretic run was run at 260 V in the running buffer (1X) 25 mM Tris, 192 mM Glycine and 0.1 % SDS (pH 8.3). A protein molecular weight marker (Precision Plus Protein™ Kaleidoscope™ protein standard, Bio-Rad Laboratories, UK) was also run on the gels. The protein bands were subsequently detected using the Pierce Silver Stain Kit (Thermo Fisher Scientific, UK) as per manufacturer instructions. All gels were imaged using the Bio-Rad Gel Doc EZ Imager and processed using Bio-RaD Gel Doc EZ imaging system.

5.3.2.7 Negative-stain transmission electron microscopy (TEM)

TEM with negative staining was used to image the morphology of SM-102 LNPs and their biomolecular corona, in tandem with the FI-AF4/AF4 shape factor ratio. Copper grids with carbon film 400 were used (Agar Scientific, AGS160-4) and glow-discharged prior to sample application. A volume of 10 µL of LNP suspension was applied to the grid and incubated for 15 min. Excess sample was removed by filter paper adsorption, and the grid was rinsed once with dH_2O, followed by a 5 min fixation with 2 % glutaraldehyde. Samples were then washed three times with dH_2O (30 s per wash) and 2 % uranyl acetate applied for 5 min. Excess dye was removed by blotting using filter paper, and the grids were left to dry at ambient temperature for 15 min. Samples were imaged using a JEM transmission electron microscope operated at 120 kV, at 15,000x and 60,000x magnification. ImageJ software (v.1.8.0) was used to analyse the size of SM-102 LNPs and their biomolecular corona.

5.3.2.8 Estimation of LNP surface saturation with HDL

The maximum number of HDL particles forming the corona layer around a single LNP assuming a close packed protein arrangement forming an HDL monolayer is given by the following expression:

$$\mathbf{N_{HDL} = 0.65\ x\ \left(\frac{(R_{tot}{}^3) - (R_{LNP}{}^3)}{(R_{BSA}{}^3)}\right)} \qquad \textbf{Equation 5.5 [339]}$$

where R_{LNP} is the radius of LNP, R_{HDL} is the radius of HDL, $R_{tot} = R_{LNP} + (2\ X\ R_{HDL})$. The filling factor of 0.65 is used for HDL.

It was assumed that (1) each LNP is fully surface covered with HDL (2) both HDL and LNP have a spherical geometry with a filling factor of 0.65 [340].

5.3.2.9 Estimation of the LNP-HDL corona thickness

The particle diameter of the LNP bound with a close packed single monolayer of HDL is given the following equation:

$$\mathbf{D_{LNP-HDL} = D_{LNP} + (2\ x\ D_{HDL})} \qquad \textbf{Equation 5.6}$$

where $D_{LNP\text{-}HDL}$ is the diameter LNP-HDL corona, D_{LNP} is the diameter of LNP and D_{HDL} is the diameter of HDL.

5.3.2.10 Statistical analysis

Statistical analysis was performed with one-way ANOVA followed by Tukey's multiple comparisons for post-hoc analysis for normally distributed data, and the Kruskal–Wallis test followed by Dunn's multiple comparisons test for non-normally distributed data. Statistical significance was considered at $p < 0.05$; *$p < 0.05$, **$p < 0.01$, ***$p < 0.001$, ****$p < 0.0001$. All data were analyzed using GraphPad Prism 10 (GraphPad Software Inc). Cumulative frequency distribution plots for RG (radius of gyration), RH (hydrodynamic radius) and SF (shape factor) were plotted using cumulative distribution function on GraphPad Prism 10. The percentile values 10 %, 50 % and 90 % of the distributions were calculated using the TREND function on Microsoft Excel.

5.4 Results

5.4.1 Baseline analysis of SM-102 LNP formulations and HDL

SM-102 LNPs (composed of SM-102: Cholesterol: DSPC: DMG-PEG 2000 at % molar ratios 50:38.5:10:1.5 respectively) were prepared by toroidal mixing. Batch-mode DLS and ELS were used to profile their size and charge parameters for four independent batches. Similarly, HDL size and charge was profiled to gain an understanding of the impact of co-incubation with LNP and storage at physiologically-relevant temperature (37 °C) for 24 hours to form the SM-102-LNP-HDL biomolecular corona. It is important to note that the concentration of 0.4 mg/mL of HDL reflects the total concentration of HDL in human plasma and was calculated to have excess HDL in the LNP-HDL mixture (Section 5.4.6). This ensures the ability reach the Limit of Detection (LOD) when using AF4 and FI-AF4.

All measured SM-102 batches had a *Z*-average of 60-64 nm and a PDI of < 0.1 (**Table 5.2**). The encapsulation efficiency of LNPs was measured at > 85 %, which indicates a 15 % presence of free mRNA in the LNP solution (**Table 5.2**). All SM-102-LNPs formulated were negatively charged in formulation buffer (pH 7.4) (-5 to -6 mV) potentially due to the presence of negatively charged Poly(A) molecules.

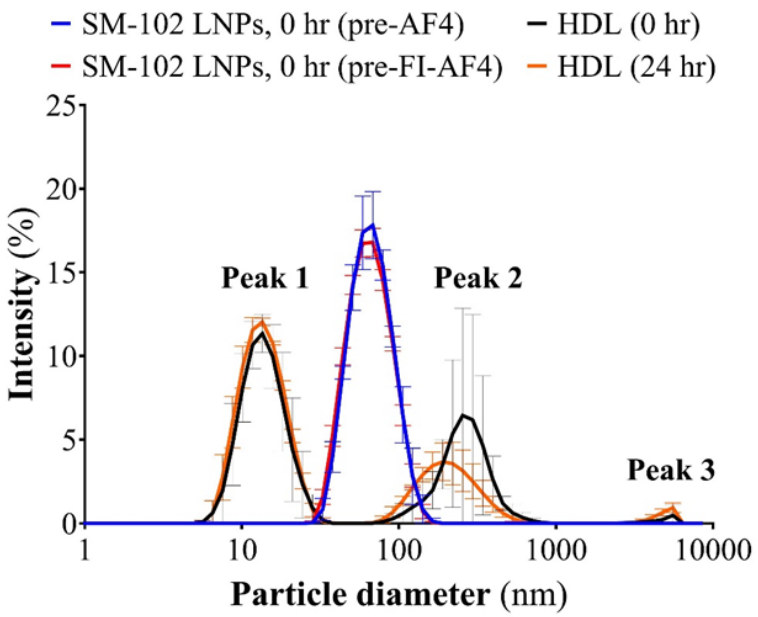

Figure 5.2 Dynamic Light Scattering (DLS) intensity-based size distribution. Analysis of SM-102 LNPs (control) and High-Density Lipoprotein (HDL) (0.4 mg/mL) (control) particle size distribution prior to Asymmetric Flow Field-Flow Fractionation (AF4) and Frit-Inlet (FI) AF4 (FI-AF4). Data are shown as mean ± SD, N=3 independent batches, n=3 technical replicates for HDL and N=2, n=3 for SM-102 LNPs for each AF4 modality.

HDL-PBS (control) at both 0 hr and 24 hrs incubation showed three subpopulations at hydrodynamic diameters of ~14 nm (peak 1), ~200 nm (peak 2) and > 1000 nm (peak 3) (**Table 5.2** and **Figure 5.2**). The size of HDL was measured to estimate its surface adsorption onto LNPs. HDL showed a negative zeta potential (-9 mV to -11 mV) attributed to its negatively charged phospholipids and acidic residues on apolipoproteins (Apo-AI), which carry a negative charge at physiologic pH. The surface charge is an important attribute to detect the formation of the LNP-HDL biomolecular corona later in the study.

Table 5.2 Baseline Critical Quality Attributes (CQAs) quantified for SM-102 LNPs and High-Density Lipoprotein (HDL). Data are shown as mean ± SD, N=3 independent batches, n=3 technical replicates for HDL and N=2, n=3 for SM-102 LNPs for batch 1 (B1) and batch 2 (B2) and N=2, n=3 for batch 3 (B3) and batch 4 (B4).

		Distribution analysis		Cumulant analysis		Zeta potential (mV)	Encapsulation efficiency (%)
Sample	**Incubation time (hr)**	**Peak**	**Particle diameter (nm)**	***Z*-Average (nm)**	**PDI**		
HDL	0	1	14.2 (± 1.0)	-	0.356 (± 0.011)	-10.1 (± 5.3)	-
		2	265.7 (± 18.9)				
		3	1600.4 (± 1686.4)				
	24	1	14.1 (± 0.3)		0.473 (± 0.079)	-9.7 (± 2.4)	-
		2	214.8 (± 16.4)				
		3	3249.0 (± 145.7)				
SM-102 LNPs (B1 and B2) (AF4)	0	-	-	63.3 (± 0.9)	0.082 (± 0.023)	-5.4 (± 1.1)	98 (± 1)
SM-102 LNPs (B3 and B4) (FI-AF4)	0	-	-	61.8 (± 0.9)	0.092 (± 0.010)	-5.5 (± 0.6)	87 (± 4)

5.4.2 Calculation of LNP surface coating with HDL

The calculation of HDL surface coverage on LNPs is included to assess whether the HDL in the LNP-HDL mixture is present in excess implying full LNP coating, and to determine the amount of unbound HDL, allowing direct comparison with the free HDL signal observed in the AF4 fractogram. The maximum number of HDL particles forming the corona layer around a single LNP assuming a close packed protein arrangement forming an HDL monolayer was estimated.

Using **Equation 5.5**, where R_{LNP} (DLS) is 31.7 nm (batches 1 and 2), R_{HDL} is 7.1 nm, R_{tot} = 45.9 nm. Based on these measurements, it was estimated that per SM-102 LNP, there were **118 surface-bound HDL** molecules following a 24-hour incubation.

The concentration of SM-102 LNPs was measured as **7.9×10^{11} particles/mL** (B1 and B2) by NTA, which indicates that there needs to be a maximum of **9.3×10^{13} particles/mL** of HDL ($7.9 \times 10^{11} \times 118$ HDL per LNP) to achieve complete saturation of SM-102 LNP surfaces with HDL.

Concentration of HDL used is 0.4 mg/mL with molecular weight of 175,000 g/mol, resulting in **2.3 x 10^{-9} moles/mL** (0.0004 g / 175,000 g/mole) of HDL. Using Avogadro's number 6.02×10^{23} $moles^{-1}$, there are **1.4×10^{15} particles/mL** of HDL ([2.3 x 10^{-9} moles/mL x [6.02×10^{23}]). This indicates that LNP surface saturation with HDL has been reached with an excess concentration of HDL in the LNP-HDL mixture. Under all experimental conditions and LNP batches examined, HDL saturation has been reached with an excess factor of HDL concentration of **~15** (1.4×10^{15} / 9.3 x 10^{13} particles/mL).

5.4.3 Calculation of the expected LNP-HDL corona size

The expected LNP-HDL particle diameter was calculated using **Equation 5.6** assuming a close packed protein arrangement forming HDL monolayer around a single SM-102 LNP. Example, using AF4, the experimental D_h for LNP-PBS (B1-B2) and HDL-PBS was measured averaged at 56.8 nm and 14.1 nm respectively. Using **Equation 5.6**, expected D_h is calculated as follow:

$$\text{Expected } D_h \text{ for LNP} - \text{HDL} = 56.8 + (2 \text{ x } 14.1) = 85 \text{ nm}$$

Experimentally, measured D_h using AF4-DLS was 130.8 nm. This suggests that HDL might not have formed a monolayer upon binding. The results also indicate that HDL exhibited structural rearrangement such as conformational ensembles or formed extended assemblies upon binding to LNPs, deviating from its native conformation.

Table 5.3 Estimated and measured particle diameter (D_h) using DLS, NTA, AF4, and FI-AF4. Samples represent SM-102 LNPs incubated in PBS (pH 7.4) (LNP-PBS) (control), HDL 0.4 mg/mL incubated PBS (HDL-PBS) (control) and SM-102-LNPs incubated in 0.4 mg/mL HDL (LNP-HDL). Time-points indicate 24 hr incubation at 37 °C.

Technique	Actual LNP-PBS (24 hr) (D_h)	Actual HDL-PBS (24 hr) (D_h)	Expected LNP-HDL (24 hr) (D_h)	Actual LNP-HDL (24 hr) (D_h)
DLS (B1 and B2)	63.3	14.1	91.5	-
DLS (B3 and B4)	61.8		90	-
NTA (B1 and B2)	73.4		101.60	-
NTA (B3 and B4)	76.4		104.60	-
AF4 (B1 and B2)	56.8		85	130.8
FI-AF4 (B3 and B4)	54.4		82.6	155.2

5.4.4 Conventional AF4 and FI-AF4 for the high-resolution separation and characterization of LNP-HDL biomolecular corona

Monitoring changes in LNP characteristics in polydisperse systems containing protein is inherently complex and challenging. Techniques such as DLS cannot be used to measure *in situ* changes in particle geometry and size. Therefore, a gentle separation technique and the use of multiple orthogonal in-line detectors is needed to enable the isolation and multiparametric evaluation of LNP fate. In this thesis, AF4 multiplexed with UV, MALS and DLS detectors was used to measure SM-102 LNP interactions with HDL. Using AF4 LNP-HDL complexes were isolated from bulk unbound HDL and analysed by online AF4-UV-MALS-DLS. Fractions were recovered for further analysis for particle size, surface charge and lipoprotein content.

The performance of the AF4 method was confirmed by the percent recovery of LNP-PBS (0 hr) which yielded recoveries >70 % for both modalities (**Supplementary Table S5.5**). Overall, both conventional AF4 and FI-AF4 have shown comparable elution profiles for the UV, MALS and DLS detectors. The elution profile for UV 260 nm showed an earlier high intensity peak for HDL (< 30 min at ~ 20 mV) followed by a lower intensity HDL peak (30-50 min at < 5 mV) (**Figure 5.3**). The FI-AF4 elution profile for both MALS and UV have shown a higher resolution compared to AF4, as it has eluted different sub-populations of HDL (population 1) for both 0 and 24 hr (**Figure 5.3B** and **Figure 5.3D**). Comparing both AF4 modalities for the separation of HDL at 0 hr and 24 hr incubation time-points, the 24 hr samples displayed a higher peak intensity for both UV and MALS detectors indicating a larger particle size or structural change formation over the 24 hr incubation of HDL (**Figure 5.3**). The major peak for LNP-PBS at 0 hr has eluted at ~28 min for AF4 and ~36 min for FI-AF4. The major peak for LNP-PBS at 24 hr eluted at approximately the same elution time as the 0 hr for both AF4 modalities (**Figure 5.3**). This finding is similar to the previous study for SM-102 LNPs incubated for 24 hr [177]. The elution profiles of LNP-PBS and HDL-PBS are comparable between conventional and FI-AF4 methods, indicating that neither separation modality induces aggregation. The consistent peak shapes and retention times suggest that both LNP and HDL maintain structural integrity during fractionation.

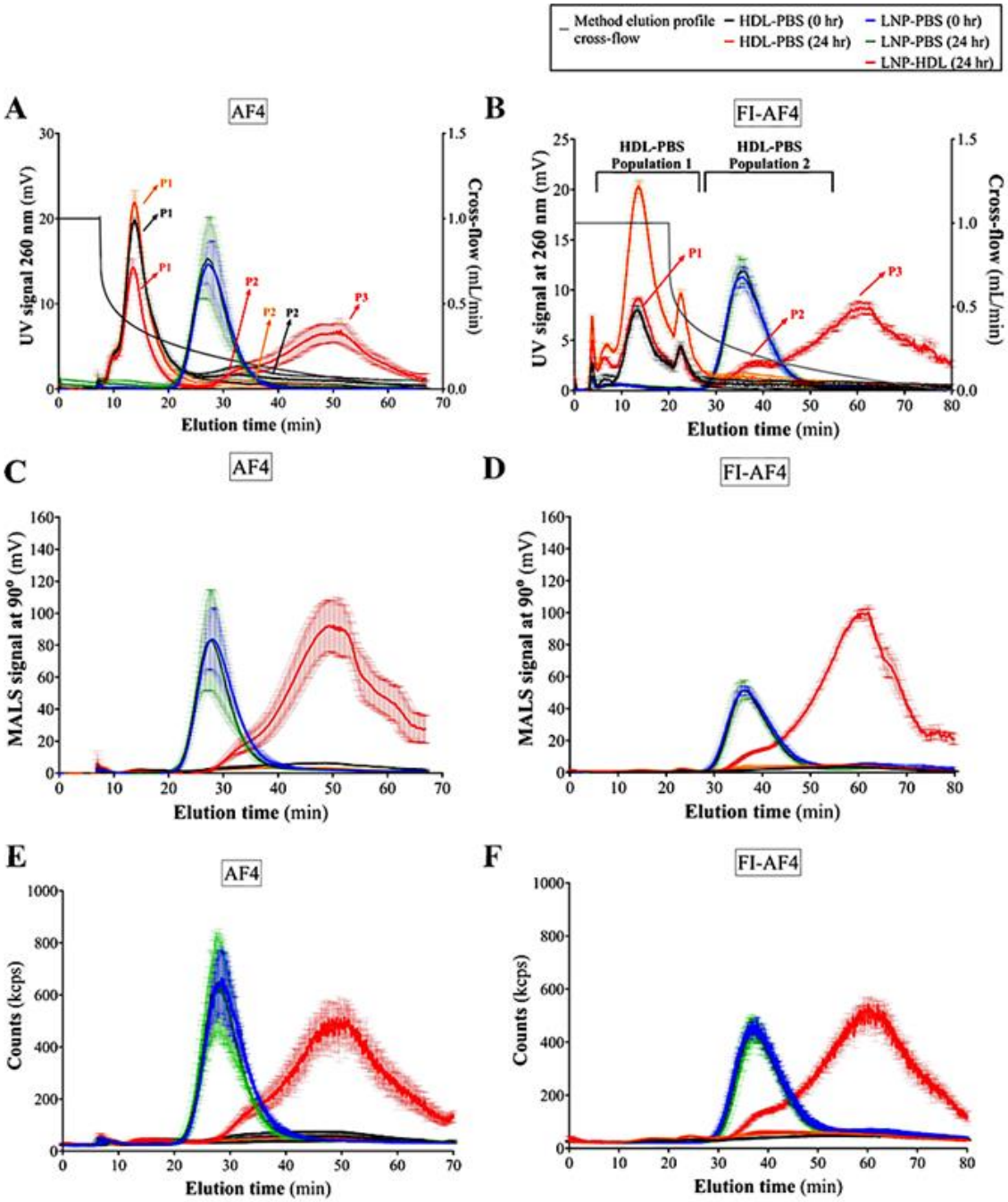

Figure 5.3 Fractograms of conventional Asymmetric Flow Field Flow Fractionation (AF4) and Frit-Inlet (FI) AF4 (FI-AF4). Fractograms represent SM-102 LNPs incubated in PBS (control), HDL 0.4 mg/mL incubated in PBS (control) and SM-102-LNPs incubated in 0.4 mg/mL HDL (LNP-HDL). Plots represent (A) and (B) AF4-UV (260 nm) fractograms for AF4 and FI-AF4 modalities respectively, (C) and (D) AF4-MALS (90°) fractograms for AF4 and FI-AF4 modalities respectively, (E) and (F) AF4-DLS fractograms for AF4 and FI-AF4 modalities respectively. Time-points indicate 0 hr (control) and 24 hr incubation at 37 °C. Results are shown as mean ± S.D, N=2 independent batches for each modality, n=3 replicate injections for each batch.

The LNP-HDL biomolecular corona exhibited a heterogenous elution profile with three distinct peaks (**Figure 5.3**). Peak 1 eluted (< 20 min), co-eluted with HDL-PBS population 1 (**Figure 5.3A** and **Figure 5.3B**), indicating free HDL in the LNP-HDL mixture. Peak 2 (**Figure 5.3A** and **Figure 5.3B**) (~ 30 - 40 min), represented an emerging SM-102 LNP-HDL complex with lower molecular weight than LNP-PBS, but a higher scattering intensity than HDL-PBS. Peak 3 (~40 min), exhibited the highest MALS and DLS signal intensities, suggesting the formation of a larger, abundant, higher molecular weight heterogeneous subpopulation, consistent with LNP-HDL complex formation. These findings confirm that both AF4 modalities effectively separate intact LNP-HDL corona, free HDL and newly formed subpopulations in the LNP-HDL mixture.

5.4.5 Separation and online analysis of SM-102 LNP-HDL complexes

Structural properties of SM-102 LNPs and LNP-HDL complexes were assessed using AF4 and FI-AF4 coupled with MALS and DLS detectors. LNP-PBS exhibited consistent R_h (~29 nm) at 0 and 24 hr, confirming method suitability (**Figure 5.2** and **Table 5.4**). In contrast, LNP-HDL complexes showed increased R_h and R_g across the elution profile (**Figure 5.4**), with peak 3 displaying the largest dimensions (R_h up to 77.6 (± 0.2) nm and R_g up to 67.2 (± 0.8) nm for FI-AF4) compared to LNP-PBS (24 hr) (**Figure 5.4** and **Table 5.4**). Broader R_h and R_g distributions (50–80 nm) for LNP-HDL peaks 2 and 3 further supported formation of larger heterogeneous complexes.

Shape factor analysis revealed near-spherical geometry for LNP-PBS (0 hr and 24 hr; ~0.67-0.75), while LNP-HDL complexes exhibited higher values (>0.775), consistent with rod-like or irregular structures. Peak 3 showed the greatest deviation (0.854-0.867), confirming significant structural changes upon HDL association. Collectively, these findings demonstrate that HDL corona formation increases particle size and alters geometry, highlighting dynamic protein-nanoparticle interactions (**Figure 5.4** and **Table 5.4**).

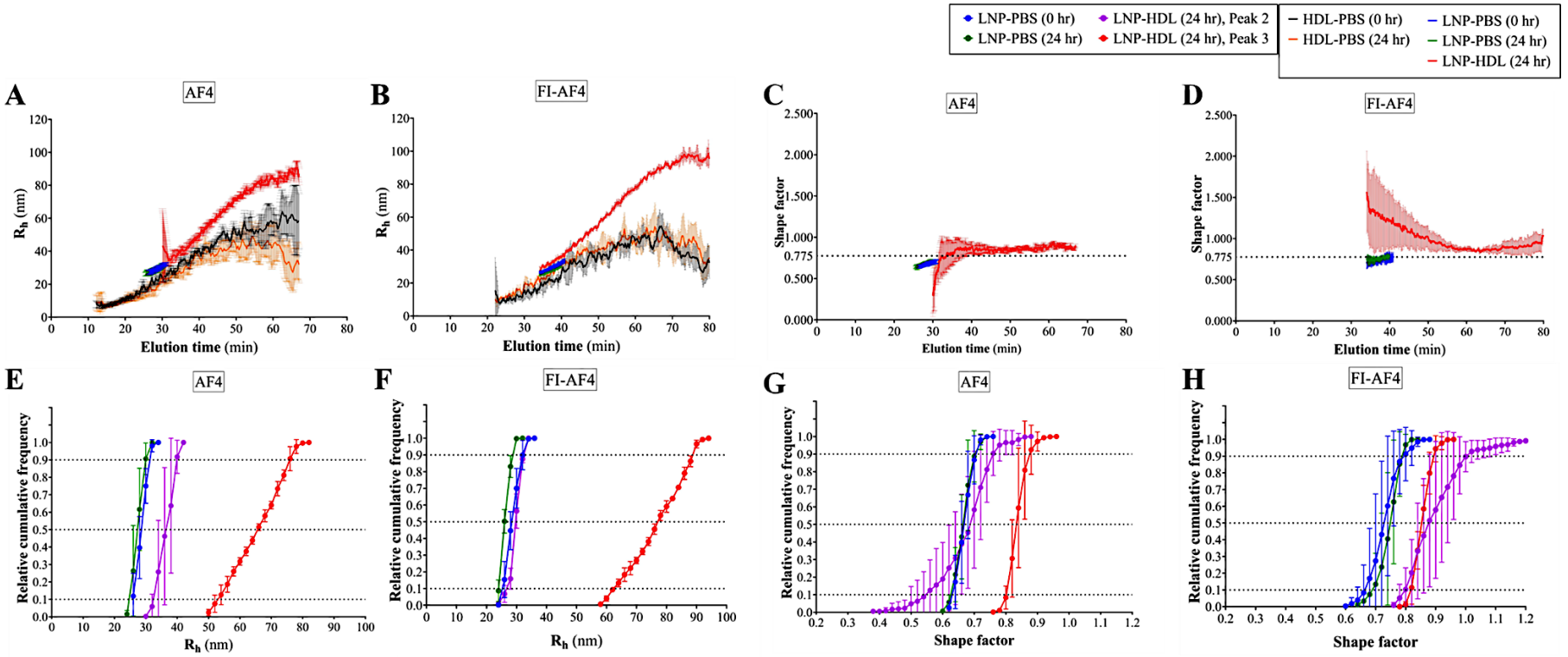

Figure 5.4 Hydrodynamic radius (R_h), radius of gyration (R_g) and shape factor (R_g/R_h) obtained for SM-102 LNPs incubated in PBS (control), 0.4 mg/mL High-Density Lipoprotein (HDL) incubated in PBS (control) and SM-102-LNPs incubated in 0.4 mg/mL HDL (LNP-HDL). Plots represent (A) and (B) R_h obtained by coupling AF4 and Frit-Inlet AF4 (FI-AF4) respectively to DLS detector, (C) and (D) shape factor obtained by coupling AF4 and FI-AF4 respectively to DLS and MALS detectors, (E) and (F) R_h distributions obtained by AF4 and FI-AF4 respectively, (G) and (H) shape factor distributions obtained by AF4 and FI-AF4 respectively. Time-points indicate 0 hr (control) and 24 hr incubation at 37 °C. Results are shown as mean ± S.D, N=2 independent batches for each modality, n=3 replicate injections for each batch. Dotted lines in plots (E) to (H) correspond to the cumulative percentages of 10 %, 50 %, and 90 %.

Table 5.4 Radius of gyration (R_g), hydrodynamic radius (R_h) and shape factor (R_g/R_h) measured using conventional Asymmetrical Flow Field-Flow Fractionation (AF4) and Frit Inlet AF4 (FI-AF4). Measurements were carried out for SM-102 LNPs and 0.4 mg/mL High-Density Lipoprotein (HDL) incubated in PBS (control) (LNP-PBS and HDL-PBS respectively) and SM-102 LNPs incubated with 0.4 mg/mL HDL (LNP-HDL). Time-points include 0 hr (control) and 24 hr incubation at 37 ºC. Results are shown as mean N=2 n=3 replicates for each batch. B1 and B2 represent batches 1 and 2 respectively analysed by AF4, B3 and B4 represent batches 3 and 4 respectively analysed by FI-AF4. A dash (-) indicates data not measured.

Sample	AF4 (B1 and B2)			FI-AF4 (B3 and B4)		
	R_g (nm)	**R_h (nm)**	**Shape Factor**	**R_g (nm)**	**R_h (nm)**	**Shape Factor**
LNP-PBS (0 hr)	20.0 (± 0.3)	29.5 (± 0.9)	0.678 (± 0.016)	21.9 (± 1.0)	29.6 (± 0.9)	0.738 (± 0.046)
LNP-PBS (24 hr)	19.1 (± 0.4)	28.4 (± 1.2)	0.674 (± 0.017)	20.5 (± 1.1)	27.2 (± 0.4)	0.753 (± 0.032)
LNP-HDL (24 hr-Peak 1)	-	-	-	-	-	-
LNP-HDL (24 hr-Peak 2)	25.6 (± 2.9)	37.6 (± 2.2)	0.681 (± 0.040)	34.4 (± 16.0)	40.4 (± 16.7)	0.858 (± 0.138)
LNP-HDL (24 hr-Peak 3)	53.4 (± 3.4)	65.4 (± 1.7)	0.846 (± 0.022)	67.2 (± 0.8)	77.6 (± 0.2)	0.865 (± 0.011)

5.4.6 Analysis of pooled AF4 fractions by NTA

After performing AF4-based fractionation of SM-102 LNP-HDL complexes from incubation media, fractions corresponding to each fractogram peak were recovered for analysis of their particle hydrodynamic diameter, size distribution, concentration, zeta potential and protein content.

The NTA particle size distributions for the main particle populations were relatively narrow (70-80 nm) suggesting a homogenous particle size distribution (**Figure 5.5A** and **Figure 5.5D)**. A significant reduction of 9.5 nm was observed between FI-AF4 pre- and post-fractionation at 24 hr time-point. Overall, the particle size following fractionation for both modalities were comparable (**Figure 5.5C**). Both AF4 modalities also showed comparable span of the size distribution (<1), with no significant change in sample polydispersity observed

post-fractionation (**Figure 5.5D**) indicating that the AF4 conditions used for both modalities maintained sample homogeneity.

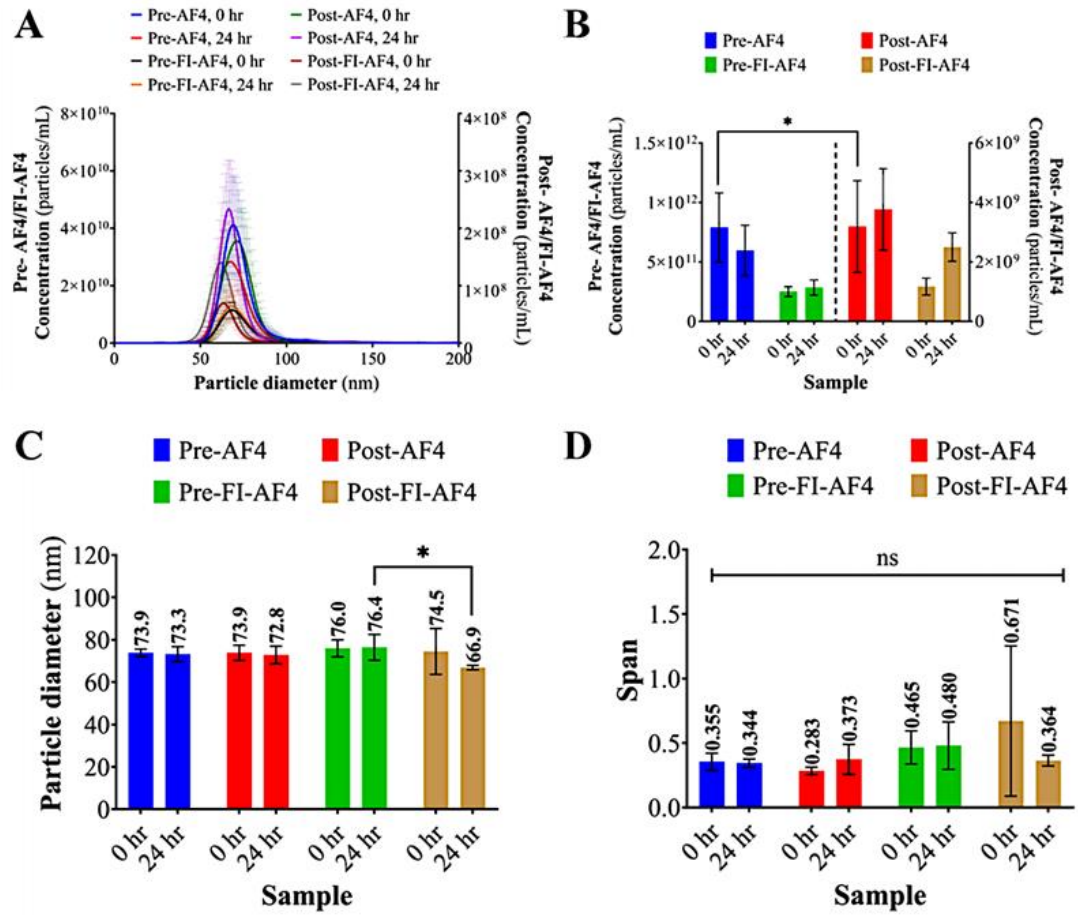

Figure 5.5 NTA parameters for SM-102 LNPs at 0 hr (control) and 24 hr incubation at 37 °C. Plots represent pre- and post-AF4 separation for (A) particle concentration per particle diameter (B) particle concentration (C) particle dimeter and (D) span (D90 - D10) / D50). Kruskal-Wallis test followed by post-hoc Dunn's test for plots (B-D), *p < 0.05. Error bars represent ± SD, N=2, n=3 for each AF4 modality. The dotted line in plot (B) distinguishes pre- and post- fractions.

Post-AF4 fractionation samples resulted in a lower measured particle concentration at both 0 and 24 hr time-points (~50 % reduction in particle concentration), indicating particle loss due to dilution effects during AF4-based separation and potential particle adsorption on the AF4 system manifolds and membrane (**Figure 5.5A**, **Figure 5.5B** and **Table 5.5**).

Table 5.5 Comparison of particle concentration using NTA for SM-102 LNPs measured pre- and post-AF4 based separation. Results are shown as mean N=2, n=3 replicates for FI-AF4 and AF4. B1 and B2 represent batches 1 and 2 respectively analysed by AF4, B3 and B4 represent batches 3 and 4 respectively analysed by FI-AF4.

AF4 Modality	Incubation time-point (hr)	Concentration (particles/mL)		Concentration difference between pre-AF4 and post-AF4 (%)
		Pre-AF4	Post-AF4	
AF4 (B1 and B2)	0	7.9×10^{11} ($\pm 2.9 \times 10^{11}$)	3.2×10^{9} ($\pm 1.5 \times 10^{9}$)	50
	24	6.0×10^{11} ($\pm 2.1 \times 10^{11}$)	3.8×10^{9} ($\pm 1.4 \times 10^{9}$)	49
FI-AF4 (B3 and B4)	0	2.5×10^{11} ($\pm 4.1 \times 10^{10}$)	1.2×10^{9} ($\pm 2.8 \times 10^{8}$)	50
	24	2.8×10^{11} ($\pm 6.4 \times 10^{10}$)	2.5×10^{9} ($\pm 4.8 \times 10^{8}$)	49

Zeta potential analysis confirmed negative surface charges for all SM-102 LNP samples (~ -3 to -11 mV) across both AF4 modalities (**Figure 5.6**). HDL-PBS fractions exhibited moderately negative values at 0 hr and 24 hr (F1: -8.9 mV; F2: -5.8 mV), with minimal variation between time points, indicating surface charge stability (**Figure 5.6).**

LNP-HDL post-AF4 samples showed relatively stable zeta potentials in the -8.5 to -9.7 mV range (**Figure 5.6**), implying that the LNP-HDL biomolecular corona retained surface characteristics similar to HDL rather than being dominated by LNP properties. Post-AF4 fractions has zeta potential of -9.2 (± 4.0) mV (HDL-PBS, 0 hr), -10.9 (± 2.7) mV (LNP-PBS, 0 hr), and -9.7 (± 2.9) mV and -7.4 (± 0.6) mV (LNP-HDL, 24 hr, peak 3), confirming that the AF4 fractionation did not alter surface charge characteristics, or no significant destabilization or shift in zeta potential occurred post-AF4.

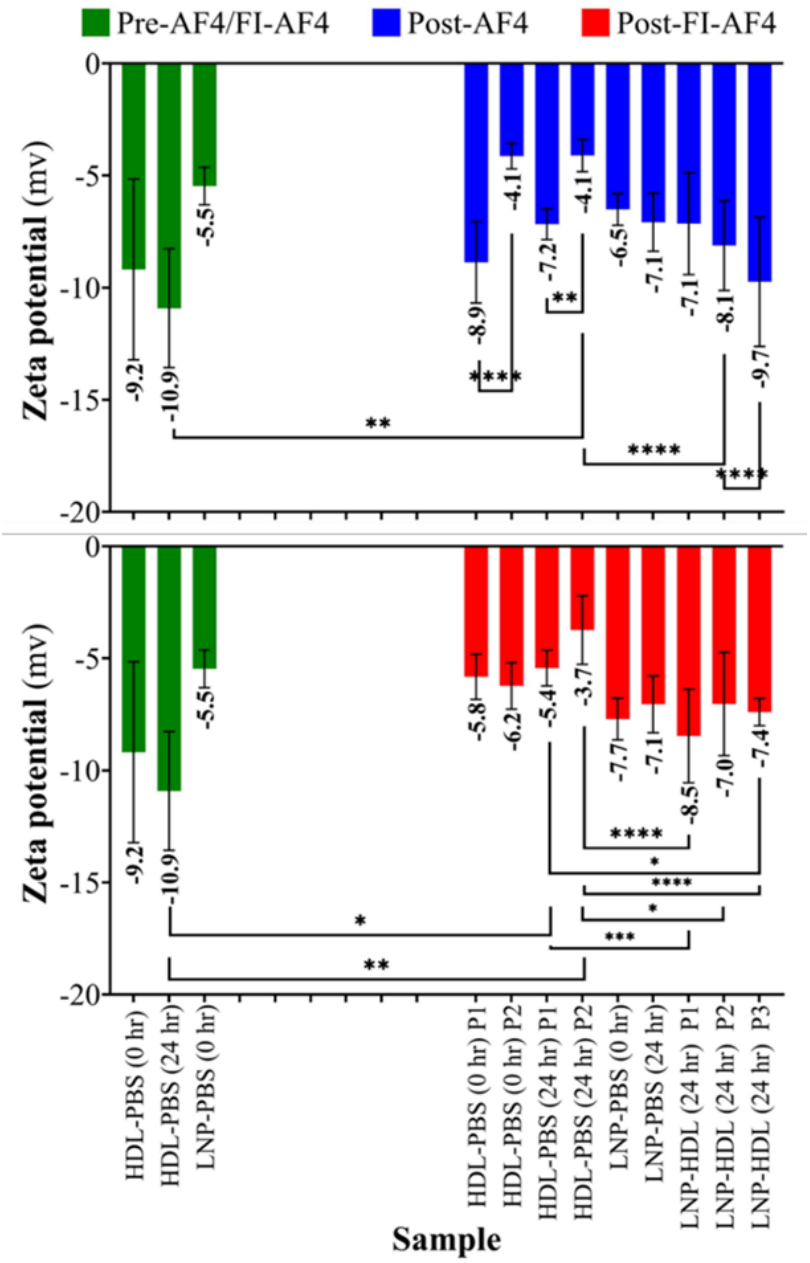

Figure 5.6 Zeta potential of SM-102 LNPs (control) (LNP-PBS) and SM-102 LNPs incubated in HDL for 24 hours (LNP-HDL). Zeta potential was measure pre- and post-AF4 and FI-AF4. Time-points indicate 0 hr (control) and 24 hr incubation at 37 °C. Results are shown as mean ± S.D, N=2 independent batches for each modality, n=3 replicate injections for each batch. Statistical analysis was performed using Kruskal-Wallis non- parametric test followed by post-hoc Dunn's test, *p < 0.05, **p < 0.01, ****p < 0.0001. Peaks 1-3 (P1-P3) represent the different peaks in the AF4-DLS fractogram.

5.4.7 Analysis of SM-102 LNP-HDL complexes by SDS-PAGE with Silver staining

SDS-PAGE coupled to silver staining was used to resolve the apolipoprotein fractions associated with LNP-HDL biomolecular corona pre- and post- AF4 fractionation. Silver staining due to its sensitivity limit of detection (0.25 ng [371]), which is necessary for post-AF4 analysis where samples are diluted during fractionation.

5.4.7.1 Analysis of SM-102 LNPs and HDL post-AF4 fractionation

Post-AF4 HDL-PBS fractions displayed band A at MW of ~50-70 kDa (apolipoprotein dimers or aggregates) and band B at MW of ~25-37 kDa, corresponding to Apo-AI, Apo-AIV, ApoE, and ApoL-I (**Figure 5.7A**). Bands A and B are also present in the pre-AF4 samples for HDL-PBS (**Supplementary Figure S5.3)**. The presence of the bands for both pre- and post-AF4 samples confirms the integrity of the apolipoproteins post-AF4 fractionation. The presence of band A in the LNP-PBS samples likely reflects HDL carryover from earlier AF4 runs, resulting in the appearance of characteristic HDL band A (**Figure 5.7B**).

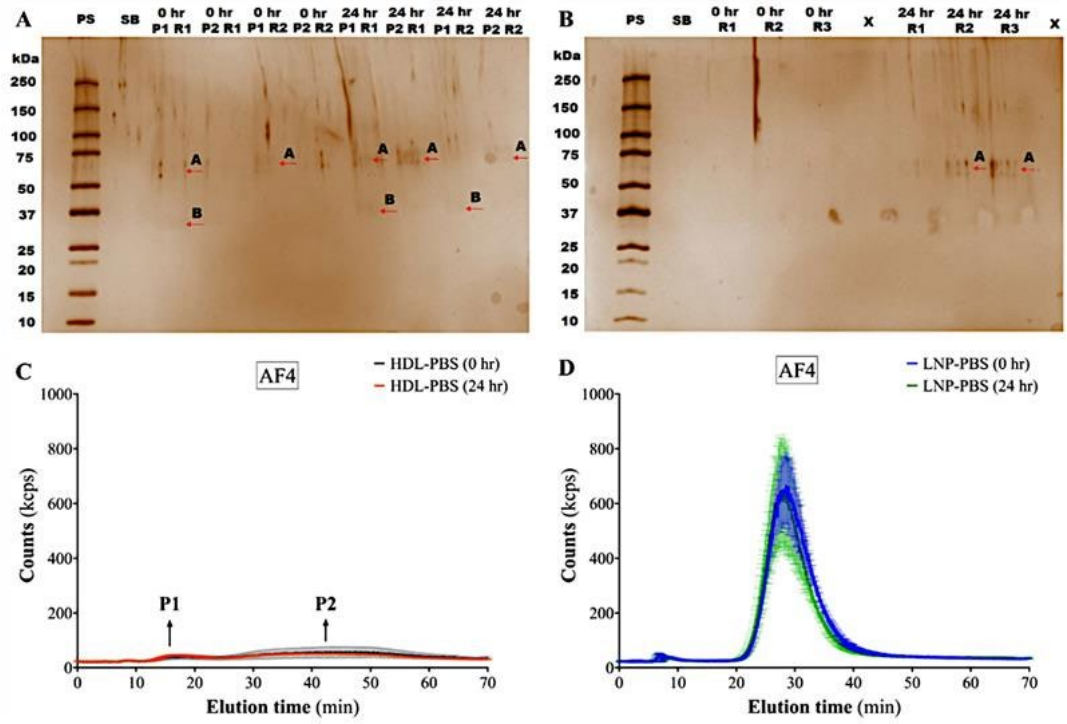

Figure 5.7 Silver-stained SDS-PAGE using 4-20 % gradient polyacrylamide gel for the fractions collected following AF4 fractionation for pre-spun samples. Gels represent (A) High-Density Lipoprotein (HDL) incubated in PBS (control) (HDL-PBS) (B) SM-102 LNPs incubated in PBS (control) (LNP-PBS). All plots show 0 hr (control) and 24 hr incubation at 37 ^{o}C. Protein bands marked with a red arrow corresponding to band A at MW of ~50-70 kDa (apolipoprotein dimers or aggregates) and band B at MW of ~25-37 kDa (Apo-AI, ApoA-IV, Apo-E, and apo-LI), (C) AF4 coupled to DLS (AF4-DLS) fractogram for HDL-PBS and (D) LNP-PBS. Peaks 1 and 2 (P1 and P2) represent the different peaks in the AF4-DLS elution profiles with R1, R2 and R3 representing replicates 1, 2 and 3 respectively. Abbreviations: PS Protein Standard molecular weight (kDa); SB Sample Buffer. Lanes marked with (X) correspond to blank lanes.

5.4.7.2 Concentrating the LNP-HDL fractions by using spin-column

Spun LNP-HDL fractions appeared to induce protein degradation or aggregation leading to smearing and poorly resolved bands (**Figure 5.8**). LNP-HDL samples show molecular weight bands (> 100 kDa). However, the presence of multiple components with high intensity in LNP-HDL (peak 1) suggests a higher concentration of HDL present compared to the fractions in LNP-HDL (peak 2 and peak 3) fractions. This indicates the presence of HDL in the three eluted peaks in the AF4-DLS elution profile**.**

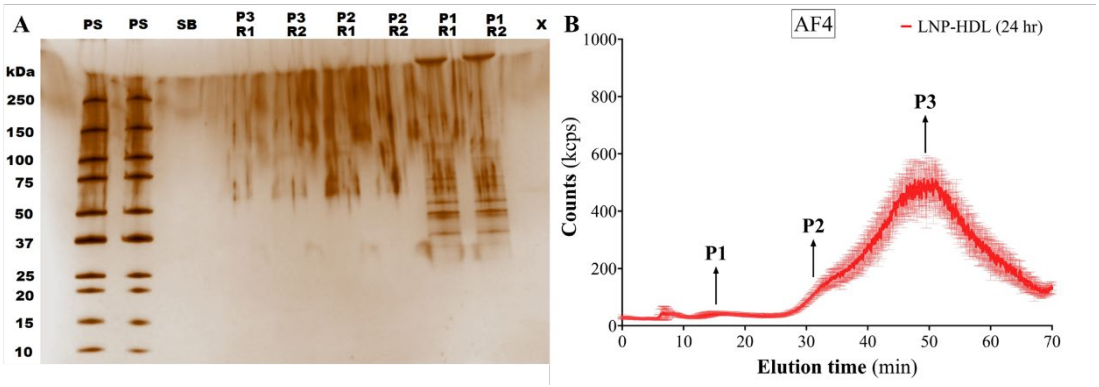

Figure 5.8 Silver-stained SDS-PAGE using 4-20 % gradient polyacrylamide gel for the fractions collected following conventional Asymmetric Flow Field Flow Fractionation (AF4). Sample represent SM-102 LNPs incubated in High-Density Lipoprotein for 24 hours at 37 °C (LNP-HDL) post-spin column (A). Peaks 1, 2 and 3 represent the AF4-DLS elution profiles for LNP-HDL, with R1, R2 and R3 representing replicates 1, 2 and 3 respectively (B). Abbreviations: PS Protein Standard molecular weight (kDa); SB Sample Buffer. Lane marked with (X) correspond to blank lane.

The post-spun LNP-HDL samples were also analysed using the 10 % polyacrylamide gel to compare whether the polyacrylamide gel percentage has an impact on protein resolution (**Supplementary Figure S5.4)**. The 10 % polyacrylamide gel showed a single band (Z) compared to the multiple MW components as discrete bands in the 4-20 % polyacrylamide gel (**Figure 5.8**). This difference is related to the variation in pore size between the 10 % and 4–20 % polyacrylamide gels. The 10 % gels have a uniform pore size, which limits resolution. High-molecular weight proteins migrate poorly and may appear as a single band (band Z) (**Supplementary Figure S5.4**), while low-molecular weight proteins are not well resolved since pores are relatively large. In contrast, 4-20 % gels have variable pore sizes. This gradient allows proteins of different molecular weights to be separated more effectively; in the case of HDL, larger proteins resolve at the low % region near the top of the gel, while smaller protein components are resolved in the higher % region toward the bottom.

5.4.8 Negative-stain transmission electron microscopy (TEM)

AF4 shape factor morphology was confirmed by analysis of LNP negative stain-TEM micrographs, where morphology was imaged to cross-compare orthogonal techniques (**Figure 5.9**). Comparable with FI-AF4/AF4 data, a round morphology for LNP-PBS (~0.750) and LNP-HDL (~0.850) (**Table 5.4**) was imaged. LNP-HDL at 24 hr shows altered surface

structure of approximately ~ 30 nm in particle R_h. This could be identified as LNP-HDL (24 hr, peak 2) in the FI-AF4/AF4 fractogram having a particle R_h of 37.6 (± 2.2) nm (**Figure 5.3**).

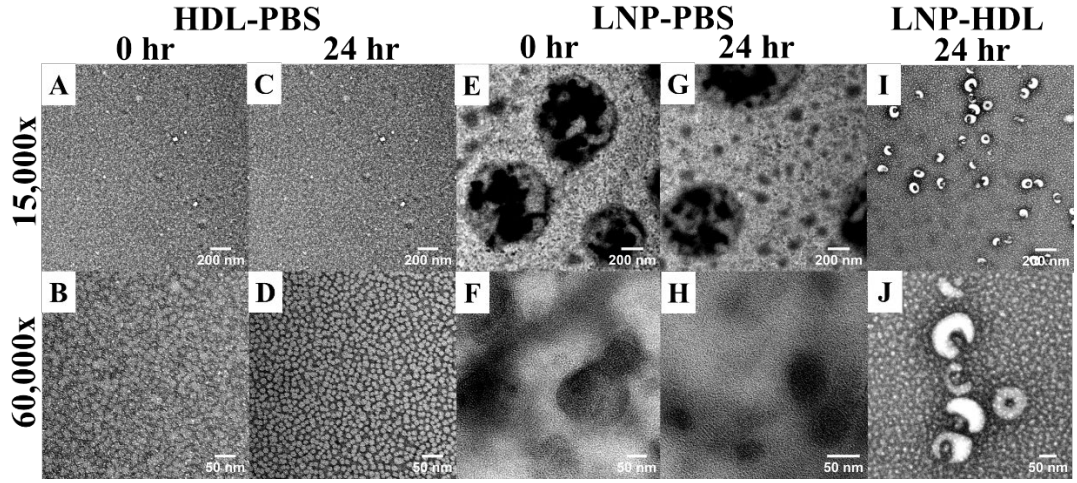

Figure 5.9 Negative stain TEM of High-Density Lipoprotein-control (HDL-PBS), SM-102 LNPs-control (LNP-PBS) and SM-102 LNPs incubated in 0.4 mg/mL HDL. Time-points indicate 0 hr (control) and 24 hr incubation at 37 °C (n=1).

SM-102-LNPs (**Figure 5.9 E-H**) exhibited disrupted morphology, with dense internal domains, consistent with compromised LNP integrity potentially associated with Poly(A) instability. Hence, despite AF4/FI-AF4 suggested a round LNP population, negative-stain TEM imaging identified morphological heterogeneity, which was not captured by the analytical workflow.

5.5 Discussion

This study aimed to optimise and integrate a multi-technique workflow for the physicochemical characterisation of LNPs and HDL biomolecular corona, using AF4 coupled to multi-detector (MALS, UV and DLS). The importance of the study is to determine whether LNPs have an affinity for HDL lipoproteins as these would deliver them to the liver for sequestration. The LNP biomolecular corona would then alter the uptake and transport of the LNPs into target cells [372]. The study suggests that LNP biomolecular corona should be characterized in the buffer and protein specific manner and not merely based on generalizations obtained from the literature. The study of particles of interest in physiologically-relevant environments is also recommended by Hajipour *et al.* [373].

A key technical challenge in LNP corona analysis lies in preventing disruption of LNP attributes and change in the biomolecular corona integrity. Separation of LNPs in a matrix rich

in lipoproteins is challenging due to the susceptibility of lipoproteins to aggregate which results in similar size and density properties to exogenous nanoparticles which does not allow effective separation [374]. Therefore, it critically important to firstly develop soft separation methodologies to isolate diverse and complex corona compositions and secondly determine the interactions formed between LNPs and biologically relevant individual biomolecules.

AF4 successfully separated the particle populations into three distinct peaks with differing size distributions, surface charges, and protein profiles. The separation by size using AF4 allowed for the collection of each separate fraction for downstream analysis. DLS and zeta potential measurements confirmed that most particle populations were within the expected nanometre size range and maintained a stable, negative surface charge over the tested timeframe. Zeta potential and NTA measurements confirmed that the physical characteristics of the recovered particles remained stable, but the overall yield was reduced compared to the injected load (~ 50-fold reduction in concentration between pre- and post-AF4 for both conventional and FI modalities).

The AF4 separation profiles were consistent with the size-based fractionation expected for the LNP-HDL complex. All three detectors (UV, MALS and DLS) support the formation of distinct nanoparticle populations upon incubation of LNPs with HDL. While HDL alone contributes minimally to the scattering signal due to its smaller size and lower mass, the LNP-HDL sample exhibited a pronounced and delayed peak with significantly higher intensity compared to LNP controls. This elevated signal is consistent with MALS data showing increased size, as well as the broadened UV elution profile. The higher counts and shifted elution suggest that LNP-HDL interactions result in particle remodelling or fusion, rather than simple surface association or co-elution. Collectively, the AF4-UV, AF4-MALS, and AF4-DLS fractograms all converge to indicate the formation of novel, heterogeneous LNP-HDL assemblies with distinct physicochemical properties.

The previous LNP-protein corona study by Abdulrahman *et al*. [177] has shown a non-significant difference in R_g and R_h in the of SM-102-LNP-Control and SM-102-LNPs bound to BSA (same LNPs prototype and same LNPs synthesis conditions as this study) [177]. However, this study has shown that the size distributions and shape factor vary significantly between SM-102-LNPs-Control and SM-012-LNPs bound to HDL. This suggests that the composition of the biomolecular corona is influenced not only by the chemistry and structural geometry of the cationic lipids, but also by the specific biomolecule forming the biomolecular corona. A study by Cederval *et al.* [142] has also revealed that binding and dissociation parameters vary as a function of protein identity as well as the physicochemical characteristics

of the copolymers nanoparticle surface. An increase in shape factor was observed for fractions containing a developed biomolecular corona compared to LNP-control or HDL-control. The shape factor calculated by integrating AF4-MALS-DLS provides insight into particle conformation, with values close to 0.775 [309] typically indicating a compact, spherical particle, and higher values reflecting more elongated or loosely packed structures. Such an increase in R_g results in elongation may arise from HDL adsorbing in partially unfolded conformations, forming protruding domains and creating an irregular size corona (deviating from the spherical conformation of shape factor 0.775). These conformational changes have important implications for biological interactions, as corona morphology can modulate receptor recognition [158], clearance rates [145], and cellular uptake [375] pathways.

The increase in particle size upon LNP-HDL biomolecular corona formation suggests that HDL did not distribute evenly on the LNP surface. A homogeneous coating would be expected to produce a greater size increase. This suggests that folding of HDL on LNP is more pronounced than a simple binary of folded or unfolded of apolipoproteins, as the tertiary structure of a apolipoproteins may change to β-sheets instead of α-helices upon interaction. This is visible from peak 2 (LNP-HDL in AF4-UV-MALS-DLS) of the AF4 and FI-AF4 but was absent in HDL-control. SDS-PAGE revealed HDL complexity, with peak 1 of LNP-HDL (AF4-MALS fractogram) containing the highest abundance and diversity of protein species, while peaks 2 and 3 of LNP-HDL (AF4-MALS and AF4-UV fractogram) exhibited progressively lower protein content and simpler banding patterns. Hence, all LNP-HDL fractions (peaks 1-3) have shown the presence of apolipoproteins in this fraction.

When HDL approach the LNP surface, the forces govern the HDL-LNP interactions can disrupt the non-covalent interactions holding the HDL conformation (hydrophobic, electrostatic, hydrogen bonds and Van der Waals). This can result in unfolding and conformational changes of the lipoprotein structure [355, 376]. Furthermore, the surface of the LNP is hydrophilic (polar heads of phospholipids). Previous studies have demonstrated that when a protein comes into close contact with a hydrophilic surface, they undergo an orientational changes which expose its hydrophilic patches [353, 377]. This could explain the unexpected size differences and changes and shape factor. Sebastiani *et al.* showed that ApoE binding induces significant reorganization of the LNP's internal structure [363].

Both conventional AF4 and FI-AF4 were evaluated for their ability to fractionate LNP-HDL biomolecular corona. LNP-HDL is a dynamic system in which proteins adsorb and desorb from the LNP, hence the AF4 captures a single moment in time which reaches the detector [378]. Separation performance was similar between AF4 and FI-AF4 modality in terms of

elution order and peak profile, with both modalities resolving a single population for LNP-PBS (control), and three major particle populations for LNP-HDL (peaks 1-3) distinguished by size. In the case of HDL-PBS, FI-AF4 had a high separation power by separating different low molecular weight populations for HDL compared to conventional which has eluted a single population.

The SDS-PAGE analysis of human HDL in this study revealed major protein bands within the ranges of approximately 25-37 kDa, 50-75 kDa, and 100-250 kDa. The bands between 25-37 kDa are consistent with the expected molecular weights of the principal HDL apolipoproteins, notably ApoA-I (molecular weight of ~30 kDa), A-IV (MW ~46 kDa), Apo-E (MW ~36 kDa) and ApoL-I (MW ~44 kDa) (**Supplementary Table S5.1)**. The doublet (50-75 kDa) band likely represents oligomeric forms of ApoA-I by the fusion of HDL particles forming HDL_2 as previously described by Gursky [379]. The presence of a distinct band between 100-250 kDa may indicate the occurrence of apolipoprotein aggregates. A band between 54-60 kDa for plasma HDL was also reported in a previous study by S. A. Brantmeier S.A, Grummer R.R, and R. L. Ax R. L [380]. The precise identification of individual apolipoproteins within HDL was challenging due to the inherent heterogeneity and compositional complexity of HDL particles (**Figure 5.1**). Human HDL comprises a diverse mixture of apolipoproteins and HDL-associated proteins such as lipoprotein-specific proteins include lecithin cholesterol acyltransferase (LCAT), CETP (cholesteryl ester transfer protein), and paraoxonase-1 (PON1) [381]. Several proteins may co-migrate within similar molecular weight ranges on SDS-PAGE, making it difficult to assign each observed band to a specific protein solely based on electrophoretic mobility. Furthermore, the interaction between HDL and LNP (forming LNP-HDL) can alter migration behaviour, leading to apparent molecular weights that differ from theoretical monomeric values.

NTA and zeta potential profiles of FI-AF4 fractions were similar to those from conventional AF4, indicating that the AF4 modality did not alter particle size or surface charge. FI-AF4 offered improved recovery consistency for low-abundance fractions and may be preferable when minimising AF4 channel membrane interactions, which is critical for fragile or aggregation-prone nanoparticles. For the present study, the conventional AF4 modality was used for detailed biophysical analysis of LNP-PBS, HDL-PBS and LNP-HDL, while FI modality served as a complementary approach to validate that the LNP-HDL biomolecular corona is not induced by the AF4 conventional modality. Fuentes *et al*. carried out a head-to-head study comparing FI-AF4 and concentration AF4 on a mixture of glycogen and pullulan [368]. The study showed that the resolution in the channel was higher for conventional AF4

compared to FI-AF4 [368]. This contradicts our study which showed a higher resolution for FI-AF4 compared to AF4 in the case of HDL separation, and comparable resolution for the LNP-HDL.

The combination of AF4 with downstream analytical techniques enabled robust separation and in-depth characterization of LNP biomolecular corona, providing valuable insight into how LNPs interact with endogenous lipoproteins such as HDL. These findings are crucial for advancing next-generation nanoparticle therapeutics with improved targeting, stability, and bioavailability.

Limitations and next steps

Although this study investigated the separation of a SM-102-LNP-HDL corona into different sub-populations, it did not assess the binding affinity between HDL and LNPs. Given the dynamic nature of the LNP biomolecular corona, association-dissociation studies could provide valuable insight into the kinetics of LNP-HDL interactions. Extending such analyses to other biomolecules of interest, such as complement proteins may further elucidate how corona composition modulates LNP physicochemical properties and influences delivery outcomes. Techniques such as surface plasmon resonance (SPR) could be employed to quantitatively determine LNP-biomolecule binding affinities.

Another limitation of this study is that the collected LNP-HDL AF4 fractions were not further evaluated for biological activity or cellular uptake *in vitro* using protein expression and functional delivery assays. Previous findings by Voke *et al.* [150] indicate that increased cellular uptake does not necessarily correspond to enhanced mRNA expression due to protein corona-mediated lysosomal sequestration of LNPs. Therefore, assessing the cellular expression and functional delivery of the isolated LNP-HDL fractions would provide valuable insight into the relationship between corona composition and cellular uptake.

Chapter 6: General Discussion

This thesis aimed to develop an advanced analytical pipeline to study three LNP formulations and separate LNPs from complex biological matrices as part of an experimental workflow for studying LNP bio-nano interactions. The goals of this thesis were achieved by optimisation and integration of a multi-technique workflow for the physicochemical characterisation of LNPs and LNPs incubated with biomolecules (BSA and HDL) using DLS, NTA, multi-detector AF4, ELS and SDS-PAGE coupled to silver staining. LNPs are composed of a mRNA payload along with ionizable cationic lipid, phospholipid, cholesterol and pegylated lipid components.

Currently there remains a knowledge gap on LNP formulation interactions with biomolecules, and subsequent LNP biological fate following formation of the biomolecular corona. The biomolecular corona is critical for predicting and controlling LNP behaviour in biological environments. The LNP biomolecular corona is the portion of the LNP encountered by cells, receptors, and immune components, and it therefore governs biodistribution, cellular uptake pathways, immune recognition, and clearance kinetics. For drug delivery applications, biomolecular interactions are particularly important. The biomolecular corona can alter LNP size, surface charge, and colloidal stability, directly influencing circulation half-life and organ targeting. For example, enrichment of apolipoproteins may promote receptor-mediated uptake through hepatic or lipoprotein receptors [382], while adsorption of complement factors can accelerate opsonisation and clearance by the mononuclear phagocyte system [378]. The composition of the corona can also modulate endosomal escape and intracellular trafficking, ultimately affecting delivery efficiency of encapsulated nucleic acids or small molecules [383]. This thesis addressed a critical gap in early drug development of LNPs by understanding the physicochemical attributes of the biomolecular corona. By elucidating how corona formation alters particle size, charge, and protein composition, the work provides new insights into the factors that shape LNP behaviour in biological systems.

Evaluating LNP formulation stability using orthogonal analytical techniques

The rapid development of LNPs as drug delivery systems, particularly in the context of mRNA vaccines and nucleic acid therapeutics, has highlighted the importance of accurate and comprehensive analysis of their physicochemical characterization. LNP formulation physicochemical properties constitute CQAs, which regulators require to be rigorously defined, measured, and controlled for throughout the product lifecycle. One of these, includes retention of physicochemical stability following frozen storage, which has culminated in the inclusion of cryoprotectants in LNP formulations. Sucrose preserves the physicochemical

properties of LNPs during storage, thereby prolonging shelf life and maintaining functionality over extended durations. In chapter 2, I set out to explore the use of orthogonal analytical approaches to profile inter-batch differences in DOTAP LNPs and the impact of downstream processing on their CQAs. A key finding from this study was that different LNP batches (batches 1 and 2) exhibited distinct AF4 elution profiles, despite being prepared under identical manufacturing conditions and yielding very similar DLS and ELS readouts. Moreover, while LNPs are commonly described in the literature as spherical structures, DOTAP-based LNPs demonstrated a shape factor deviating from a spherical structure, consistent with a rod-like morphology. Such structural information could not have been captured using conventional batch-mode techniques such as DLS or NTA. Moreover, the non-spherical structure of these particles would render them unsuitable for analysis by both DLS and NTA.

Chapter 2 also demonstrated that no single method can be used to comprehensively characterise LNPs. However, while it emphasized the importance of using higher resolution analytical approaches during early formulation development, this chapter is associated with some inherent limitations. To further enhance its broader uptake on a large-scale by regulators and industry, a greater emphasis on the standardization of the LNP characterisation pipeline and interlaboratory harmonisation will be required. Poly(A) was used a model payload in this chapter; therefore, the physicochemical profiles of the LNP formulations could not be correlated with biological performance metrics such as mRNA transfection efficiency, biodistribution, or immunogenicity. Without this correlation, the practical relevance of the measured attributes to therapeutic efficacy and safety remains uncertain.

AF4 method development beyond ISO guidelines

Guidelines for the quality assessment and characterization of LNPs are still under development, with ongoing efforts aimed at standardization and the establishment of robust analytical methods. Traditional techniques, such as DLS remain widely used due to their accessibility, low cost and minimal training requirements. However, DLS is limited by lower resolution and reliance on batch-mode analysis, which precludes the detection of heterogeneity within LNP samples. In the early stages of AF4 method development, DLS was incorporated into the initial characterization workflow. Nevertheless, it proved inadequate for identifying aggregates or resolving sub-populations, as larger particles disproportionately scatter more light compared to smaller ones. To overcome these limitations, an AF4-based protocol was established in this chapter for the analysis of nanoparticle mixtures composes of LNPs and BSA. Increasing the cross-flow rate in AF4 (0.75 to 1.5 mL/min) enabled the identification of three distinct LNP subpopulations which can be identified as the free BSA (peak 1), LNP-

BSA corona complex (peak 2) and LNP aggregates (peak 3). Although ISO/TS 21362 '*Nanotechnologies - Analysis of nano-objects using asymmetrical flow and centrifugal field-flow fractionation*,' [236] provides guidelines for analysing nanoparticles using AF4, the protocol is primarily suited for monodisperse formulations and is less effective for heterogeneous, multi-particle systems. This limitation arises from the reliance on resolution calculations that assume Gaussian peak distributions, which are not always representative of real samples. Consequently, the guidelines do not adequately address non-Gaussian peak distributions. In addition, while the standard recommends a recovery rate of ≥70 %, it does not provide guidance for cases where recovery exceeds 100 %. I provided guidance for this in chapter 2. In this study, AF4 recoveries > 100 % were observed, likely due to sample overloading (BSA used 35 mg/mL) and the high sensitivity of the UV detector. While these results still indicate that the AF4 method developed is acceptable, further adjustments are required such as reducing the sensitivity of the UV detector or using a lower protein concentration. However, reducing the protein content below physiologically-relevant levels could limit the biological relevance of these findings, and in some cases, even when the protein concentration is high and recovery exceeds 100 %, the AF4 method is still considered valid as it has separated the different sample components.

An important consideration when interpreting AF4 data is that each peak in the fractogram corresponds to a distinct particle sub-population characterized by differences in size. Averaging data across all detected peaks can obscure underlying heterogeneity, particularly when minor sub-populations exert disproportionate effects on biological behaviour, such as cellular uptake or immunogenicity. Therefore, it is essential to analyse each peak individually, linking the physicochemical attributes of each subpopulation with formulation characteristics and biological outcomes. For example, in chapter 3, a higher shape factor was consistently observed for peak 3 fractogram species compared to the LNP-control. The shape factor, defined as the ratio of R_g to R_h, serves as a useful indicator of protein binding. DLS determines the R_h by measuring the Brownian motion of particles. R_h reflects the solvation layer around the particle. The MALS detector provides the R_g based on angular light scattering relative to the nanoparticle's centre of mass. Since protein adsorption occurs at the nanoparticle surface, additional mass accumulates externally, increasing the shape factor values. A higher shape factor of the LNP-corona compared to LNP-control not only signals protein corona formation but also indicates deviations from spherical morphology (~1), with larger values suggesting rod-like structures [308]. These physicochemical characteristics could only be identified through the coupling of DLS and MALS with AF4, as conventional batch-mode DLS and

NTA are unable to resolve LNP morphology or detect protein corona formation through morphology characteristics.

The choice of MALS fitting model in AF4 for extrapolating the R_g is often mentioned but not always justified in the literature [113, 177]. The different MALS fitting models can yield varying R_g values, and this variability highlights the importance of a systematic approach to model selection. Rather than selecting a model arbitrarily or without reporting fit quality, I evaluated multiple models using the coefficient of determination (R^2) and the root mean square error (RMSE) to identify the most appropriate fit for each nanoparticle population. Although the Zimm model is commonly applied for protein analysis, the model was not suitable for reliable R_g determination using either Zimm or alternative models (chapter 3). For larger particles (>10 nm), corresponding to peak 2 and peak 3 in the elution profile, the coated sphere model provided the best fit based on the statistical criteria (chapter 3).

LNP biomolecular corona comparing different ionizable lipids

In chapter 4, the physicochemical interactions underlying biomolecular corona formation with BSA were evaluated for two ionizable LNP formulations, MC3-LNPs and SM-102-LNPs. Ionizable lipids are the most critical component of LNPs due to their role in the encapsulation mRNA and its cytosolic release. MC3 and SM-102 are ionizable lipids used in clinically approved LNP-based therapeutics. MC3 is the key ionizable lipid in Onpattro® (patisiran), while SM-102 is employed in the Moderna mRNA-1273 COVID-19 vaccine. Both MC3 and SM-102 lipids serve to encapsulate and protect nucleic acid payloads, and their ionizable nature facilitates efficient endosomal escape and cytoplasmic release of the therapeutic RNA. Analysis of shape factor indicated a shape factor of 0.783 for SM-102-BSA and 0.741 and 0.795 (peaks 1 and 2) for MC3-BSA, confirming interaction between LNPs and BSA. However, although the same protein was employed to investigate protein corona formation, differences between the LNP-Control and the protein corona were observed only for MC3 LNPs whereas non-significant for SM-102 LNPs. These variations in shape factor values can be linked to the distinct ionizable lipid compositions, SM-102 contains a branched tail with extended aliphatic side chains, whereas MC3 consists of unsaturated linear chains. Such structural differences result in distinct packing geometries, cylindrical for MC3 and cone-like for SM-102. Consequently, the lipid packing influences the surface chemistry of the nanoparticles, leading to differential interactions with BSA.

The MC3 and SM-102 LNPs prepared in this study both incorporated a PEGylated lipid, commonly employed to reduce opsonization. This study has unanswered gaps as to whether the inhibition of protein corona formation arises from the ionizable lipid, the PEGylated lipid,

or is instead dependent on the specific biomolecule involved. Onpattro® (patisiran) mRNA therapeutic utilises PEG2000-C-DMG. In contrast, Moderna's COVID-19 vaccine incorporates PEG2000-DMG, while Pfizer-BioNTech's COVID-19 vaccine employs PEG2000-ALC-0159. While all these three PEGylated lipids serve the primary purpose of reducing opsonization and prolonging systemic circulation, differences in their chemistry reflect design strategies tailored to the intended therapeutic application. In this study, PEG-lipid selection can also serve as a basis for examining biomolecular corona formation, since variations in PEG chemistry and stability may directly affect the extent and nature of protein adsorption at the LNP surface.

Taken together, the findings from chapters 4 and 5, which both examined SM-102 LNPs, demonstrate that LNPs do not exhibit uniform physicochemical behaviour when interacting with different biomolecules. For instance, SM-102 LNPs underwent particle shrinkage in the presence of BSA, whereas exposure to HDL led to an increase in particle size. These outcomes highlight that relying on a single biomolecule for assessment can yield incomplete or potentially misleading conclusions regarding LNP behaviour. Both chapters also involved biomolecules in excess (BSA in chapter 4 and HDL in chapter 5), under the assumption that a monolayer would form around the LNP surface. Although theoretical predictions were made to estimate the radius of the biomolecular corona, the empirical results diverged from these predictions. This discrepancy arises from the numerous assumptions inherent in the theoretical calculation, including **(1)** a monolayer coverage, **(2)** both LNPs and biomolecules are hard spheres, **(3)** uniform biomolecule orientation across the LNP surface, **(4)** the absence of conformational changes upon adsorption, and **(5)** no aggregation occurring during incubation of the biomolecule with LNPs. Such geometric estimates do not fully capture the behaviour of LNPs in dynamic biological environments, where interactions are more complex, and structurally variable.

Outlook

Comprehensive physicochemical characterisation of LNPs, together with the isolation of LNPs from the biomolecular corona and in-depth analysis of biomolecular interactions, underpins the rational design of nanoparticle systems. By anticipating or engineering the LNP biomolecular corona, unwanted immune responses can be prevented, targeting to specific tissues can be improved, and therapeutic efficacy enhanced. Thus, studying biomolecular corona formation is not only important for understanding fundamental LNP biology but is also critical for improving the safety and efficacy of LNP-based therapeutics. The methodological pluralism of the thesis aligns with the regulatory direction for nanomedicine characterization.

Both the FDA and EMA explicitly recommend orthogonal methods in their quality guidance documents, reflecting recognition that single-method physicochemical characterisation may lead to misleading conclusions [FDA, 2021]. By integrating complementary methods, this thesis has demonstrated a forward-looking approach consistent with emerging quality by design (QbD) principles in pharmaceutical development.

One of the main challenges encountered in this thesis was the lab-scale limited volume available for LNP manufacturing, which restricted the number of analytical techniques that could be applied to each batch. Preparing additional batches would have introduced inter-batch variability in physicochemical attributes, which may affect the extent to which these findings can be generalised across independently produced LNP formulations. Although data from multiple batches were combined to calculate averages, the resulting standard deviations were high. Consequently, consecutive experiments, including *in vitro* and *in vivo* studies, could not be performed using a single batch (< 4 mL total LNP volume). Manufacture scale up would require greater amounts of ionizable lipids (SM-102 and MC3) and the use of identical stirrer models for dialysis, as variations in stirrer type could introduce differences in LNP physicochemical properties, thereby reducing reproducibility within a single batch.

It is important to note that the LNP biomolecular corona formed *in situ* may not directly correspond to the corona observed under *in vitro* and *in vivo* conditions. The *in situ* study performed in this thesis for the biomolecules HDL and BSA was performed using binary mixtures and may therefore display divergent behaviours *in vitro* and *in vivo*. Establishing *in vivo* correlations presents an additional challenge, as the composition of the protein corona can vary significantly between species. For example, the corona formed in mice may differ from that in rats due to differences in the biological milieu. This interspecies variability in the immune system further complicates the translation of corona studies into reliable biological outcomes.

If the overarching goal is to achieve extrahepatic targeting (by functionalising the LNP through the biomolecular corona), examining only the physicochemical properties of the biomolecular corona is insufficient. A critical next step is to investigate cellular internalisation of LNPs in the presence of a specific biomolecule and to assess whether such biomolecules facilitate or hinder LNP uptake. These experiments would strengthen the conclusion that the biomolecular corona modulates cellular uptake and biodistribution. Moreover, cellular uptake studies can be correlated with the physicochemical attributes of LNPs, further demonstrating the central role of the biomolecular corona in LNP development. Conducting such evaluations during the pre-clinical phase may also reduce the unnecessary use of animals, aligning with the 3Rs

principle of Replacement, Reduction, and Refinement. As a future direction, pre-clinical translation could be advanced using lab-on-a-chip and organoid models before progression to *in vivo* studies. These platforms would enable a more detailed investigation of shear forces, binding affinities, and surface adsorption, while also providing insights into the role of the protein corona in modulating these interactions.

Further studies can be carried out on detailed imaging analyses of LNPs, both in stability assessments and in evaluating their interactions within biological environments. While physicochemical characterization provided valuable information on size, charge, and stability, complementary imaging approaches such as cryo-electron microscopy (cryo-EM) offers deeper insights into LNP morphology and link these observations to the shape factor values obtained. Although pristine SM-102 LNPs were imaged using negative staining and transmission electron microscopy (TEM) [310], revealing a spherical morphology, a significant gap remains in understanding how morphology changes upon corona formation of LNPs with different biomolecules. Imaging could reveal the localization of adsorbed biomolecules or the formation of structural features, such as blebs in DOTAP LNPs, which were associated with a shape factor of ~1 (indicative of rod-like morphology). Comparing pristine LNPs with their protein corona-coated counterparts through such imaging techniques would allow stronger correlations to be established between physicochemical attributes, corona composition, and cellular uptake, particularly in the context of HDL interactions.

Studies which can further strengthen the research is the spectroscopic evaluation of secondary structure changes in the proteins adsorbed onto the LNPs. Circular dichroism (CD) spectroscopy can be implemented as a valuable tool to establish conformational alterations in the LNP biomolecular corona protein layer. CD could show that upon binding of APOE to LNPs, the structure may undergo conformational rearrangements. The amphipathic α-helices of the C-terminal domain can unfold and reorient to embed within the LNP surface, shifting ApoE from a compact to a more extended conformation. This new conformation exposes the N-terminal receptor-binding regions, thereby enhancing interactions with Low-Density-Lipoprotein (LDL) receptors. Since such structural changes can significantly influence protein functionality, immune recognition, and LNP fate, the absence of CD analysis limits the mechanistic understanding of how the biomolecular corona may modulate LNP behaviour. Incorporating CD studies in future work could therefore provide important insights into the structural biology of biomolecule-nanoparticle interactions, particularly in single-component

biological media. **Figure 6.1** represents a schematic illustration of potential project future work.

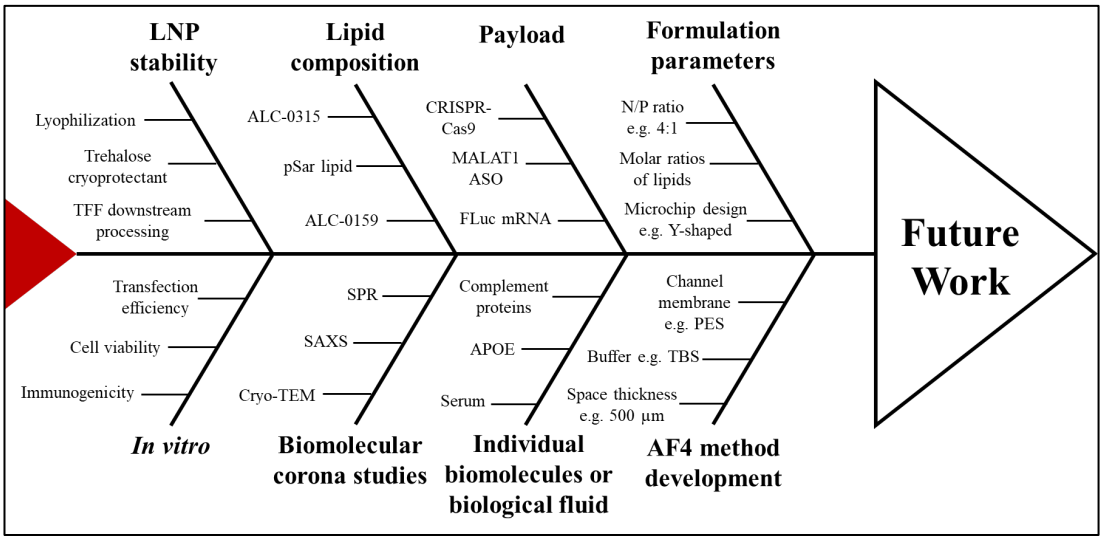

Figure 6.1 Fishbone diagram showing potential project future work. Abbreviations: TFF tangential flow filtration, ALC-0315 [(4-Hydroxybutyl)azanediyl]di(hexane-6,1-diyl) bis(2-hexyldecanoate), pSar polysarcosine, ALC-0159 methoxypolyethyleneglycoloxy(2000)-N,N-ditetradecylacetamide, CRISPR-Cas9 clustered regularly interspaced short palindromic repeats and associated protein 9, MALAT1 metastasis associated lung adenocarcinoma transcript 1, ASO antisense oligonucleotide, FLuc mRNA firefly luciferase messenger RNA, N/P nitrogen/phosphate, PES polyethersulfone, TBS tris-buffered saline, APOE apolipoprotein E, SPR surface plasmon resonance, SAXS small-angle x-ray scattering, Cryo-TEM cryo-transmission electron microscopy.

This work has already contributed to strengthening analytical capabilities within the immediate research group by establishing robust and reproducible AF4 workflows for the characterisation and separation of LNP drug delivery systems. The development of AF4-based methodologies and protocol alongside the evaluation of physicochemical attributes and biomolecular interactions provided a transferable framework that can be readily adopted and extended within the research group for the study of diverse nanoparticle formulations such as silk and polymeric nanoparticles. This orthogonal analytical pipeline can be extended to other therapeutic modalities such as antibodies.

Beyond the local setting, these approaches contribute to the broader field of orthogonal physicochemical characterisation by addressing key challenges associated with the characterisation of heterogeneous nano-mixtures and standardisation of AF4 analysis. the

recent update of the ISO guideline (ISO 21362:2026 *Nanotechnologies - Analysis of nano-objects using asymmetrical flow and centrifugal field-flow fractionation* [384]) in February 2026 highlights the increasing importance of standardised protocols for the characterisation of polydisperse nanoparticle systems.

In summary, this thesis highlights the value of employing orthogonal analytical techniques to achieve a comprehensive understanding of pre-clinical LNP behaviour, particularly in relation to biomolecular corona formation. By combining complementary characterisation technique with corona studies, researchers can better predict LNP performance, thereby informing the rational design of next-generation nanomedicines. Importantly, this work establishes a foundational framework for LNP characterisation, which supports the progression of these systems towards clinical translation.

Appendix

Supplementary for Chapter 2: Profiling LNP Physicochemical Attributes Using Orthogonal Analytical Techniques.

Table S2.1 FI-AF4 evaluation of DOTAP-LNPs for membrane pre-conditioning for six injection runs. Table displays highest peak signal intensity for UV (280 nm) and MALS (90°) detectors. Refer to **Supplementary Figure S2.1A** and **S2.1B** for UV (280 nm) and MALS (90°) elution profile.

Run	Highest peak signal intensity	
	UV (280 nm)	**MALS (90°)**
1	0.63	5.59
2	0.78	5.87
3	0.89	6.82
4	1.00	7.47
5	1.03	8.26
6	1.05	8.5

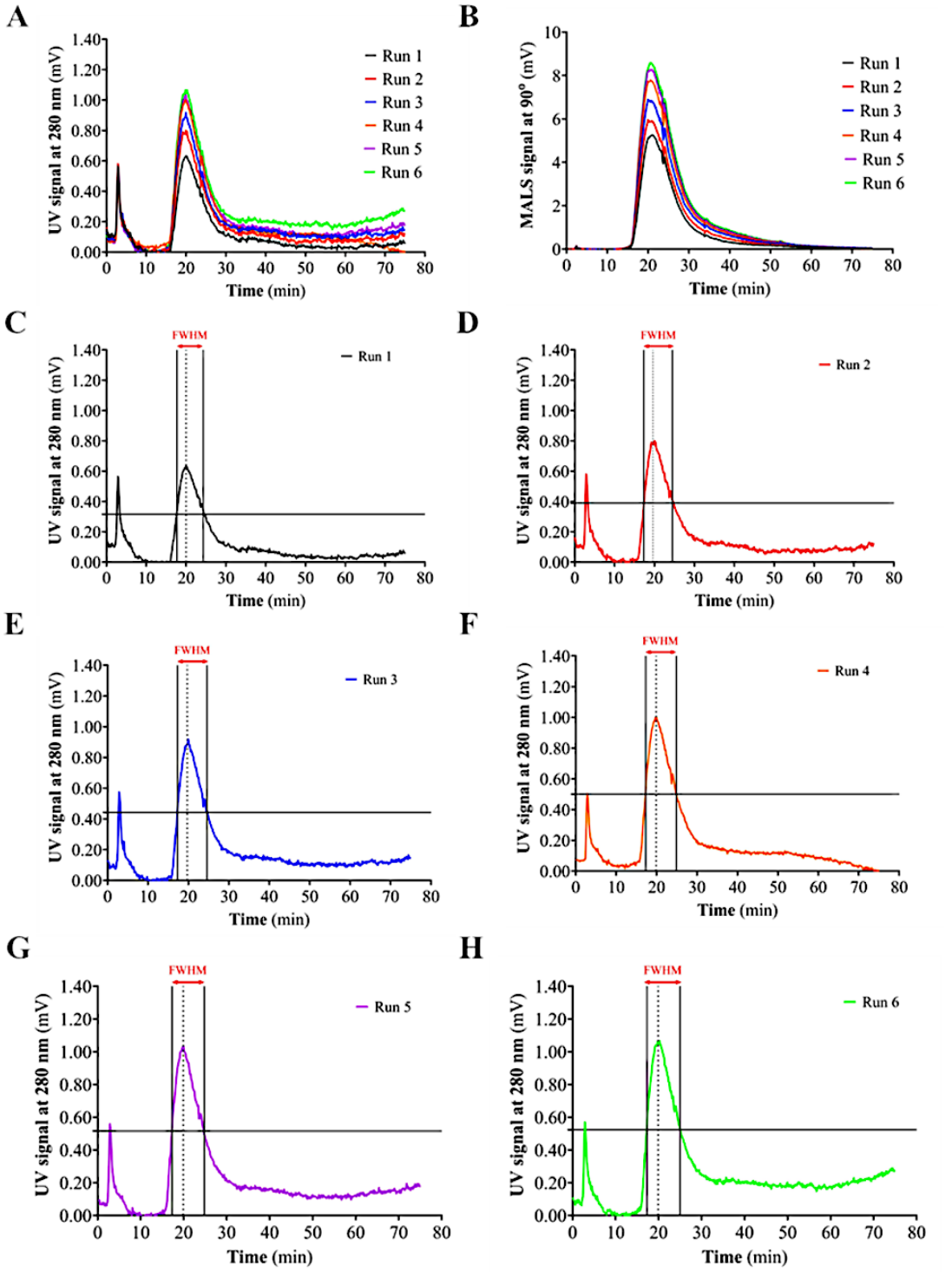

Figure S2.1 FI-AF4 evaluation of DOTAP-LNPs post-dialysis. Plots represent (A) UV elution profile at 280 nm wavelength (B) MALS (90°) elution profile and (C) to (H) UV signal at 280 nm wavelength elution profile for runs 1-6 respectively, (n=1). Lines in Figures (A) to (H) indicate the Full Width at Half Maximum (FWHM).

Table S2.2 FI-AF4 evaluation of DOTAP-LNPs for UV (280 nm) membrane pre-conditioning for six injection runs. Table displays the elution time for Full Width at Half Maximum (FWHM) calculation and area under the FWHM. The area (VMin) is obtained from NovaFFF software. Refer to **Supplementary Figure S2.1** for UV elution profile and FWHM time-points.

Run	Time FWHM (1) (min)	Time FWHM (2) (min)	Peak width (min)	Area (VMin)
1	17.7	24.3	6.6	3.33
2	17.3	24.5	7.2	4.83
3	17.3	24.6	7.3	5.13
4	17.3	24.9	7.6	5.80
5	17.3	24.8	7.5	5.98
6	17.3	25.0	7.7	6.44

Table S2.3 Percent recovery (%) of DOTAP-LNPs. Recovery estimated from the ratio of peak area applying cross-flow to the peak of the unfractionated sample without cross-flow. Results are shown as mean ± S.D of n=3. Recoveries were measured using the UV detector set at 280 nm.

Sample type	Recovery (%)
Day 0, LNP batch 1	97.1 (± 7.9)
Day 0, LNP batch 2	97.3 (± 5.7)
1X F/T LNP	13.8 (± 1.9)

Supplementary for Chapter 3: Multi-Detector Frit-Inlet Asymmetric Flow Field-Flow Fractionation Method Development for Nanoparticle Mixtures: Deeper Analysis Beyond ISO Quality Standards.

Table S3.1 Comparison of descriptive statistics for Nanoparticle Tracking Analysis (NTA) descriptors for MC3-LNP for 0 hour (control) and incubated for 24 hours at 37 ºC in 35 mg/mL Bovine Serum Albumin (BSA). Span describes the distribution width (D90-D10) / D50. Results are shown as mean ± S.D of three independent measurements.

	MC3-PBS (0 hr)	**MC3-PBS (24 hr)**	**MC3-BSA (24 hr)**
Concentration (particles/mL)	3.6×10^{11} ($\pm 6.8 \times 10^{10}$)	2.4×10^{11} ($\pm 2.0 \times 10^{11}$)	1.4×10^{12} ($\pm 5.9 \times 10^{11}$)
Mean (nm)	80.4 (± 19.3)	96.1 (± 9.4)	80.7 (± 1.8)
Mode (nm)	60.2 (± 4.8)	69.9 (± 6.9)	66.2 (± 2.5)
Span	1.00 (± 0.62)	1.11 (± 0.04)	0.61 (± 0.04)

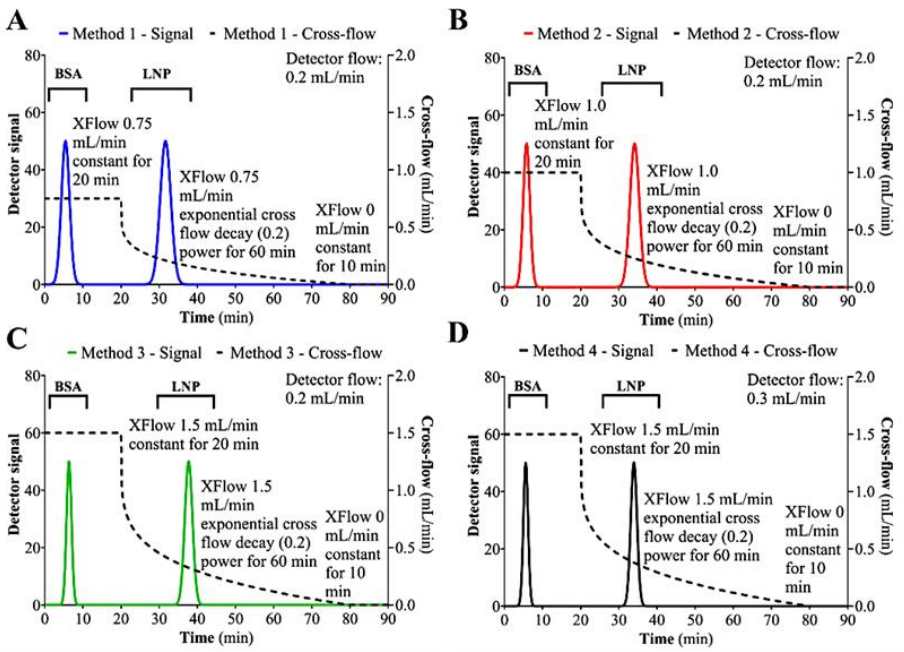

Figure S3.1 FI-AF4 method simulation for MC3-LNP-BSA mixtures using the NovaAnalysis software. Shown is a fractionation profile of Bovine Serum Albumin (BSA) and LNP peaks for (A) Method 1 (B) Method 2 (C) Method 3 and (D) Method 4. The profile obtained by simulating a linear cross-flow (XFlow) gradient with an initial flow rate within 20 min and dropping to 0 mL/min over 45 min at an exponential decay at power 0.2 with the final elution at 0 mL/min cross flow for 10 min. Dotted line shows the cross-flow profile over the run time duration.

Table S3.2 Average FI-AF4-UV signal intensities (mv) measured at UV 260 nm and 280 nm for Lipid Nanoparticles (LNP) and Bovine Serum Albumin (BSA) respectively. Refer to **Supplementary Figure S3.1** for details of FI-AF4 methods 1-4 and **Figure 3.7** for peak identity. Methods 1 and 2 did not identify peak 3 (-). RSD: relative standard deviation.

Peak identity	**Replicate injections**	**Method**			
		1	**2**	**3**	**4**
		Signal intensity (mV)			
BSA	Rep 1	607.4	739.0	986.3	985.3
	Rep 2	609.9	987.2	985.9	986.1
	Rep 3	257.9	987.3	986.0	986.1
	Average ± RSD	597.7 (± 3.2)	904.5 (± 15.8)	986.1 (± 0.0)	985.8 (± 0.0)
LNP Peak 1	Rep 1	22.9	31.4	22.0	15.2
	Rep 2	24.9	32.5	22.5	16.3
	Rep 3	26.8	31.7	22.7	16.3
	Average ± RSD	24.9 (± 7.8)	31.9 (± 1.8)	22.4 (± 1.7)	15.9 (± 3.8)
LNP Peak 2	Rep 1	12.3	4.6	11.2	7.4
	Rep 2	14.3	4.7	11.3	7.2
	Rep 3	15.8	5.0	11.0	7.2
	Average ± RSD	14.1 (± 12.5)	4.8 (± 4.0)	11.2 (± 1.3)	7.3 (± 2.0)
LNP Peak 3	Rep 1	-	-	1.5	0.9
	Rep 2			1.6	1.0
	Rep 3			1.4	1.0
	Average ± RSD			1.5 (± 8.5)	1.0 (± 3.5)

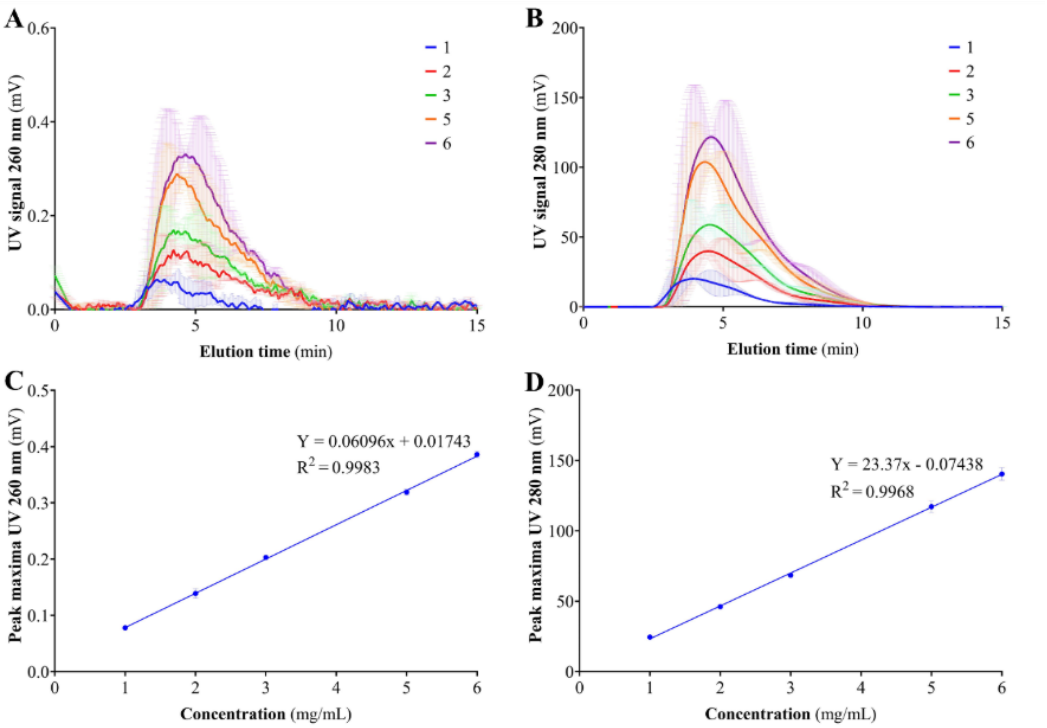

Figure S3.2 Regression of linear function of UV (260 and 280 nm) detector signal peak maxima. Plots represent AF4-UV fractogram for Bovine Serum Albumin (BSA) (1-6) mg/mL for (A) UV 260 nm (B) UV 280 nm and the corresponding linearity for (C) UV 260 nm and (D) UV 280 nm.

Table S3.3 Coefficient of Determination (R^2) and normalised Root Mean Square Error (RMSE) calculated for the predicted and actual values for MALS scattering fit models (Zimm, coated sphere, random coil and Debye). The R^2 and RMSE undefined refer to metrics which could not be calculated as the slope of the $R(\theta)$ versus $\sin^2(\theta/2)$ plot is zero indicating an invalid model fit. Methods 1 and 2 did not identify LNP peak 3 (-). Results are shown as mean ± S.D for at least n=2.

Peak	Method	Zimm	Coated Sphere	Random Coil	Debye
BSA	1	RMSE and R^2 undefined	RMSE 0.03 (± 0.000) R^2 0.22 (± 0.09)	RMSE and R^2 undefined	RMSE 0.002 (± 0.001) R^2 0.33 (± 0.00)
	2		RMSE 0.006 (± 0.001) R^2 0.41 (± 0.08)	RMSE 0.006 (± 0.000) R^2 0.43 (± 0.02)	RMSE 0.006 (± 0.000) R^2 0.48 (± 0.01)
	3		RMSE 0.008 (± 0.003) R^2 0.52 (± 0.28)	RMSE 0.009 (± 0.003) R^2 0.51 (± 0.28)	RMSE 0.007 (± 0.001) R^2 0.30 (± 0.08)
	4		RMSE 0.006 (± 0.001) R^2 0.50 (± 0.10)	RMSE 0.006 (± 0.001) R^2 0.57 (± 0.03)	RMSE 0.006 (± 0.000) R^2 0.59 (± 0.03)
LNP Peak 1	1	RMSE and R^2 undefined	RMSE 0.006 (± 0.005) R^2 0.97 (± 0.03)	RMSE 0.004 (± 0.000) R^2 0.98 (± 0.00)	RMSE 0.003 (± 0.000) R^2 0.99 (± 0.00)
	2		RMSE 0.008 (± 0.002) R^2 0.96 (± 0.02)	RMSE 0.000 (± 0.000) R^2 0.95 (± 0.02)	RMSE 0.009 (± 0.001) R^2 0.96 (± 0.01)
	3		RMSE 0.011 (± 0.004) R^2 0.98 (± 0.01)	RMSE 0.011 (± 0.004) R^2 0.98 (± 0.02)	RMSE 0.009 (± 0.002) R^2 0.89 (± 0.06)
	4		RMSE 0.008 (± 0.000) R^2 0.95 (± 0.00)	RMSE 0.008 (± 0.000) R^2 0.95 (± 0.01)	RMSE 0.007 (± 0.000) R^2 0.96 (± 0.00)

Table S3.3 (cont.)

Peak	Method	Zimm	Coated Sphere	Random Coil	Debye
LNP Peak 2	1	RMSE and R^2 undefined	RMSE 0.005 (± 0.000) R^2 0.99 (± 1.00)	RMSE 0.005 (± 0.000) R2 1.00 (± 0.00)	RMSE 0.004 (± 0.000) R^2 1.00 ± 0.00
	2		RMSE 0.017 (± 0.003) R^2 1.00 (± 0.00)	RMSE 0.025 (± 0.004) R^2 0.99 (± 0.00)	RMSE 0.048 (± 0.006) R^2 0.98 (± 0.00)
	3		RMSE 0.084 (± 0.031) R^2 0.98 (± 0.01)	RMSE 0.073 (± 0.008) R^2 0.99 (± 0.00)	RMSE 0.009 (± 0.002) R2 0.94 (± 0.09)
	4		RMSE 0.007 (± 0.000) R^2 0.99 (± 0.00)	RMSE 0.008 (± 0.000) R^2 0.99 (± 0.00)	RMSE 0.006 (± 0.001) R^2 1.00 (± 0.000)
LNP Peak 3	1	RMSE and R^2 undefined	-	-	-
	2				
	3		RMSE 0.096 (± 0.043) R^2 0.98 (± 0.01)	RMSE 0.075 (± 0.010) R^2 0.98 (± 0.00)	RMSE 0.189 (± 0.019) R^2 0.90 (± 0.02)
	4		RMSE 0.107 (± 0.005) R^2 0.97 (± 0.00)	RMSE 0.072 (± 0.020) R^2 0.99 (± 0.00)	RMSE 0.244 (± 0.010) R^2 0.86 (± 0.01)

Table S3.4 Average shape factor (R_g/R_h) calculated from peaks integrated in **Figure 3.10** and **Figure 3.13** for MC3-LNPs incubated in 35 mg/mL Bovine Serum Albumin (BSA) for 24 hours at 37 °C. Methods 1 and 2 did not identify Peak 3 (-). Results are shown as mean ± S.D for n=3.

Method	**LNP Peak Identity**		
	Peak 1	**Peak 2**	**Peak 3**
1	0.735 (± 0.007)	0.794 (± 0.003)	-
2	0.792 (± 0.008)	0.853 (± 0.011)	-
3	0.709 (± 0.027)	0.765 (± 0.009)	1.069 (± 0.040)
4	0.741 (± 0.019)	0.794 (± 0.007)	1.263 (± 0.116)

Supplementary for Chapter 4: Frit-Inlet-Asymmetric Flow Field-Flow Fractionation for the Comparative Analysis of the Biomolecular Corona Formation of Two LNP Prototypes (MC3-LNP and SM-102-LNP).

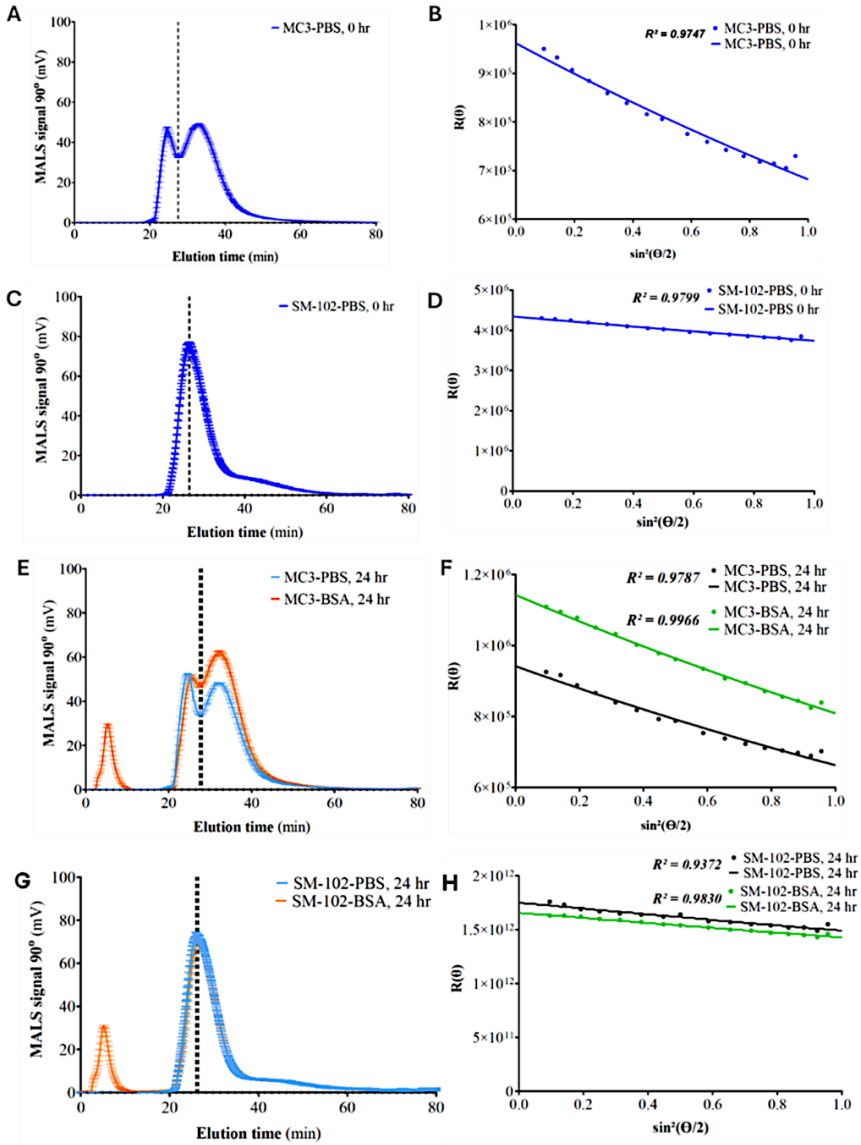

Figure S4.1 FI-AF4-MALS fractogram traces and corresponding sphere model fits for (A) and (B) MC3-LNPs at 0 hour (control), (C) and (D) SM-102-LNPs at 0 hour (control) (E) and (F) MC3-LNPs at 24 hours in 35 mg/mL Bovine Serum Albumin (BSA), and (G) and (H) SM-102-LNPs incubated in 35 mg/mL BSA for 24 hours. Plots A, C, E and G show error bars which represent triplicate injections with mean ± SD, n=3. Dashed lines represent centre of each peak. Symbol (■) in (B), (D), (F) and (H) denotes the goodness of fit (R^2) for the sphere model.

Table S4.1 Percent recovery (%) of MC3-LNPs (control), SM-102-LNPs (control), MC3-LNPs and SM-102-LNPs incubated in 35 mg/mL Bovine Serum Albumin (BSA). Time-points indicate 0 hour (control) and 24 hours incubation at 37 °C. MC3-LNPs and SM-102-LNPs estimated from the ratio of peak area applying cross-flow to the peak of the unfractionated sample at cross-flow 0 mL/min. Results are shown as mean ± S.D of n=3. Recoveries were measured using the UV detector set at 260 nm.

	Time-point (hr)	**Sample**	**Recovery (%)**
MC3-LNPs	0	MC3-PBS	97 (± 2)
	24	MC3-PBS	91 (± 8)
		MC3-BSA	105 (± 8)
SM-102-LNPs	0	SM-102-PBS	111 (± 13)
	24	SM-102-PBS	88 (± 13)
		SM-102-BSA	130 (± 15)

Table S4.2 Hydrodynamic radius (R_h), radius of gyration (R_g) and shape factor for MC3-LNPs (control), SM-102-LNPs (control), MC3-LNPs and SM-102-Lipid Nanoparticles (LNPs) incubated in 35 mg/mL Bovine Serum Albumin (BSA). Time-points indicate 0 hour (control) and 24 hours incubation at 37 ºC. Results are shown as mean ± S.D of triplicate injections for each sample. The (-) indicates no peak detected. Peaks 1-2 are identified in **Figure 4.5**.

	Time-point (hr)	**Sample**	**R_h (nm)**		**R_g (nm)**		**Shape Factor (R_g/ R_h)**	
			Peak 1	**Peak 2**	**Peak 1**	**Peak 2**	**Peak 1**	**Peak 2**
MC3-LNPs	0	MC3-PBS	25.0 (± 0.2)	39.5 (± 0.2)	17.9 (± 0.5)	30.3 (± 0.2)	0.718 (± 0.017)	0.769 (± 0.007)
	24	MC3-PBS	24.7 (± 0.0)	39.8 (± 0.0)	17.6 (± 0.4)	30.6 (± 0.4)	0.713 (± 0.018)	0.769 (± 0.011)
		MC3-BSA	25.6 (± 0.1)	38.9 (± 0.2)	19.0 (± 0.2)	30.8 (± 0.2)	0.741 (± 0.006)	0.795 (± 0.004)
SM-102-LNPs	0	SM-102-PBS	29.9 (± 0.1)	-	22.9 (± 0.2)	-	0.766 (± 0.007)	-
	24	SM-102-PBS	29.9 (± 0.2)	-	24.1 (± 0.3)	-	0.806 (± 0.012)	-
		SM-102-BSA	29.5 (± 0.1)	-	23.0 (± 1.0)	-	0.783 (± 0.034)	-

Supplementary for Chapter 5: The Use of Frit-Inlet and Conventional Asymmetric Flow Field-Flow Fractionation Modalities for the Separation, Isolation and Downstream Analyses of SM-102-LNP Prototype and High-Density Lipoprotein Biomolecular Corona.

Table S5.1 Apolipoproteins in human HDL identified [385]. Molecular weights are derived from UniProt database.

Protein name	Molecular weight (Da)
ApoA-I	30,778
ApoA-II	17,252
ApoA-IV	37,049.57
ApoC-I	5,679
ApoC-II	11,284
ApoC-III	10,852
ApoC-IV	14,553
ApoD	16,885
ApoE	36,154
ApoF	35,399
ApoL-I	43,974
ApoM	21,253

Table S5.2 Nanoparticle Tracking Analysis (NTA) dilutions used for the analysis of SM-102 LNPs incubated in PBS (control) pre- (before) and post- (after) Asymmetric Flow Field-Flow Fractionation (AF4) using the conventional (AF4) and Frit-Inlet (FI-AF4) modality. Time-points include 0 hour (control) and 24-hour incubation at 37 ºC.

Modality	Dilution			
	Pre-AF4 / FI-AF4		Post-AF4 / FI-AF4	
	LNP-PBS (0 hr)	LNP-PBS (24 hr)	LNP-PBS (0 hr)	LNP-PBS (24 hr)
AF4	2000	2000	10	10
FI-AF4	1000	1000	5	5

Table S5.3 Nanoparticle Tracking Analysis (NTA) descriptors SM-102 LNPs incubated in PBS (control) measured before (pre-) and after (post-) Asymmetrical Flow Field-Flow fractionation (AF4). Measurements were carried out for conventional AF4 (Batch 1 (B1) and Batch 2 (B2)) and FI-AF4 (Frit-Inlet AF4) (Batch 3 (B3) and Batch 4 (B4)). Time-points include 0-hour (control) and 24-hour incubation at 37 ºC. Results are shown as mean ± S.D for N=2 n=3 replicates for each AF4 modality.

AF4 Modality	Incubation time-point (hr)	Mean		Mode		D10		D50		D90	
		Pre-AF4	Post-AF4	Pre-AF4	Post-AF4	Pre-AF4	Post-AF4	Pre-AF4	Post-AF4	Pre-AF4	Post-AF4
Conventional (B1 and B2)	**0**	73.9 (± 1.7)	73.9 (± 3.6)	69.1 (± 1.4)	69.5 (± 3.6)	61.6 (± 0.3)	62.5 (± 3.6)	70.8 (± 0.5)	71.1 (± 3.7)	86.7 (± 4.9)	82.6 (± 3.7)
	24	73.3 (± 3.5)	72.8 (± 4.1)	69.7 (± 4.3)	66.1 (± 1.3)	61 (± 2.4)	59.6 (± 0.8)	70.6 (± 3.2)	67.4 (± 1.0)	85.3 (± 5.3)	84.8 (± 8.5)
Frit-Inlet (B3 and B4)	**0**	76.0 (± 4.0)	74.5 (± 10.8)	68.4 (± 2.1)	63.9 (± 1.1)	60.8 (± 1.5)	57.3 (± 1.3)	70.9 (± 2.2)	65.6 (± 2.4)	93.9 (± 11.3)	102.4 (± 41.9)
	24	76.4 (± 6.1)	66.9 (± 1.1)	68.7 (± 2.4)	61.9 (± 0.6)	61.0 (± 3.6)	54.1 (± 1.3)	71.0 (± 3.6)	62.9 (± 0.4)	95.7 (± 19.1)	77.0 (± 2.7)

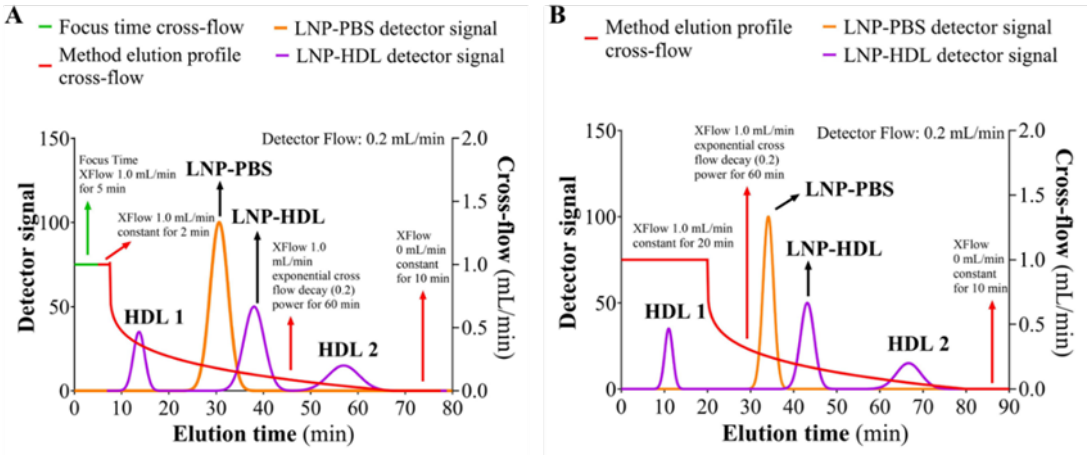

Figure S5.1 Asymmetric Flow Field-Flow Fractionation (AF4) (conventional and Frit-Inlet (FI-AF4)) simulation using NovaAnalysis software for SM-102 LNPs incubated in PBS (control) (LNP-PBS) and SM-102 LNPs incubated with High-Density Lipoprotein 0.4 mg/mL (LNP-HDL). Plots represent (A) method simulation for conventional AF4. The profile obtained by simulating a focus cross-flow of 1.0 mL/min, an initial cross-flow rate at 1.0 mL/min for 2 min and dropping to 0 mL/min over 60 min at an exponential decay at power 0.2 with the final elution at 0 mL/min cross flow for 10 min and (B) method simulation for FI-AF4 by simulating a linear cross-flow at 1.0 mL/min at 20 min and dropping to 0 mL/min over 60 min at an exponential decay at power 0.2 with the final elution at 0 mL/min cross flow for 10 min. Detector flow set at 0.2 mL/min for both conventional AF4 and FI-AF4 modalities. Red line in plots (A) and (B) shows the cross-flow profile over the run time duration.

Table S5.4 Parameters (mass (%) and particle radius (nm)) input in the NovaAnalysis software for method simulations in **Supplementary Figure S5.1**. Samples represent SM-102 LNPs incubated in PBS (control) (LNP-PBS) and SM-102-LNPs incubated with 0.4 mg/mL High-Density Lipoprotein (LNP-HDL) at 37 ºC for 24 hours. Mass refers to the approximate relative amount of a LNP and HDL component in the sample. The radius values were obtained from the DLS measurements in **Table 5.2**.

Sample	Particle	Mass (%)	Radius (nm)
LNP-PBS	LNP	100	30
LNP-HDL	HDL 1	35	7
	LNP-HDL	50	44 (30+7+7/2)
	HDL 2	15	107

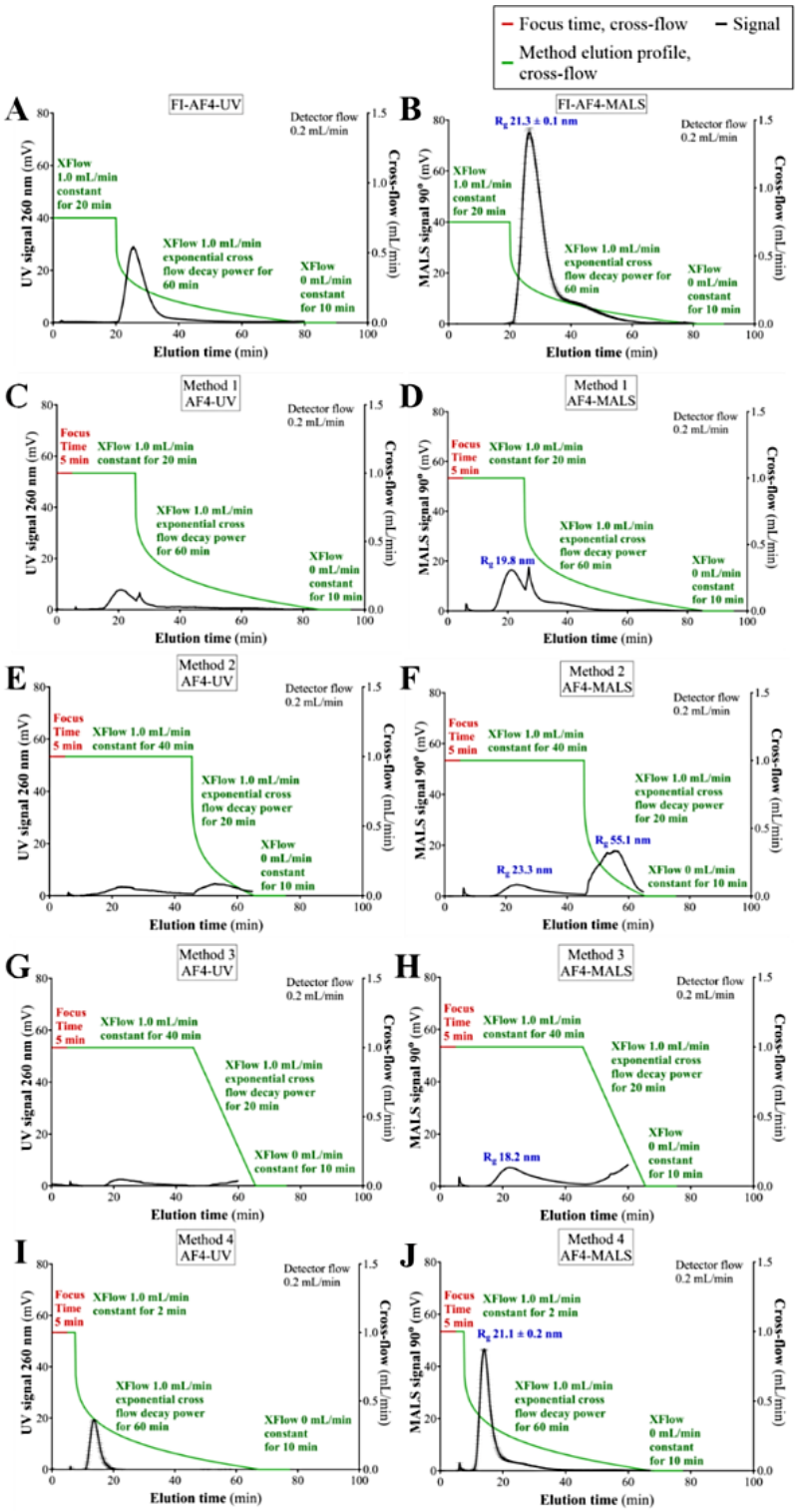

Figure S5.2 Asymmetric Flow Field-Flow Fractionation (AF4) (conventional (AF4) and Frit-Inlet (FI-AF4)) for SM-102 LNP-PBS (control) method development. Figures (A) and (B) represent FI-AF4 elution profiles for UV 260 nm and MALS (90°) respectively and (C) to (J) conventional AF4 method development. Plots show error bars which represent N=2 n=3 replicates for each AF4 modality. R_g: radius of gyration.

Table S5.5 Percent recovery (%) of SM-102 LNPs incubated PBS (control) (LNP-PBS), High-Density Lipoprotein (HDL) (HDL-PBS) (control) and SM-102 LNP incubated in 0.4 mg/mL HDL (LNP-HDL). Time-points indicate 0 hour (control) and 24 hours incubation at 37 ºC. Recovery estimated from the ratio of peak area applying cross-flow to the peak of the unfractionated sample at 0 mL/min cross-flow. Results are shown as mean ± S.D (N=2, at least 2 run-to-run injections for each batch). Recovery was measured using the UV detector set at 260 nm for LNP-PBS and LNP-HDL and 280 nm for HDL-PBS. Symbol (-) represents recoveries not measured.

Sample	Modality	Recovery (%)
LNP-PBS (0 hr)	AF4	116 (± 4)
	FI-AF4	102 (± 8)
LNP-PBS (24 hr)	AF4	132 (± 13)
	FI-AF4	52 (± 4)
HDL-PBS (0 hr)	AF4	107 (± 5)
	FI-AF4	-
LNP-HDL (24 hr)	AF4	80 (± 28)
	FI-AF4	-

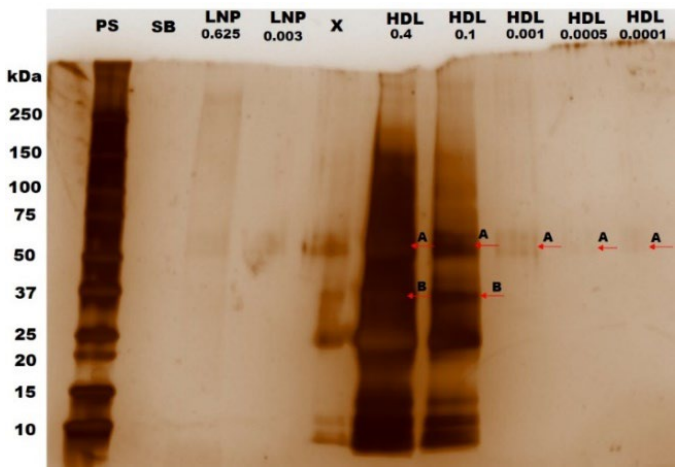

Figure S5.3 Silver-stained SDS-PAGE using 4-20 % gradient polyacrylamide gel of SM-102 LNPs incubated in PBS (control) and High-Density Lipoprotein (HDL) incubated in PBS (control) pre- Asymmetric Flow Field-Flow Fractionation (AF4). LNP lipid concentrations are represented by 0.625 and 0.003 mg/mL. HDL concentrations are represented by of 0.4, 0.1, 0.001, 0.0005 and 0.0001 mg/mL. Protein bands of interest marked with a red arrow corresponding to Band (A) at MW of ~50-70 kDa (apolipoprotein dimers or aggregates) and Band (B) at MW of ~25-37 kDa (Apo-AI, ApoA-IV, ApoE, and ApoL-I). Lane marked with (X) corresponds to blank lane. PS: Protein Standard molecular weight (kDa), SB: Sample Buffer.

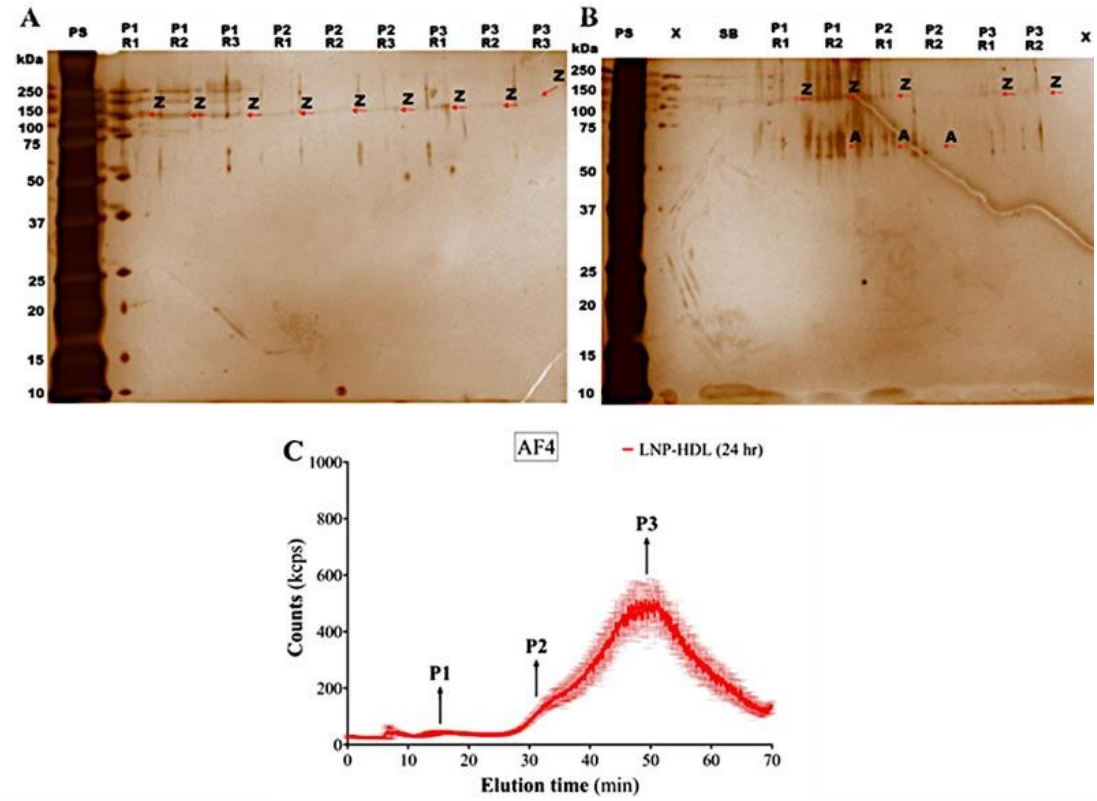

Figure S5.4 Silver-stained SDS-PAGE using 10 % polyacrylamide gel for the fractions collected following conventional Asymmetric Flow Field Flow Fractionation (AF4). Fractions represent SM-102 LNPs incubated in High-Density Lipoprotein (LNP-HDL) at 37 ºC for 24 hours. Plot (A) represents pre-spin column sample, while plot (B) post-spin sample and (C) AF4 coupled to Dynamic Light Scattering (DLS) (AF4-DLS) fractogram for LNP-HDL. Peaks P1, P2 and P3 represent the AF4-DLS elution profiles for LNP-HDL, with R1, R2 and R3 representing replicates 1, 2 and 3 respectively. Protein bands marked with a red arrow corresponding to Band (Z) at MW of ~150 kDa (oligomeric apolipoproteins) apolipoprotein dimers or aggregates) and Band (A) at MW of ~50-75 kDa (ApoA-IV). Lanes marked with (X) correspond to blank lanes. PS: Protein Standard molecular weight (kDa), SB: Sample Buffer.

References

1. Barenholz, Y., *Doxil(R)--the first FDA-approved nano-drug: lessons learned.* J Control Release, 2012. **160**(2): p. 117-34.
2. Li, M., et al., *The nano delivery systems and applications of mRNA.* Eur J Med Chem, 2022. **227**: p. 113910.
3. Swetha, K., et al., *Recent Advances in the Lipid Nanoparticle-Mediated Delivery of mRNA Vaccines.* Vaccines (Basel), 2023. **11**(3).
4. Zhao, Y., et al., *Rational design of lipid nanoparticles: overcoming physiological barriers for selective intracellular mRNA delivery.* Curr Opin Chem Biol, 2024. **81**: p. 102499.
5. Schoenmaker, L., et al., *mRNA-lipid nanoparticle COVID-19 vaccines: Structure and stability.* Int J Pharm, 2021. **601**: p. 120586.
6. Viger-Gravel, J., et al., *Structure of Lipid Nanoparticles Containing siRNA or mRNA by Dynamic Nuclear Polarization-Enhanced NMR Spectroscopy.* J Phys Chem B, 2018. **122**(7): p. 2073-2081.
7. Kulkarni, J.A., et al., *On the role of helper lipids in lipid nanoparticle formulations of siRNA.* Nanoscale, 2019. **11**(45): p. 21733-21739.
8. Research, G.V., *Lipid Nanoparticle Market Analysis Report (2025 - 2030)*.
9. Kon, E., et al., *Targeting cancer with mRNA-lipid nanoparticles: key considerations and future prospects.* Nat Rev Clin Oncol, 2023. **20**(11): p. 739-754.
10. Akinc, A., et al., *The Onpattro story and the clinical translation of nanomedicines containing nucleic acid-based drugs.* Nat Nanotechnol, 2019. **14**(12): p. 1084-1087.
11. Walther, J., et al., *Comparative analysis of lipid Nanoparticle-Mediated delivery of CRISPR-Cas9 RNP versus mRNA/sgRNA for gene editing in vitro and in vivo.* Eur J Pharm Biopharm, 2024. **196**: p. 114207.
12. Close, A.M. and A.G. Handbook, *Grading of Recommendations, Assessment, Development, and Evaluation (GRADE): Moderna mRNA RSV Vaccine (mResvia) in older adults About.*
13. EMA, *Comirnaty COVID-19 mRNA Vaccine Assessment Report*. 2021.
14. Diseases, N.C.f.I.a.R.D.U.S.D.o.V., *Moderna COVID-19 vaccine (also known as Spikevax) overview and safety*. 2022: National Center for Immunization and Respiratory Diseases (U.S.).
15. Wang, T., et al., *Lipid nanoparticle technology-mediated therapeutic gene manipulation in the eyes.* Mol Ther Nucleic Acids, 2024. **35**(3): p. 102236.
16. (EMA), E.M.A., *Onpattro Assessment Report*. 2018.
17. FDA, *Spikevax Package Insert, Summary Basis for Regulatory Action*. 2021.
18. Fabiani, M., et al., *Effectiveness of the Comirnaty (BNT162b2, BioNTech/Pfizer) vaccine in preventing SARS-CoV-2 infection among healthcare workers, Treviso province, Veneto region, Italy, 27 December 2020 to 24 March 2021.* Euro Surveill, 2021. **26**(17).
19. Moderna TX, I., *FDA Approval Letter - MNEXSPIKE*, U.S.F.D. Administration, Editor. 2025.
20. *The untapped potential of mRNA–lipid nanoparticles.* Nature Reviews Bioengineering, 2025. **3**(9): p. 715-715.
21. Juliano, R., et al., *Biological barriers to therapy with antisense and siRNA oligonucleotides.* Mol Pharm, 2009. **6**(3): p. 686-95.
22. Yin, H., et al., *Non-viral vectors for gene-based therapy.* Nat Rev Genet, 2014. **15**(8): p. 541-55.
23. Organization, W.H., *Messenger RNA encoding the full-length SARS-CoV-2 spike glycoprotein.* World Health Organization: Geneva, Switzerland, 2020.
24. Administration, U.F.a.D., *ONPATTRO full prescribing information. FDA, Washington DC. 2018*.

25. Yang, L., et al., *Recent Advances in Lipid Nanoparticles for Delivery of mRNA.* Pharmaceutics, 2022. **14**(12).
26. Scalzo, S., et al., *Ionizable Lipid Nanoparticle-Mediated Delivery of Plasmid DNA in Cardiomyocytes.* Int J Nanomedicine, 2022. **17**: p. 2865-2881.
27. Kasiewicz, L.N., et al., *GalNAc-Lipid nanoparticles enable non-LDLR dependent hepatic delivery of a CRISPR base editing therapy.* Nat Commun, 2023. **14**(1): p. 2776.
28. Semple, S.C., et al., *Rational design of cationic lipids for siRNA delivery.* Nat Biotechnol, 2010. **28**(2): p. 172-6.
29. Rele, S., *COVID-19 vaccine development during pandemic: gap analysis, opportunities, and impact on future emerging infectious disease development strategies.* Hum Vaccin Immunother, 2021. **17**(4): p. 1122-1127.
30. Anderson, E.J., et al., *Safety and Immunogenicity of SARS-CoV-2 mRNA-1273 Vaccine in Older Adults.* N Engl J Med, 2020. **383**(25): p. 2427-2438.
31. Gillmore, J.D., et al., *CRISPR-Cas9 In Vivo Gene Editing for Transthyretin Amyloidosis.* N Engl J Med, 2021. **385**(6): p. 493-502.
32. Leung, A.K., et al., *Microfluidic Mixing: A General Method for Encapsulating Macromolecules in Lipid Nanoparticle Systems.* J Phys Chem B, 2015. **119**(28): p. 8698-706.
33. Deshpande A, M.M., Daftardar SB, Patel M, Boddu SHS, Nesamony J., *Solid lipid nanoparticles in drug delivery: Opportunities and challenges.* Emerging Nanotechnologies for Diagnostics, Drug Delivery and Medical Devices, 2017: p. 291-330.
34. FDA, *MRESVIA Package Insert*. 2024.
35. FDA, *Comirnaty Package Insert, Summary Basis for Regulatory Action* 2021.
36. Terada, T., et al., *Protective Effect of Edaravone against Cationic Lipid-Mediated Oxidative Stress and Apoptosis.* Biol Pharm Bull, 2021. **44**(1): p. 144-149.
37. Henderson, L.J., *Concerning the relationship between the strength of acids and their capacity to preserve neutrality.* American Journal of Physiology-Legacy Content, 1908. **21**(2): p. 173-179.
38. Tesei, G., et al., *Lipid shape and packing are key for optimal design of pH-sensitive mRNA lipid nanoparticles.* Proceedings of the National Academy of Sciences, 2024. **121**(2): p. e2311700120.
39. Gilleron, J., et al., *Image-based analysis of lipid nanoparticle-mediated siRNA delivery, intracellular trafficking and endosomal escape.* Nat Biotechnol, 2013. **31**(7): p. 638-46.
40. Schlich, M., et al., *Cytosolic delivery of nucleic acids: The case of ionizable lipid nanoparticles.* Bioeng Transl Med, 2021. **6**(2): p. e10213.
41. Eygeris, Y., et al., *Chemistry of Lipid Nanoparticles for RNA Delivery.* Acc Chem Res, 2022. **55**(1): p. 2-12.
42. Wittrup, A., et al., *Visualizing lipid-formulated siRNA release from endosomes and target gene knockdown.* Nature Biotechnology, 2015. **33**(8): p. 870-876.
43. Patel, P., N.M. Ibrahim, and K. Cheng, *The Importance of Apparent pKa in the Development of Nanoparticles Encapsulating siRNA and mRNA.* Trends Pharmacol Sci, 2021. **42**(6): p. 448-460.
44. Whitehead, K.A., et al., *Degradable lipid nanoparticles with predictable in vivo siRNA delivery activity.* Nat Commun, 2014. **5**: p. 4277.
45. Hald Albertsen, C., et al., *The role of lipid components in lipid nanoparticles for vaccines and gene therapy.* Adv Drug Deliv Rev, 2022. **188**: p. 114416.
46. Israelachvili, J.N., S. Marcelja, and R.G. Horn, *Physical principles of membrane organization.* Q Rev Biophys, 1980. **13**(2): p. 121-200.
47. Sato, Y., et al., *Understanding structure-activity relationships of pH-sensitive cationic lipids facilitates the rational identification of promising lipid nanoparticles for delivering siRNAs in vivo.* J Control Release, 2019. **295**: p. 140-152.

48. Maier, M.A., et al., *Biodegradable lipids enabling rapidly eliminated lipid nanoparticles for systemic delivery of RNAi therapeutics.* Mol Ther, 2013. **21**(8): p. 1570-8.
49. Hajj, K.A. and K.A. Whitehead, *Tools for translation: non-viral materials for therapeutic mRNA delivery.* Nature Reviews Materials, 2017. **2**(10): p. 17056.
50. Verbeke, R., et al., *Three decades of messenger RNA vaccine development.* Nano Today, 2019. **28**: p. 100766.
51. Jung, H.N., et al., *Lipid nanoparticles for delivery of RNA therapeutics: Current status and the role of in vivo imaging.* Theranostics, 2022. **12**(17): p. 7509-7531.
52. LoPresti, S.T., et al., *The replacement of helper lipids with charged alternatives in lipid nanoparticles facilitates targeted mRNA delivery to the spleen and lungs.* J Control Release, 2022. **345**: p. 819-831.
53. Zhang, J., et al., *Interaction of cholesterol-conjugated ionizable amino lipids with biomembranes: lipid polymorphism, structure-activity relationship, and implications for siRNA delivery.* Langmuir, 2011. **27**(15): p. 9473-83.
54. Regelin, A.E., et al., *Biophysical and lipofection studies of DOTAP analogs.* Biochim Biophys Acta, 2000. **1464**(1): p. 151-64.
55. Harper, P.E., et al., *X-Ray Diffraction Structures of Some Phosphatidylethanolamine Lamellar and Inverted Hexagonal Phases*.* Biophysical Journal, 2001. **81**(5): p. 2693-2706.
56. Cheng, X. and R.J. Lee, *The role of helper lipids in lipid nanoparticles (LNPs) designed for oligonucleotide delivery.* Adv Drug Deliv Rev, 2016. **99**(Pt A): p. 129-137.
57. Koynova, R. and M. Caffrey, *Phases and phase transitions of the phosphatidylcholines.* Biochim Biophys Acta, 1998. **1376**(1): p. 91-145.
58. Kulkarni, J.A., et al., *The current landscape of nucleic acid therapeutics.* Nat Nanotechnol, 2021. **16**(6): p. 630-643.
59. Yanez Arteta, M., et al., *Successful reprogramming of cellular protein production through mRNA delivered by functionalized lipid nanoparticles.* Proc Natl Acad Sci U S A, 2018. **115**(15): p. E3351-E3360.
60. Sakurai, F., et al., *Effects of erythrocytes and serum proteins on lung accumulation of lipoplexes containing cholesterol or DOPE as a helper lipid in the single-pass rat lung perfusion system.* Eur J Pharm Biopharm, 2001. **52**(2): p. 165-72.
61. Mendonca, M.C.P., et al., *Design of lipid-based nanoparticles for delivery of therapeutic nucleic acids.* Drug Discov Today, 2023. **28**(3): p. 103505.
62. Rodrigueza, W.V., P.H. Pritchard, and M.J. Hope, *The influence of size and composition on the cholesterol mobilizing properties of liposomes in vivo.* Biochim Biophys Acta, 1993. **1153**(1): p. 9-19.
63. Murao, A., et al., *Targeting efficiency of galactosylated liposomes to hepatocytes in vivo: effect of lipid composition.* Pharm Res, 2002. **19**(12): p. 1808-14.
64. Kulkarni, J.A., et al., *On the Formation and Morphology of Lipid Nanoparticles Containing Ionizable Cationic Lipids and siRNA.* ACS Nano, 2018. **12**(5): p. 4787-4795.
65. Haberland, M.E. and J.A. Reynolds, *Self-association of cholesterol in aqueous solution.* Proc Natl Acad Sci U S A, 1973. **70**(8): p. 2313-6.
66. Pinkwart, K., et al., *Nanoscale dynamics of cholesterol in the cell membrane.* J Biol Chem, 2019. **294**(34): p. 12599-12609.
67. Kawaguchi, M., et al., *Effect of Cholesterol Content of Lipid Composition in mRNA-LNPs on the Protein Expression in the Injected Site and Liver After Local Administration in Mice.* J Pharm Sci, 2023. **112**(5): p. 1401-1410.
68. Borah, A., et al., *From in vitro to in Vivo: The Dominant role of PEG-Lipids in LNP performance.* Eur J Pharm Biopharm, 2025: p. 114726.
69. Prencipe, G., et al., *PEG branched polymer for functionalization of nanomaterials with ultralong blood circulation.* Journal of the American Chemical Society, 2009. **131**(13): p. 4783-4787.

70. Ge, X., et al., *Rationale and Application of PEGylated Lipid-Based System for Advanced Target Delivery of siRNA.* Front Pharmacol, 2020. **11**: p. 598175.
71. Belliveau, N.M., et al., *Microfluidic Synthesis of Highly Potent Limit-size Lipid Nanoparticles for In Vivo Delivery of siRNA.* Mol Ther Nucleic Acids, 2012. **1**(8): p. e37.
72. Göppert, T.M. and R.H. Müller, *Polysorbate-stabilized solid lipid nanoparticles as colloidal carriers for intravenous targeting of drugs to the brain: comparison of plasma protein adsorption patterns.* J Drug Target, 2005. **13**(3): p. 179-87.
73. He, Z.Y., et al., *Recent development of poly(ethylene glycol)-cholesterol conjugates as drug delivery systems.* Int J Pharm, 2014. **469**(1): p. 168-78.
74. McSweeney, M.D., et al., *Anaphylaxis to Pfizer/BioNTech mRNA COVID-19 Vaccine in a Patient With Clinically Confirmed PEG Allergy.* Front Allergy, 2021. **2**: p. 715844.
75. Kang, D.D., et al., *Engineering LNPs with polysarcosine lipids for mRNA delivery.* Bioact Mater, 2024. **37**: p. 86-93.
76. Wang, M.M., et al., *Elucidation of lipid nanoparticle surface structure in mRNA vaccines.* Scientific Reports, 2023. **13**(1): p. 16744.
77. Cheng, M.H.Y., et al., *Induction of Bleb Structures in Lipid Nanoparticle Formulations of mRNA Leads to Improved Transfection Potency.* Adv Mater, 2023. **35**(31): p. e2303370.
78. Robnik, B., K. Naumoska, and Z. Časar, *A novel testing approach for oxidative degradation dependent incompatibility of amine moiety containing drugs with pegs in solid-state.* Pharmaceutics, 2020. **12**(1): p. 37.
79. Jannin, V., J. Musakhanian, and D. Marchaud, *Approaches for the development of solid and semi-solid lipid-based formulations.* Advanced drug delivery reviews, 2008. **60**(6): p. 734-746.
80. Xu, Y., et al., *AGILE platform: a deep learning powered approach to accelerate LNP development for mRNA delivery.* Nature communications, 2024. **15**(1): p. 6305.
81. Miao, L., et al., *Delivery of mRNA vaccines with heterocyclic lipids increases anti-tumor efficacy by STING-mediated immune cell activation.* Nat Biotechnol, 2019. **37**(10): p. 1174-1185.
82. Chen, J., et al., *Combinatorial design of ionizable lipid nanoparticles for muscle-selective mRNA delivery with minimized off-target effects.* Proceedings of the National Academy of Sciences, 2023. **120**(50): p. e2309472120.
83. Guimaraes, G.J., J. Kim, and M.G. Bartlett, *Characterization of mRNA therapeutics.* Mass Spectrom Rev, 2024. **43**(5): p. 1066-1090.
84. Roberts, T.C., R. Langer, and M.J.A. Wood, *Advances in oligonucleotide drug delivery.* Nat Rev Drug Discov, 2020. **19**(10): p. 673-694.
85. Perenkov, A.D., et al., *In Vitro Transcribed RNA-Based Platform Vaccines: Past, Present, and Future.* Vaccines (Basel), 2023. **11**(10).
86. Kowalski, P.S., et al., *Delivering the messenger: advances in technologies for therapeutic mRNA delivery.* Molecular Therapy, 2019. **27**(4): p. 710-728.
87. FDA, *Summary Basis for Regulatory Action - MNEXSPIKE.* 2025.
88. Wang, J., et al., *Probing the interaction mechanisms of lipid nanoparticle-encapsulated mRNA with surfaces of diverse functional groups: Implication for mRNA transport.* Chemical Engineering Science, 2025. **301**: p. 120693.
89. Zhang, K., et al., *Duplex Structure of Double-Stranded RNA Provides Stability against Hydrolysis Relative to Single-Stranded RNA.* Environ Sci Technol, 2021. **55**(12): p. 8045-8053.
90. Han, J.P., et al., *In vivo delivery of CRISPR-Cas9 using lipid nanoparticles enables antithrombin gene editing for sustainable hemophilia A and B therapy.* Sci Adv, 2022. **8**(3): p. eabj6901.
91. Chheda, U., et al., *Factors Affecting Stability of RNA - Temperature, Length, Concentration, pH, and Buffering Species.* J Pharm Sci, 2024. **113**(2): p. 377-385.

92. Athaydes Seabra Ferreira, H., et al., *Cryoprotectant optimization for enhanced stability and transfection efficiency of pDNA-loaded ionizable lipid nanoparticles.* Int J Pharm, 2024. **665**: p. 124696.
93. Nakamura, K., K. Aihara, and T. Ishida, *Importance of Process Parameters Influencing the Mean Diameters of siRNA-Containing Lipid Nanoparticles (LNPs) on the in Vitro Activity of Prepared LNPs.* Biol Pharm Bull, 2022. **45**(4): p. 497-507.
94. Biswas, A., et al., *Advances in top-down and bottom-up surface nanofabrication: techniques, applications & future prospects.* Adv Colloid Interface Sci, 2012. **170**(1-2): p. 2-27.
95. Wang, X., et al., *Preparation of selective organ-targeting (SORT) lipid nanoparticles (LNPs) using multiple technical methods for tissue-specific mRNA delivery.* Nature Protocols, 2023. **18**(1): p. 265-291.
96. Subraveti, S.N., et al., *Synthesizing Lipid Nanoparticles by Turbulent Flow in Confined Impinging Jet Mixers.* JoVE, 2024(210): p. e67047.
97. Younis, M.A., et al., *Ultra-small lipid nanoparticles encapsulating sorafenib and midkine-siRNA selectively-eradicate sorafenib-resistant hepatocellular carcinoma in vivo.* Journal of Controlled Release, 2021. **331**: p. 335-349.
98. Naderi Sohi, A., et al., *Development of an mRNA-LNP Vaccine against SARS-CoV-2: Evaluation of Immune Response in Mouse and Rhesus Macaque.* Vaccines (Basel), 2021. **9**(9).
99. Biscaia-Caleiras, M., et al., *Rational formulation and industrial manufacturing of lipid-based complex injectables: Landmarks and trends.* J Control Release, 2024. **373**: p. 617-639.
100. Agency, E.M., *Guideline on the quality aspects of mRNA vaccines.* 2025.
101. Shepherd, S.J., D. Issadore, and M.J. Mitchell, *Microfluidic formulation of nanoparticles for biomedical applications.* Biomaterials, 2021. **274**: p. 120826.
102. Roces, C.B., et al., *Manufacturing Considerations for the Development of Lipid Nanoparticles Using Microfluidics.* Pharmaceutics, 2020. **12**(11).
103. Cytiva. *Cytiva Nanoparticle Formulation Systems.* 2025; Available from: https://www.cytivalifesciences.com/en/us/shop/lipid-nanoparticle-instruments-and-reagents/nanoparticle-formulation-systems?sort=NameAsc&chunk=1.
104. Webb, C., et al., *Using microfluidics for scalable manufacturing of nanomedicines from bench to GMP: A case study using protein-loaded liposomes.* Int J Pharm, 2020. **582**: p. 119266.
105. Osouli-Bostanabad, K., et al., *Microfluidic Manufacture of Lipid-Based Nanomedicines.* Pharmaceutics, 2022. **14**(9).
106. Maeki, M., et al., *Understanding the formation mechanism of lipid nanoparticles in microfluidic devices with chaotic micromixers.* PLoS One, 2017. **12**(11): p. e0187962.
107. Abdelkarim, M., et al., *Hydrodynamic focusing to synthesize lipid-based nanoparticles: Computational and experimental analysis of chip design and formulation parameters.* J Control Release, 2025. **387**: p. 114192.
108. Cui, H.-h., Z.-h. Silber-Li, and S.-n. Zhu, *Flow characteristics of liquids in microtubes driven by a high pressure.* Physics of fluids, 2004. **16**(5): p. 1803-1810.
109. Guimaraes Sa Correia, M., et al., *Microfluidic manufacturing of phospholipid nanoparticles: Stability, encapsulation efficacy, and drug release.* Int J Pharm, 2017. **516**(1-2): p. 91-99.
110. Kupetz, E. and H. Bunjes, *Lipid nanoparticles: drug localization is substance-specific and achievable load depends on the size and physical state of the particles.* J Control Release, 2014. **189**: p. 54-64.
111. McMillan, C., et al., *Tailoring lipid nanoparticle dimensions through manufacturing processes.* RSC Pharm, 2024. **1**(4): p. 841-853.
112. Zhao, P., et al., *Long-term storage of lipid-like nanoparticles for mRNA delivery.* Bioact Mater, 2020. **5**(2): p. 358-363.

113. Davidson, C.G., et al., *The use of orthogonal analytical approaches to profile lipid nanoparticle physicochemical attributes.* Nano Futures, 2024. **8**(3): p. 035001.
114. Agency, E.M., *Spikevax - Summary Of Product Characteristics*. 2021.
115. FDA, *mNEXSPIKE - Prescribing Information* 2025.
116. Gilleron, J., et al., *Image-based analysis of lipid nanoparticle–mediated siRNA delivery, intracellular trafficking and endosomal escape.* Nature biotechnology, 2013. **31**(7): p. 638-646.
117. Sahay, G., et al., *Efficiency of siRNA delivery by lipid nanoparticles is limited by endocytic recycling.* Nature Biotechnology, 2013. **31**(7): p. 653-658.
118. Jayaraman, M., et al., *Maximizing the potency of siRNA lipid nanoparticles for hepatic gene silencing in vivo.* Angew Chem Int Ed Engl, 2012. **51**(34): p. 8529-33.
119. Zhang, C., et al., *Modification of Lipid-Based Nanoparticles: An Efficient Delivery System for Nucleic Acid-Based Immunotherapy.* Molecules, 2022. **27**(6).
120. Menon, I., et al., *Fabrication of active targeting lipid nanoparticles: Challenges and perspectives.* Materials Today Advances, 2022. **16**: p. 100299.
121. Digiacomo, L., et al., *PEGylation-Dependent Cell Uptake of Lipid Nanoparticles Revealed by Spatiotemporal Correlation Spectroscopy.* ACS Pharmacol Transl Sci, 2024. **7**(10): p. 3004-3010.
122. Tyrrell, D.A., V.J. Richardson, and B.E. Ryman, *The effect of serum protein fractions on liposome-cell interactions in cultured cells and the perfused rat liver.* Biochim Biophys Acta, 1977. **497**(2): p. 469-80.
123. Lynch, I. and K.A. Dawson, *Protein-nanoparticle interactions.* Nano Today, 2008. **3**(1): p. 40-47.
124. Monopoli, M.P., et al., *Biomolecular coronas provide the biological identity of nanosized materials.* Nat Nanotechnol, 2012. **7**(12): p. 779-86.
125. Gharibi, H., et al., *A uniform data processing pipeline enables harmonized nanoparticle protein corona analysis across proteomics core facilities.* Nat Commun, 2024. **15**(1): p. 342.
126. UniProt. *Universal Protein Resource*. Available from: https://www.uniprot.org/.
127. Weaving, G., G.F. Batstone, and R.G. Jones, *Age and sex variation in serum albumin concentration: an observational study.* Ann Clin Biochem, 2016. **53**(Pt 1): p. 106-11.
128. Dati, F., et al., *Consensus of a group of professional societies and diagnostic companies on guidelines for interim reference ranges for 14 proteins in serum based on the standardization against the IFCC/BCR/CAP Reference Material (CRM 470). International Federation of Clinical Chemistry. Community Bureau of Reference of the Commission of the European Communities. College of American Pathologists.* Eur J Clin Chem Clin Biochem, 1996. **34**(6): p. 517-20.
129. Lowe, G., et al., *Epidemiology of coagulation factors, inhibitors and activation markers: The Third Glasgow MONICA Survey I. Illustrative reference ranges by age, sex and hormone use.* British journal of haematology, 1997. **97**(4): p. 775-784.
130. Obici, L., et al., *The new apolipoprotein A-I variant leu(174) --> Ser causes hereditary cardiac amyloidosis, and the amyloid fibrils are constituted by the 93-residue N-terminal polypeptide.* Am J Pathol, 1999. **155**(3): p. 695-702.
131. Florea, G., et al., *Apolipoprotein A-II, a Player in Multiple Processes and Diseases.* Biomedicines, 2022. **10**(7).
132. Ogun, A.S. and A. Adeyinka, *Biochemistry, transferrin.* 2018.
133. Trust, S.T.H.N.F. *Complement C3 and C4*. 2022.
134. Naryzny, S.N. and O.K. Legina, *Haptoglobin as a Biomarker.* Biochem Mosc Suppl B Biomed Chem, 2021. **15**(3): p. 184-198.
135. T. Carroll, M.K., G. McElvaney, *Laboratory Testing for Alpha-1 Antitrypsin Deficiency (AATD)*. 2019.
136. Piktel, E., et al., *Plasma gelsolin: indicator of inflammation and its potential as a diagnostic tool and therapeutic target.* International journal of molecular sciences, 2018. **19**(9): p. 2516.

137. Digiacomo, L., et al., *An apolipoprotein-enriched biomolecular corona switches the cellular uptake mechanism and trafficking pathway of lipid nanoparticles.* Nanoscale, 2017. **9**(44): p. 17254-17262.
138. Rampado, R., et al., *Recent Advances in Understanding the Protein Corona of Nanoparticles and in the Formulation of "Stealthy" Nanomaterials.* Frontiers in Bioengineering and Biotechnology, 2020. **8**.
139. Vogt, C., et al., *Proteomics Analysis Reveals Distinct Corona Composition on Magnetic Nanoparticles with Different Surface Coatings: Implications for Interactions with Primary Human Macrophages.* PLoS One, 2015. **10**(10): p. e0129008.
140. Kelly, P.M., et al., *Mapping protein binding sites on the biomolecular corona of nanoparticles.* Nat Nanotechnol, 2015. **10**(5): p. 472-9.
141. Vroman, L., *Effect of absorbed proteins on the wettability of hydrophilic and hydrophobic solids.* Nature, 1962. **196**: p. 476-7.
142. Cedervall, T., et al., *Understanding the nanoparticle-protein corona using methods to quantify exchange rates and affinities of proteins for nanoparticles.* Proc Natl Acad Sci U S A, 2007. **104**(7): p. 2050-5.
143. Nel, A.E., et al., *Understanding biophysicochemical interactions at the nano-bio interface.* Nat Mater, 2009. **8**(7): p. 543-57.
144. Cedervall, T., et al., *Detailed identification of plasma proteins adsorbed on copolymer nanoparticles.* Angew Chem Int Ed Engl, 2007. **46**(30): p. 5754-6.
145. Tenzer, S., et al., *Rapid formation of plasma protein corona critically affects nanoparticle pathophysiology.* Nat Nanotechnol, 2013. **8**(10): p. 772-81.
146. Chakraborty, D., K.R. Ethiraj, and A. Mukherjee, *Understanding the relevance of protein corona in nanoparticle-based therapeutics and diagnostics.* RSC Adv, 2020. **10**(45): p. 27161-27172.
147. Xia, Z., et al., *Nanoscale surface curvature modulates nanoparticle-protein interactions.* Colloids Surf B Biointerfaces, 2020. **190**: p. 110960.
148. Wallevik, K., *Isoelectric focusing of bovine serum albumin: Influence of binding of carrier ampholytes.* Biochimica et Biophysica Acta (BBA) - Protein Structure, 1973. **322**(1): p. 75-87.
149. Lai, W., et al., *Interaction of gold and silver nanoparticles with human plasma: Analysis of protein corona reveals specific binding patterns.* Colloids Surf B Biointerfaces, 2017. **152**: p. 317-325.
150. Voke, E., et al., *Protein corona formed on lipid nanoparticles compromises delivery efficiency of mRNA cargo.* Nat Commun, 2025. **16**(1): p. 8699.
151. Walkey, C.D., et al., *Nanoparticle size and surface chemistry determine serum protein adsorption and macrophage uptake.* J Am Chem Soc, 2012. **134**(4): p. 2139-47.
152. Lundqvist, M., et al., *Nanoparticle size and surface properties determine the protein corona with possible implications for biological impacts.* Proceedings of the National Academy of Sciences of the United States of America, 2008. **105**(38): p. 14265-14270.
153. Moghimi, S.M., A.C. Hunter, and J.C. Murray, *Long-circulating and target-specific nanoparticles: theory to practice.* Pharmacol Rev, 2001. **53**(2): p. 283-318.
154. Gustafson, H.H., et al., *Nanoparticle Uptake: The Phagocyte Problem.* Nano Today, 2015. **10**(4): p. 487-510.
155. Salvati, A., et al., *Transferrin-functionalized nanoparticles lose their targeting capabilities when a biomolecule corona adsorbs on the surface.* Nature Nanotechnology, 2013. **8**(2): p. 137-143.
156. Akinc, A., et al., *Targeted delivery of RNAi therapeutics with endogenous and exogenous ligand-based mechanisms.* Mol Ther, 2010. **18**(7): p. 1357-64.
157. Ritz, S., et al., *Protein Corona of Nanoparticles: Distinct Proteins Regulate the Cellular Uptake.* Biomacromolecules, 2015. **16**(4): p. 1311-1321.

158. Lara, S., et al., *Identification of Receptor Binding to the Biomolecular Corona of Nanoparticles.* ACS Nano, 2017. **11**(2): p. 1884-1893.
159. Kulkarni, J.A., et al., *Lipid Nanoparticle Technology for Clinical Translation of siRNA Therapeutics.* Acc Chem Res, 2019. **52**(9): p. 2435-2444.
160. Sebastiani, F., et al., *Apolipoprotein E Binding Drives Structural and Compositional Rearrangement of mRNA-Containing Lipid Nanoparticles.* ACS Nano, 2021. **15**(4): p. 6709-6722.
161. Chu, R., et al., *Lipid nanoparticles as the drug carrier for targeted therapy of hepatic disorders.* J Mater Chem B, 2024. **12**(20): p. 4759-4784.
162. Woitok, M.M., et al., *Lipid-encapsulated siRNA for hepatocyte-directed treatment of advanced liver disease.* Cell Death Dis, 2020. **11**(5): p. 343.
163. Kim, M., et al., *Engineered ionizable lipid nanoparticles for targeted delivery of RNA therapeutics into different types of cells in the liver.* Sci Adv, 2021. **7**(9).
164. Crielaard, B.J., et al., *An in vitro assay based on surface plasmon resonance to predict the in vivo circulation kinetics of liposomes.* J Control Release, 2011. **156**(3): p. 307-14.
165. Owens, D.E., 3rd and N.A. Peppas, *Opsonization, biodistribution, and pharmacokinetics of polymeric nanoparticles.* Int J Pharm, 2006. **307**(1): p. 93-102.
166. Kim, H.R., et al., *Analysis of plasma protein adsorption onto PEGylated nanoparticles by complementary methods: 2-DE, CE and Protein Lab-on-chip® system.* Electrophoresis, 2007. **28**(13): p. 2252-2261.
167. Pozzi, D., et al., *Effect of polyethyleneglycol (PEG) chain length on the bio-nano-interactions between PEGylated lipid nanoparticles and biological fluids: from nanostructure to uptake in cancer cells.* Nanoscale, 2014. **6**(5): p. 2782-92.
168. Mak, I.W., N. Evaniew, and M. Ghert, *Lost in translation: animal models and clinical trials in cancer treatment.* American journal of translational research, 2014. **6**(2): p. 114.
169. Francia, V., et al., *A magnetic separation method for isolating and characterizing the biomolecular corona of lipid nanoparticles.* Proc Natl Acad Sci U S A, 2024. **121**(11): p. e2307803120.
170. Daramy, K., et al., *Nanoparticle Isolation from Biological Media for Protein Corona Analysis: The Impact of Incubation and Recovery Protocols on Nanoparticle Properties.* J Pharm Sci, 2023.
171. Feingold, K.R., *Introduction to Lipids and Lipoproteins*, in *Endotext*, K.R. Feingold, et al., Editors. 2000: South Dartmouth (MA).
172. Giridhar, G., R.K.N.R. Manepalli, and G. Apparao, *Chapter 3 - Size-Exclusion Chromatography*, in *Thermal and Rheological Measurement Techniques for Nanomaterials Characterization*, S. Thomas, et al., Editors. 2017, Elsevier. p. 51-65.
173. Francia, V.Y., K.; Deville, S.; Reker-Smit, C.; Nelissen, I.; Salvati, A., *Corona Composition Can Affect the Mechanisms Cells Use to Internalize Nanoparticles.* Acs Nano., 2019.
174. Liau, B., et al., *Quantitative analysis of mRNA-lipid nanoparticle stability in human plasma and serum by size-exclusion chromatography coupled with dual-angle light scattering.* Nanomedicine, 2024. **58**: p. 102745.
175. Caputo, F., et al., *Measuring Particle Size Distribution by Asymmetric Flow Field Flow Fractionation: A Powerful Method for the Preclinical Characterization of Lipid-Based Nanoparticles.* Mol Pharm, 2019. **16**(2): p. 756-767.
176. Abdulrahman, R., Punnabhum, P., Daramy, K., Davidson, C., Treacher, K., Capomaccio, R., Vasey, C., Perrie, Y., Rattray, Z. *Investigating the critical quality attributes of lipid nanoparticle prototypes in protein containing media*. in *The Federation of Analytical Chemistry and Spectroscopy Societies (FACSS) and the SciX*. 2023. Nevada, USA. .
177. Abdulrahman, R., et al., *Frit-inlet asymmetric flow field-flow fractionation for the analysis of lipid nanoparticle-protein interactions.* J Chromatogr A, 2025. **1743**: p. 465663.

178. Donno, R., et al., *Nanomanufacturing through microfluidic-assisted nanoprecipitation: Advanced analytics and structure-activity relationships.* International Journal of Pharmaceutics, 2017. **534**(1-2): p. 97-107.
179. Bittrich, E., et al., *Structural Profiling of Lipid Nanoparticles at Sub-10 nm Resolution via Online AF4 Coupled to SAXS and SANS.* 2025.
180. Agency., E.M., *Guideline on the quality aspects of mRNA vaccines.* 2025, European Medicines Agency.
181. Taha, M.S., et al., *Critical quality attributes in the development of therapeutic nanomedicines toward clinical translation.* Drug Deliv Transl Res, 2020. **10**(3): p. 766-790.
182. Lindsay, S., et al., *Exploring the Challenges of Lipid Nanoparticle Development: The In Vitro-In Vivo Correlation Gap.* Vaccines (Basel), 2025. **13**(4).
183. Simon, C.G., Jr., et al., *Orthogonal and complementary measurements of properties of drug products containing nanomaterials.* J Control Release, 2023. **354**: p. 120-127.
184. Singh, R. and J.W. Lillard, Jr., *Nanoparticle-based targeted drug delivery.* Exp Mol Pathol, 2009. **86**(3): p. 215-23.
185. Barua, S. and S. Mitragotri, *Challenges associated with Penetration of Nanoparticles across Cell and Tissue Barriers: A Review of Current Status and Future Prospects.* Nano Today, 2014. **9**(2): p. 223-243.
186. Zhang, J.X., Z.; Zhang, N.; Zhong, J., *Nanosuspension drug delivery system: preparation, characterization, postproduction processing, dosage form, and application.* 2017. 413-443.
187. Griffiths, P.C., et al., *Probing the interaction of nanoparticles with mucin for drug delivery applications using dynamic light scattering.* Eur J Pharm Biopharm, 2015. **97**(Pt A): p. 218-22.
188. Stokes, G., *On the theories ofinternal friction offluids in motion.* Trans Cam Philos Soc, 1845(8): p. 287-305.
189. Amin, S.B., G.; Pathak, J.; Roberts, C.; Sarangapani, P., *Protein aggregation, particle formation, characterization & rheology.* Current Opinion in Colloid & Interface Science, 2014. **5**(19): p. 438-449.
190. Danaei, M., et al., *Impact of Particle Size and Polydispersity Index on the Clinical Applications of Lipidic Nanocarrier Systems.* Pharmaceutics, 2018. **10**(2).
191. Letao Xu, X.W., Yun Liu, Guangze Yang, Robert J. Falconer, Chun-Xia Zhao, *Lipid Nanoparticles for Drug Delivery.* Advanced NanoBiomed Research, 2021. **2**(2).
192. Vogelaar, A., et al., *Use of Microfluidics to Prepare Lipid-Based Nanocarriers.* Pharmaceutics, 2023. **15**(4).
193. Sadat, S.M., S.T. Jahan, and A. Haddadi, *Effects of size and surface charge of polymeric nanoparticles on in vitro and in vivo applications.* Journal of Biomaterials and Nanobiotechnology, 2016. **7**(02): p. 91.
194. FDA, *Liposome Drug Products: Chemistry, Manufacturing, and Controls; Human Pharmacokinetics and Bioavailability; and Labeling Documentation*. 2018.
195. Filipe, V., A. Hawe, and W. Jiskoot, *Critical evaluation of Nanoparticle Tracking Analysis (NTA) by NanoSight for the measurement of nanoparticles and protein aggregates.* Pharm Res, 2010. **27**(5): p. 796-810.
196. Comfort, N., et al., *Nanoparticle Tracking Analysis for the Quantification and Size Determination of Extracellular Vesicles.* J Vis Exp, 2021(169).
197. Fuller, M. and I. Köper, *Polyelectrolyte-Coated Gold Nanoparticles: The Effect of Salt and Polyelectrolyte Concentration on Colloidal Stability.* Polymers (Basel), 2018. **10**(12).
198. Smith, M.C., et al., *Zeta potential: a case study of cationic, anionic, and neutral liposomes.* Anal Bioanal Chem, 2017. **409**(24): p. 5779-5787.
199. Alexis, F., et al., *Factors affecting the clearance and biodistribution of polymeric nanoparticles.* Mol Pharm, 2008. **5**(4): p. 505-15.

200. Ding, S., et al., *Overcoming blood-brain barrier transport: Advances in nanoparticle-based drug delivery strategies.* Mater Today (Kidlington), 2020. **37**: p. 112-125.
201. Simberg, D., et al., *DOTAP (and other cationic lipids): chemistry, biophysics, and transfection.* Crit Rev Ther Drug Carrier Syst, 2004. **21**(4): p. 257-317.
202. Wall, S., *The history of electrokinetic phenomena.* Current Opinion in Colloid & Interface Science, 2010. **15**(3): p. 119-124.
203. Carvalho, P.M., et al., *Application of Light Scattering Techniques to Nanoparticle Characterization and Development.* Front Chem, 2018. **6**: p. 237.
204. Delgado, A.V., et al., *Measurement and interpretation of electrokinetic phenomena.* J Colloid Interface Sci, 2007. **309**(2): p. 194-224.
205. Ma, Y., R. VanKeulen-Miller, and O.S. Fenton, *mRNA lipid nanoparticle formulation, characterization and evaluation.* Nat Protoc, 2025. **20**(9): p. 2618-2651.
206. Arezki, Y., et al., *Surface charge influences protein corona, cell uptake and biological effects of carbon dots.* Nanoscale, 2022. **14**(39): p. 14695-14710.
207. Giddings, J.C., *Field-flow fractionation: analysis of macromolecular, colloidal, and particulate materials.* Science, 1993. **260**(5113): p. 1456-65.
208. Daniel, S., et al., *Quality by Design for enabling RNA platform production processes.* Trends Biotechnol, 2022. **40**(10): p. 1213-1228.
209. Mildner, R., et al., *Improved multidetector asymmetrical-flow field-flow fractionation method for particle sizing and concentration measurements of lipid-based nanocarriers for RNA delivery.* Eur J Pharm Biopharm, 2021. **163**: p. 252-265.
210. Kim, Y.B., et al., *Evaluation of exosome separation from human serum by frit-inlet asymmetrical flow field-flow fractionation and multiangle light scattering.* Anal Chim Acta, 2020. **1124**: p. 137-145.
211. Ferreira, H.M.-A., B.; Montoro A.; Encinar, JR.; Costa-Fernández, J., *Capabilities of asymmetrical flow field – Flow fractionation on-line coupled to different detectors for characterization of water-stabilized quantum dots bioconjugated to biomolecules.* Talenta, 2020. **206**.
212. Worldwide, M.I., *Static light scattering technologies for GPC/SEC explained.* 2013.
213. Carpenter, D.K., *Dynamic Light Scattering with Applications to Chemistry, Biology, and Physics (Berne, Bruce J.; Pecora, Robert).* Journal of Chemical Education, 1977. **54**(10): p. A430.
214. Laboratory, E.N.C., *FFF-MALS method development and measurements of size and molecular weight*. 2016.
215. *EUNCL - Measuring particle size distribution of nanoparticle enabled medicinal products, the joint view of EUNCL and NCI-NCL. A step by step approach combining orthogonal measurements with increasing complexity*
216. Quattrini, F., et al., *Correction to: Asymmetric flow field-flow fractionation as a multifunctional technique for the characterization of polymeric nanocarriers.* Drug Deliv Transl Res, 2021. **11**(2): p. 396.
217. Some D, J.C., *WP2611: Characterization of nanopharmaceuticals with field-flow frac-tionation and light scattering (FFF-MALS-DLS)*
218. Hu, Y., R.M. Crist, and J.D. Clogston, *The utility of asymmetric flow field-flow fractionation for preclinical characterization of nanomedicines.* Anal Bioanal Chem, 2020. **412**(2): p. 425-438.
219. Patil, S.V., Lee, D. M., Ratna, B. R., Ahmed, K., Kennedy, E. M., and McNeil, S. E. , *Characterization of Nanoparticles Intended for Drug Delivery*. Vol. 697. 2011: Humana Press, Springer.
220. Qureshi, R.K.W., *Optimization of Asymmetrical Flow Field-Flow Fractionation.* 2011.

221. Takechi-Haraya, Y., et al., *Current Status and Challenges of Analytical Methods for Evaluation of Size and Surface Modification of Nanoparticle-Based Drug Formulations.* AAPS PharmSciTech, 2022. **23**(5): p. 150.
222. Wadhwa, A., et al., *Opportunities and Challenges in the Delivery of mRNA-based Vaccines.* Pharmaceutics, 2020. **12**(2).
223. Aggarwal, P., et al., *Nanoparticle interaction with plasma proteins as it relates to particle biodistribution, biocompatibility and therapeutic efficacy.* Advanced Drug Delivery Reviews, 2009. **61**(6): p. 428-437.
224. Liu, K., et al., *Multiomics analysis of naturally efficacious lipid nanoparticle coronas reveals high-density lipoprotein is necessary for their function.* Nat Commun, 2023. **14**(1): p. 4007.
225. Ai, L., et al., *Lyophilized mRNA-lipid nanoparticle vaccines with long-term stability and high antigenicity against SARS-CoV-2.* Cell Discov, 2023. **9**(1): p. 9.
226. Packer, M., et al., *A novel mechanism for the loss of mRNA activity in lipid nanoparticle delivery systems.* Nat Commun, 2021. **12**(1): p. 6777.
227. (EMA), E.M.A., *Liposome Drug Products*. 2018.
228. Ramirez, L.M.F., et al., *Characterization of dextran particle size: How frit-inlet asymmetrical flow field-flow fractionation (FI-AF4) coupled online with dynamic light scattering (DLS) leads to enhanced size distribution.* Journal of Chromatography A, 2021. **1653**: p. 462404.
229. Klein, M., et al., *Advanced nanomedicine characterization by DLS and AF4-UV-MALS: Application to a HIV nanovaccine.* J Pharm Biomed Anal, 2020. **179**: p. 113017.
230. Velimirovic, M., et al., *Joint Forces of HR-Spicp-MS and EAF4-MALS for Characterization of Gold Nanorods Conjugated with Synthetic Glycopolymers.* Materials Proceedings, 2021. **4**(1): p. 93.
231. Graewert, M.A., et al., *Quantitative size-resolved characterization of mRNA nanoparticles by in-line coupling of asymmetrical-flow field-flow fractionation with small angle X-ray scattering.* Sci Rep, 2023. **13**(1): p. 15764.
232. Bian, J., et al., *The Power of Field-Flow Fractionation in Characterization of Nanoparticles in Drug Delivery.* Molecules, 2023. **28**(10).
233. Zhang, T., et al., *Optimized lipid nanoparticles (LNPs) for organ-selective nucleic acids delivery in vivo.* iScience, 2024. **27**(6): p. 109804.
234. Agency., E.M., *Onpattro - Summary Of Product Characteristics.* 2018.
235. Agency, E.M., *Comirnaty - **Summary Of Product Characteristics***. 2020.
236. Standardization, E.C.F., *Nanotechnologies — Analysis of nano-objects using asymmetrical-flow and centrifugal field-flow fractionation*. 2021.
237. Gervais, C., et al., *Cleaning Marble with Ammonium Citrate.* Studies in Conservation, 2010. **55**: p. 164-176.
238. Babick, F., *Dynamic light scattering (DLS)*, in *Characterization of nanoparticles*. 2020, Elsevier. p. 137-172.
239. Lin, S.-C., et al., *Compatible blends of polyvinylidene fluoride and aromatic polyimide*. 2001, Google Patents.
240. Darvishmanesh, S., et al., *Novel polyphenylsulfone membrane for potential use in solvent nanofiltration.* Journal of Membrane Science, 2011. **379**(1-2): p. 60-68.
241. Ma, X., et al., *Exploration of mRNA nanoparticles based on DOTAP through optimization of the helper lipids.* Biotechnol J, 2023. **18**(11): p. e2300123.
242. Ball, R.L., P. Bajaj, and K.A. Whitehead, *Achieving long-term stability of lipid nanoparticles: examining the effect of pH, temperature, and lyophilization.* Int J Nanomedicine, 2017. **12**: p. 305-315.
243. Kamiya, M., et al., *Stability Study of mRNA-Lipid Nanoparticles Exposed to Various Conditions Based on the Evaluation between Physicochemical Properties and Their Relation with Protein Expression Ability.* Pharmaceutics, 2022. **14**(11).

244. Muramatsu, H., et al., *Lyophilization provides long-term stability for a lipid nanoparticle-formulated, nucleoside-modified mRNA vaccine.* Mol Ther, 2022. **30**(5): p. 1941-1951.
245. Hou, X., et al., *Lipid nanoparticles for mRNA delivery.* Nature Reviews Materials, 2021. **6**(12): p. 1078-1094.
246. Shirane, D., et al., *Development of an alcohol dilution–lyophilization method for preparing lipid nanoparticles containing encapsulated siRNA.* Biological and Pharmaceutical Bulletin, 2018. **41**(8): p. 1291-1294.
247. Abdulrahman, R., Ibrahem, H., Mahmood, A., Treacher, K. and R. Capomaccio, Vasey, C., Perrie, Y., Rattray, Z. . *Assessing lipid nanoparticle protein corona formation and cytocompatibility.* in *The Academy of Pharmaceutical Sciences*. 2023. Reading, UK: British Journal of Pharmacy.
248. Simonsen, J.B., *A perspective on bleb and empty LNP structures.* Journal of Controlled Release, 2024. **373**: p. 952-961.
249. Hadji, H. and K. Bouchemal, *Effect of micro- and nanoparticle shape on biological processes.* Journal of Controlled Release, 2022. **342**: p. 93-110.
250. McMillan, C., et al., *Influence of ionisable lipid and sterol variations on lipid nanoparticle properties and performance.* Journal of Controlled Release, 2025: p. 114056.
251. Preston, K.B. and T.W. Randolph, *Stability of lyophilized and spray dried vaccine formulations.* Advanced Drug Delivery Reviews, 2021. **171**: p. 50-61.
252. Patel, S., et al., *Naturally-occurring cholesterol analogues in lipid nanoparticles induce polymorphic shape and enhance intracellular delivery of mRNA.* Nat Commun, 2020. **11**(1): p. 983.
253. Zhang, L., et al., *Role of PEGylated lipid in lipid nanoparticle formulation for in vitro and in vivo delivery of mRNA vaccines.* J Control Release, 2025. **380**: p. 108-124.
254. Payne, J.E.C.P., *Ionizable Cationic Lipid for RNA Delivery*. 2017, Arcturus Therapeutics, Inc.: United States.
255. Hussain, M., et al., *Mind the Age Gap: Expanding the Age Window for mRNA Vaccine Testing in Mice.* Vaccines (Basel), 2025. **13**(4).
256. Smith, O.A., et al., *Impact of Metabolic States on SARS-CoV-2 Vaccine Responses in Mouse Models of Obesity and Diabetes.* COVID, 2025. **5**(1).
257. Rurik, J.G., et al., *CAR T cells produced in vivo to treat cardiac injury.* Science, 2022. **375**(6576): p. 91-96.
258. Nakamura, T., et al., *The Effect of Size and Charge of Lipid Nanoparticles Prepared by Microfluidic Mixing on Their Lymph Node Transitivity and Distribution.* Mol Pharm, 2020. **17**(3): p. 944-953.
259. Lee, K., et al., *Adjuvant incorporated lipid nanoparticles for enhanced mRNA-mediated cancer immunotherapy.* Biomater Sci, 2020. **8**(4): p. 1101-1105.
260. Zhang, Y., et al., *STING Agonist-Derived LNP-mRNA Vaccine Enhances Protective Immunity Against SARS-CoV-2.* Nano Lett, 2023. **23**(7): p. 2593-2600.
261. Materials, A.S.f.T.a., *Standard Practice for Workforce Education in Nanotechnology Characterization*. 2020.
262. Caputo, F., et al., *Toward an international standardisation roadmap for nanomedicine.* Drug Deliv Transl Res, 2024. **14**(9): p. 2578-2588.
263. Guerrini, G., et al., *Characterization of nanoparticles-based vaccines for COVID-19.* Nature Nanotechnology, 2022. **17**(6): p. 570-576.
264. Forrester, J., et al., *Low-Cost Microfluidic Mixers: Are They up to the Task?* Pharmaceutics, 2025. **17**(5): p. 566.
265. Fedotov, P.S., et al., *Fractionation and characterization of nano- and microparticles in liquid media.* Anal Bioanal Chem, 2011. **400**(6): p. 1787-804.
266. Kuntsche, J., C. Decker, and A. Fahr, *Analysis of liposomes using asymmetrical flow field-flow fractionation: separation conditions and drug/lipid recovery.* J Sep Sci, 2012. **35**(15): p. 1993-2001.

267. Hupfeld, S., D. Ausbacher, and M. Brandl, *Asymmetric flow field-flow fractionation of liposomes: 2. Concentration detection and adsorptive loss phenomena.* J Sep Sci, 2009. **32**(20): p. 3555-61.
268. Decker, C., et al., *Selective partitioning of cholesterol and a model drug into liposomes of varying size.* Chemistry and Physics of Lipids, 2012. **165**(5): p. 520-529.
269. Plavchak, C.L., et al., *Utilization of AF4 for characterizing complex nanomaterial drug products: Reexamining sample recovery and its impact on particle size distribution as a quality attribute.* Journal of Chromatography A, 2025. **1743**: p. 465703.
270. Hansen, M. and J.D. Clogston, *Nanoparticle Size Distribution and Stability Assessment Using Asymmetric-Flow Field-Flow Fractionation.* Methods Mol Biol, 2024. **2789**: p. 21-29.
271. Bohsen, M.S., et al., *Interaction of liposomes with bile salts investigated by asymmetric flow field-flow fractionation (AF4): A novel approach for stability assessment of oral drug carriers.* Eur J Pharm Sci, 2023. **182**: p. 106384.
272. Jia, X., et al., *Enabling online determination of the size-dependent RNA content of lipid nanoparticle-based RNA formulations.* J Chromatogr B Analyt Technol Biomed Life Sci, 2021. **1186**: p. 123015.
273. Caputo, F., et al., *Asymmetric-flow field-flow fractionation for measuring particle size, drug loading and (in)stability of nanopharmaceuticals. The joint view of European Union Nanomedicine Characterization Laboratory and National Cancer Institute - Nanotechnology Characterization Laboratory.* J Chromatogr A, 2021. **1635**: p. 461767.
274. Gasco, R., et al., *Asymmetric flow field-flow fractionation for comprehensive characterization of hetero-aggregates made of nano-silver and extracellular polymeric substances.* J Chromatogr A, 2025. **1739**: p. 465507.
275. Plavchak, C.L., et al., *Determination of particle number concentration for biological particles using AF4-MALS: Dependencies on light scattering model and refractive index.* J Chromatogr A, 2024. **1737**: p. 465460.
276. Shakiba, S., et al., *Asymmetric flow field-flow fractionation (AF4) with fluorescence and multi-detector analysis for direct, real-time, size-resolved measurements of drug release from polymeric nanoparticles.* J Control Release, 2021. **338**: p. 410-421.
277. Hiemenz, C., et al., *Characterization of Virus Particles and Submicron-Sized Particulate Impurities in Recombinant Adeno-Associated Virus Drug Product.* J Pharm Sci, 2023. **112**(8): p. 2190-2202.
278. Ventouri, I.K., et al., *Characterizing Non-covalent Protein Complexes Using Asymmetrical Flow Field-Flow Fractionation On-Line Coupled to Native Mass Spectrometry.* Anal Chem, 2023. **95**(19): p. 7487-7494.
279. Boughbina-Portoles, A., et al., *Reliable assessment of carbon black nanomaterial of a variety of cell culture media for in vitro toxicity assays by asymmetrical flow field-flow fractionation.* Anal Bioanal Chem, 2023. **415**(11): p. 2121-2132.
280. Moreira-Alvarez, B., et al., *AF4-UV/VIS-MALS-ICPMS/MS for the characterization of the different nanoparticulated species present in oligonucleotide-gold nanoparticle conjugates.* Talanta, 2023. **256**: p. 124309.
281. Geissler, F., et al., *Optimization of hyphenated asymmetric flow field-flow fractionation for the analysis of silver nanoparticles in aqueous solutions.* Anal Bioanal Chem, 2021. **413**(27): p. 6889-6904.
282. Hsu, T.W., et al., *Revealing cholesterol effects on PEGylated HSPC liposomes using AF4-MALS and simultaneous small- and wide-angle X-ray scattering.* J Appl Crystallogr, 2023. **56**(Pt 4): p. 988-993.
283. Sajid, A., M. Castronovo, and F.M. Goycoolea, *On the Fractionation and Physicochemical Characterisation of Self-Assembled Chitosan-DNA Polyelectrolyte Complexes.* Polymers (Basel), 2023. **15**(9).

284. Gonzalez-Espinosa, Y., et al., *Characterisation of chitosan molecular weight distribution by multi-detection asymmetric flow-field flow fractionation (AF4) and SEC.* Int J Biol Macromol, 2019. **136**: p. 911-919.
285. Makan, A.C., et al., *Advanced analysis of polymer emulsions: Particle size and particle size distribution by field-flow fractionation and dynamic light scattering.* J Chromatogr A, 2016. **1442**: p. 94-106.
286. Bria, C.R.M., et al., *Asymmetrical flow field-flow fractionation for improved characterization of human plasma lipoproteins.* Anal Bioanal Chem, 2019. **411**(3): p. 777-786.
287. Bria, C.R. and S.K. Williams, *Impact of asymmetrical flow field-flow fractionation on protein aggregates stability.* J Chromatogr A, 2016. **1465**: p. 155-64.
288. Burchard, W., M. Schmidt, and W. Stockmayer, *Information on polydispersity and branching from combined quasi-elastic and intergrated scattering.* Macromolecules, 1980. **13**(5): p. 1265-1272.
289. Tande, B.M., et al., *Viscosimetric, hydrodynamic, and conformational properties of dendrimers and dendrons.* Macromolecules, 2001. **34**(24): p. 8580-8585.
290. Chen, Y., et al., *Asymmetrical flow field-flow fractionation coupled with multi-angle laser light scattering for stability comparison of virus-like particles in different solution environments.* Vaccine, 2016. **34**(27): p. 3164-3170.
291. Safenkova, I.V., et al., *Complex analysis of concentrated antibody-gold nanoparticle conjugates' mixtures using asymmetric flow field-flow fractionation.* J Chromatogr A, 2016. **1477**: p. 56-63.
292. Shen, C.-H., *Chapter 7 - Quantification and analysis of nucleic acids*, in *Diagnostic Molecular Biology (Second Edition)*, C.-H. Shen, Editor. 2023, Academic Press. p. 181-208.
293. Simonian, M.H., *Spectrophotometric determination of protein concentration.* Curr Protoc Cell Biol, 2002. **Appendix 3**: p. Appendix 3B.
294. Caldwell, K.D., et al., *Sample overloading effects in polymer characterization by field-flow fractionation.* Journal of Applied Polymer Science, 1988. **36**(3): p. 703-719.
295. Arfvidsson, C. and K.G. Wahlund, *Mass overloading in the flow field-flow fractionation channel studied by the behaviour of the ultra-large wheat protein glutenin.* J Chromatogr A, 2003. **1011**(1-2): p. 99-109.
296. Wijnhoven, J.E., et al., *Influence of injected mass and ionic strength on retention of water-soluble polymers and proteins in hollow-fibre flow field-flow fractionation.* Journal of Chromatography A, 1996. **732**(2): p. 307-315.
297. Debye, P., *Molecular-weight Determination by Light Scattering.* The Journal of Physical and Colloid Chemistry, 1947. **51**(1): p. 18-32.
298. Reinmuth-Selzle, K., et al., *Determination of the protein content of complex samples by aromatic amino acid analysis, liquid chromatography-UV absorbance, and colorimetry.* Anal Bioanal Chem, 2022. **414**(15): p. 4457-4470.
299. Marioli, M. and W.T. Kok, *Recovery, overloading, and protein interactions in asymmetrical flow field-flow fractionation.* Anal Bioanal Chem, 2019. **411**(11): p. 2327-2338.
300. Bria, C.R.M., et al., *Semi-preparative asymmetrical flow field-flow fractionation: A closer look at channel dimensions and separation performance.* Journal of Chromatography A, 2017. **1499**: p. 149-157.
301. Roessner, D. and W.-M. Kulicke, *On-line coupling of flow field-flow fractionation and multi-angle laser light scattering.* Journal of Chromatography A, 1994. **687**(2): p. 249-258.
302. Bohren, C.F. and D.R. Huffman, *Absorption and scattering of light by small particles*. 2008: John Wiley & Sons.
303. Andersson, M., B. Wittgren, and K.G. Wahlund, *Accuracy in multiangle light scattering measurements for molar mass and radius estimations. Model calculations and experiments.* Anal Chem, 2003. **75**(16): p. 4279-91.

304. Baalousha, M., et al., *Size fractionation and characterization of natural colloids by flow-field flow fractionation coupled to multi-angle laser light scattering.* J Chromatogr A, 2006. **1104**(1-2): p. 272-81.
305. Renaud, O. and M.-P. Victoria-Feser, *A robust coefficient of determination for regression.* Journal of Statistical Planning and Inference, 2010. **140**(7): p. 1852-1862.
306. Nevitt, J. and G.R. and Hancock, *Improving the Root Mean Square Error of Approximation for Nonnormal Conditions in Structural Equation Modeling.* The Journal of Experimental Education, 2000. **68**(3): p. 251-268.
307. Hundschell, C.S., F. Jakob, and A.M. Wagemans, *Molecular weight dependent structure of the exopolysaccharide levan.* Int J Biol Macromol, 2020. **161**: p. 398-405.
308. Lohrke, J., A. Briel, and K. Mader, *Characterization of superparamagnetic iron oxide nanoparticles by asymmetrical flow-field-flow-fractionation.* Nanomedicine (Lond), 2008. **3**(4): p. 437-52.
309. Hansen, M. and J.D. Clogston, *Assessment of Protein Binding Using Asymmetric-Flow Field-Flow Fractionation Combined with Multi-angle Light Scattering and Dynamic Light Scattering.* Methods Mol Biol, 2024. **2789**: p. 31-34.
310. Davidson, C.G., et al., *The Use of Enhanced Analytical Pipelines for the Characterization of Poly(A) and Poly(A)-LNP Formulation Critical Quality Attributes.* Molecular Pharmaceutics, 2025.
311. Roamcharern, N., et al., *Evaluating the impact of bioinspired counterion inclusion on silk nanoparticle physicochemical attributes and physical stability.* Nanoscale advances, 2025. **7**(18): p. 5519-5535.
312. Marassi, V., et al., *Native characterization and QC profiling of human amniotic mesenchymal stromal cell vesicular fractions for secretome-based therapy.* Talanta, 2024. **276**: p. 126216.
313. Qureshi, R. and W. Kok, *Optimization of asymmetrical flow field-flow fractionation (AF4).* 2010.
314. Wahlund, K.G., *Flow field-flow fractionation: critical overview.* J Chromatogr A, 2013. **1287**: p. 97-112.
315. Sitar, S., et al., *Pitfalls in Size Characterization of Soft Particles by Dynamic Light Scattering Online Coupled to Asymmetrical Flow Field-Flow Fractionation.* Anal Chem, 2017. **89**(21): p. 11744-11752.
316. Johann, C., *Developments in Field-Flow Fractionation Coupled to Light Scattering.* 2020.
317. Kerker, M., *The scattering of light and other electromagnetic radiation: physical chemistry: a series of monographs*. Vol. 16. 2013: Academic press.
318. Iavicoli, P., et al., *Application of Asymmetric Flow Field-Flow Fractionation hyphenations for liposome-antimicrobial peptide interaction.* J Chromatogr A, 2015. **1422**: p. 260-269.
319. Hupfeld, S., *Size characterisation of liposomes using asymmetrical flow field-flow fractionation : factors influencing fractionation and size determination.* 2009.
320. El Hadri, H., et al., *Optimization of flow field-flow fractionation for the characterization of natural colloids.* Anal Bioanal Chem, 2014. **406**(6): p. 1639-49.
321. Fuentes, C., et al., *Application of asymmetric flow field-flow fractionation (AF4) and multiangle light scattering (MALS) for the evaluation of changes in the product molar mass during PVP-b-PAMPS synthesis.* Anal Bioanal Chem, 2018. **410**(16): p. 3757-3767.
322. Von der Kammer, F., et al., *Separation and characterization of nanoparticles in complex food and environmental samples by field-flow fractionation.* TrAC Trends in Analytical Chemistry, 2011. **30**(3): p. 425-436.
323. Omar, J., et al., *Optimisation of asymmetric flow field-flow fractionation for the characterisation of nanoparticles in coated polydisperse TiO(2) with applications in*

food and feed. Food Addit Contam Part A Chem Anal Control Expo Risk Assess, 2016. **33**(12): p. 1775-1784.
324. Ly, H.H., et al., *Optimization of Lipid Nanoparticles for saRNA Expression and Cellular Activation Using a Design-of-Experiment Approach.* Mol Pharm, 2022. **19**(6): p. 1892-1905.
325. Paunovska, K., et al., *A Direct Comparison of in Vitro and in Vivo Nucleic Acid Delivery Mediated by Hundreds of Nanoparticles Reveals a Weak Correlation.* Nano Lett, 2018. **18**(3): p. 2148-2157.
326. Trinh, D.N., et al., *Biomolecular Corona Stability in Association with Plasma Cholesterol Level.* Nanomaterials (Basel), 2022. **12**(15).
327. Pozzi, D., et al., *The biomolecular corona of nanoparticles in circulating biological media.* Nanoscale, 2015. **7**(33): p. 13958-66.
328. Walczyk, D., et al., *What the cell "sees" in bionanoscience.* Journal of the American Chemical Society, 2010. **132**(16): p. 5761-5768.
329. Deng, Z.J., et al., *Nanoparticle-induced unfolding of fibrinogen promotes Mac-1 receptor activation and inflammation.* Nature nanotechnology, 2011. **6**(1): p. 39-44.
330. Walkey, C.D. and W.C. Chan, *Understanding and controlling the interaction of nanomaterials with proteins in a physiological environment.* Chemical Society Reviews, 2012. **41**(7): p. 2780-2799.
331. Debnath, M., et al., *Protein Corona Formation on Lipid Nanoparticles Negatively Affects the NLRP3 Inflammasome Activation.* Bioconjug Chem, 2023. **34**(10): p. 1766-1779.
332. McEvoy, M., et al., *Improved particle counting and size distribution determination of aggregated virus populations by asymmetric flow field-flow fractionation and multiangle light scattering techniques.* Biotechnol Prog, 2011. **27**(2): p. 547-54.
333. Evjen, T.J., et al., *Physicochemical characterization of liposomes after ultrasound exposure - mechanisms of drug release.* J Pharm Biomed Anal, 2013. **78-79**: p. 118-22.
334. Parot, J., et al., *Quality assessment of LNP-RNA therapeutics with orthogonal analytical techniques.* J Control Release, 2024. **367**: p. 385-401.
335. Capomaccio, R., et al., *Determination of the structure and morphology of gold nanoparticle-HSA protein complexes.* Nanoscale, 2015. **7**(42): p. 17653-7.
336. Winzen, S., et al., *Complementary analysis of the hard and soft protein corona: sample preparation critically effects corona composition.* Nanoscale, 2015. **7**(7): p. 2992-3001.
337. Bohmert, L., et al., *Isolation methods for particle protein corona complexes from protein-rich matrices.* Nanoscale Adv, 2020. **2**(2): p. 563-582.
338. Medscape. *Albumin Reference Range*. Available from: https://emedicine.medscape.com/article/2054430-overview?form=fpf.
339. Dridi, N., et al., *Probing Protein Corona Formation around Gold Nanoparticles: Effects of Surface Coating.* ACS Nano, 2024. **18**(12): p. 8649-8662.
340. Cebula, D.J., R.K. Thomas, and J.W. White, *Small angle neutron scattering from dilute aqueous dispersions of clay.* Journal of the Chemical Society, Faraday Transactions 1: Physical Chemistry in Condensed Phases, 1980. **76**(0): p. 314-321.
341. 4, T.C.I.T.S., *ISO 22412:2025 Particle size analysis — Dynamic light scattering (DLS)*. 2025.
342. Suzuki, Y. and H. Ishihara, *Difference in the lipid nanoparticle technology employed in three approved siRNA (Patisiran) and mRNA (COVID-19 vaccine) drugs.* Drug Metab Pharmacokinet, 2021. **41**: p. 100424.
343. Binici, B., et al., *The Role of Biological Sex in Pre-Clinical (Mouse) mRNA Vaccine Studies.* Vaccines (Basel), 2024. **12**(3).
344. Wyatt, P.J., *Light scattering and the absolute characterization of macromolecules.* Analytica chimica acta, 1993. **272**(1): p. 1-40.

345. Ahmad, M., et al., *Differentiation of HSA and BSA and Instantaneous Detection of HSO(3) (-) Using Confined Space of Serum Albumins and Live Cell Imaging of Exogenous/Endogenous HSO(3)().* ACS Omega, 2023. **8**(2): p. 2639-2647.
346. Hoover, B.M. and R.M. Murphy, *Evaluation of Nanoparticle Tracking Analysis for the Detection of Rod-Shaped Particles and Protein Aggregates.* Journal of Pharmaceutical Sciences, 2020. **109**(1): p. 452-463.
347. Chen, S., et al., *Surface hydration: Principles and applications toward low-fouling/nonfouling biomaterials.* Polymer, 2010. **51**: p. 5283-5293.
348. Partikel, K., et al., *Effect of nanoparticle size and PEGylation on the protein corona of PLGA nanoparticles.* Eur J Pharm Biopharm, 2019. **141**: p. 70-80.
349. Bouchemal, K., *New challenges for pharmaceutical formulations and drug delivery systems characterization using isothermal titration calorimetry.* Drug Discov Today, 2008. **13**(21-22): p. 960-72.
350. Vonarbourg, A., et al., *Parameters influencing the stealthiness of colloidal drug delivery systems.* Biomaterials, 2006. **27**(24): p. 4356-73.
351. Klibanov, A.L., et al., *Amphipathic polyethyleneglycols effectively prolong the circulation time of liposomes.* FEBS Lett, 1990. **268**(1): p. 235-7.
352. Suzuki, T., et al., *PEG shedding-rate-dependent blood clearance of PEGylated lipid nanoparticles in mice: Faster PEG shedding attenuates anti-PEG IgM production.* Int J Pharm, 2020. **588**: p. 119792.
353. Rabe, M., D. Verdes, and S. Seeger, *Understanding protein adsorption phenomena at solid surfaces.* Advances in Colloid and Interface Science, 2011. **162**(1): p. 87-106.
354. Leckband, D. and J. Israelachvili, *Intermolecular forces in biology.* Q Rev Biophys, 2001. **34**(2): p. 105-267.
355. Wang, X., et al., *Rearrangement of protein structures on a gold nanoparticle surface is regulated by ligand adsorption modes.* Nanoscale, 2021. **13**(48): p. 20425-20436.
356. Ferraresso, F., et al., *Comparison of DLin-MC3-DMA and ALC-0315 for siRNA Delivery to Hepatocytes and Hepatic Stellate Cells.* Mol Pharm, 2022. **19**(7): p. 2175-2182.
357. Borjesdotter, A.M., et al., *Lipid nanoparticle properties explored using online asymmetric flow field-flow fractionation coupled with small angle X-ray scattering: Beyond average characterisation.* Int J Pharm, 2025. **668**: p. 124940.
358. Dane, E.L., et al., *New ionizable lipids for non-viral mRNA delivery with secondary amine cyclic ether head groups.* RSC Med Chem, 2025.
359. Guo, K., et al., *A novel ionizable lipid with comprehensive improvements in transfection potency, immune profile and safety of lipid nanoparticle.* J Control Release, 2025. **386**: p. 114126.
360. Hwang, Y.H., et al., *Robust, Scalable Microfluidic Manufacturing of RNA-Lipid Nanoparticles Using Immobilized Antifouling Lubricant Coating.* ACS Nano, 2025. **19**(1): p. 1090-1102.
361. Roy-Chowdhury, N. and J. Roy-Chowdhury, *Chapter 72—Liver Physiology and Energy Metabolism.* Sleisenger and Fordtran's Gastrointestinal and Liver Disease (Ninth Edition); Feldman, M., Friedman, LS, Brandt, LJ, Eds: p. 1207-1225.
362. Zhang, L., et al., *Morphology and structure of lipoproteins revealed by an optimized negative-staining protocol of electron microscopy.* J Lipid Res, 2011. **52**(1): p. 175-84.
363. Sebastiani, F., et al., *Screening of the binding affinity of serum proteins to lipid nanoparticles in a cell free environment.* J Colloid Interface Sci, 2022. **610**: p. 766-774.
364. Huang, R., et al., *Apolipoprotein A-I structural organization in high-density lipoproteins isolated from human plasma.* Nat Struct Mol Biol, 2011. **18**(4): p. 416-22.
365. Simon, J., et al., *Exploiting the biomolecular corona: pre-coating of nanoparticles enables controlled cellular interactions.* Nanoscale, 2018. **10**(22): p. 10731-10739.

366. Giddings, J.C., *A new separation concept based on a coupling of concentration and flow nonuniformities.* Separation Science, 1966. **1**(1): p. 123-125.
367. Moon, M.H., H. Kwon, and I. Park, *Stopless flow injection in asymmetrical flow field-flow fractionation using a frit inlet.* Anal Chem, 1997. **69**(7): p. 1436-40.
368. Fuentes, C., et al., *Comparison between conventional and frit-inlet channels in separation of biopolymers by asymmetric flow field-flow fractionation.* Analyst, 2019. **144**(15): p. 4559-4568.
369. Chuan, Y.P., et al., *Quantitative analysis of virus-like particle size and distribution by field-flow fractionation.* Biotechnol Bioeng, 2008. **99**(6): p. 1425-33.
370. Yohannes, G., et al., *Asymmetrical flow field-flow fractionation technique for separation and characterization of biopolymers and bioparticles.* J Chromatogr A, 2011. **1218**(27): p. 4104-16.
371. Beer, L.A. and D.W. Speicher, *Protein Detection in Gels Using Fixation.* Curr Protoc Protein Sci, 2018. **91**: p. 10.5.1-10.5.20.
372. Hellstrand, E., et al., *Complete high-density lipoproteins in nanoparticle corona.* FEBS J, 2009. **276**(12): p. 3372-81.
373. Hajipour, M.J., et al., *Personalized protein coronas: a "key" factor at the nanobiointerface.* Biomater Sci, 2014. **2**(9): p. 1210-1221.
374. Lima, T., et al., *Understanding the Lipid and Protein Corona Formation on Different Sized Polymeric Nanoparticles.* Sci Rep, 2020. **10**(1): p. 1129.
375. Aliyandi, A., et al., *Correlating Corona Composition and Cell Uptake to Identify Proteins Affecting Nanoparticle Entry into Endothelial Cells.* ACS Biomater Sci Eng, 2021. **7**(12): p. 5573-5584.
376. Zhang, L., et al., *Dual effects of fibrinogen decoration on the tuning of silica nanoparticles-induced autophagic response: The implication of sedimentation and internalization.* Journal of Hazardous Materials, 2021. **408**: p. 124467.
377. Shemetov, A.A., I. Nabiev, and A. Sukhanova, *Molecular interaction of proteins and peptides with nanoparticles.* ACS nano, 2012. **6**(6): p. 4585-4602.
378. Chen, F., et al., *Complement proteins bind to nanoparticle protein corona and undergo dynamic exchange in vivo.* Nature nanotechnology, 2017. **12**(4): p. 387-393.
379. Gursky, O., *Structural stability and functional remodeling of high-density lipoproteins.* FEBS Letters, 2015. **589**(19, Part A): p. 2627-2639.
380. Brantmeier, S.A., R.R. Grummer, and R.L. Ax, *Concentrations of High Density Lipoproteins Vary Among Follicular Sizes in the Bovine1.* Journal of Dairy Science, 1987. **70**(10): p. 2145-2149.
381. von Eckardstein, A., et al., *High-density lipoprotein revisited: biological functions and clinical relevance.* Eur Heart J, 2023. **44**(16): p. 1394-1407.
382. Paunovska, K., et al., *The Extent to Which Lipid Nanoparticles Require Apolipoprotein E and Low-Density Lipoprotein Receptor for Delivery Changes with Ionizable Lipid Structure.* Nano Lett, 2022. **22**(24): p. 10025-10033.
383. Bleshøy, S.V., *BPS2025 - Varying protein corona compositions affect endosomal escape propensities of selective organ-targeting lipid nanoparticles.* Biophysical Journal, 2025. **124**(3): p. 593a.
384. 229, T.C.I.T., *ISO 21362:2026 Nanotechnologies — Analysis of nano-objects using asymmetrical flow and centrifugal field-flow fractionation*. 2026.
385. Kontush, A., et al., *Structure of HDL: Particle Subclasses and Molecular Components*, in *High Density Lipoproteins: From Biological Understanding to Clinical Exploitation*, A. von Eckardstein and D. Kardassis, Editors. 2015, Springer International Publishing: Cham. p. 3-51.